An Experimental Investigation and a Multiscale Electro-thermo-mechanical Model of a Flat Pin High Power Electrical Connector

by

Santosh V. Angadi

A dissertation submitted to the Graduate Faculty of
Auburn University
in partial fulfillment of the
requirements for the Degree of
Doctor of Philosophy

Auburn, Alabama
December 12, 2011

Keywords: Electrical connector, multi-physics,
finite element model/experiment

Approved by

Robert Jackson, Chair, Associate Professor of Mechanical Engineering
Song-Yul Choe, Associate Professor of Mechanical Engineering
Jeffrey Suhling, Professor of Mechanical Engineering
George Flowers, Professor of Mechanical Engineering

Abstract

Hybrid and electrical vehicles (HEV) are the next evolutionary step in automobile technology. However, the electrical systems which propel HEVs are fundamentally different from conventional technologies. Therefore, a few limiting technologies will delay widespread HEV success such as the battery, power electronics and connectors. The high temperatures, vibrations, humidity, and contamination in a vehicle can reduce the reliability of these technologies.

HEV electrical connectors conduct much more power and are more susceptible to failure and reliability problems than the connectors in conventional vehicles. Thus, in this work, a 40A high power electrical connector, used in HEVs, has been studied extensively by both modeling and experimental approaches.

In this work, a multi-physics (involving structural, electric and thermal coupled fields) finite element model considering multi-scale rough surface contact of the 40A high power connector is created. This cutting-edge model includes the coupled effects of nano to macro-scale surface roughness, contact pressures, electrical and thermal contact resistances, stresses, displacements, applied currents, electric potential (voltage drop), current density, temperature, Joule heating and thermal expansion. It is a powerful tool that can be used for fundamental connector characterization, prototype evaluation and design.

A few prominent findings were made from the results of the 40A connector model. It appears that the current flows mostly through very small regions that are usually near the

contacting surfaces in the connector, thereby suggesting that the available conducting material can be more efficiently used by developing optimized connector designs. Interestingly, from the 40A connector model, it was found that the temperature rise (ΔT or change in temperature) in the bulk material is not very high, although ΔT values measured experimentally indicate otherwise. Through analytical calculations and experimental measurements of ΔT for the cable and the connector, it is believed that a large portion of the temperature rise in actual 40A connectors is due to the Joule heating in the supply cables. However, the local asperity temperature is also theoretically calculated and should be very high at the contact, which could cause an increased oxidation rate and surface melting.

Coming to the experimental investigation in this work, 40A connectors were tested under both stationary as well as vibrating situations. For stationary tests, an increase in connector resistance and connector temperatures with an increase in applied currents is noticed. Also, more importantly, the same increasing trend of connector resistance with respect to applied currents is observed in both the 40A connector model and the stationary connector tests.

An environmentally controlled and accelerated 40A connector test methodology was designed and created to characterize connector degradation and fretting under vibrating conditions. This includes the necessary hardware to control connector conditions and to monitor current, voltage drop, connector resistance (R) and connector temperature (T) in real time. A series of parametric tests were completed where the effects of vibration direction, amplitude, frequency, temperature and humidity on R and T were studied.

Based on the accelerated test results, larger increases in the values of average and maximum R occur from vibrations in the Y direction (perpendicular to cable axis (Z)). Significant change in R and T (either, average or maximum) occurs at the highest vibration

frequency of 200 Hz and in the Y direction. Increase in R could be due to an increase in T, fretting corrosion and wear. Also, frictional heating and increased Joule heating lead to an increase in T.

Acknowledgements

I wish to acknowledge my sincere gratitude to my advisor, Dr. Robert L. Jackson, for his great motivation, continuous support and encouragement during the course of this study. I would like to thank my committee members, Dr. Song-Yul Choe, Dr. Jeffrey C. Suhling, Dr. George T. Flowers and University Reader, Dr. Robert Dean at Auburn University for their continuous support in this study. I deeply acknowledge and extend gratitude for financial support from the NSF Center for Advanced Vehicle and Extreme Environment Electronics ($CAVE^3$) at Auburn University.

I would like to express deep gratitude and gratefulness to my parents, grandparents, sister, brother-in-law, relatives for their enduring love, immense moral support and encouragement towards accomplishing this goal in my life. I also wish to thank all my colleagues at Auburn and friends for their friendship and help.

Table of Contents

List of Tables

List of Figures

List of Abbreviations

A	area of contact
$\overline{A}$	individual asperity area of contact
A_n	nominal contact area
a	radius of the area of contact
C	critical yield stress coefficient
d	separation of mean asperity height
E	elastic modulus
E'	$E/(1-\nu^2)$
f	spatial frequency (reciprocal of wavelength)
k	thermal conductivity
P	contact force
$\overline{P}$	individual asperity contact force
$\overline{p}$	mean pressure
p^*	average pressure for complete contact
S_y	yield strength
Er_i	electrical contact resistance per scale or frequency level
ECR	electrical contact resistance
TCR	thermal contact resistance

Greek Symbols

η	area density of asperities
λ	asperity wavelength
ρ_L	electrical resistivity of surface material
Δ	asperity amplitude
v	Poisson's ratio

Subscripts

E	elastic regime
P	plastic regime
c	critical value at onset of plastic deformation
i	scale or frequency level
JGH	from Johnson, Greenwood, and Higginson [2]
asp	asperity
L	electrical

CHAPTER 1

Background

1.1 Hybrid Electric Vehicles (HEVs)

With the appearance of electric and hybrid electric vehicles, designers are faced with new challenges. The goal of basic vehicle design is to generate high power while minimizing weight and drag forces to maximize fuel economy. With that in mind, the major car companies are continuously juggling with the decisions of electric motor and internal combustion engine (ICE) sizes and power, battery size and capacity, and most importantly how to maximize the potential of each constituent through precise controls. For instance, when implementing the electric motor and advanced battery chemistries, there is obviously additional power available to the vehicle, but there is also the additional weight for the motors to overcome. Through the design process, slight variations are made to accepted configurations, but for the most part there are a few basic blueprints for the design of all hybrid electric and electric vehicles.

There are two major designs of electric vehicles that currently capture the majority of the market. First, hybrid electric vehicles (HEV) incorporate an electric motor along with the standard ICE to provide additional power to decrease fuel consumption while recharging the battery at specified portions of the driving cycle. In addition, there are plug-in hybrid electric vehicles (PHEV), which rely on the traditional ICE and the energy supplied by an externally charged battery to power an electric motor.

Hybrid configurations appear in a variety of arrangements with the major classifications being the ‘parallel’ and ‘series’ configurations. In a series hybrid, the system consists of an ICE and an electric motor connected in series, although the vehicle only experiences a driving force from the electric motor. As a result, all the electrical energy must pass through both the motors and the generator raising the cost substantially.

The parallel hybrid configuration also incorporates an ICE and electric motor and can be engaged separately or simultaneously to achieve maximum fuel economy. Parallel hybrid allows for a wide range of uses while series hybrids are reserved for specific applications. Typically, parallel hybrids employ only the electric motor for city travel and utilize the ICE engine for highway travel. Ideally the electric motor, ICE, and battery would be used in unison to obtain greater performance. As a result of the complex multiple motor systems, advanced transmissions such as continuously variable transmissions (CVT) are incorporated. A popular design receives around 50% peak power from the ICE while relying on the electric motor and battery for the additional boost. When the battery is not needed, the generator proceeds to charge the battery during highway travel or through regenerative braking.

1.2 Motivation

Connectors are an important and critical component of any vehicle containing electrical components. Detachable connectors are desired for durable and easily removed connections. This is especially important for the easy replacement and repair of electrical components. Connectors in HEVs are known to carry very high currents (high power) [3] and due to this there can be a tremendous increase in temperature in these parts during service. High power and the automotive environment (high temperature, vibrations, humidity, etc.) can cause degradation and failure of the connectors. If the connector contacts degrade, the contact resistance can increase and cause other problems with the power electronics and controls of the electrical power drive system. Eventually connectors could catastrophically fail and become either permanently welded together or effectively non-conductive.

High electrical power is required for new vehicles which use electrical propulsion (Hybrids, Plug-in, Fuel Cell, etc.). Therefore, the electrical components (connectors, batteries, power electronics, wiring harnesses, etc.) in these vehicles must be able to handle these higher powers. Hence, the main motivation of the current work is to study the reliability and performance of 40A (high power) connectors used in HEV vehicles through modeling and experiment. More specifically, a joint effort of multiscale rough surface contact/multi-physics finite element modeling and experimental testing of these connectors under both vibrating (that is, accelerated test conditions) and stationary conditions has been carried out.

1.3 Literature review

The fretting behavior occurring in various contact regions of electrical connectors has been an important area of research for three decades. Fretting wear and corrosion are the two major degradation mechanisms, which have been the focus of most research studies. Contact degradation, caused by fretting, occurs as a result of relative motion between two surfaces and this degradation decreases the performance of the contact. This section reviews existing literature on the performance and fretting of electrical connectors in chronological order. This includes both experimental and theoretical work. There are very few papers on fretting in high power connectors and so the focus is mainly on conventional low power connectors.

Switchgear connectors show limitations for applications with high currents [4]. Additionally, due to their size, high resistance and high rack-on forces, several problems arise. Allen [4] suggests that usage of large quantities of independent and well defined contact spots is a solution for many of their problems. Current sustainability and resistance were analyzed and comparison is made with the experiment.

In the work by Olsson and Oberg [5], by taking into consideration structural design variables, data related to testing of current cycle for electrical contact resistance and service of longer duration were analyzed. For the condition of the surface force that is held constant, a study was done on the significance of the contact pressure distribution. Using the finite elements method, stresses are calculated at the contact surface. Contact resistance is reduced and good stability at longer durations is observed for high contact pressures. The connectors' aging properties are also affected largely by the contact pressure distribution at the surface. From the study, the methods of surface preparation are shown to greatly affect the aging phenomena.

Intermetallic phases generation and fretting are the two aging phenomena that are documented at the contact surfaces.

A model has been developed by Bryant [6] to determine the electrical contact usable lifetime and contact resistance at any fretting cycle. Several key variables such as frequency and fretting amplitude, contact coating thickness, applied current, normal load, etc. are included into this model [6]. A few important observations can be made from this work. With time, the contact resistance increases in a monotonic fashion. However, large increases in contact resistance can be seen after the initial period. The time to failure of contacts found in field measurements compares well with that predicted by the model.

On subjecting a contact to a high number of cycles or as a result of long term usage, the contacts may be thermo-mechanically damaged. In addition, the contacts may get oxidized or contaminated. Under these situations, the contacts are prone to failure due to the added resistance of the less conductive layers. Thus, this paper by Minowa and Nakamura [7] studies the contact surface state along with the electric conductivity through the finite element method approach. Within a contact spot, the distribution of current density was also determined.

The study by Ando and Imori [8] investigates the properties of contact resistance on the connector contacts that are plastically deformed. Experiments involving needle type contacts that are inserted inside a plane plate contact were carried out. The experimental results correlated well with those obtained from a tunnel resistivity based theory on contact resistance. The material at the contact is the base metal, which necessitates a key issue of the surface film structural disruption at the contact to be addressed.

Rudolphi and Jacobson [9] studied two types of silver plated copper electrical contacts by subjecting them to rolling effects testing in a crossed cylinder contact configuration. One of the two types of silver plated copper contacts contained a middle layer of nickel.

Gross plastic fretting is a type of degradation mechanism that involves plastic deformation of electrical contacts [9]. Both vibrations and large contact forces lead to gross plastic fretting in electrical contacts. In both near elastic and plastic conditions, three regimes of fretting are defined. These three plastic deformation regimes, namely, gross weld, temporary weld and gross slip, have specific influence or impact on friction, adhesion and surface damage.

In a normal crossed cylinders test, the cylinders are held in a fixed position. However, the paper by Rudolphi and Jacobson [9] reported that when only a single of the two cylinders in this crossed cylinders test is allowed to rotate angularly rather than holding it fixed, the damage imparted to the surface is immensely lowered, frictional stresses are greatly lowered and this may facilitate the electrical contact life under vibration conditions to be prolonged. More friction is seen in the case of sliding than on rolling. This is a well established fact. Also, under vibration situations of electrical contacts, the damage to the contact area can be minimized if the slip is reduced. Fretting corrosion does not occur if the coating of silver does not show wear and thus allows the contact resistance to be low and stable. The study on angular rolling contact of the silver coated copper contact shows that the contact resistance is increased due to an intermediate layer of nickel in copper contacts with a silver coating compared to those contacts without the nickel layer [9].

Copper alloy based electrical contacts are largely plated with tin, which is a low cost material. Tristani, et al. [10] developed a mechanical model based on the very nature or appearance (with respect to shape) of the tangential force-displacement curves obtained by

conducting tests on fretting corrosion for connector terminals. This model deals with the wear track profile, stiffness as well as the dynamic friction coefficient. Following the study of the plots [10], two key observations are that over the complete fretting cycle, sliding is not seen in connector terminals. Also, the stiffness, normal force and wear region profiles affect fretting duration differently for each particular type of electrical contact.

The work by Antler [11] deals with the fretting degradation mechanism, studying the contact materials behaviour and the factors influencing the contact resistance. In addition, the recommendations to control the fretting process in the case of electronic connectors are presented [11]. The fretting process may result in unstable contact resistance in a vibrating connector. During fretting, there will be build up of an insulating layer of oxide on the electrical contact surface. Naturally occurring vibrations and thermal fluctuations (cycling) cause the movement of electrical contacts leading to their fretting. If the frequency of vibration is low, then the number of cycles to cause failure of the contact is also few, but this finding seems questionable. The contact connection is stabilized either by lowering the fretting vibration amplitude or increasing the normal load at the contact. Fretting failure is common when tin is used as a plating material in most of its alloys. A better contact is a contact that is made up of only tin compared to the one containing a combination of tin and gold. The failure of the contacts due to fretting can be prevented generally through the use of lubrication at the contact. Lubricating the contacts may allow for longer lives and extend the use of contacts that have already failed in the non-lubricated condition.

According to Swingler [12], fretting corrosion is among the primary failure mechanisms occurring at the electrical contact interface in automotive connectors. This type of corrosion causes contact resistance to increase irradically. Fretting corrosion is induced at electrical

contacts or at contacting regions in components of connector samples by employing a fretting apparatus or test set up subjected to low frequencies. The influence of the varying thermal expansion coefficients of the materials for the components of a connector is simulated or modeled by using low frequency. The initial occurrence of the contact resistance of high values at the contacting regions is delayed by powering the connector at low frequencies. Oxidation of the contact surface is predicted to be hastened due to the temperature rise from Joule heating. However, considering the fretting conditions used in this work, there was dominance of films' electrical breakdown. Two other observations from this work are: (a) less conductive debris is seen at the ends of the wear region of the fretting subjected contact surface or interface, and (b) due to fretting under low frequencies, there is a marginal effect from frictional heating.

In the work by Swingler and McBride [13], studies related to the fundamental aspects and that are performed on terminals of the connectors, available on a commercial basis, are combined through the development of the reliability model on multicontacts. Two key issues are taken into account. At first, for a contact interface with a single contact, the contact resistance could regain its lower value once a high contact resistance value is reached. Then, for terminals with many contact interfaces, the simultaneous occurrences of the individual interface failures will lead to the failure of whole connector.

A paper by Malucci [14] deals with the studies on fretting corrosion of tin plated electrical contacts. Laboratory tests involve vibrations and thermal cycling in accelerated conditions. These tests aroused the development of an empirical model. As fretting advanced, several observations such as electrical stability and formation of an oxide film on the contact surface were made [14]. A fretting amplitude parameter helped to determine the threshold

behaviour at which fretting corrosion begins or initiates. Fretting motion is caused either by thermal cycling or natural vibration in real or actual connectors.

In another paper, fretting corrosion is induced in contacts present in connectors through vibration tests and each connector is subjected to only one vibration frequency [15]. The contacts are plated with tin alloy. Several frequencies and vibration levels are applied during the experimental tests. Contact resistance is chosen as the parameter to characterize the performance of the connectors. For each of the vibration frequency, fretting degradation is initiated once a threshold state is demonstrated by the connectors.

The high temperature coefficient difference between the constriction resistance and the film resistance is used to distinguish these two resistances by Takano [16]. The contact resistance was measured by employing a 'low DC voltage method'. A very thin insulating gap between the contacts causes the generation of film or tunnel resistance along with the constriction resistance seen in the electrodes or contacts. The work theorizes that tunneling (film) resistance together with constriction resistance leads to total contact resistance. Due to film resistance instability, the film resistance's content is also an important variable for electrical contact reliability studies.

Micro-scale wear tracks are observed by He and Xu [17] on failed electrical contacts. Due to contacting materials, a debris of wear is created when micro motion occurs. Additionally, by micro motion, oxidation of contacting materials and contact resistance (varying and high) are seen. Shocks as well as vibration lead to micro motion and are analyzed.

Random profiles of vibration are employed to test the connectors by Flowers, et al. [18]. The authors created a model wherein the rate of fretting corrosion in the early stage is related to the threshold levels of vibration, the profile of vibration and the dynamic features of the test configuration. The model correlates very well with the experimental results. During the

vibration tests, a specific threshold is seen no matter what the vibration profile that is implemented to excite the entire system.

Vibration tests were carried out by Ben Jemaa and Carvou [19] for an automotive connector terminal to study the amount of wear and its electrical behavior. The authors demonstrated that as the amount of wear increases, the constriction or contact voltage also increases on the order of millivolts and as the amount of degradation (that is, fretting) further increases, the arcing voltage (nearly 12 V) is observed. In addition, when the contact voltage is increased to melting and then arcing voltage, it causes thermal effects and this increases the amount of degradation. This mechanism relates to the case of a high power connector. The surface of the connector terminal in this work is also tin coated (similar to the 40A connector considered in the current work that has tin as the surface finish).

The true area of contact at the contacting locations is the primary parameter that influences both contact resistance and friction. The key parameters are both contact resistance as well as friction in switches and connectors in which sliding contact occurs. Higher contact force leads to lower contact resistance values. However, there is a rise in the friction force. The present work by Tamai [20] developed an equation that relates the friction and contact resistance. Additionally, experimental studies were conducted on the friction and contact resistance relationship for different contact surfaces subjected to various operating conditions.

Park, et al. [21] studied the behavior of fretting related wear for copper alloy electrical contacts containing tin plating and the contact resistance dependency on fretting wear. Contact resistance was noticed to be stable and low during the initial cycles. In order to explain this observation, the authors developed a model on the basis of contact zone variation and depth of wear versus fretting cycles. Scanning electron microscope (SEM), X-ray mapping, energy

dispersive X-ray scanning and EDX spot analysis were used to examine the changes that occur in the contact area zone and to estimate the amount of tin coating wear and wear debris buildup with respect to fretting cycles. As the tin coating is removed continuously, the area of the fretted zone linearly increased until approximately 8000 cycles are reached. This expansion of the fretted zone becomes saturated once the maximum limit of the fretting length is reached. The electrically conduction path established due to consistent constant contact area leads to the observance of stable and low contact resistance until 8000 cycles are reached. Key regimes of fretting corrosion as well as fretting wear are demonstrated on the basis of contact resistance variation with respect to fretting cycles. Fretting corrosion phenomenon, occurring in electrical contacts with tin plating, becomes more complicated due to the mutual dependence of the amount of oxidation and wear [21].

A small power connector is analyzed for its thermal behavior by Wang and Xu [22]. It was noticed that Joule heating caused an increase in the contact resistance. The paper discusses the connector failure mechanism which can be used to improve the connector design or structure. Finite element analysis is employed to analyze the connector temperature distribution. The experimental and finite element analysis results show a better correlation.

Ossart, et al. [23] analyzed multilayer electrical contacts for their electromechanical behavior through numerical simulation. A thin surface layer of tin protects a ball-plane contact that is made of a CuZn alloy material. Contact resistance of the entire component is calculated through a finite element coupled field (mechanical and electrical) analysis. Experimental results are compared to the simulation results. When considering low tin layer resistivity values, a decent agreement is noticed between the model calculations and the experimental measurements for tin layer thicknesses in the range of 1 – 10 μm.

Through the fretting corrosion process, the degradation of the electrical contacts is primarily caused by the vibration and relative motion of contact surfaces. In the work by Carvou and Jemaa [24], the contact interface's electrical response was examined by subjecting it to vibration and its variations were characterized while fretting is in progress. Vibrations in large numbers were imposed on an individual point contact under conditions of 50 μm amplitude and 100 Hz. A circuit (10A and 14V) of resistive type constituted the contact. Electrical phenomena cause fluctuations/variations to appear, which is dependent on the stage of degradation. The faster fluctuations correspond to perturbation of electrical conduction. The fluctuations that are slow correlate better to the period of vibration. Also, the work examines the occurrence of self heating due to contact voltage being high owing to current levels being of high values.

Park, et al. [25] studied various factors that affect fretting corrosion of tin plated electrical contacts. These factors include normal load, applied current, frequency, fretting amplitude, temperature and humidity. In the conducted fretting corrosion tests, the gross slip fretting of the electrical contacts is considered. Contact resistance versus fretting cycles curves are generated from the tests and the information on the duration required to attain a contact resistance threshold point of 100mΩ can also be obtained from the experimental tests on fretting corrosion. The fretting corrosion mechanism in the case of tin-plated electrical contacts is explained on the basis of studies done on surface profile variations and contact zone changes through laser scanning microscope (LSM) and other techniques.

According to Park, et al. [25], the lifetime or longevity of electrical contacts bearing tin plating on their surfaces is enhanced considerably by lubricating the contacts. The tin plating wear rate is also enhanced when higher frequencies are used. However, higher oxidation rates are noticed when lower frequencies are employed during tests on fretting corrosion. The higher the

fretting amplitude, the higher is the amount of oxidation that is observed. In reality, humidity (that is, moisture or water vapour in condensed form) functions like a lubricant and this lubricant reduces the tin plating wear rate. Also, when normal loads are higher, the tin plating wear rate is also higher. However, at smaller normal loads, there is a higher oxidation rate. The oxide film is broken leading to a firm electrical contact when the applied current load is higher [25].

In the work by Abdi and Benjemaa [26], a laser probe is used to determine the contact force through the spring deflection measurement. Contact resistance, insertion force and contact force obtained from contact deflection are measured during insertion. A larger contact region is created depending upon the width of the spring. The effect of the connector geometry variables on the insertion force, the contact force and the contact resistance has been demonstrated.

For various contact geometries and contact loads, the changes in contact resistance were determined in a study by Abdi, et al. [27]. New high copper alloy samples were tested by insertion and indentation methods. Contact models, with and without roughness, were generated in ANSYS^{TM} and a profilometer was used to measure the actual roughness. For indentation tests with lower forces, a close agreement was seen between experimental results and the results of the numerical model that considers roughness. The work also establishes the contact force and contact resistance relation.

The work by McBride [28] investigated the intermittency events taking place at high frequencies during the process of fretting in in-vivo electrical contact surfaces. The fretting process study related the surface wear to the contact resistance, for various applied forces. The intermittency events while fretting and the performance of the contact surface were largely affected by the fretting cycle amplitude.

A contacting pair of a blade and receptacle was studied initially by means of a finite element based model in a simplistic 2D way and the model was correlated to experiments [29]. The work by Chen, et al. [30] is an extension to this initial primary study in that for the above connector set up or configuration, an extensive 3D model was developed and the effects of several parameters were evaluated such as normal force, friction coefficient at the interface, wire mass, etc. through analysis. The model was tested and validated through several experiments. This study shows that the effect of connector design changes on the fretting phenomenon can be evaluated by using finite element based analysis and simulation.

In the work by Chudnovsky, et al. [31], experimental direct measurements of the temperature of powered contact surfaces in a low voltage circuit breaker were analyzed statistically. The contact interfaces of 3200A low voltage circuit breakers were studied for their thermal behavior under both “aged” (in an artificial way) and new conditions. A circuit breaker with three phases is considered and data for each phase having four points of contact is gathered or obtained experimentally. A reliable mathematical model stating the relation among the rise in temperature in electrical contact interfaces and large variations in current was found.

At different applied currents, brass electrical contacts that have a tin coating were studied by Park, et al. [32] for fretting corrosion. The variation of contact resistance with respect to fretting cycles is addressed in detail. Scanning electron microscope (SEM), laser SEM, and the X ray based dispersive analysis technique are employed to study the surface profile, surface morphology and contact area chemical element distribution. Also, these tools are used to estimate the oxidation amount and the extent of damage caused by fretting of the surface [32]. Due to the application of currents, either higher or lower values, the contacts naturally get degraded and this is explained by the electrical as well as thermal behavior or effects of the

interface where electrical contact occurs. Smaller values of current tend to enhance the longevity of electrical contacts and delay the failure of the contact. When applied current values are higher, wear debris, comprising of oxide, in increasing amounts is formed in the contact area. This accelerates the tin coated electrical contacts degradation. Good agreement between the fretted tin surface profile together with surface morphology and experimental results is established from this work.

Based on the literature review, it is evident that a multi-physics finite element model, considering surface characteristics, of a high power connector is unavailable to date. Secondly, experimental studies on vibration based fretting degradation in case of high power connectors used particularly in HEVs is completely missing in the literature. Once the oil reserves become exhausted or as a result of shortage of oil across the globe, it is well known that HEVs will be highly popular and will dominate the automobile industry and transportation sector. Hence, the current research focuses on the behavior of high power connectors (and more specifically a flat pin 40A connector) employed in HEVs through both multi-physics (mechanical, electrical and thermal coupled fields) finite element simulation including multiscale rough surface contact and experimental approaches. Experimental testing of 40A connectors involves stationary as well as accelerated vibration test conditions. The fretting effects in these connectors due to vibration are studied in detail in this work.

CHAPTER 2

Multi-scale Rough Surface Contact Model

2.1 Introduction

At higher magnifications, it is evident that an electrical contact or any engineering surface possesses roughness although it appears smooth on a macroscopic scale. In reality, when two surfaces come in contact with each other, they are in contact through the asperities or peaks on their surfaces [33]. This implies that there is a reduced real area of contact between two contacting surfaces. The load is carried by the asperities on the contacting surfaces. Due to the relatively high load being carried by the isolated asperities, they usually deform in an elasto-plastic manner. A smaller real area of contact causes constriction for the flow of electric current and conduction of heat between the surfaces. This constriction phenomena together with poorly conducting impurities present on the surfaces (for example, oxides) leads to electrical contact resistance (ECR) and thermal contact resistance (TCR). However, in the case of TCR, due to gaps between the contacting surfaces, the heat transfer may also occur through convection.

There are many different methods to model the contact of rough surfaces including statistical [34-38], fractal [39-43], and multiscale models [44-46]. The fractal mathematics based methods were derived to account for different scales of surface features not accounted for by the statistical models. The multiscale models were developed to alleviate the assumptions imposed by fractal mathematics and to also improve how the material deformation mechanics are considered. This work uses a fast Fourier transform to convert the data into a series of stacked

sinusoids (see Figure 2-1). Also, the surface characteristics necessary to obtain convergence of the iterative multiscale scheme are examined.

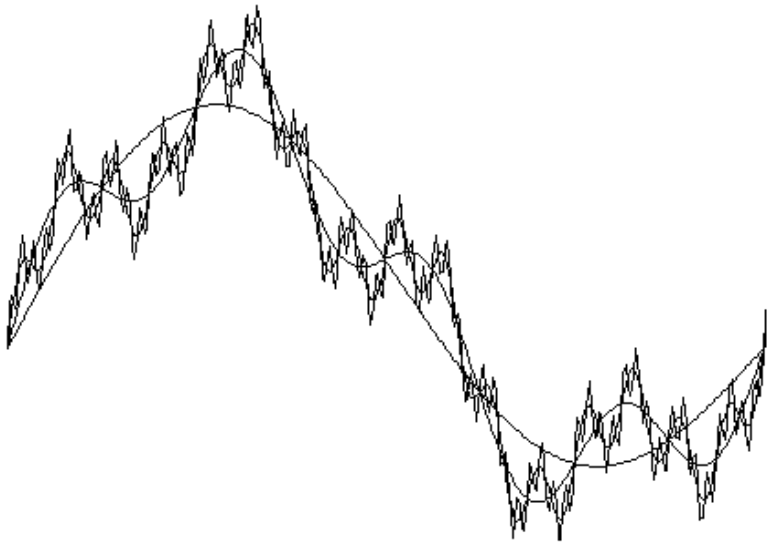

Figure 2-1: Schematic depicting the decomposition of a surface into superimposed sine waves. Each line represents a different scale of roughness

2.2 Model

2.2.1 Multi-scale perfectly elastic contact

The multi-scale model derived by Jackson and Streator [46] uses the same direction of thought as Archard [47], but provides a method that can be easily applied to real surfaces. First, a stylus profilometer was used to measure the surface data for 40A connectors, as shown in Figure 2-2. Second, a fast Fourier transform is performed on the surface profile data. Then, the resulting data is a summation of a series of sine and cosine waves. The complex forms of the sine and cosine terms at each scale are combined using a complex conjugate to provide the amplitude of the waveform at each scale for further calculations.

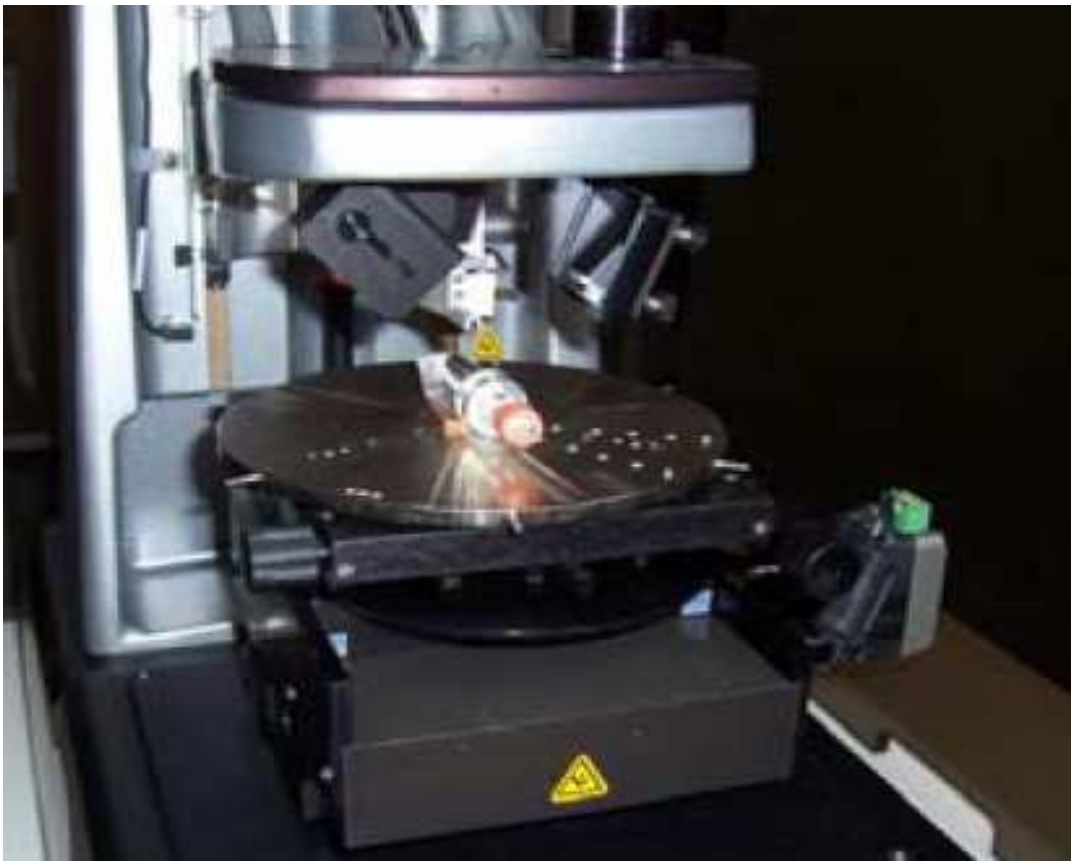

Figure 2-2: Surface profilometer

Each frequency is considered a scale or layer of asperities which are stacked iteratively upon each other. In equation form these relationships are given by:

$$A = \left(\prod_{i=1}^{i_{max}} \overline{A_i} \eta_i \right) A_n \tag{2-1}$$

$$P = \overline{P_i} \eta_i \overline{A_{i-1}} \tag{2-2}$$

where A is the real area of contact, η is the areal asperity density, P is the contact load, A_n is the nominal contact area, and the subscript i denotes a scale or frequency level, with i_{max} denoting the highest scale considered. Note that $\eta_i=2(f_i)^2$ because there are actually two sinusoidal asperity peaks for each square area of *1/f* x *1/f*. Each scale is modeled using a sinusoidal contact

model. Equations previously derived by Jackson and Streator [46] by fitting to the data given by Johnson, Greenwood, and Higginson [2] are used:

$$\left(A_{JGH}\right)_1 = \frac{\pi}{f^2}\left[\frac{3}{8\pi}\frac{\bar{p}}{p*}\right] \tag{2-3}$$

$$\left(A_{JGH}\right)_2 = \frac{1}{f^2}\left(1-\frac{3}{2\pi}\left[1-\frac{\bar{p}}{p*}\right]\right) \tag{2-4}$$

For $\frac{\bar{p}}{p*} \geq 0.8$ $\qquad \bar{A}_i = \left(A_{JGH}\right)_2$ (2-5)

For $\frac{\bar{p}}{p*} < 0.8$ $\qquad \bar{A}_i = \left(A_{JGH}\right)_1\left(1-\left[\frac{\bar{p}}{p*}\right]^{1.51}\right)+\left(A_{JGH}\right)_2\left(\frac{\bar{p}}{p*}\right)^{1.04}$ (2-6)

where $p*$ is the average pressure to cause complete contact between the surfaces of a single scale and is given by [2] as:

$$p^* = \sqrt{2}\pi E'\Delta_i f_i \tag{2-7}$$

2.2.2 Multi-scale elastic-plastic contact

However, many of the asperities at the different scales undergo plastic deformation. Therefore, an elastic-plastic sinusoidal contact model is needed to consider this effect. The equations used in the current work to calculate the elastic-plastic contact are derived from FEM results by Krithivasan and Jackson [48]. The methodology is very similar to that of the perfectly elastic case with the exception that a different set of formulas is used once a calculated critical pressure is reached. The critical load and area are given by:

$$P_c = \frac{1}{6\pi}\left(\frac{1}{\Delta f^2 E'}\right)^2\left(\frac{C}{2}\cdot S_y\right)^3 \tag{2-8}$$

$$A_c = \frac{2}{\pi}\left(\frac{CS_y}{8\Delta f^2 E'}\right)^2 \tag{2-9}$$

where C is given as

$$C = 1.295\cdot\exp(0.736v) \tag{2-10}$$

At low loads, $P<P_c$, and consequently small areas of contact, it is acceptable to assume that any deformation of the asperities in contact will behave perfectly elastically. However, as load increases to the critical value, plastic deformation will begin to occur within the asperities. To evaluate the plastic deformation we replace Eq. (2-3) with:

$$A_P = 2(A_c)^{\frac{1}{1+d}}\left(\frac{3\overline{p}}{4CS_y f^2}\right)^{\frac{d}{1+d}} \tag{2-11}$$

$$d = 3.8\cdot\left(\frac{E'}{S_y}\cdot\Delta f\right)^{0.11} \tag{2-12}$$

This replacement results in the following equation for contact area [48] at a single scale, *i*:

$$\overline{A_i} = (A_P)\left(1-\left[\frac{\overline{p}}{p_P^*}\right]^{1.51}\right)+(A_{JGH})_2\left(\frac{\overline{p}}{p_P^*}\right)^{1.04} \tag{2-13}$$

$$\frac{p_P^*}{p^*} = \left(\frac{11}{4\cdot\Delta/\Delta c+7}\right)^{3/5} \tag{2-14}$$

$$\Delta c = \frac{\sqrt{2}\cdot S_y\exp\left(\frac{2v}{3}\right)}{3\pi E' f} \tag{2-15}$$

Δc in Eq. (2-15) refers to the critical amplitude and the sinusoid always exhibits elastic deformation below Δc.

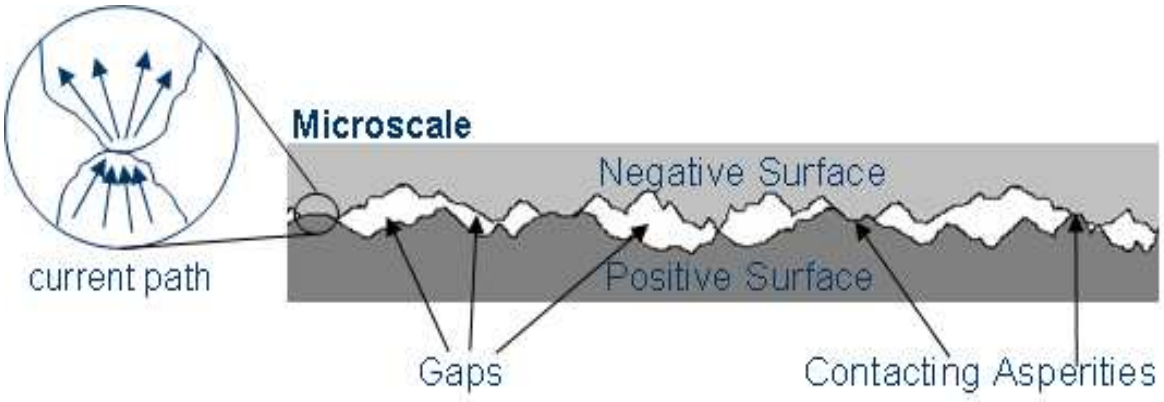

Figure 2-3: Schematic of "bottlenecked" current flow through asperities

2.2.3 Electrical contact resistance model

One of the concerns of this work is calculating the effect of surface roughness on electrical resistance (see Figure 2-3). Assuming that the surfaces in contact are conductors, the goal is to determine how the flow of current between surfaces is affected by the true area of contact for each load level. Since only a few, scattered asperities are actually in contact for any given load level, the current is restricted to very small contact patches when compared to the area of the entire surface. As the current flows through these asperity peaks, it will be effectively "bottlenecked" resulting in some resistance to the conduction as seen in Figure 2-3.

Holm [49] gives a simple formula to calculate the electrical resistance due to asperity contact.

$$Er_{asp} = \frac{\rho_{L1} + \rho_{L2}}{4a} \tag{2-16}$$

where *Er* refers to the resistance value, a is the radius of contact, and ρ is the specific electrical resistance, or resistivity, of the respective surfaces. However, this equation is only good for a single asperity. In the case of both multi-scale and statistical techniques, additional equations are required to calculate resistance for the entire surface.

The multi-scale sinusoidal method presented here is an iterative method that calculates area and resistance for each particular scale. The first step is to calculate the average radius of contact per scale *i*:

$$a_i = \sqrt{\frac{A_i}{2 \cdot \pi \cdot A_{i-1} \cdot f^2}} \tag{2-17}$$

Once the average contact radius is established, Eq. (2-16) is implemented to calculate resistance per asperity per level. This is a very similar technique to that used for thermal contact. Oftentimes, an alleviation factor is used in thermal contact resistance calculations to account for the effect of a large contact radius, *a*, in relation to the asperity tip radius, *R*. For the sinusoidal case, it is assumed that the tip of the asperity is similar to a hemisphere so the radius of curvature at the tip is used. Since electrical and thermal contact resistances are very mathematically similar, it stands to reason that the alleviation factor, Ψ, should also be included for electrical contact resistance. Though there are various ways to calculate this factor [50], the simplified version offered by Cooper, et al. [51] is chosen for this work:

$$\Psi_i = \left(1 - \sqrt{A_i / A_{i-1}}\right)^{1.5} \tag{2-18}$$

The alleviation factor, Ψ_i, is combined with the resistance value and the result is summed over all possible iteration levels to find the total electrical contact resistance (*ECR*) for the entire surface in contact.

$$ECR_{total} = \sum_{i=1}^{i_{max}} \Psi_i Er_i / (\eta_i A_{i-1}) \tag{2-19}$$

It is important to note that this technique calculates the resistance for each scale and then sums them over all scales to calculate the total. Also, the method does not change depending on

the inclusion of plasticity since all resistance calculations are done after obtaining the contacting area.

This work assumes real material properties for all the results gathered. The material of choice is tin since it is used to plate the 40A connectors. The surface profile is measured from the 40A connector surface using a stylus profilometer.

Once the data is gathered, a Fast Fourier Transform is performed as mentioned before. The result is then converted into a single amplitude for each scale via the complex conjugate. Then the multi-scale models can be calculated as described above.

2.2.4 Asperity temperature rise model

Since the current flow is concentrated through a few isolated asperity contacts on the surface, the temperature rise can be quite high and can cause failure of the connector surfaces. In fact, it is believed that most if not all electrical contacts have welding between the asperity contacts due to these high temperatures (see work by Bowden and Williamson [1] and Figure 2-4).

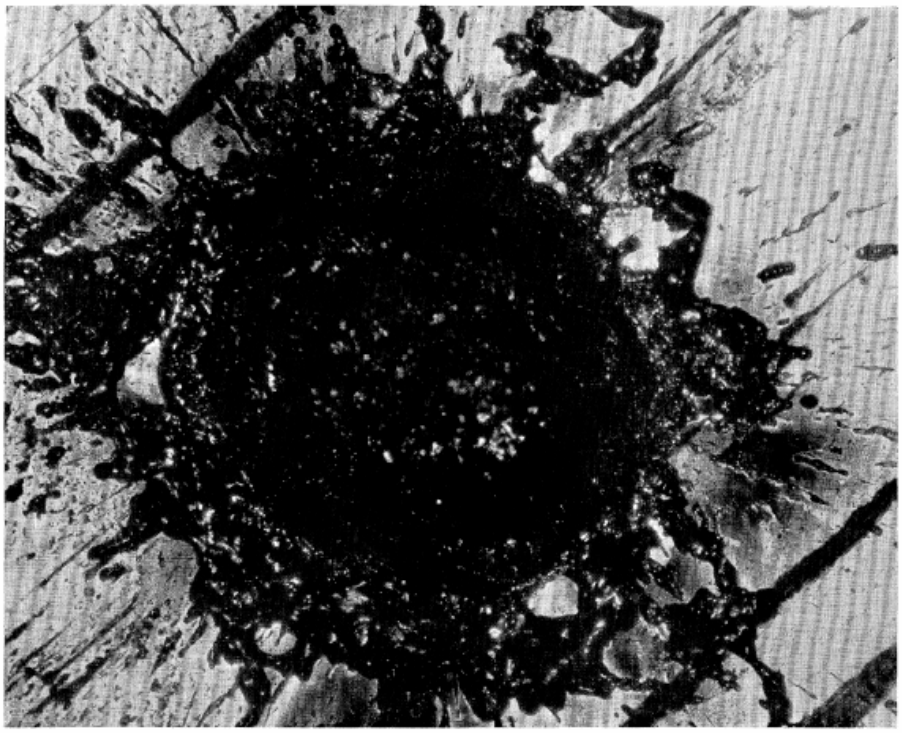

Figure 2-4: Damaged electric contact which had apparently melted and violently exploded due to the application of a high current [1]

Kohlraush [52] provides a fundamental theoretical relationship to calculate the temperature rise from the bulk material to the contact area of an asperity (translated in [53]). Holm [49] and Braunovic, et al. [54] provide a formula derived from Kohlraush's theory to predict the asperity temperature rise in a closed form solution, given as

$$\frac{I}{A} = \frac{4L\left(T_m^{\,2} - T_o^{\,2}\right)^{1/2}}{\pi\rho a} \tag{2-20}$$

where I is the current flow through the asperity, A is the area of contact, L is Lorenz's coefficient ($2.4 \cdot 10^{-8}$ $(V/K)^2$), ρ is the electrical resistivity of the asperity material, a is the contact radius, T_o is the temperature at the base of the asperity, and T_m is the temperature on the top surface of the asperity.

Therefore, one can calculate the temperature rise across the asperity to be:

$$T_m - T_o = \sqrt{\left(\frac{I\rho}{4La}\right)^2 + T_o^2} - T_o \tag{2-21}$$

Then, the temperature rise across the multiscale rough surface can be calculated by summing the temperature rise across each scale.

$$T_{\max} = \sum_{i=1}^{i\max} \sqrt{\left(\frac{I\rho}{4La_i}\right)^2 + T_{i-1}^2} - T_{i-1} \tag{2-22}$$

Equation (2-22) can then be used within the multiscale model framework to make a prediction of the local maximum temperature on the surfaces. This is important because even if the bulk temperature predicted by the multi-physics FEM models is fairly low, the local temperature on the asperities in contact can be quite high. These high temperatures on the asperities can cause the asperities to weaken and increase the contact area, thus actually decreasing contact resistance. However, the high temperatures can also cause excessive melting, chemical reactions, and surface degradation which could also increase the contact area.

2.3 Model predictions

For simplicity, first the contact force and contact resistance of the surfaces are predicted without considering the local asperity temperatures predicted by Eq. (2-22). Actual measured surface profile data and the material properties of the surface plating on the connectors are used in the multiscale models.

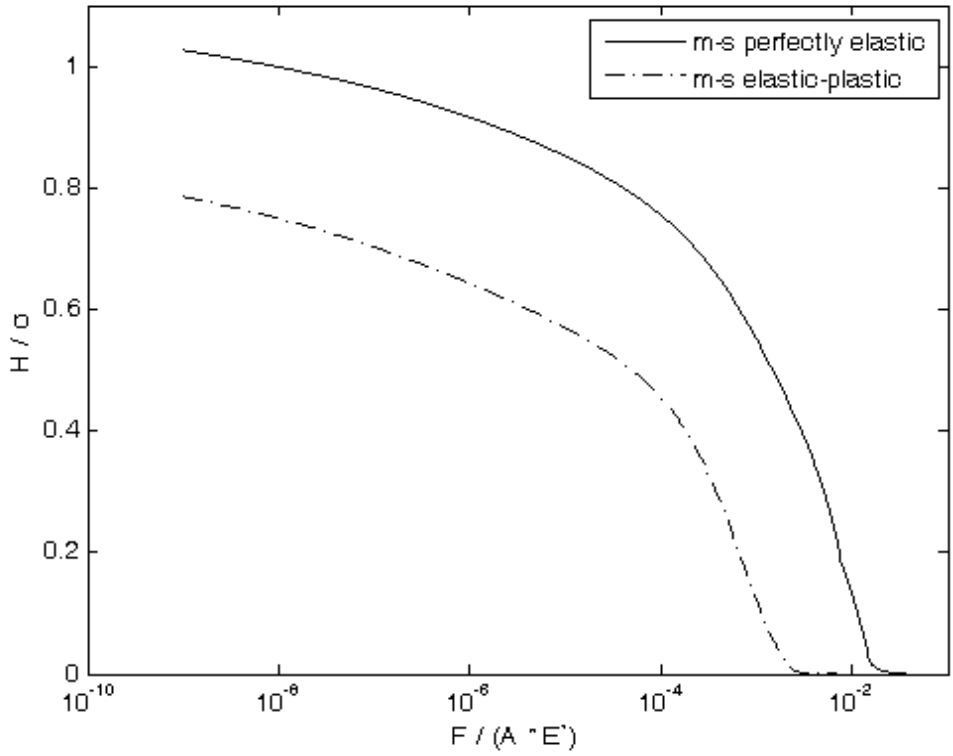

Figure 2-5: The model predicted surface separation vs. force for the 40A connector surfaces

The predicted surface separation as a function of contact force for the 40A connector surfaces and material properties are shown in Figure 2-5. It appears that the connector surfaces can carry a higher load and therefore the surfaces come into complete contact.

The predicted electrical contact resistance as a function of load for the 40A connector surfaces is shown in Figure 2-6. It is interesting to note that the contact resistance appears to decrease more rapidly with load once a certain threshold load is reached. The results shown in Figure 2-5 and Figure 2-6 are also used in the multi-physics FEM model of the 40A connector.

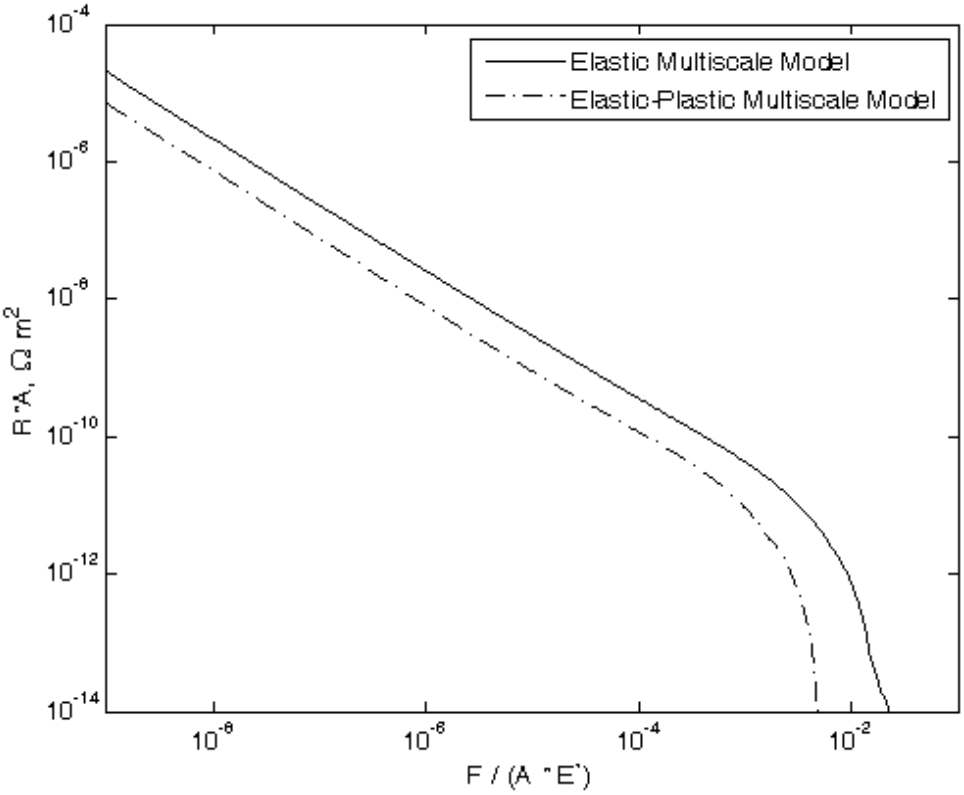

Figure 2-6: The model predicted electrical contact resistance for the 40A connector surfaces

Finally, the local temperature rise model given by Eq. (2-22) was used to predict the highest temperature on the surfaces. The current used in the model was taken from the FEM multi-physics model. Since the current flow is not distributed uniformly across the surfaces in the FEM results, the highest value of the current density on the contacting surfaces predicted by the 40A connector model was used. Using this value, the model predicted that, at these isolated locations, the asperity temperature would be much higher than the melting point of the surface plating. These contacts result in the surface welding together and enhance the chemical reactions and surface degradation.

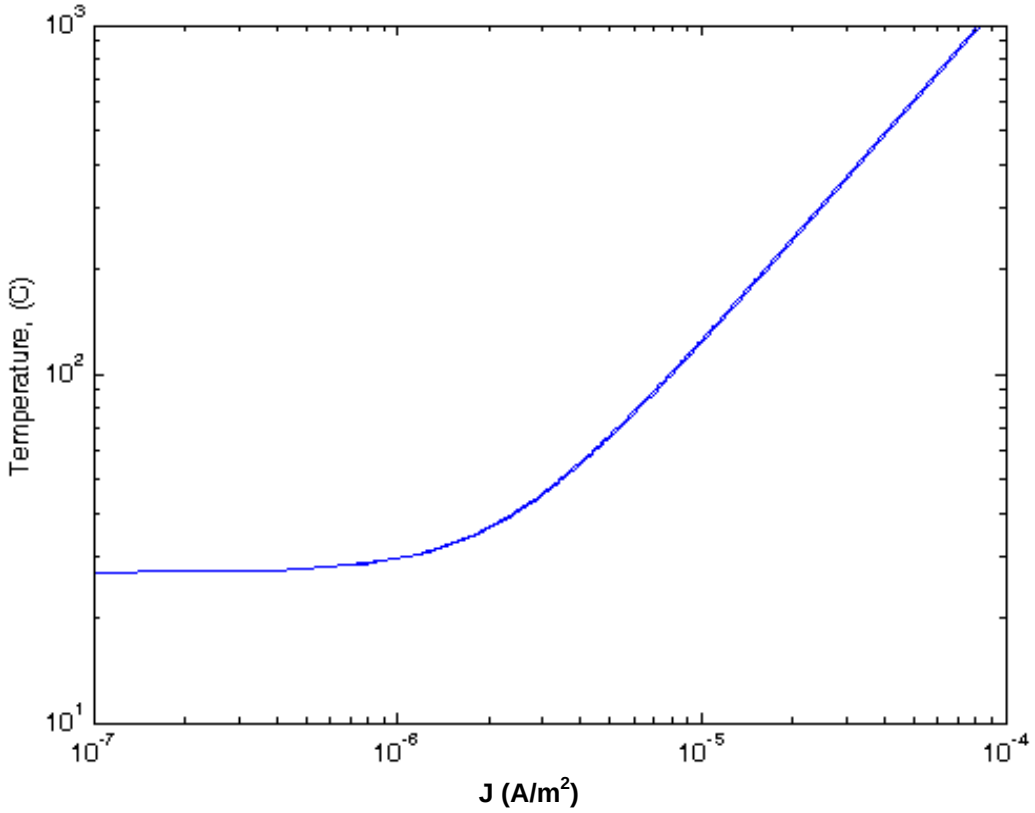

Figure 2-7: Variation of local asperity temperature with current density

From Figure 2-7, it can be noticed that once the current density reaches $3x10^{-6}$ A/m^2 there is a linear increase in local asperity temperature (calculated using Eq. (2-22)) with an increase in current density. It is predicted that the asperities on the connector surfaces are indeed melting. Melting will initially improve the contact and reduce contact resistance. During fretting these heated surfaces will also be more susceptible to permanent surface damage. However, these temperature predictions will not be used further in this work.

CHAPTER 3

Multi-physics Finite Element Model including Multi-scale Rough Surface Contact

A new method that employs only ANSYS™, a commercial finite element software package, to reach convergence is established to solve the multi-physics finite element and multi-scale rough surface contact based model of the connectors. This new method is simpler and enables faster convergence than the original iterative Matlab™ and ANSYS™ coupled technique [55]. Thus, there is no need for an external code to run simultaneously with ANSYS™. The coupled mechanical, electrical and thermal governing equations are solved simultaneously. A stylus profilometer is used to obtain rough surface data for contacting surfaces of 40A connectors. At the contact of surfaces in the connectors, the previously discussed multi-scale rough surface contact model is used. The contact resistance is predicted using the multi-scale rough surface contact method and is embedded in the multi-physics FEM. This robust methodology gives a more complete view of connector performance. It also allows for a prediction of the stress distribution, electrical potential (voltage drop) and current density distributions, temperature distribution, electrical contact resistance (ECR), thermal contact resistance (TCR) and also the effect of their being coupled together.

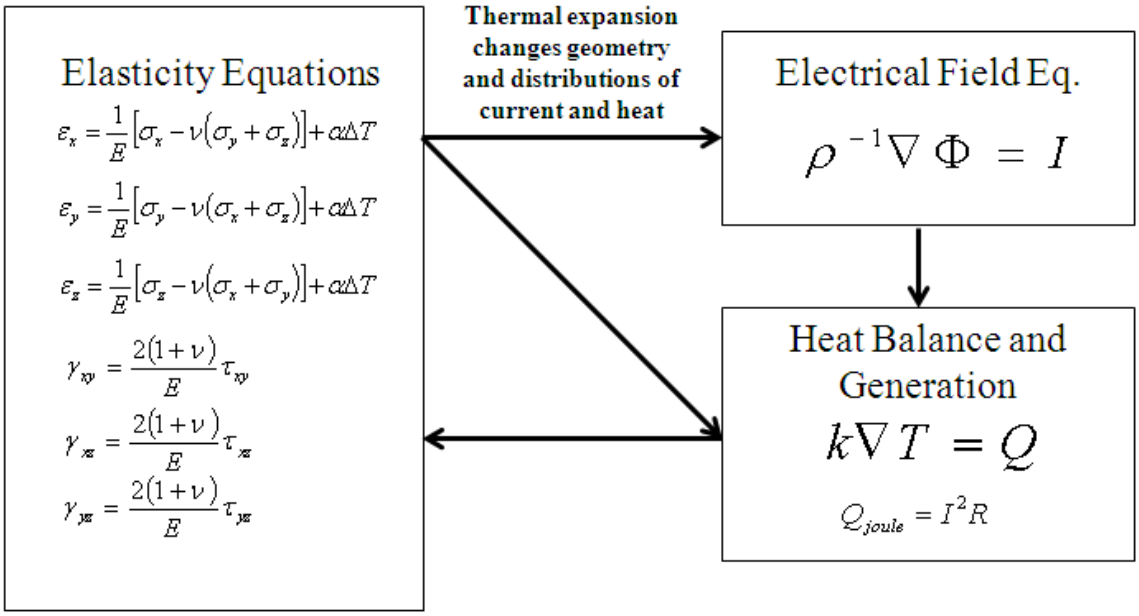

Figure 3-1: Schematic showing the coupled multi-physics field equations

The 40A connector model solves the mechanical-electric-thermal coupled fields of equations (see Figure 3-1) and thus captures effects not normally considered by conventional uncoupled finite element models and analytical calculations. In Figure 3-1, E is the elastic modulus, ν is the Poisson's ratio, σ is the normal stress, τ is the shear stress, ε is the normal strain, γ is the shear strain, I is the electrical current, Φ is the electrical potential across the connector, ρ is the electrical resistivity, k is the thermal conductivity, T is the temperature distribution, Q is the heat flux, α is the thermal expansion coefficient, and ΔT is the change in temperature of the material. For instance, heat will be generated in the connector due to Joule heating (Q_{joule}). This heating will increase the temperature (T) which will cause thermal expansion ($\alpha\Delta T$) and stresses (σ, τ) in the connector parts. This deformation will change the geometry and in turn redirect the flow of electrical current and heat.

The mechanical field of the problem considers the stresses (σ, τ) and strains (ε, γ) of the material, and how it will deform and possibly fail due to over stressing. The theory of elasticity

is used to model the deformations in the material. Then, three dimensional Hooke's law, which relates the stresses and strains via the elastic modulus (E) and Poisson's ratio (υ), is given in Cartesian coordinates (x,y,z), as shown in Figure 3-1.

The thermal and electrical fields are coupled, and the mechanical and thermal fields are coupled. For the prescribed connector geometry and boundary conditions, the multi-physics ANSYS^{TM} software (version 11) solves these equations simultaneously for more realistic predictions.

The electrical contact resistance (ECR) and thermal contact resistance (TCR) values are predicted using the multiscale model [56] from a micro and nanoscale profile of the connector surface, as discussed in chapter 2. The resulting ECR values as a function of normalized average contact pressure are given in Figure 3-2. ECR predictions considering only elastic contact and elastic-plastic contact are shown, although only the elastic-plastic results are used in the full connector model. As expected, the elastic-plastic ECR values are lower than the elastic ECR values because the model predicts more area of contact between the surfaces. For the elastic-plastic predictions, the yield strength used was 41 MPa. Note that the ECR values can be easily converted to TCR values by substituting the thermal conductance for the electrical conductance.

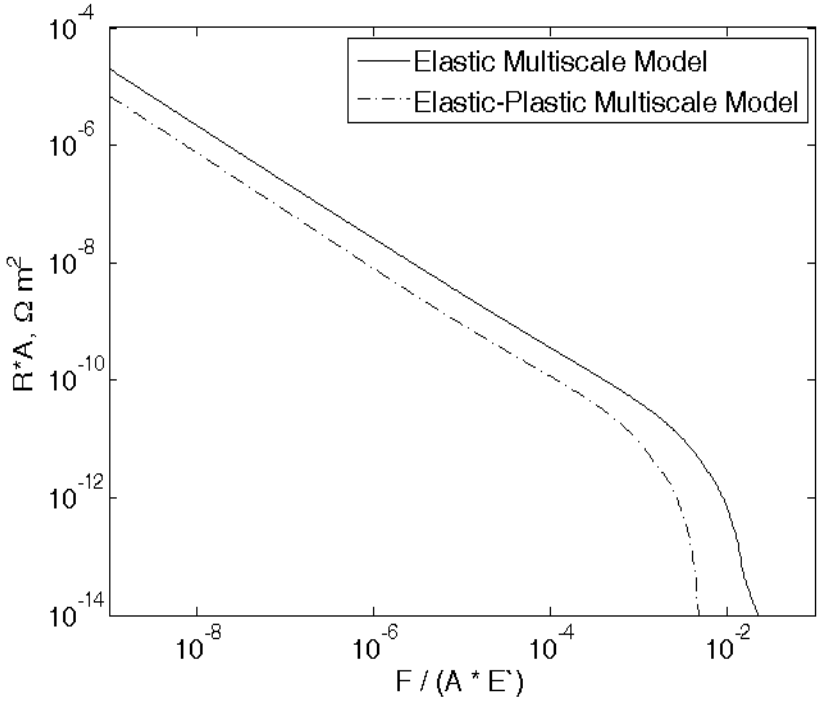

Figure 3-2: The ECR values predicted from the multiscale models to be used in the multi-physics connector model

3.1 40A connector model

Generally, electrical connectors are made up of two main parts, namely, the spring and the pin. The shape of the spring resembles a curved beam and is compliant, whereas the pin is flat. The main function of the spring is to provide a sufficient contact force between the two parts. The entire 40A connector system is shown in Figure 3-3. The geometry of the spring and pin parts of the 40A connector model is shown in isometric form in Figure 3-4. Since the cross-section of the connector varies little, except at the sidewalls, a simplified 2-D model of the 40A connector has been developed in the current work. A cross-section of the 40A connector aligning with one of the two indentation features (see Figure 3-4) in 2-D is taken and is modeled in ANSYS™. The dimensions of the model geometry in ANSYS™ are in mm.

Figure 3-3: 40A connector system

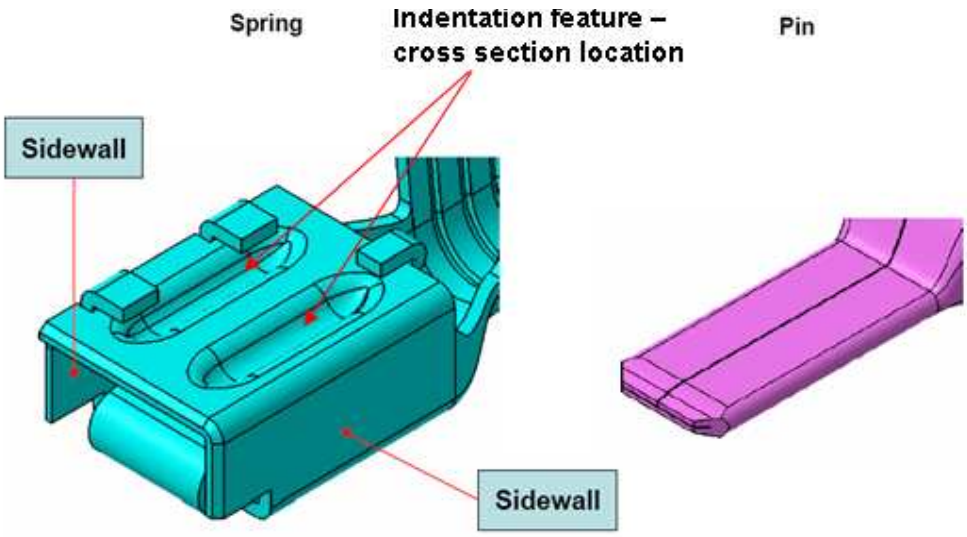

Figure 3-4: 40A connector model parts (for modeling analysis)

Several simplifying assumptions have been made in the model:

1. The bulk connector model assumes the plane stress assumption.
2. In the current model, the bulk deformation of the connector is assumed to be only perfectly elastic (multiscale rough surface contact is still considered elastic-plastic).
3. Only the steady-state solution to the problem is considered.
4. Convection/conduction from the outer surfaces of the connector parts is neglected because the properties of the plastic connector casing are considered to be a good insulator relative to the metal components.

3.1.1 Elements used in 40A connector model

The total number of elements (including PLANE223 and LINK68 elements) used in the model are 7828 (see Figure 3-5). The elements used are:

1. A 2-D 8-node direct coupled (structural-thermal-electric) Plane223 element.
2. A uniaxial coupled thermal-electric LINK68 element for electrical and thermal conduction between contacting points.
3. CONTA172 (contact element) and
4. TARGE169 (target element).

3.1.2 Methodology for 40A connector model

At first, the multi-scale rough surface contact model is used to predict the contact resistances as a function of contact pressure. The 40A connector geometry is then set up in ANSYS^{TM}. The material properties of the copper based alloy material (MZC1 alloy) used to manufacture the bulk of the 40A connector are assigned in ANSYS^{TM} (see Table 3-1). However, a tin material is used to plate the surfaces of the 40A connector and those properties are also given in Table 3-1. The properties of the plating were only used in the multiscale rough surface contact model to predict the contact resistances as a function of contact pressure resulting from the micro and nanoscale rough surface profile. The properties of the bulk material were only used in the FEM model of the macroscale connector. Notice that thermal expansion is currently not considered in the multiscale contact resistance model and so the thermal expansion coefficient of tin is not employed.

Material property	Copper based alloy material (bulk material)	Tin material (surface finish material)
Modulus of Elasticity (MPa)	$137x10^{3}$	$41.4x10^{3}$
Poisson's Ratio	0.32	0.33
Coefficient of thermal expansion (K^{-1})	$17.1x10^{-6}$	$23.8x10^{-6}$
Electrical resistivity (Ω-mm)	$2.05x10^{-5}$	$11.5x10^{-5}$
Thermal conductivity (W/mm-K)	$316x10^{-3}$	$63.2x10^{-3}$

Table 3-1: Material properties for spring and pin parts of the 40A connector

The element types are then set. The mesh is shown in Figures 3-5 and 3-6. Additionally, both the spring and pin parts are meshed uniformly so that they will contact near the nodes on the opposing surface. Then, all the structural, electrical, and thermal boundary conditions are applied (see Figure 3-6). The model is constrained structurally in both the *x* and *y* directions. The electrical and thermal boundary conditions are applied suitably in the pin and spring parts of the connector such that the current and heat flow, occurring in a real connector during its operation, are simulated. In this method, the 1-D Link68 elements are placed to model the conduction of electric current and heat of the sidewalls of the spring terminal of the 40A connector (see Figure 3-6).

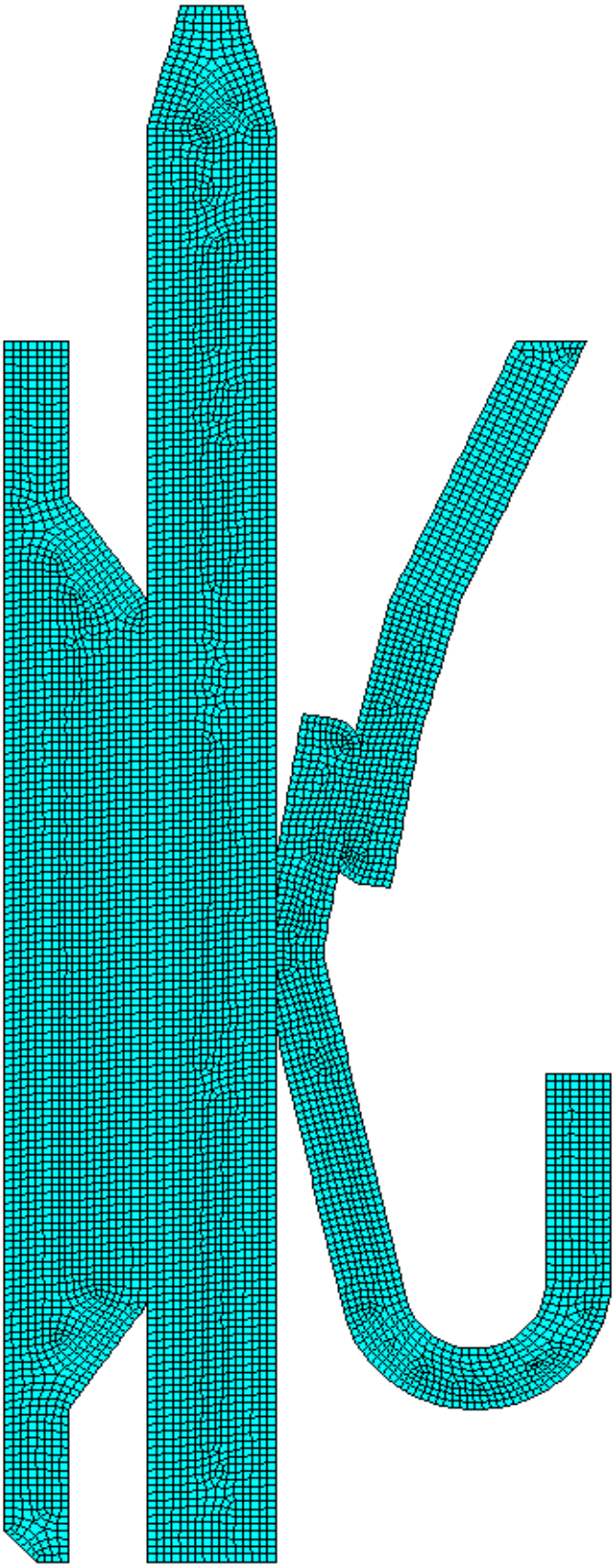

Figure 3-5: Mesh of the 40A connector model

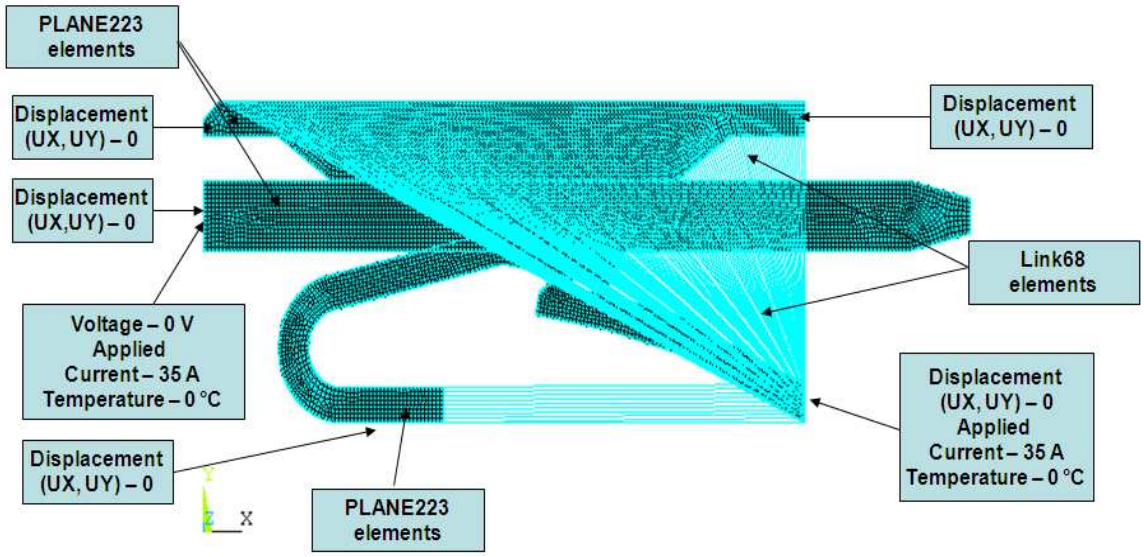

Figure 3-6: Boundary conditions for the 40A connector model

Initially, thermal expansion in the sidewalls of the connector was not considered and the model did not agree with the experiments. Therefore, the thermal deformation (δ) was included to mimic the thermal expansion of the top and bottom surfaces of the sidewalls of the spring terminal of the connector in the ANSYS™ model. In reality, due to the heating of the connector, the sidewalls of the spring terminal of the connector will undergo thermal deformation (δ), that is, thermal expansion, given by the equation

$$\delta = \alpha \Delta T_a L \tag{3-1}$$

where α is the coefficient of thermal expansion (/°C), ΔT_a is the change in temperature (°C) and L is the original height of the sidewall (mm).

ΔT_a is calculated from Eq. (3-2), which is given by:

$$\Delta T_a = T1 - T_R \tag{3-2}$$

where $T1$ is the connector temperature at the base (°C) obtained from the experiment (without vibration, see chapter 4) and T_R is the room temperature (22 °C).

To illustrate this, a sample calculation of δ is now provided for one of the applied currents (35A). For 35A of current, T1 is experimentally measured to be 47.63 °C. Therefore, ΔT_a equals 25.63 °C. Now, on substituting this value of ΔT_a into Eq. (3-1), we predict δ to be 0.00158 mm. This displacement, δ, value is then divided evenly and applied separately to each of the top-most and bottom-most surfaces of the sidewalls of the spring terminal, as shown in Figure 3-7. In this way, a total displacement (thermal deformation) of δ (0.00158 mm) is taken into account, which will help to obtain convergence in the 40A connector ANSYS™ model.

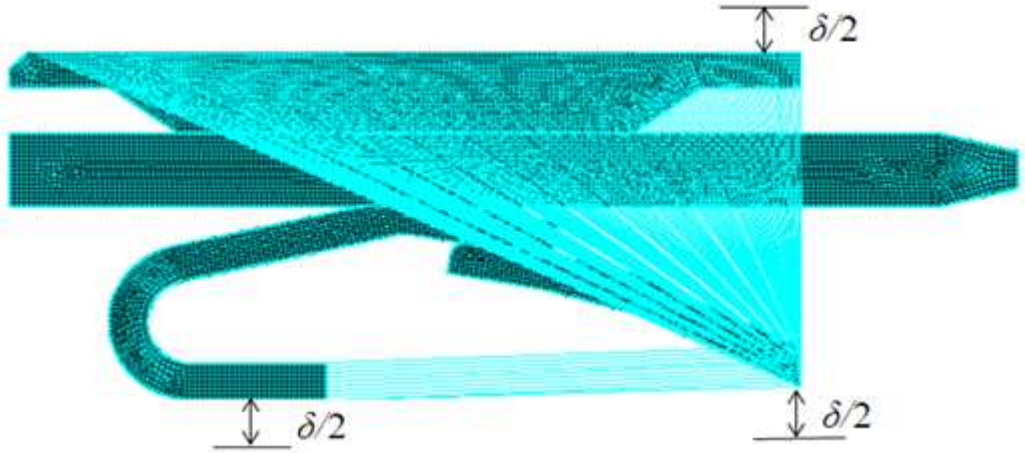

Figure 3-7: Thermal deformation (δ)

Contact pressure, ECR, TCR, thermal and electrical contact conductance calculations are performed externally before ANSYS™ is executed. To calculate the TCR from the ECR predicted by the multiscale model, the following equation (Eq. 3-3) is used.

$$TCR = \frac{ECR}{\rho k} \tag{3-3}$$

where *ECR* is the electrical contact resistance (Ω), ρ is the electrical resistivity (Ω-mm) and k is the thermal conductivity (W/mm-K).

The contact pairs for the contact regions are created using the contact and target elements for the 40A connector model. During the contact pair creation, the thermal and electrical contact resistance values as a function of contact pressure are read into ANSYS™ from external files. ANSYS™ then uses interpolation to solve for specific values of ECR and TCR as a function of contact pressure.

Initially, the above 40A connector model is run in ANSYS™ with no applied current to enhance convergence. After achieving this convergence, the results of the model without applied current are used as an initial state and the same model is run with application of 35A current so that complete convergence, involving structural, electric and thermal fields, is reached for the 40A connector. This helps the solution to converge, which can be very difficult to achieve with a coupled multi-physics model in some cases. Finally, the displacements, stresses, contact pressures, contact resistances, temperature, electric potential, current density and Joule heat distributions are obtained. A flow chart outlining the sequence of steps for solving the 40A connector model is shown in Figure 3-8.

As a check of the reasonableness of the results, after the convergence of the solution was achieved, the force balance on the pin terminal of the 40A connector was achieved for an applied current of 35A in the model. That is, when all the reaction forces in the "Y" direction (F_y) corresponding to all the nodes on the left most end of the pin terminal are summed together, the total value of F_y reaction forces obtained is 1.2 N. This means that the entire 40A connector model (geometry) within ANSYS™ is practically in an equilibrium state.

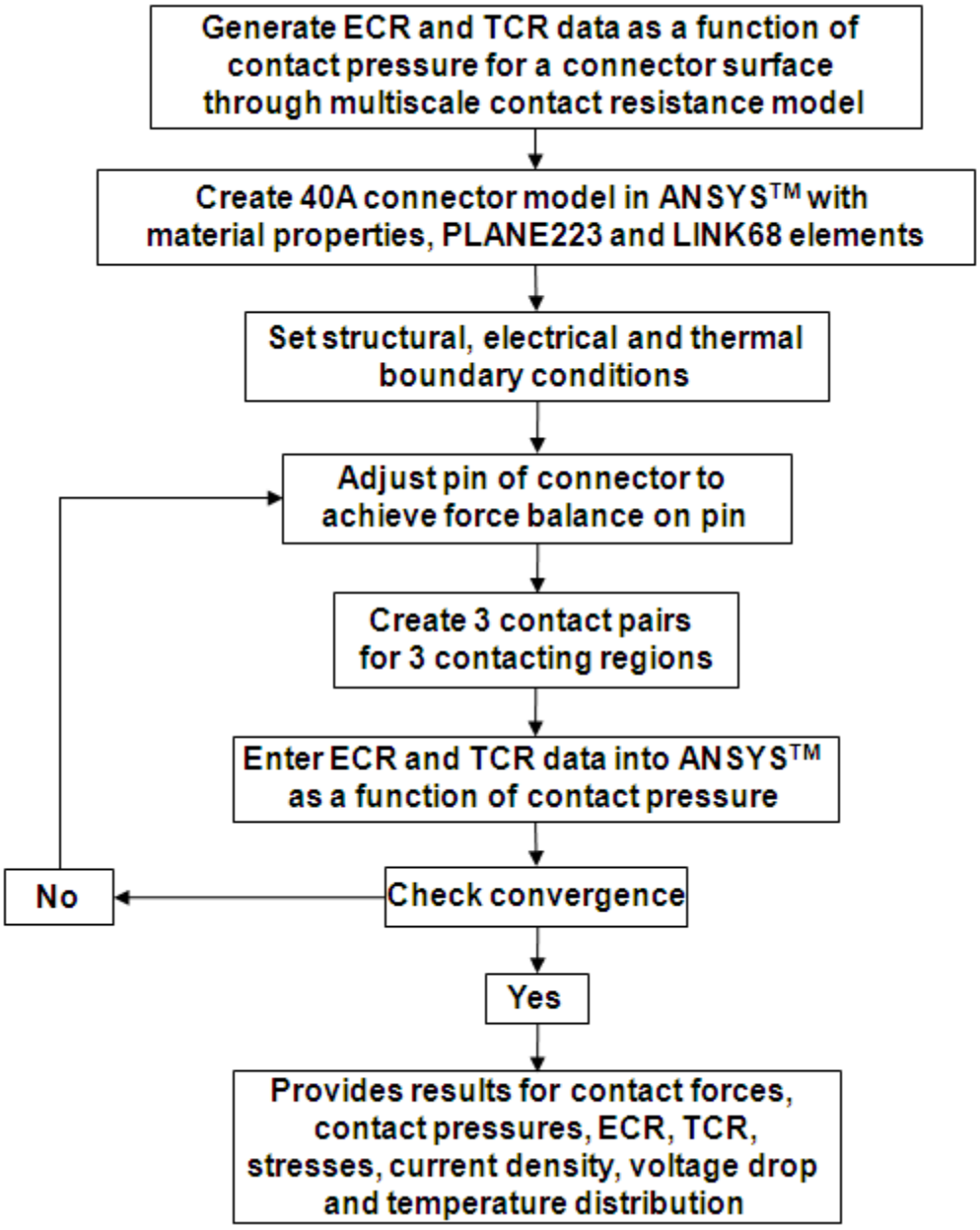

Figure 3-8: Flow chart of the 40A connector model

3.2 General results of 40A connector model

For an applied current of 35A in the connector model in ANSYS™, the displacement (Figure 3-9), von Mises stress (Figures 3-10 and 3-11), electric potential (Figure 3-12), temperature (Figure 3-13), conduction current density (Figure 3-14) distributions and Joule heat generation (Figure 3-15) in the form of contour plots are obtained.

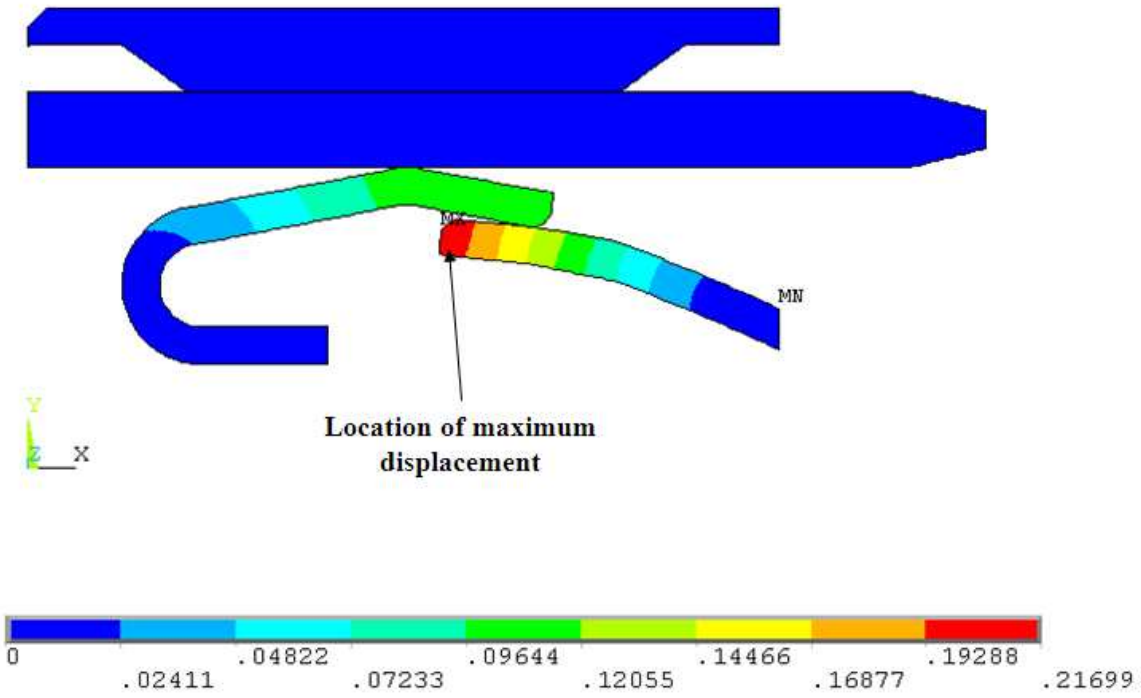

Figure 3-9: Displacement (mm) in the 40A connector

Figure 3-9 shows the displacement contour plot. Most of the displacement occurs in the bulk regions of the spring terminal that are bent. These bulk regions are the only regions in the entire connector system that can be displaced or adjusted upwards or downwards to allow the pin terminal to slide in and out of the connector (see Figure 3-9). As expected, maximum deformation (displacement) is seen at the end of the spring terminal of the connector (as indicated in the Figure 3-9) and this portion of the spring is free to move up and down or bend.

Also, minimum displacement appears at the right most fixed end of the spring (see Figure 3-9) that is constrained in both x and y directions (see Figure 3-6) in the ANSYS™ model and in reality, this region of the spring cannot undergo any displacement.

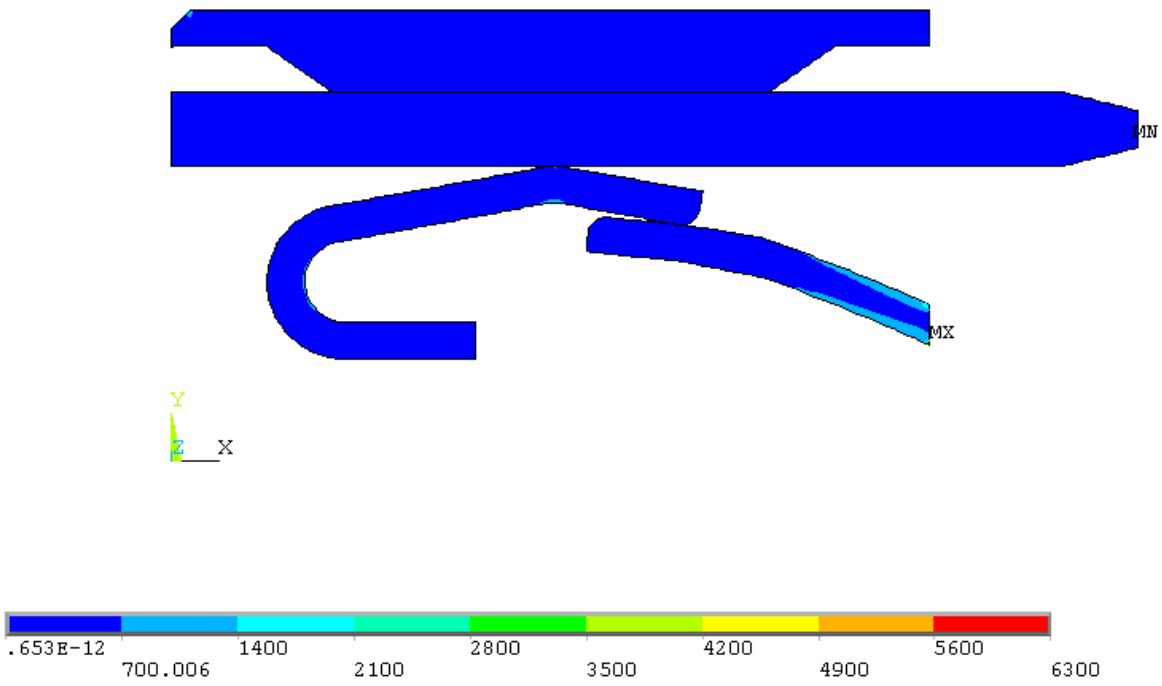

Figure 3-10: von Mises stress distribution (N/mm^2) in the 40A connector

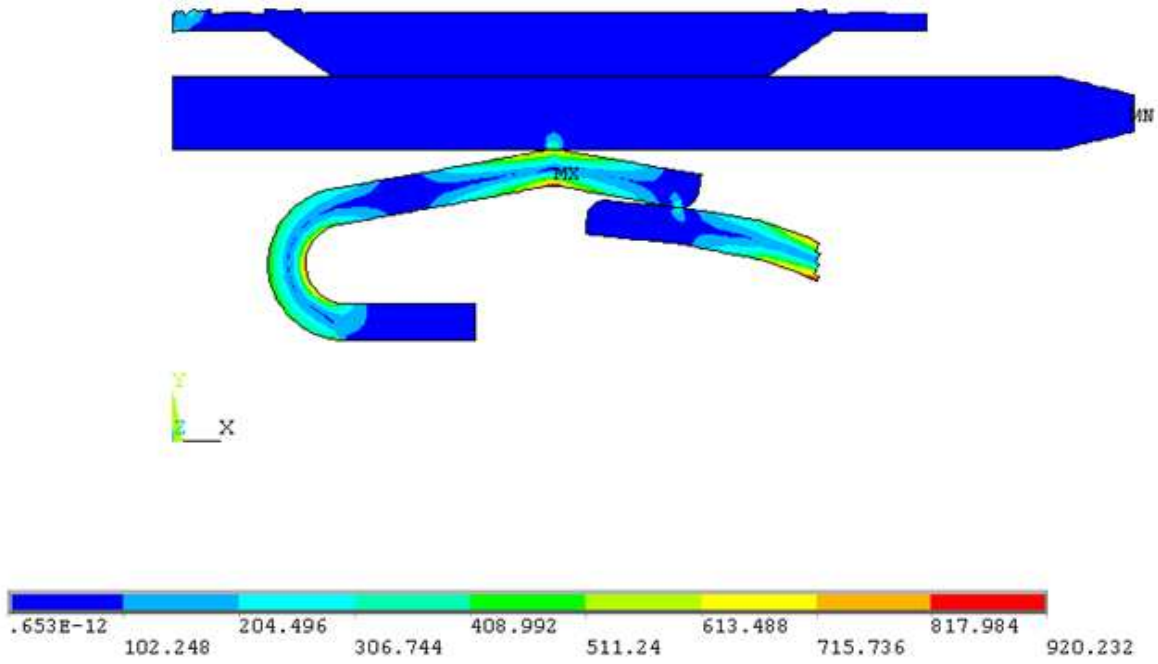

Figure 3-11: von Mises stress distribution (N/mm^2) in critical regions of the 40A connector

The von Mises stress distribution for the entire connector system is shown in Figure 3-10. However, due to high bending stresses in the spring of the connector on the far right, it is difficult to see the stress distribution in the rest of the connector. After removing a portion of the spring, as in Figure 3-11, the distribution of the von Mises stress and the critical regions are much more apparent. The maximum von Mises stress locations are marked by 'MX' in Figures 3-10 and 3-11. From Figure 3-11, it can be noticed that there are also high stresses near the concentrated contacts of the pin and springs and also where the springs are bending (near the curved regions). However, it should be noted that the stresses in the local contacts could actually be higher due to the limited mesh resolution and smaller scale asperity contacts not considered. The predicted maximum von Mises stress value of 6300 N/mm^2 in the bending portion of the spring (Figure 3-10) and 920 N/mm^2 in the bend below one of the contacts (Figure 3-11)

indicates that yielding is probably occurring in the connector because it is higher than the yield strength (for the copper alloy material used in the connector, the yield strength is 540 N/mm^2).

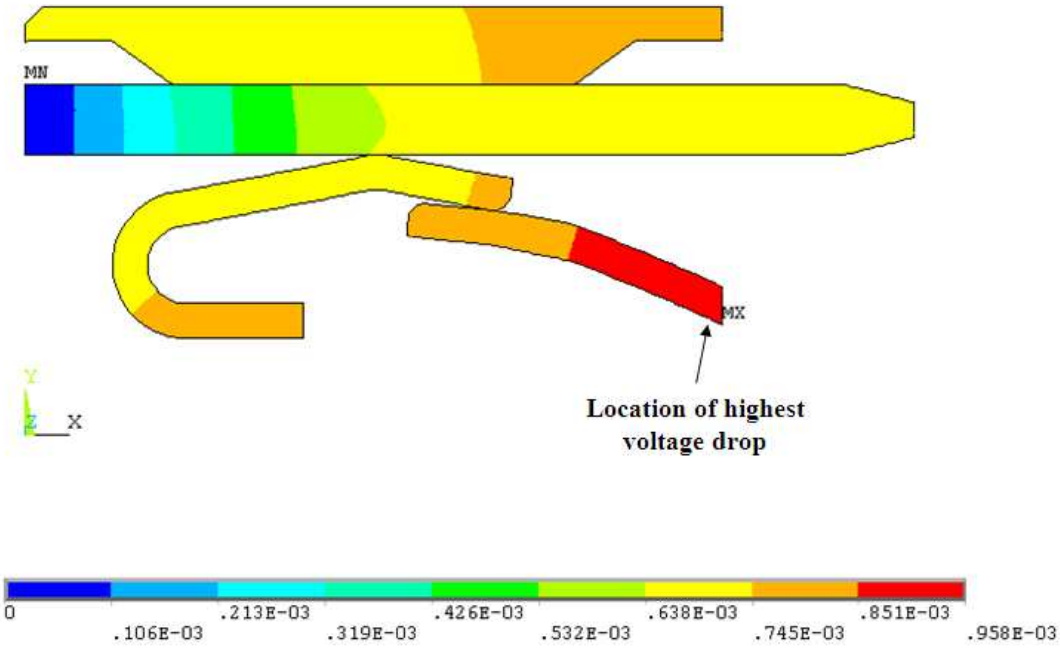

Figure 3-12: Electric potential distribution (V) in the 40A connector

Figure 3-12 shows the predicted potential drop between the ends of the connector with the maximum potential being at the spring end and the minimum being at the pin end based on the applied electrical boundary conditions. The potential drop variation is more rapid in the region of the pin terminal that corresponds to concentrated or higher current density (see Figure 3-14). Likewise, in the region where there is very low current density, the voltage variation is not as abrupt.

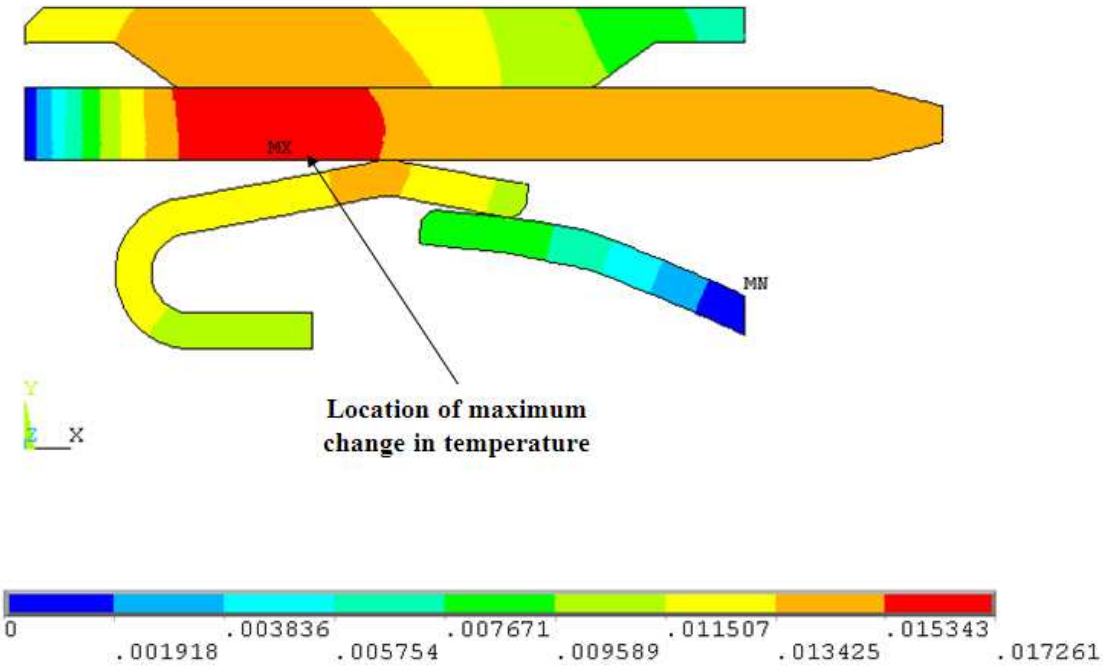

Figure 3-13: Temperature distribution (°C) in the 40A connector

As expected, as shown in Figure 3-13, higher temperature gradients (although lower in magnitude) are seen in the pin terminal and in regions where most of the current flows (that is, at the regions where there is higher current density). The temperature rise in the bulk material is not very high. However, experimental measurement of the temperature suggests that it is much higher, and it is therefore believed that this temperature rise is due to the Joule heating in the supplying cables (which are long in length). This issue is explored and explained in more detail in section 5.1. However, theoretically local asperity temperature should be very high at the contact (see section 2.2.4). Higher temperatures may appear at the microscale level when multiscale rough surface contact is considered at the contacting regions of the connector.

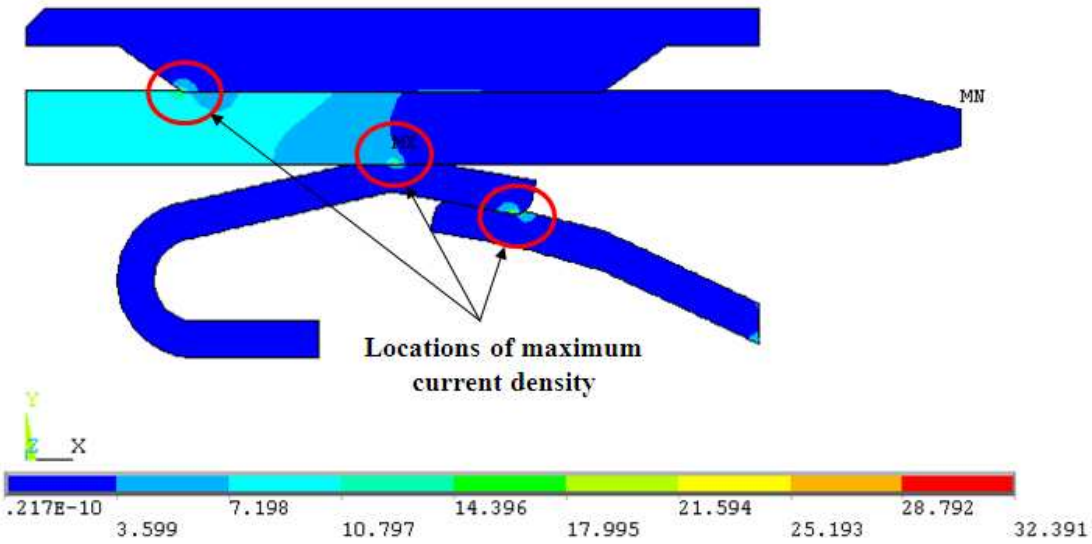

Figure 3-14: Conduction current density distribution (A/mm^2) in the 40A connector

The maximum current density and hence higher temperatures are seen at the contact of the spring and pin (Figure 3-14). Current density may be used to predict local asperity temperature analytically, but these are not simple calculations to make and there is currently no universally accepted method to do so, although we have proposed a new multiscale methodology in section 2.2.4. Most of the current is concentrated towards the left part of the connector indicating that the current follows the path of least resistance. There are clear concentrated regions of current near the contacting surfaces of the connector. It appears that the current does not distribute itself evenly across the contact regions and instead tends to flow through very small spots. Maximum current density may be reduced by redesigning the connector so that current is distributed more evenly in the connector.

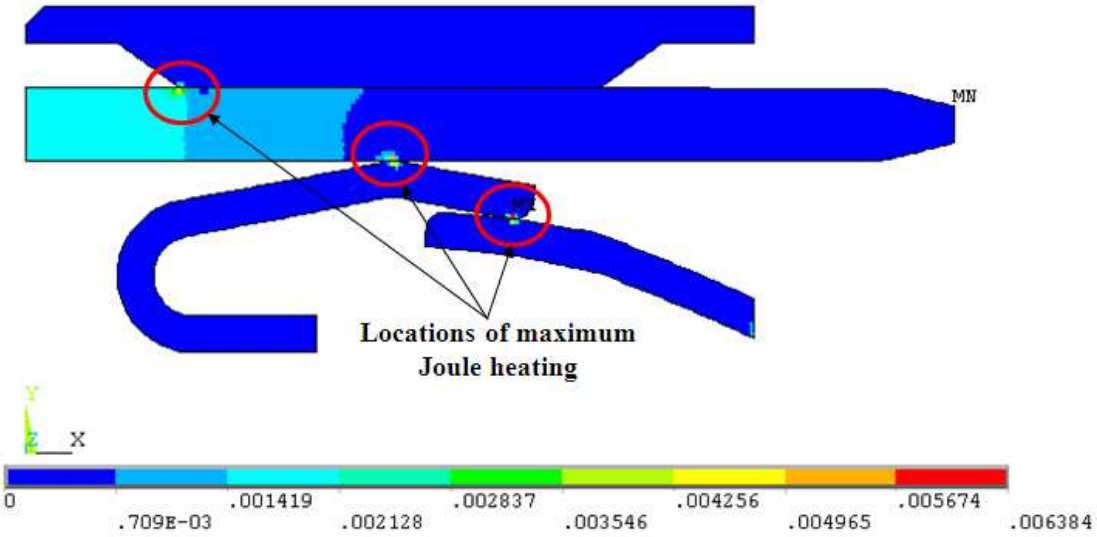

Figure 3-15: Joule heat generation per unit volume (W/mm^3) in the 40A connector

Figure 3-15 shows the Joule heat generation contour plot. It shows that Joule heating occurs in the regions where high current density is seen. Again, maximum Joule heating, as expected, appears in the region where current density (Figure 3-14) as well as temperature (Figure 3-13) is higher. Joule heating is described by Eq. (3-4) as:

$$Q_{joule} = I^2 R \tag{3-4}$$

where Q_{joule} is the Joule heat generation, I is the electrical current and ρ is the electrical resistivity. Again, at the asperity scale it is expected that very high temperatures could arise.

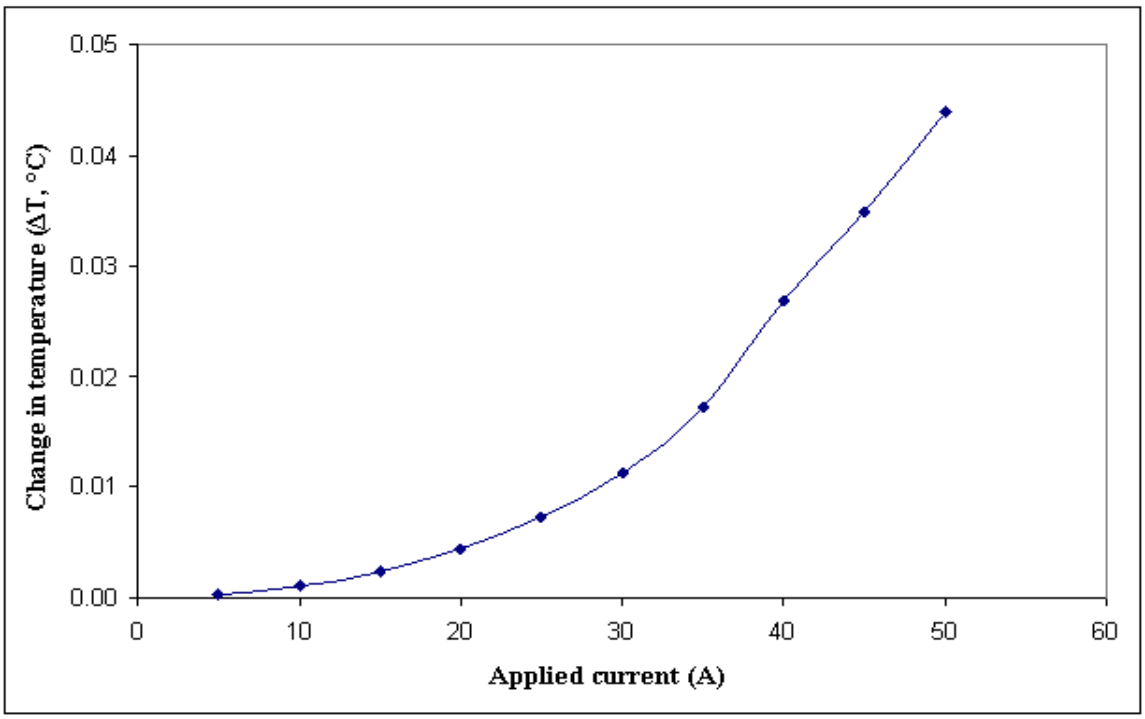

Figure 3-16: Effect of increase in current on the change in temperature in the 40A connector

In Figure 3-16, it can be noticed that the change in temperature (ΔT or temperature rise) varies with respect to the applied current in a non linear (nearly parabolic) way owing to Joule heating in the connector (Eq. 3-4). A similar trend was also noticed in an earlier modeling effort on a different electrical connector for the change in temperature versus applied current [55]. This suggests that there is consistency in the trend observed for the 40A connector investigated in this work and the one studied by Angadi, et al [55]. Again, the ΔT values for various applied currents in the model are very small. However, the experimental ΔT values are considerably high. Thus, it has been theorized and proven that the Joule heating occurring in the long supply cables causes the high temperature rise (see section 5.1).

3.3 Predictions for connector degradation by increasing ECR and TCR: 40A connector

While maintaining a constant applied current of 35A, the contact resistances (both ECR and TCR) are increased by 10%, 20%, 30%, 40%, 100% and 200% artificially to predict the possible effect of fretting and surface degradation on parameters such as maximum conduction current density (Figure 3-17), change in temperature (Figure 3-18) and voltage drop (Figure 3-19). As expected, all these 3 parameters exhibit an increase in their respective values as a result of an increase in contact resistance. Note that both ECR and TCR were increased by the same proportions.

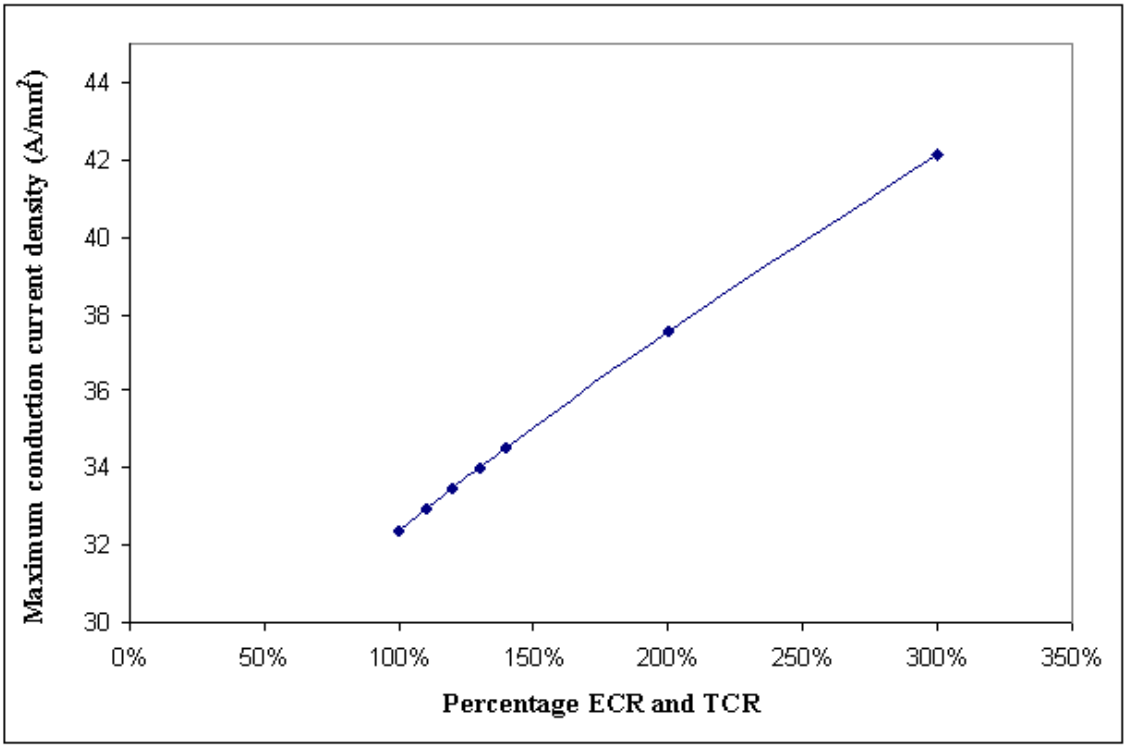

Figure 3-17: The effect of an increase in contact resistance on the maximum conduction current density in the 40A connector

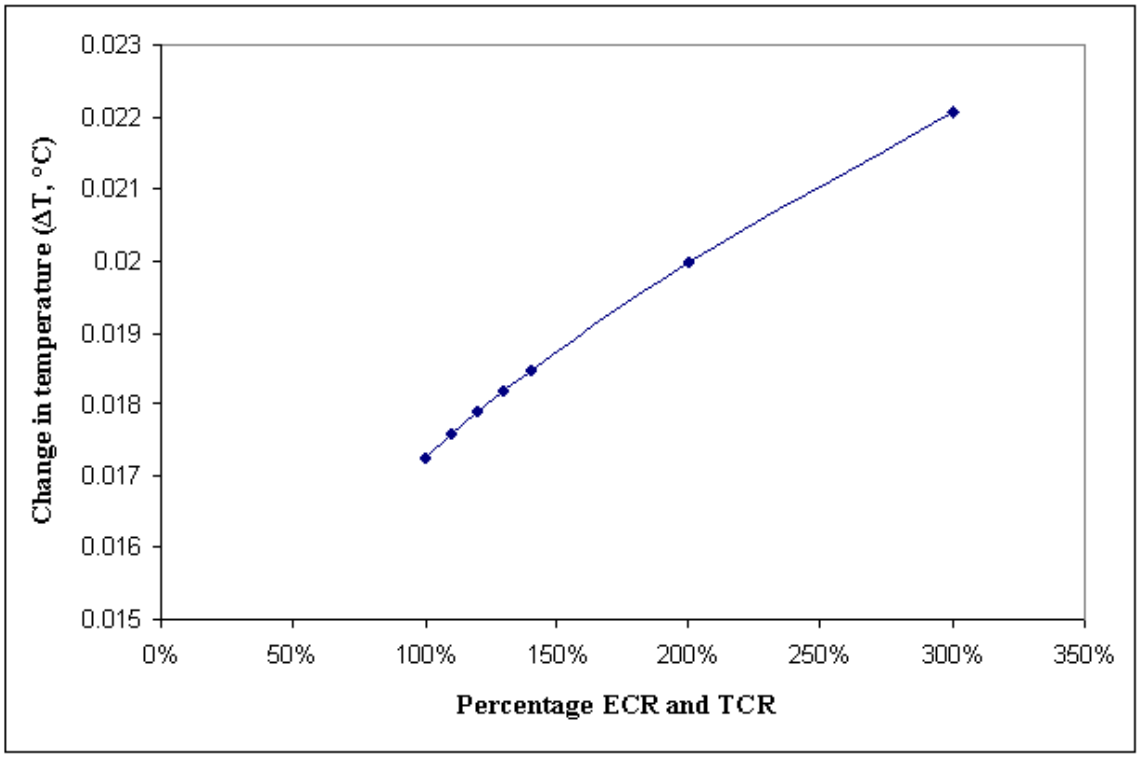

Figure 3-18: The effect of an increase in contact resistance on the change in temperature in the 40A connector

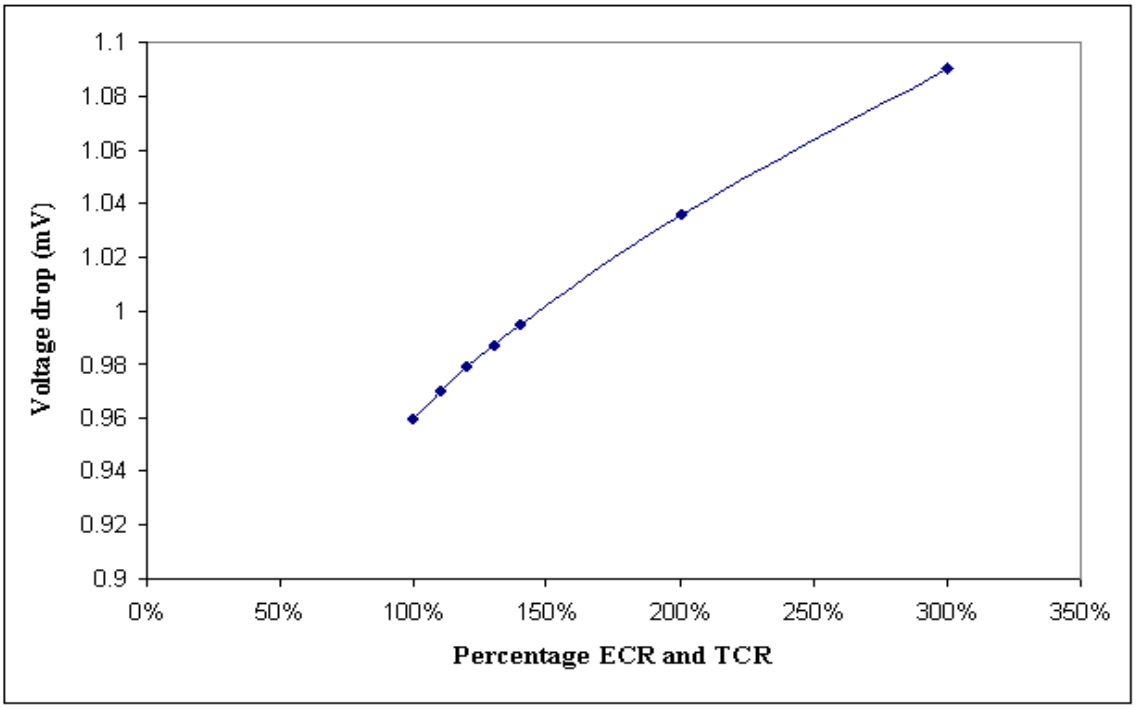

Figure 3-19: The effect of an increase in contact resistance on the voltage drop in the 40A connector

As the contact resistance is increased, the current flow in the connector is more concentrated or more bottlenecked, which causes current density to be increased, as shown in Figure 3-17. This is not an obvious finding since intuition would suggest that the maximum current density would increase proportionally to the average current density. This could cause the local asperity temperature to be much higher and cause surface softening and failure where the current density is highest.

From Figure 3-18, it can be seen that due to an increase in contact resistance, the change in temperature (temperature rise or ΔT) in the connector increases almost linearly. However, the bulk temperature rise is still relatively small, which indicates that the local temperature rise and temperature rise due to cable heating are much more important. Experimental measurements have shown that during testing the temperature of the connector increases by several more orders of magnitude, but this is believed to be due to heating of the long cables rather than connector heating due to contact resistance (see section 5.1).

Following Ohm's Law ($V = I \cdot R$), with a constant applied current, an increase in contact resistance leads to a corresponding increase in the voltage drop across the connector in a nearly linear way (Figure 3-19) although there is some nonlinearity to the curve. Therefore, the total resistance of the connector is also increased.

CHAPTER 4

Experimental Testing (without Vibration): 40A Connector

This chapter discusses with the experimental tests of 40A connectors under stationary conditions. The test results include the connector resistance (R) and connector temperature measurements that are plotted as a function of applied currents.

Eq. (4-1) clearly highlights the relationship between connector resistance (R), electrical contact resistance (ECR) and the bulk resistance ($bulk_{res}$) in the component.

$$R = ECR + bulk_{res} \tag{4-1}$$

A single Sorensen DCS-125E power supply is required to provide the DC current for the 40A connectors. The maximum current output of this power supply is 125A. The analog signals of voltage drop and transmitted current are collected by analog input modules. The temperature readings are collected by thermocouple input modules. The modules are installed in a data acquisition board.

Connector resistance is indirectly estimated by measuring the voltage drop across the connector and DC current in the power loop and then by applying Ohm's law: $V = I \cdot R$. The current going through the connector is measured by a LEM IT 400-S current transmitter. Temperature is measured by K-type thermocouples.

Experimental tests were conducted for four single 40A connectors by increasing current from 5 - 50A in steps of 5A. Therefore, the connector was tested for the same applied currents that were applied in the 40A connector multi-physics model. During the testing, the applied current was held constant for 30 minutes at each step value (for example, 35A) so that a steady state temperature is reached. After that, data were recorded before the next applied current. The voltage drop and temperatures at two locations are measured, as shown in Figure 4-1.

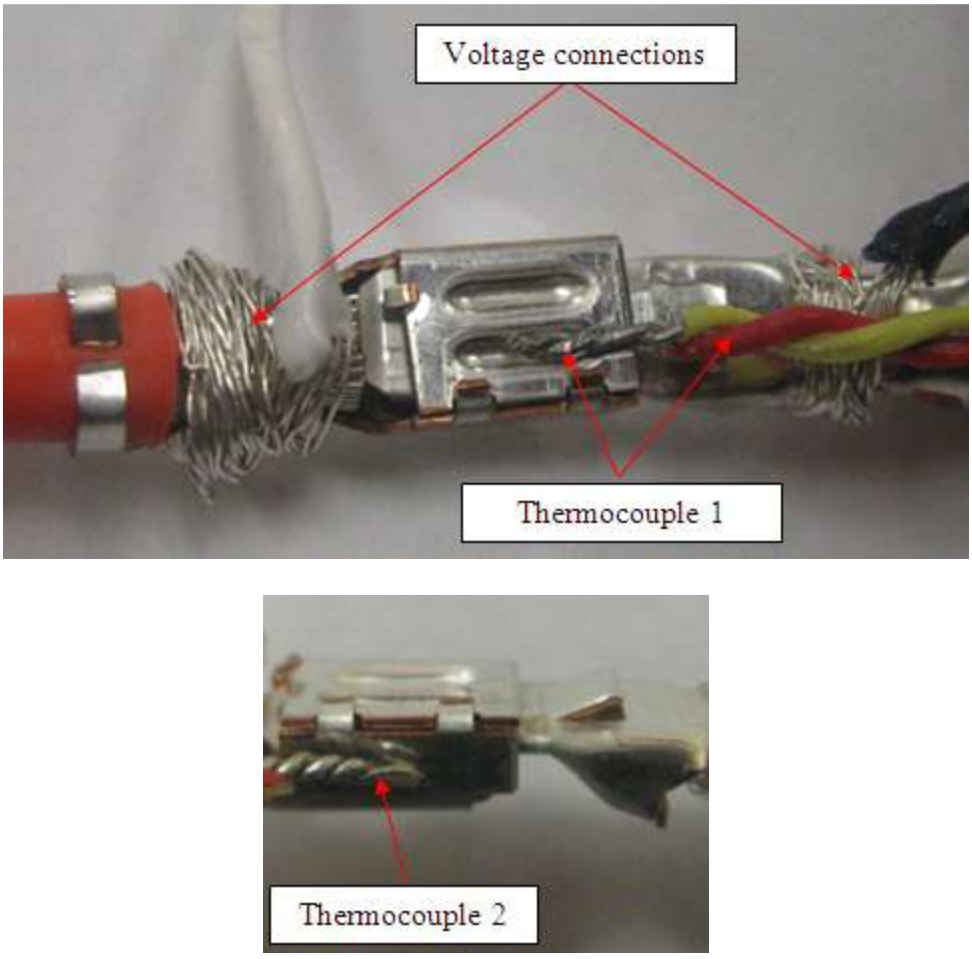

Figure 4-1: The placement of thermocouples and voltage measuring wires

In Figures 4-2 to 4-4, the connector resistance (R), connector temperature at the base (T1) and connector temperature at the side (T2) data are averaged among four tests and error bars are used to present the standard errors.

In Figure 4-2, the measured connector resistance is plotted versus applied currents. The value of nominal connector resistance provided by the manufacturer is 0.24 mΩ. From experimental testing at Auburn, the connector resistance (R) is 0.227 mΩ for an applied current of 35A. It is reassuring that this value compares very well with that provided by the manufacturer.

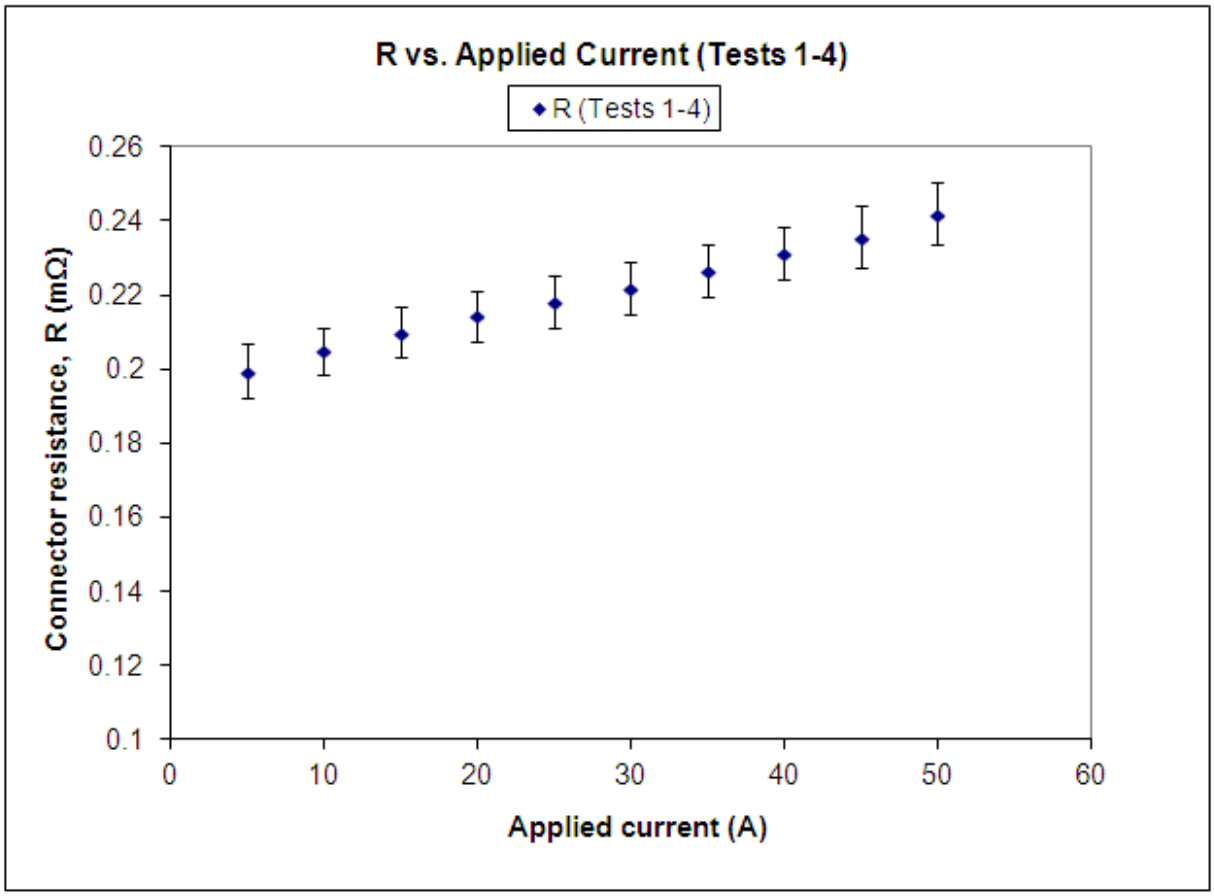

Figure 4-2: Connector resistance (R) versus constant current in the 40A connector (with error bars for all 4 tests)

An increasing trend of connector resistance versus constant currents is noticed in Figure 4-2. It is assumed that the increase of current causes more Joule heating and then shrinks the area of contact so the connector resistance increases accordingly. It could also be due to expansion causing the current to travel further through the connector, therefore increasing the resistance.

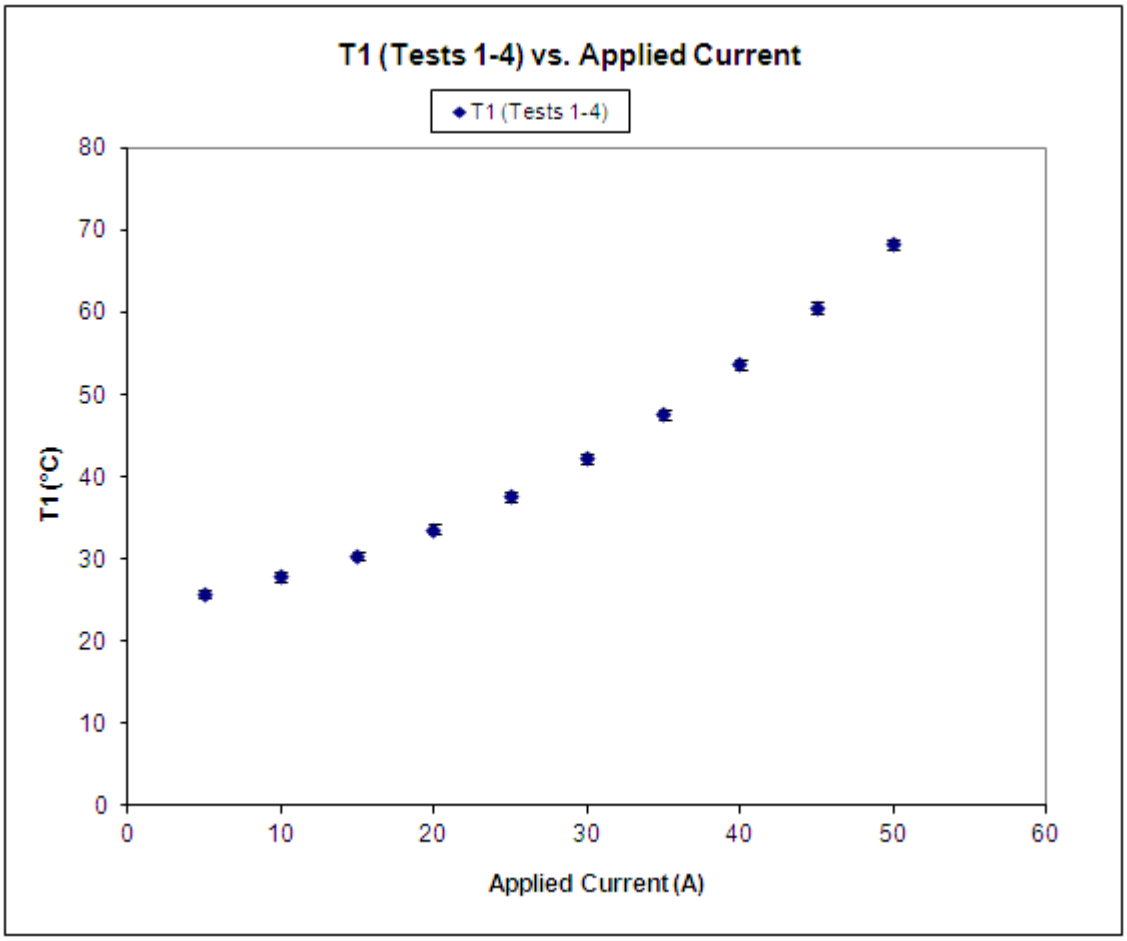

Figure 4-3: Connector temperatures at base (T1) versus constant current in the 40A connector (with error bars for all 4 tests)

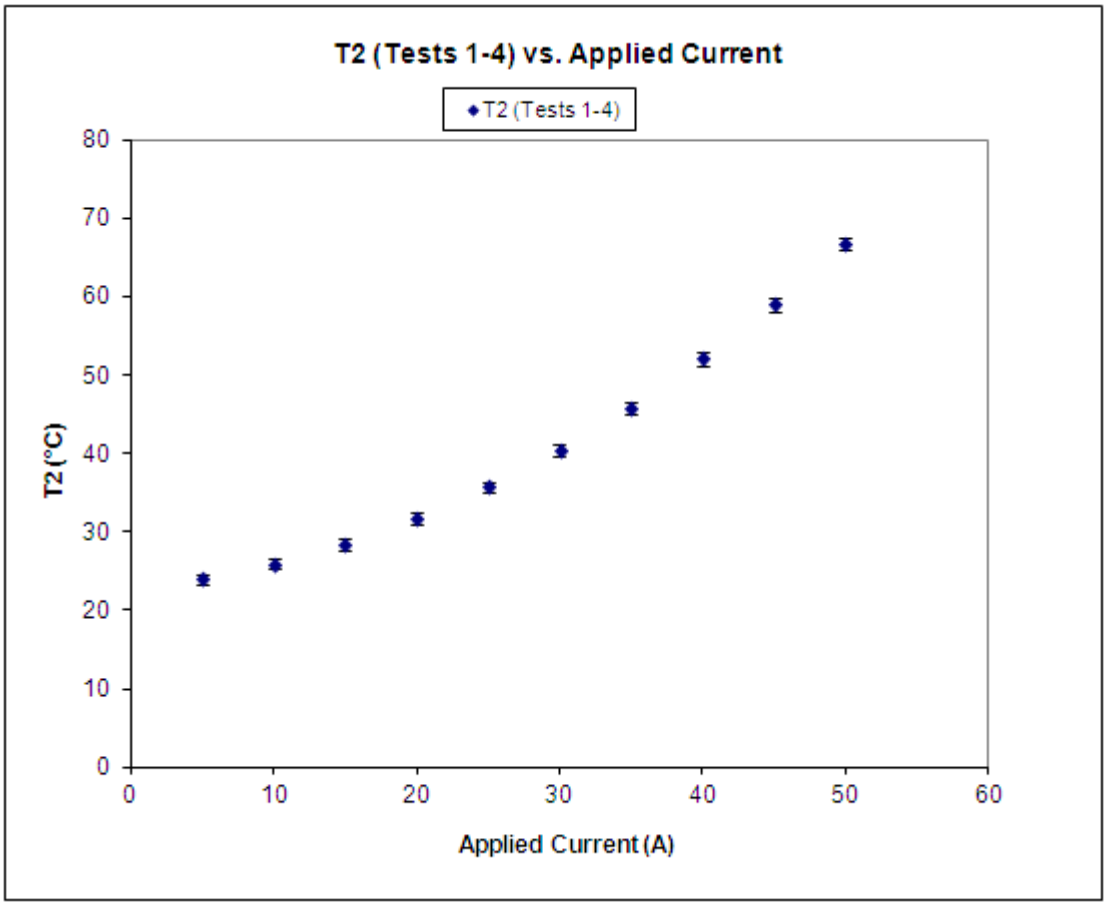

Figure 4-4: Connector temperatures at side (T2) versus constant current in the 40A connector (with error bars for all 4 tests)

The plots of connector temperatures at the base (T1) and at the side (T2) are shown in Figures 4-3 and 4-4, respectively. Notice that, as expected, T1 and T2 increase in a nonlinear way with applied current for all 4 tests (following Joule heating). Very little difference between T1 and T2 is found. This demonstrates that the temperature gradient across the connector is small and that the heating is mostly due to the cables.

Chapter 5

Comparison of Experiment and Simulation Results (without Vibration): 40A Connector

Experimental test results for connector resistance (R) are compared with that obtained from multi-physics modeling of the 40A connector. Figure 4-2 shows the variation of connector resistance with the applied current during experimental testing (without vibration) of four 40A connectors. Figure 5-1 shows the variation of connector resistance with the applied current (I) in the 40A connector model. In both the figures, an increasing trend (that is, an increase in R with an increase in applied current) was noticed. However, even though the R vs. I trend is the same, the values of R obtained from the 40A connector model and experiment are different by an order of 10. This difference can be attributed to the fact that the 40A connector model is only a 2D one and that the amount of bulk resistance between the model and experiment will be different due to the placement of the voltage wires to measure the voltage across the 40A connector.

Another important observation can be made from Figure 5-1. At an applied current of 40A in the model, there is a change in the slope of the R vs. I curve. It is possible that currents higher than 35A will cause more heating and thermal expansion of the connector leading to nonlinear changes in the connector geometry (such as changes in contact areas) or the route of the current flow.

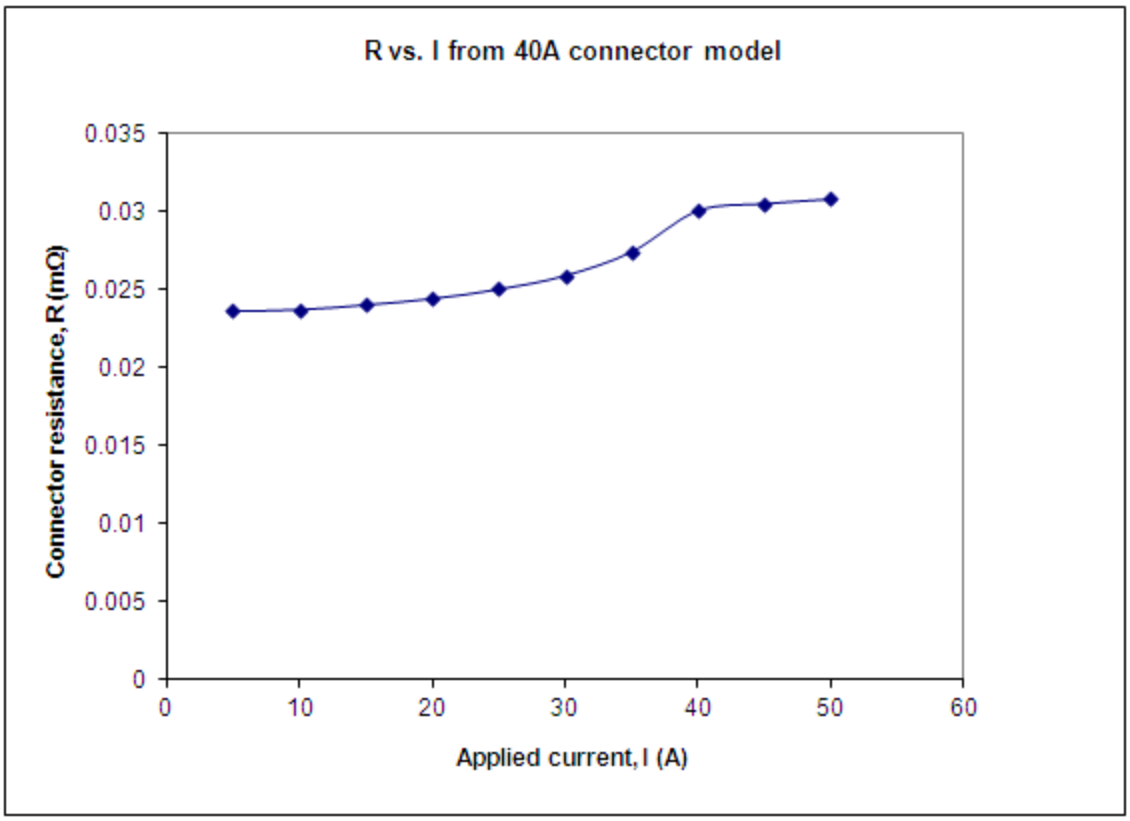

Figure 5-1: Plot of connector resistance versus applied current from 40A connector model

5.1 Analysis of temperature rises (ΔT, change in temperature) in the cable and connector

As discussed in the previous chapters, it was noticed that the temperature rise (ΔT) in the connector from the 40A connector model (multi-physics FEM model) was very low and therefore theorized that the heating was mostly coming from the cables. To prove this we have derived simple analytical predictions of ΔT (change in temperature) for the connector and also performed some simple experiments to verify them. First, we will show the derivation of these analytical predictions.

The 1-D heat conduction equation (that is, Fourier's law) is given as follows [57]:

$$q_x'' = -k(dT/dx) \tag{5-1}$$

where q_x'' is the heat flux (W/mm^2), k is thermal conductivity (W/mm-K), and dT/dx is the temperature gradient along the x direction. In addition, the following relationships are used.

$$q_x'' = q/A \tag{5-2}$$

$$A = \pi r^2 \tag{5-3}$$

where q is the heat transfer rate (W), A is the cross sectional area of the circular bar (mm^2) and r is the radius of the bar (mm).

Also, we must consider the heating due to electrical conduction (Joule heating) that is given by:

$$q = I^2 R \tag{5-4}$$

where I is the electric current (A) and R is the resistance (Ω).

Resistance for a conductor with a constant cross-section and assuming uniform current flow is given by:

$$R = (\rho x)/A \tag{5-5}$$

where ρ is the electrical resistivity (Ω-mm) and x is the length of the conductor (mm).

By substituting Eq. (5-5) into Eq. (5-4), we obtain

$$q = (I^2 \rho x)/A \tag{5-6}$$

Then, by substituting Eq. (5-6) into Eq. (5-2), we obtain

$$q_x'' = (I^2 \rho x)/A^2 \tag{5-7}$$

Eq. (5-1) can then be rewritten as:

$$\Delta T = \int_{T_1}^{T_2} dT = -\int_{0}^{L/2} (q_x^{"} / k) dx \tag{5-8}$$

And finally, on substituting Eq. (5-7) into Eq. (5-8) and on solving the Eq. (5-8) for ΔT, we obtain the simple analytical prediction (Eq. (5-9)).

$$\Delta T = -\frac{(I^2 \rho L^2)}{(8A^2 k)} \tag{5-9}$$

where ΔT is the change in temperature and L is the length of the connector.

Again, for simplicity, the connector cross-section is considered as a solid circular bar even though its actual cross-section is non-circular and not solid. The values of ρ and k for the connector are given in Table 3-1. In the analytical model, the following values were used to model the connector: r = 1.5 mm, the total length of the connector = 30 mm. For 35A, the value of ΔT calculated using Eq. (5-9) is 0.18 °C. Thus, the ΔT across the connector itself is predicted to be extremely small.

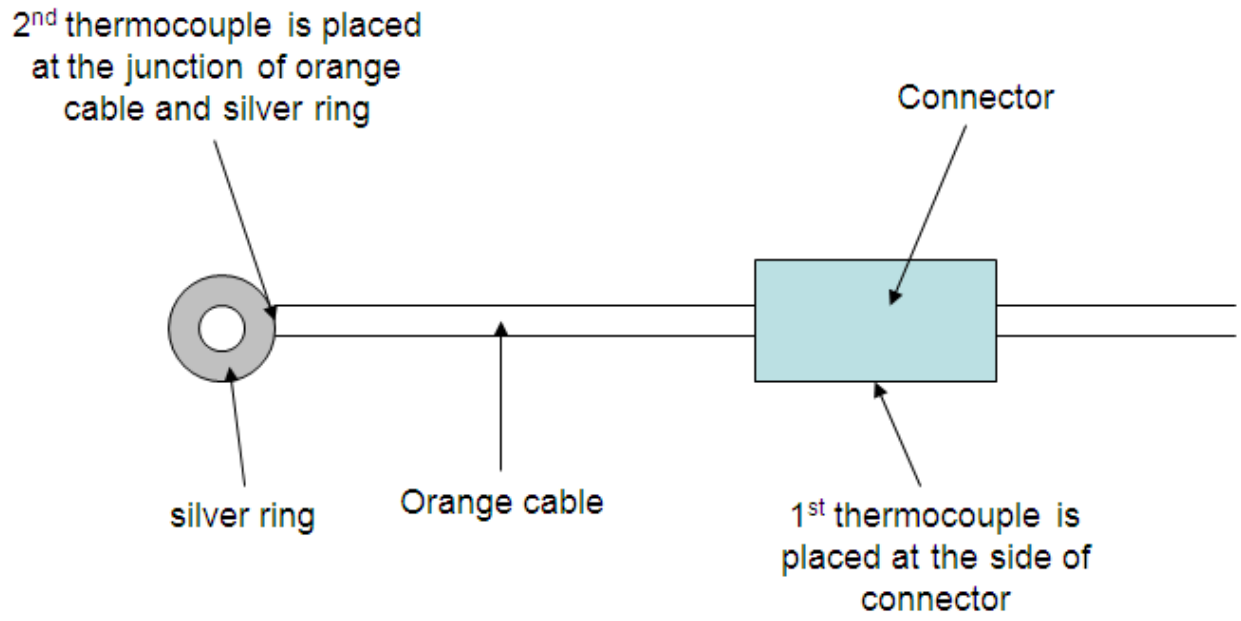

Figure 5-2: Schematic diagram of thermocouple placement on cable and connector

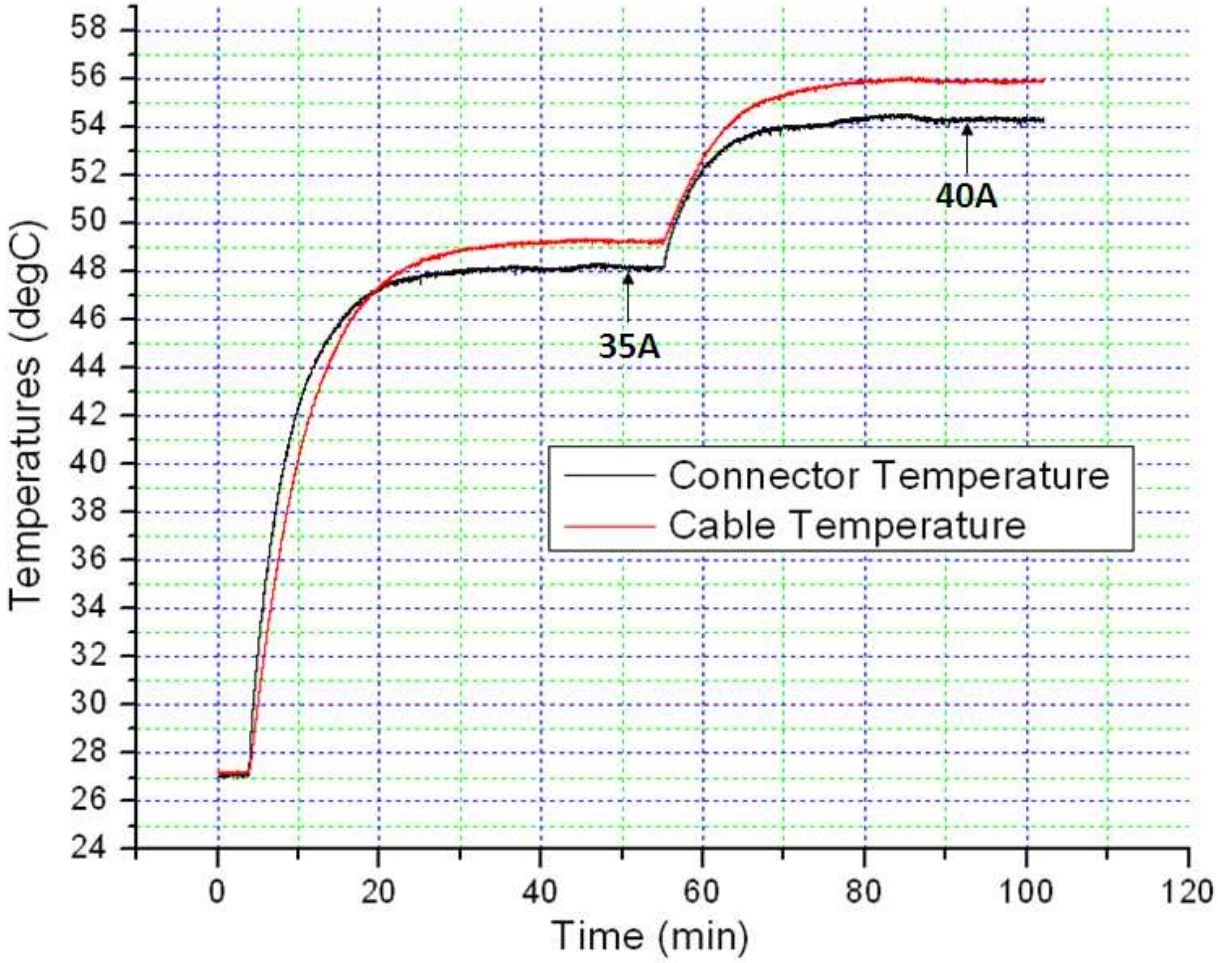

Figure 5-3: Experimental variation of cable temperature and connector temperature with time for a 40A connector at 35A and 40A applied currents

Applied current (A)	Temperature of cable (°C)	Temperature of connector (°C)	Room Temperature (°C)	ΔT (for cable) (°C)	ΔT (for connector) (°C)
35	49.26	48.16	27	22.26	21.16
40	55.95	54.33	27	28.95	27.33

Table 5-1: Experimental measurements of cable and connector temperatures and ΔT at two different applied currents

In addition to the analytical model, experimental measurements of the temperatures of both the cable and the connector on a single 40A connector have been performed. Figure 5-2 shows the schematic diagram of the placement of thermocouples to measure cable temperature and connector temperature. Figure 5-3 shows the experimental variation of cable temperature and connector temperature as a function of time for a 40A connector at 2 different applied currents of 35A and 40A. The change in temperature of the cable and the connector were read after the values had sufficient time to reach a near steady-state value. The values of steady state temperatures of the cable and the connector as well as the ΔT for the cable and the connector for applied currents of 35A and 40A are provided in Table 5-1.

Predictions from the simple analytical model and the experimental measurements both suggest that the connector temperature is governed mostly by the heat generated in the cables. This also verifies the small values of ΔT (for the connector) obtained from the multi-physics finite element model (see Figure 3-13), where only the connector (without the cable) is considered.

CHAPTER 6

Experimental Testing (with Vibration): 40A Connector

In order to investigate a connector's performance, degradation characteristics, and reliability, a connector test apparatus is developed to provide a controlled testing environment. 40A connectors are tested in a controlled environment comprising of a specified vibration amplitude, vibration frequency, temperature and humidity that mimic the conditions in an automobile. Two variables, namely, connector resistance (R) and connector temperature (T), are used to evaluate the connector performance in the accelerated tests. The measurements of R and T are also made in real time during the tests. Figure 6-1 is the overview of experimental setup that describes the design concept. Again, as mentioned in chapter 4, one Sorensen DCS-125E power supply is used to apply the DC current to the connectors.

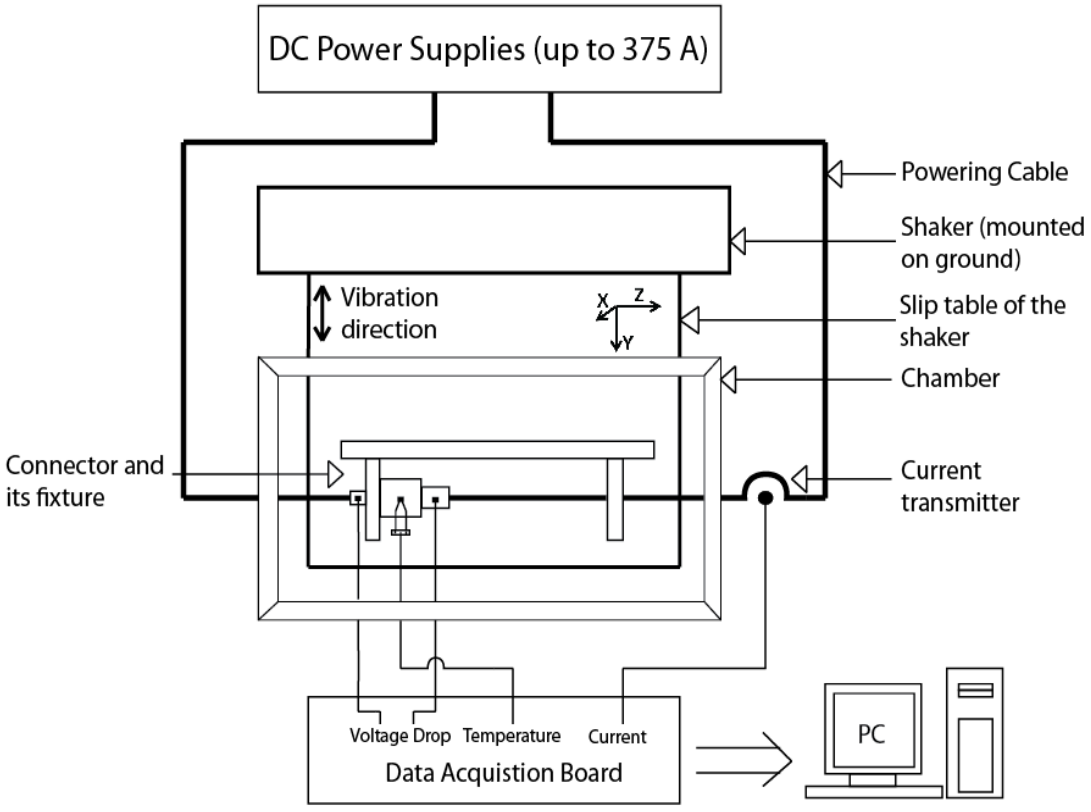

Figure 6-1: Overview of test setup

Vibration tests are performed using an amplitude-and-frequency-controlled electro-magnetic shaker (see Figure 6-2) and a CSZ (Cincinnati Sub-Zero) environmental chamber (see Figure 6-3), which enclose the connector to be tested. The environmental chamber is used to control the ambient temperature and humidity of the enclosed connector. The temperature range can be set from -200 °C to 400 °C, with 0-100 % relative humidity. The chamber is placed above the shaker so that the connector can be enclosed as shown in Figure 6-3.

Figure 6-2: Vibration shaker removed and detached from the environmental chamber

Figure 6-3: Environmental chamber

The connector to be tested is placed inside the chamber. Fixtures are specially designed to secure the connector on the shaker through the cloth that is used to insulate the inner temperature and humidity from the room environment, as shown in Figure 6-4. The power supply cable goes through a hole on top of the chamber and then connects to the power source. The measuring wires of voltage and thermocouple also go through the same hole and are then connected to the data acquisition board. The thermocouple is placed on the base of the spring terminal (that is, in the same location as of thermocouple 1 in Figure 4-1) of the 40A connector.

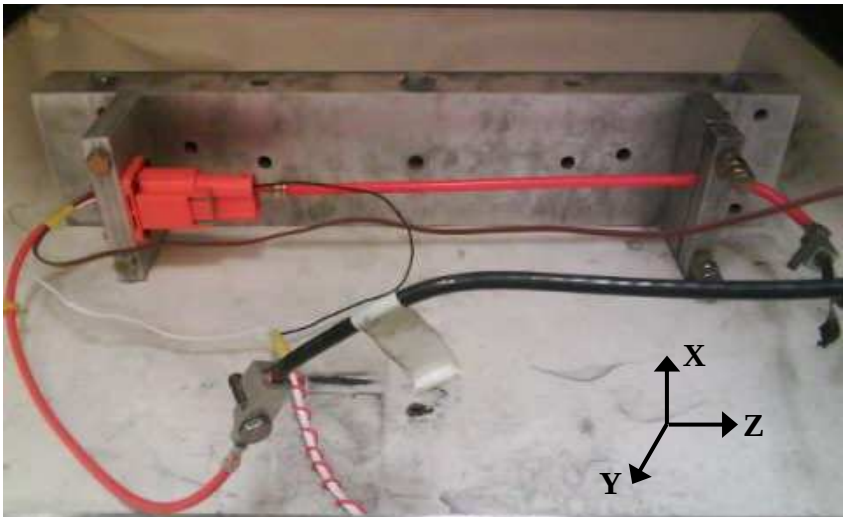

Figure 6-4: Fixture for 40A connector on the shaker
(Note: Y-axis is parallel to the slip table of the shaker, that is, ground)

The connector housing is bolted to a plate on one end of the fixture so that the connector vibrates in unison with the shaker. A clamp is also designed to fix the supplied 40A connector cable onto the other end of the fixture (see Figure 6-4). The base of the fixture is designed with multiple sets of holes so that the position of the clamp can be adjusted for different lengths of the cable. In this way, the natural frequency of the connector system can be adjusted if needed. Having longer cables involved in the vibrating system results in lower natural frequencies and generally larger displacements.

6.1 Test methodology of accelerated tests

6.1.1 Test conditions

A study on the effect of various operating conditions (such as vibration direction, vibration amplitude and vibration frequency) on connector performance is conducted and is summarized in Figure 6-5. At the same time, ambient temperature and humidity can also be controlled. The connector performance, fretting and failure mechanisms are primarily tracked by connector resistance (R). Connector temperature (T) will be also studied as an auxiliary assessment.

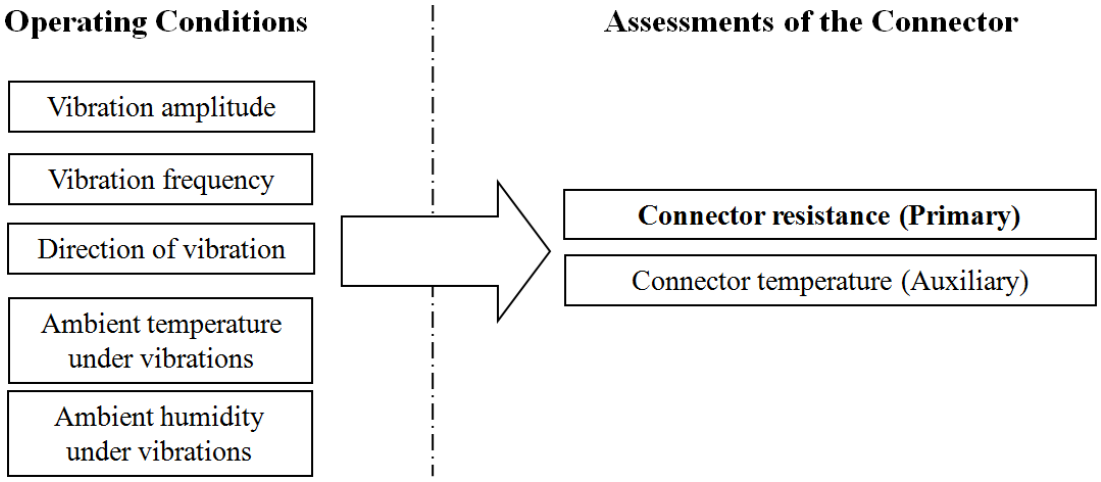

Figure 6-5: Operating conditions and assessments of connector for accelerated tests

6.1.2 Definition of coordinates for vibrations

The definition of coordinates to conduct accelerated vibration tests is shown in Figure 6-6. Z direction follows the direction of cable. The X and Y directions are perpendicular to the Z direction via the right hand rule. Vibrations in each of these directions are applied to the 40A connectors.

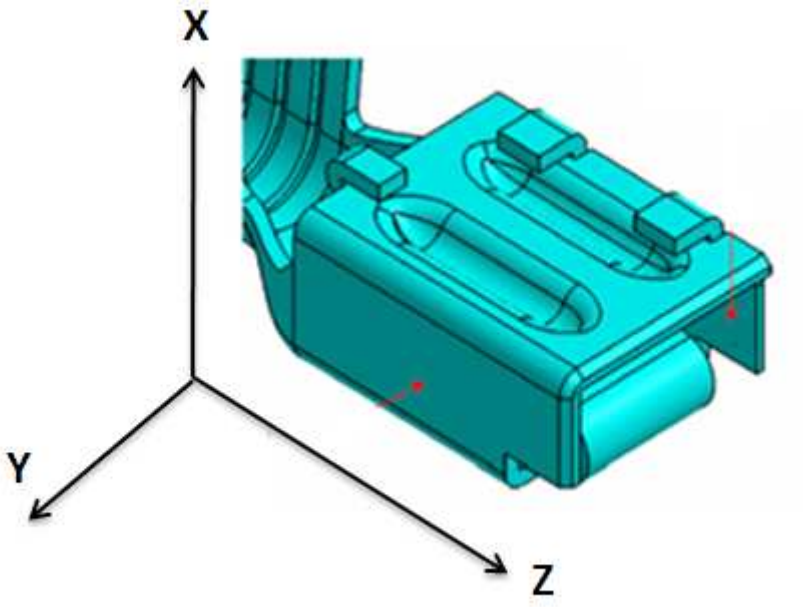

Figure 6-6: Definition of coordinates for vibrations (40A connector)

6.1.3 Test procedure

The test procedure for each test run is defined in Figure 6-7. Before vibration starts, the 40A connector should be fully heated to a steady state temperature by the constant applied current of 35A within the controlled ambient temperature and humidity environment. After vibration starts, the vibration amplitudes are increased step by step to a maximum value. The detailed test conditions for 40A connectors will be shown in the following section.

This test procedure is designed after the critical amplitude or threshold tests developed by Flowers group [15, 18]. Essentially, the amplitude is increased until significant fretting degradation occurs, which characterizes the threshold for a particular set of test conditions. In addition, this can allow for the relative fretting performance to be mapped over several different parameters.

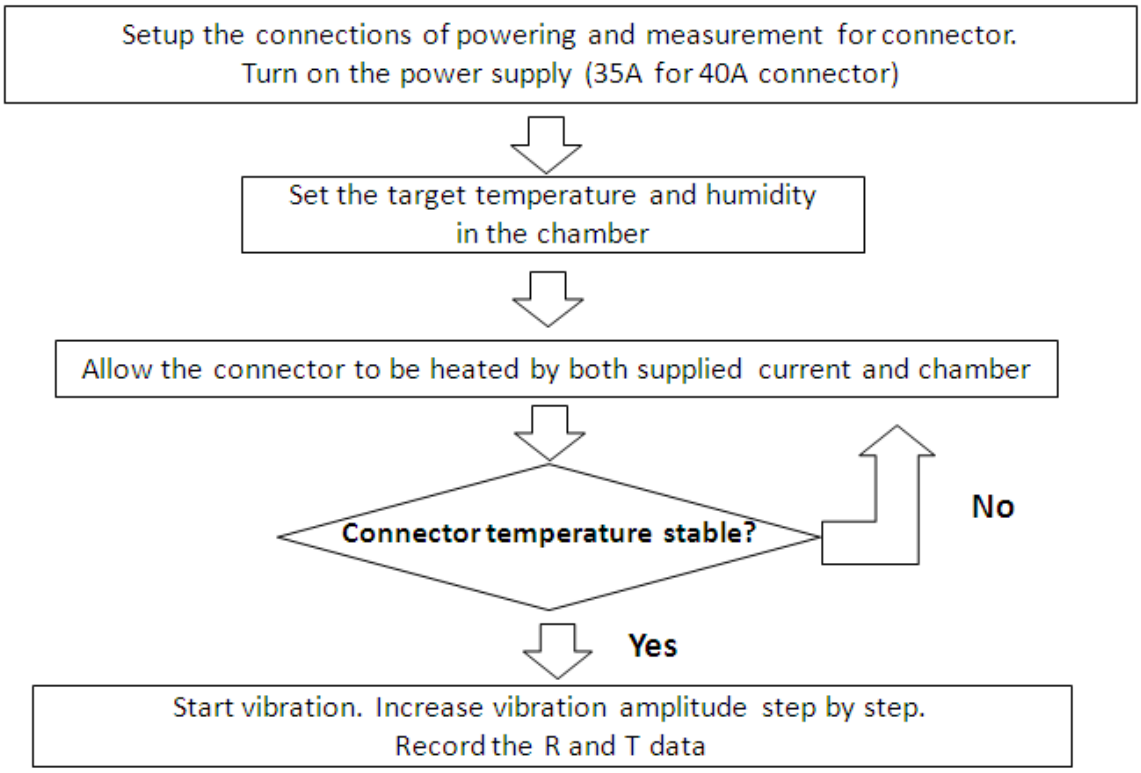

Figure 6-7: Test procedure for accelerated tests

6.2 Accelerated tests for 40A connectors

Detailed accelerated test conditions for the 40A connectors for each test run are listed in the test matrix, as shown in Table 6-1. A new connector is used for each of the iterations per test run.

<table>
<tr><th>Test Run</th><th>Frequency (Hz)</th><th>Temperature (℃)</th><th>Humidity (%RH)</th><th>Vibration Directions</th><th>Comments</th></tr>
<tr><td>T1</td><td>100</td><td>80</td><td>65</td><td>Z</td><td>Benchmark Test</td></tr>
<tr><td>T2</td><td rowspan="2">100</td><td rowspan="2">80</td><td rowspan="2">65</td><td>X</td><td rowspan="2">Vary vibration directions</td></tr>
<tr><td>T3</td><td>Y</td></tr>
<tr><td>T4</td><td>50</td><td rowspan="3">80</td><td rowspan="3">65</td><td rowspan="4">The direction that causes the most fretting</td><td rowspan="3">Vary vibration frequency</td></tr>
<tr><td>T5</td><td>150</td></tr>
<tr><td>T6</td><td>200</td></tr>
<tr><td>T7</td><td rowspan="2">100</td><td>25</td><td rowspan="2">65</td><td rowspan="2">Vary temperature</td></tr>
<tr><td>T8</td><td>120</td></tr>
</table>

Table 6-1: Test matrix of accelerated tests

Amplitudes	0.1mm	0.15mm	0.2mm	0.25mm	0.5mm	0.75mm	1.0mm
Durations	$1.2*10^5$ cycles	$1.2*10^5$ cycles	$1.2*10^5$ cycles	$1.2*10^5$ cycles	$1.2*10^5$ cycles	$1.2*10^5$ cycles	$1.2*10^5$ cycles
For 50 Hz Tests				40min	40min	40min	40min
For 100 Hz Tests				20min	20min	20min	20min
For 150 Hz Tests	15min	15min	15min	15min			
For 200 Hz Tests	10min	10min	10min	10min			

Table 6-2: Vibration amplitudes (peak-to-peak) and durations for each test run

For each test run, the vibration amplitude is increased stepwise following Table 6-2. Based on the results in some preliminary tests, the range of amplitudes that best characterized the mechanism of fretting for 40A connectors are selected, as shown in Table 6-2. The vibration cycle is fixed at $1.2x10^5$ cycles for each test and the vibration time is varied accordingly. In this way, the tests among different vibration frequencies are more comparable. For tests conducted at 50 Hz and 100 Hz, lower vibration amplitudes (less than 0.25 mm) are not considered from being applied to the connectors because they are too small and cause little variation in the connector resistance (based on our pretests). For tests with 150 Hz and 200 Hz, higher vibration amplitudes (greater than 0.25 mm) are not applied to the connectors because they exceed the maximum possible output of the shaker.

A typical raw connector resistance (R) and connector temperature (T) data vs. time along with regions of four different amplitudes for one of the iterations of a test run (T6, iteration 1, 200 Hz, 80 °C, 65 %, Y direction) is shown in Figures 6-8 and 6-9, respectively. Before the start and after the end of each vibration amplitude, the connector is rested (that is, not vibrated) for approximately 3 minutes (represented by narrow regions in Figures 6-8 and 6-9) so that the variations in R and T for the entire test iteration can be seen distinctly. Corresponding to a 200 Hz vibration frequency, the 40A connector is subjected to four different vibration amplitudes (see Table 6-2) where each of the amplitudes is applied for 10 minutes. Similarly, depending on the vibration frequency for a given test run, vibration amplitudes are applied to 40A connectors so that all the test runs in the test matrix (see Table 6-1) are completed.

The raw R and T data vs. time obtained during each iteration of all 8 test runs are filtered using a low pass filter Matlab™ code with a cut-off frequency of 0.1 Hz. The sampling frequency is 10 Hz. The graphical plots (Figures B-1 to B-48) of the filtered R and T data vs.

time for each of the iterations of all 8 test runs (that is, a total of 48 figures) are included in an appendix (Appendix B). There is electrical and mechanical noise associated with the raw and filtered R and T data vs. time. So, it can be difficult to interpret the results without first averaging or filtering the data.

In Figure 6-8, there is a sudden drop in R immediately upon the start of vibration for the first time in the test iteration at an amplitude of 0.1 mm. This is seen because the spring and pin connector terminals become more firmly in contact due to a removal of the inherent tin-oxide layer. As a result of more firm contact, the current flow increases thereby causing sudden instantaneous drop in R. Connector resistance (*R*) then becomes stable under both 0.1 mm and 0.15 mm amplitudes. At the instant of application of 0.2 mm vibration amplitude, R increases marginally and remains almost stable until the connector stops vibrating at 0.2 mm amplitude. R increases again immediately after the start of vibration at 0.25 mm amplitude. However, R oscillates up and down 3 times during the entire 10 minute duration of vibration at 0.25 mm amplitude possibly due to the aliasing effect, inherent thermal cycles or mechanical wear. Connector temperature (*T*) rise during vibration (see Figure 6-9) causes an increase in R. The rise in R could also be due to fretting corrosion and wear occurring in the connector.

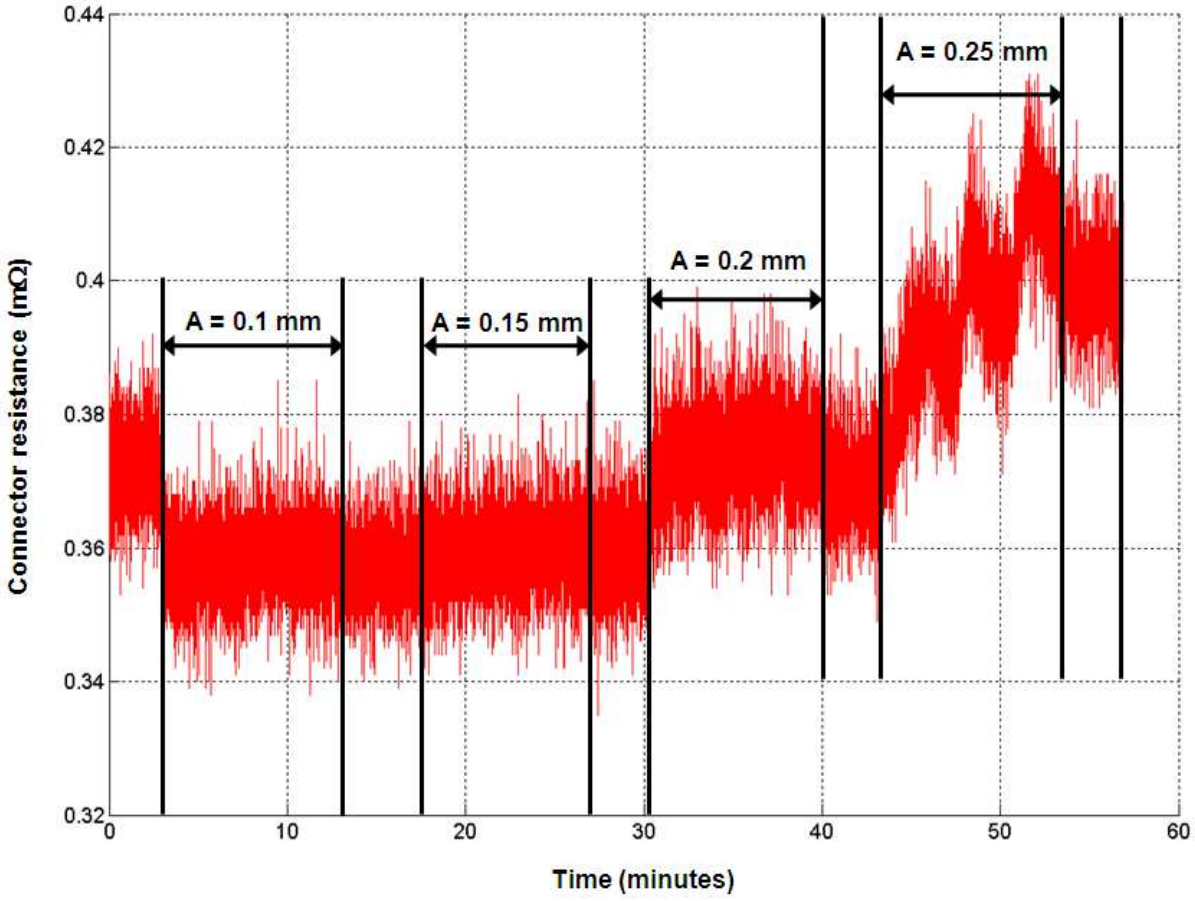

Figure 6-8: Plot of connector resistance versus time for test T6 iteration 1

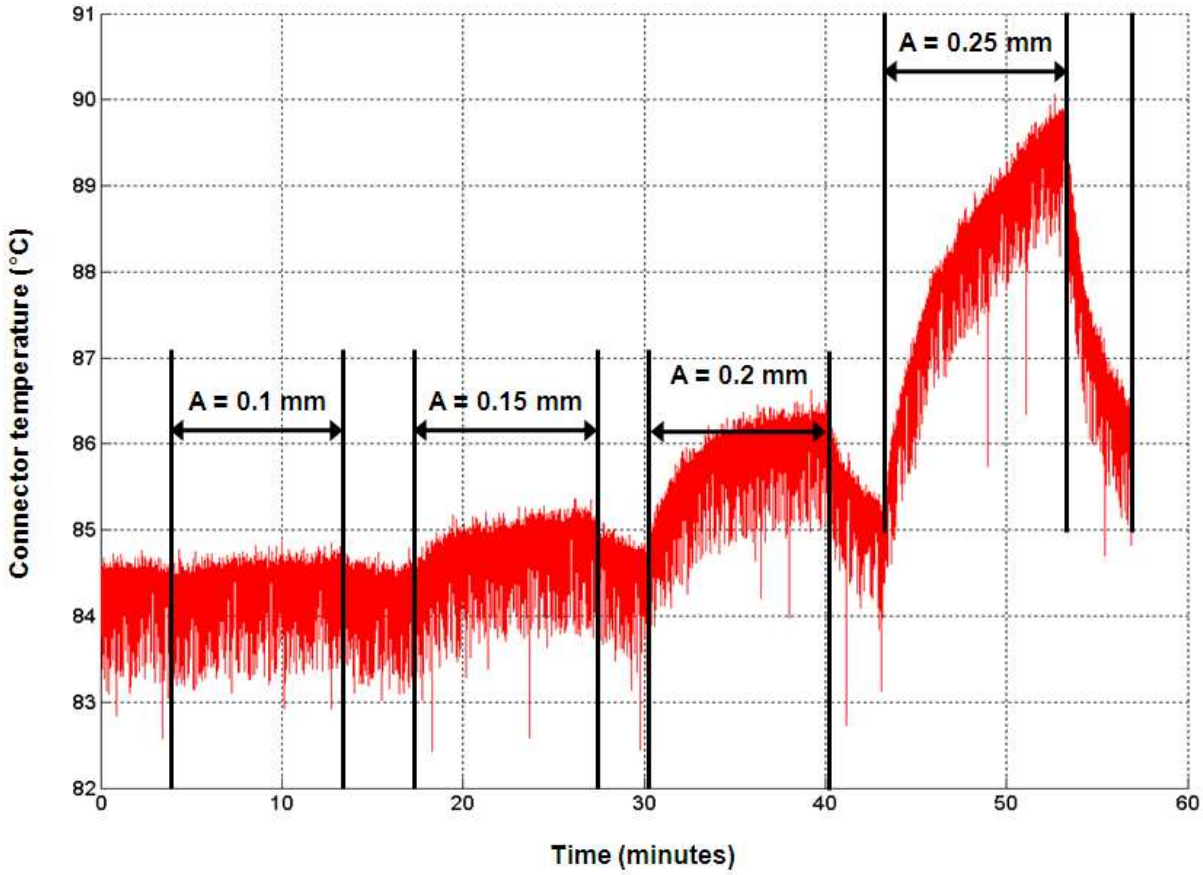

Figure 6-9: Plot of connector temperature versus time for test T6 iteration 1

Now, the variations in T with time in Figure 6-9 are discussed in detail. T remains almost constant during 0.1 mm vibration amplitude and increases marginally when the connector is vibrating at 0.15 mm and 0.2 mm amplitudes. However, a maximum rise in T is seen at a vibration amplitude of 0.25 mm. During vibration, the connector temperature (T) rises because the connector naturally experiences frictional heating and perhaps additional Joule heating because the connector resistance (R) has increased. We can also notice sudden drops in T immediately when connector stops to vibrate at the end of each of the four vibration amplitudes. From Figures 6-8 and 6-9, it is evident that the vibration amplitude of 0.2 mm in test T6 is the critical amplitude that determines the fretting threshold for 40A connectors.

Each vibration amplitude has one value of connector resistance (R) and connector temperature (T) so that one test iteration has a series of averaged and maximum Rs and Ts versus vibration amplitudes. The average values of R and T are computed by taking the average of all the filtered data points corresponding to the vibration amplitude. Among the same set of filtered data points previously considered to calculate the average value and for the same vibration amplitude, the maximum values of R and T are found.

Since each test run is repeated for 3 iterations, the average and maximum R and T values obtained from the filtered data are averaged (that is, mean) among these 3 test iterations for each of the four vibration amplitudes. In Figures 6-10 to 6-37, it is these mean values of both average and maximum R and T that are plotted with respect to the vibration amplitudes for each test run. In addition, the standard errors of average and maximum Rs and Ts among the repeating tests (per test condition) are calculated. The error bars are presented in these figures by using standard errors. Corresponding to the test run, all the test conditions (vibration direction, vibration frequency, temperature and humidity) are also stated alongside the results. In Figures 6-10 to 6-15, Figures 6-20 to 6-25 and Figures 6-30 to 6-33, identical trends of the maximum and average values for both R and T can be noticed.

The accelerated tests can be divided into three categories given below:

a) Effect of vibration direction on R and T

b) Effect of vibration frequency on R and T

c) Effect of ambient temperature on R and T

6.2.1 Effect of vibration direction on R and T

Figures 6-10, 6-12 and 6-14 show the variation of the maximum and average values of R under various vibration amplitudes in the Z, X and Y vibration directions, respectively. In Figures 6-11, 6-13 and 6-15, the changes in the maximum and average values of T versus vibration amplitudes for the same Z, X and Y directions, respectively, can be seen.

In Figure 6-10, there are no significant changes in the average and maximum R. This is because vibrations along the Z axis (test T1) cause very little relative motion of the spring and pin terminals. In test T1 (see Figure 6-11), although no drastic changes in the values of maximum T are seen, large decrements in the average T values can be seen at vibration amplitudes of 0.75 mm and 1 mm. These decrements could result from the lack of sufficient contact of the 2 terminals of the 40A connector while vibrating along the Z direction at these 2 amplitudes, unlike the good contact that occurs when the 2 terminals are not vibrating.

Slight decreasing trends in the values of both average and maximum R (test T2; Figure 6-12) can be observed for vibration amplitudes of 0.75 mm and 1 mm. As described earlier, during vibration at these 2 amplitudes, more firm contact is established between connector terminals since the layer of tin-oxide present on the surfaces of these terminals is removed. This causes more current flow and thus, leads to a reduction in R.

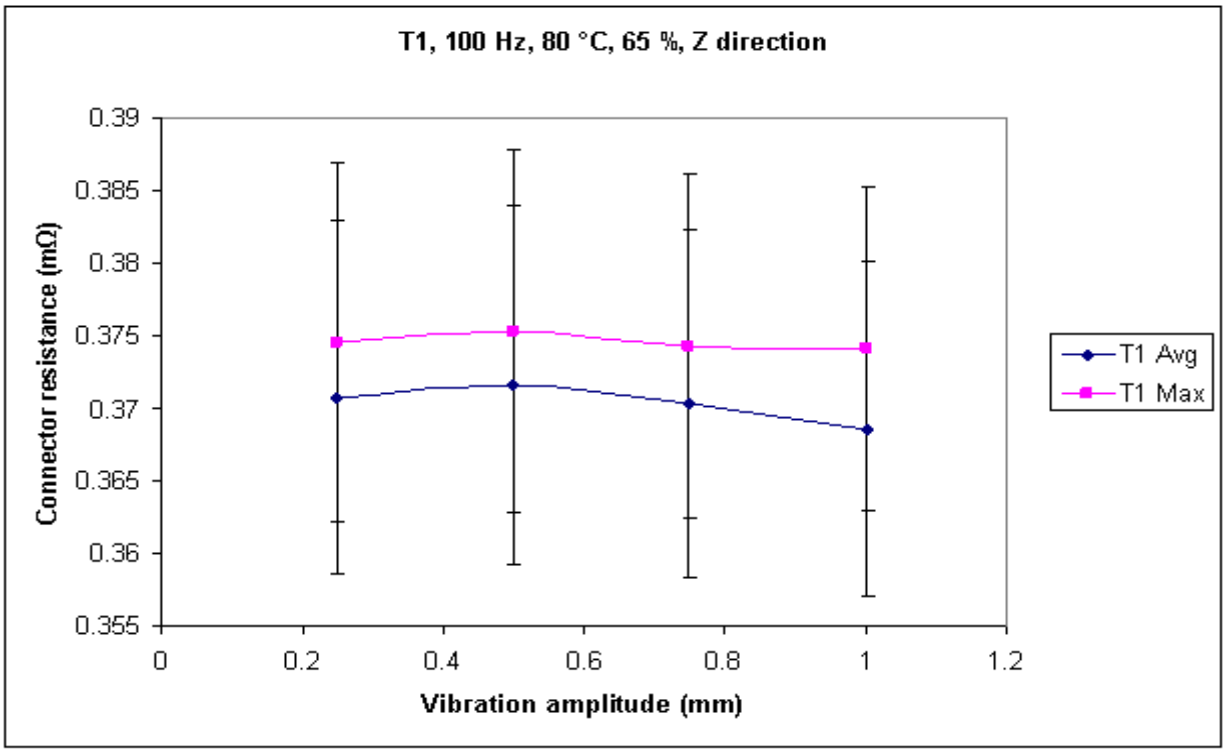

Figure 6-10: Connector resistance versus vibration amplitude for test T1

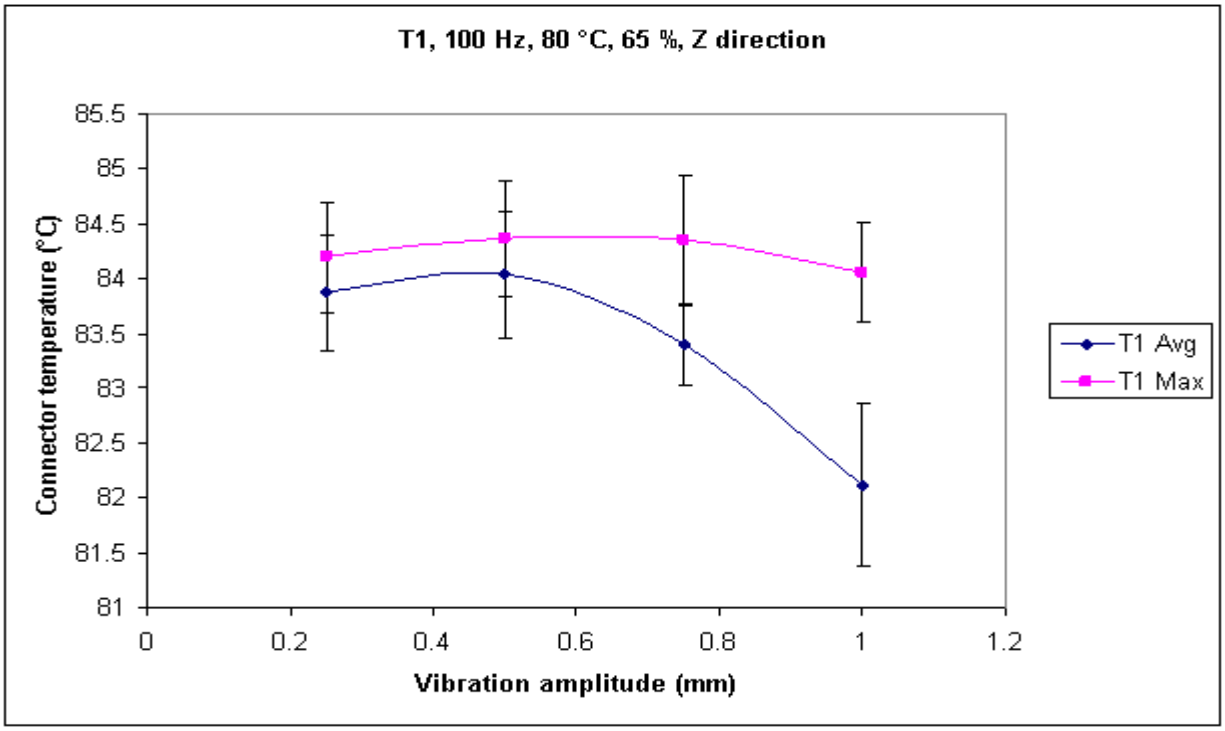

Figure 6-11: Connector temperature versus vibration amplitude for test T1

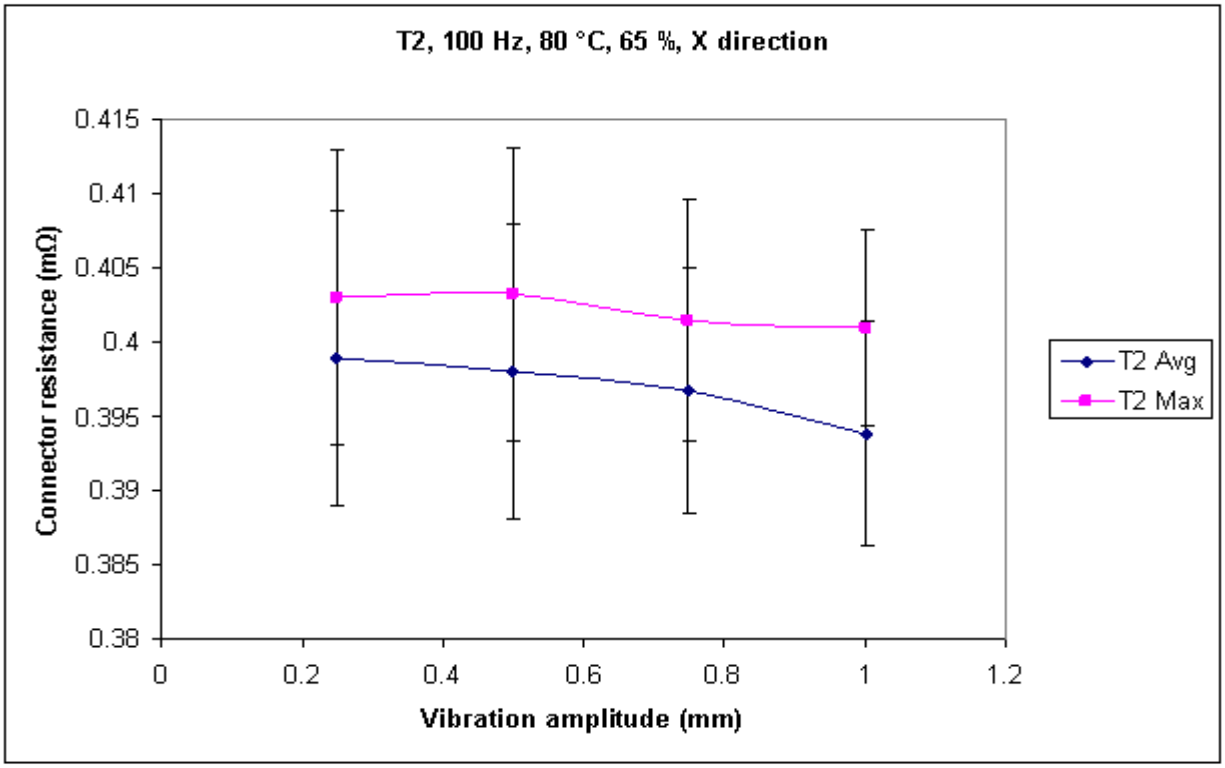

Figure 6-12: Connector resistance versus vibration amplitude for test T2

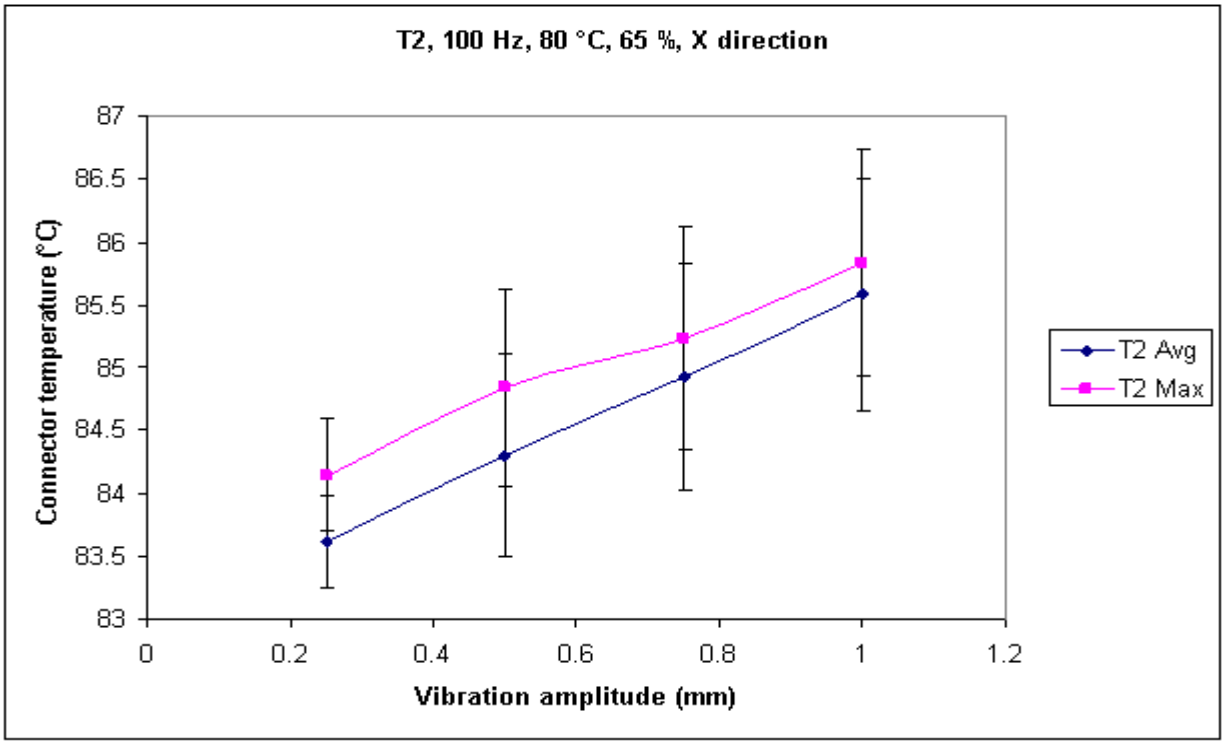

Figure 6-13: Connector temperature versus vibration amplitude for test T2

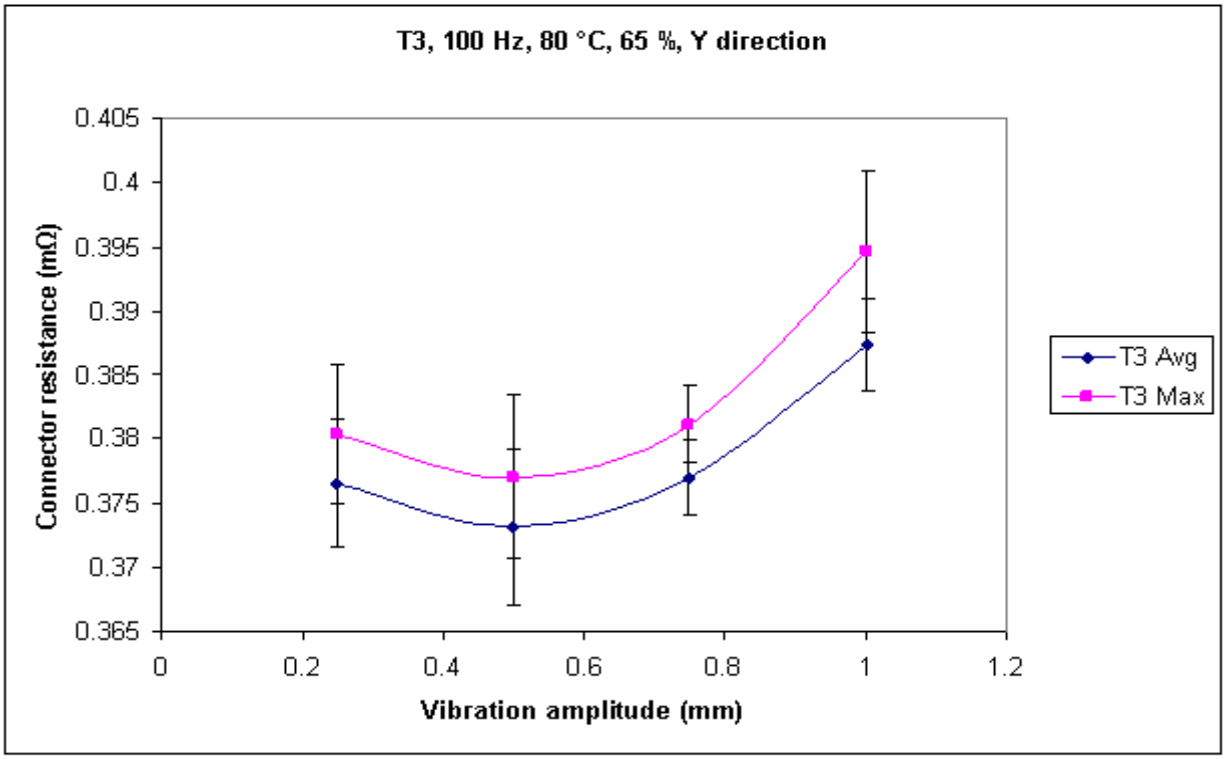

Figure 6-14: Connector resistance versus vibration amplitude for test T3

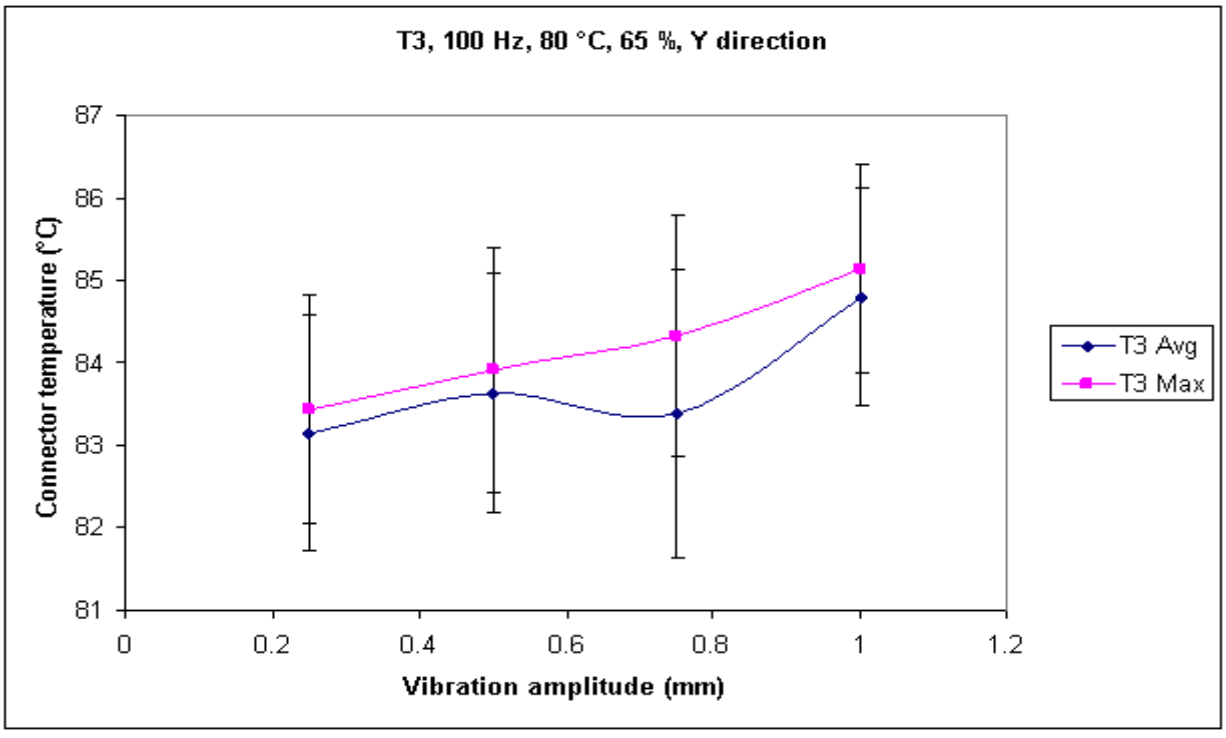

Figure 6-15: Connector temperature versus vibration amplitude for test T3

Next, the average and maximum R (see Figures 6-16 and 6-17) and the average and maximum T (Figures 6-18 and 6-19) are plotted by considering all 3 vibration directions (tests T1, T2 and T3) as a function of the vibration amplitude. It can be noticed that the vibrations in the Y direction (test T3; Figures 6-14, 6-16 and 6-17) cause, at first, a decrease in the values of average and maximum R at vibration amplitude of 0.5 mm followed by a much greater increase in these values of R (especially at amplitude of 1 mm) compared to the vibrations in the X and the Z directions. The decrement in R values again occurs due to more current flow by means of a firm contact between connector terminals. The increase in R is probably due to fretting corrosion and wear taking place in the Y direction or the connector housing is not as secure along the Y direction and so perhaps allows for more vibration. R can also increase when T increases due to frictional heating and increased Joule heating.

From Figures 6-16 and 6-17, it is evident that the values of both average and maximum R along X direction (test T2) are higher than those in tests T1 (Z direction) and T3 (Y direction). This is because the initial R measured, prior to the beginning of vibration for the first time in the T2 test iterations, itself is higher. This suggests that the R measured is different for each 40A connector even before vibration starts. Thus, higher values of the average and maximum R are measured in T2 tests. Therefore, based on the changes in R that take place between 2 different amplitudes in T3 tests, the Y direction is chosen to be the vibration direction for subsequent tests, that is, tests T4 to T8.

During the entire test duration, the average (Figures 6-15 and 6-18) and maximum (Figures 6-15 and 6-19) connector temperature (T) increases considerably under both X (test T2) and Y (test T3) directions. Again, as previously mentioned, the increase in T is due to the frictional heating exhibited by the connectors while vibrating.

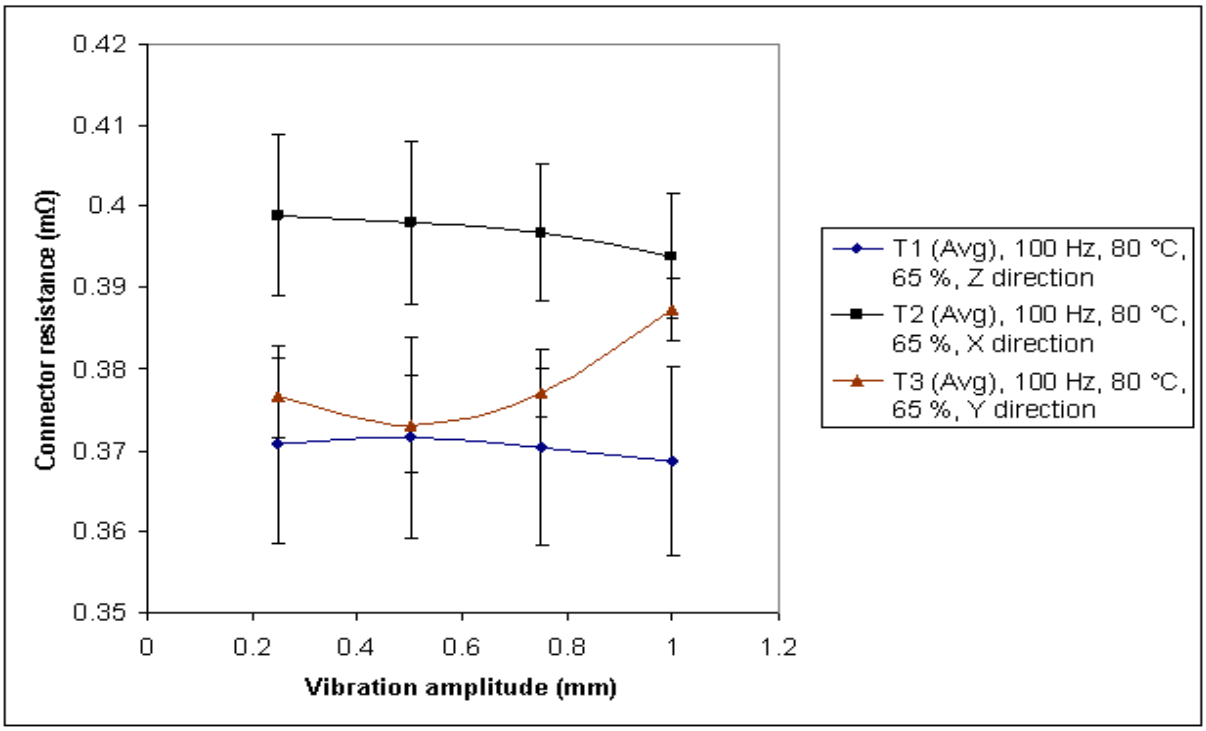

Figure 6-16: Average connector resistance versus vibration amplitude for different vibration directions

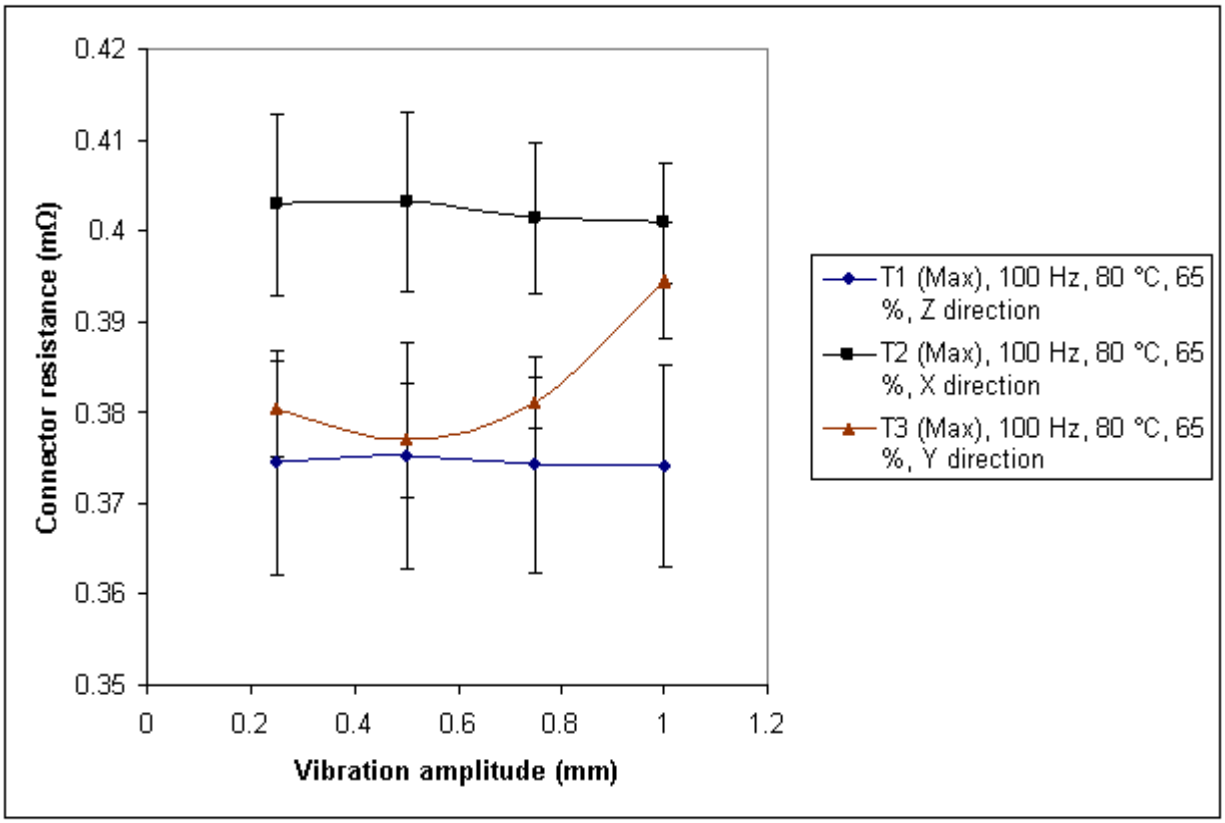

Figure 6-17: Maximum connector resistance versus vibration amplitude for different vibration directions

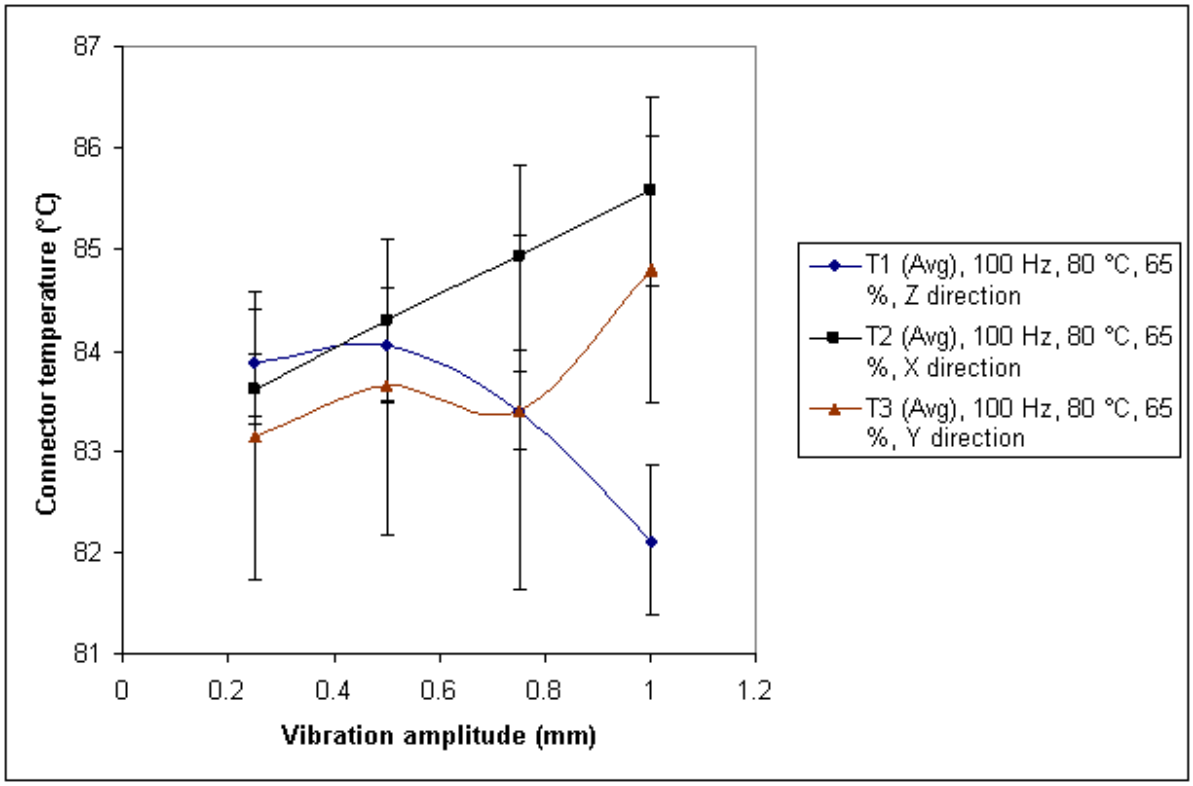

Figure 6-18: Average connector temperature versus vibration amplitude for different vibration directions

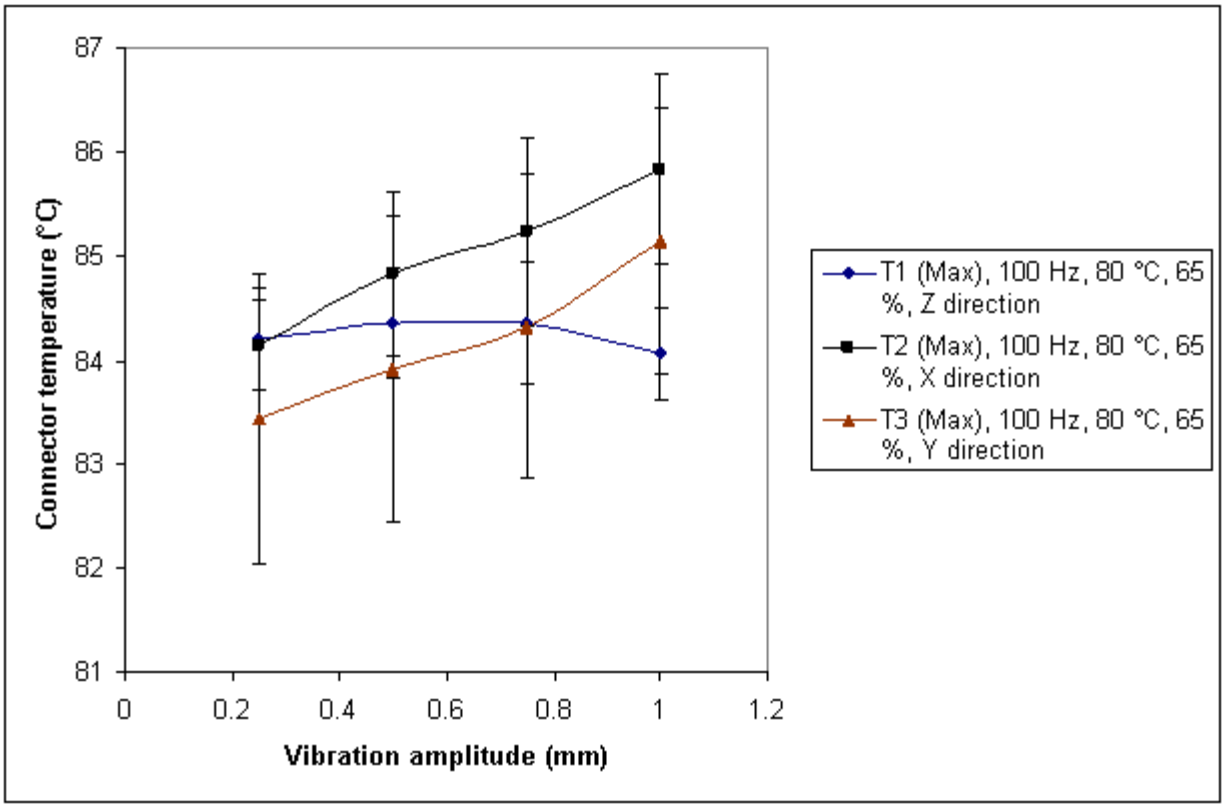

Figure 6-19: Maximum connector temperature versus vibration amplitude for different vibration directions

6.2.2 Effect of vibration frequency on R and T

In this section, the emphasis is on the effect of the vibration frequency parameter. Figures 6-20, 6-22 and 6-24 show the dependency of the average and maximum values of R on different vibration amplitudes and different vibration frequencies while maintaining the same vibration direction (Y). Likewise, Figures 6-21, 6-23 and 6-25 show the changes in the average and maximum connector temperature (T) values.

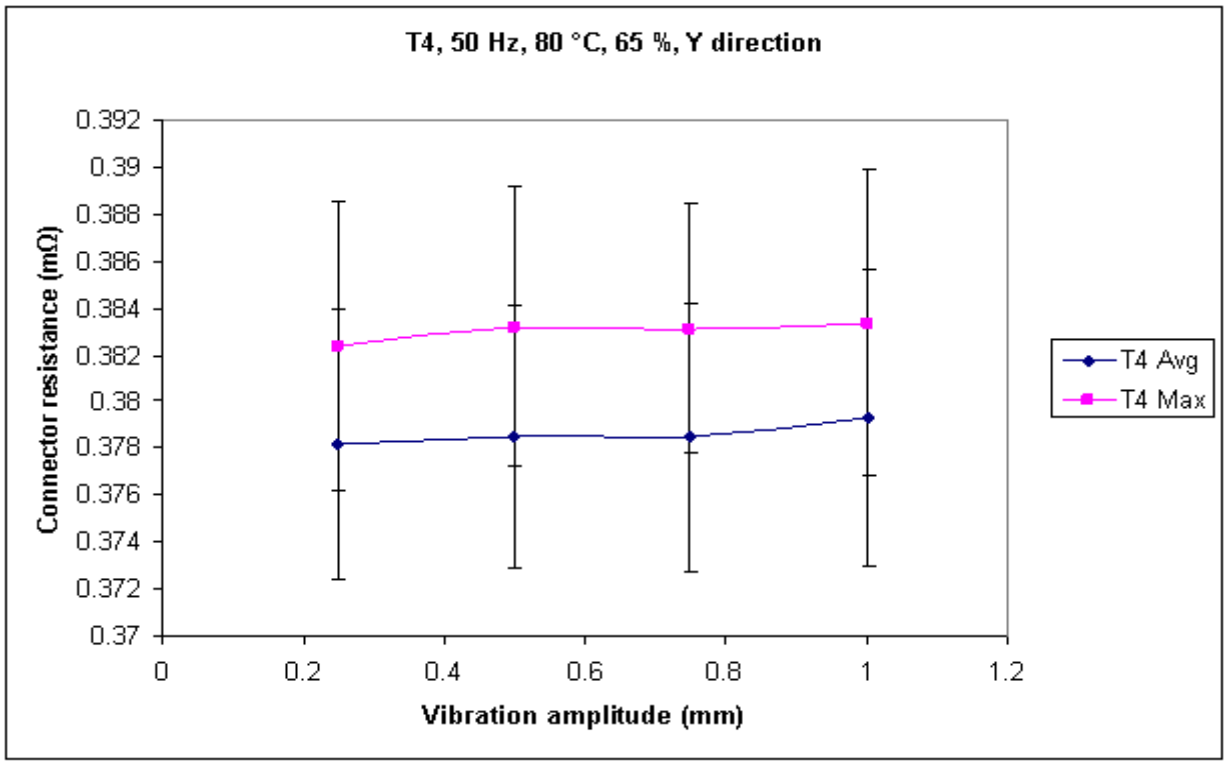

Figure 6-20: Connector resistance versus vibration amplitude for test T4

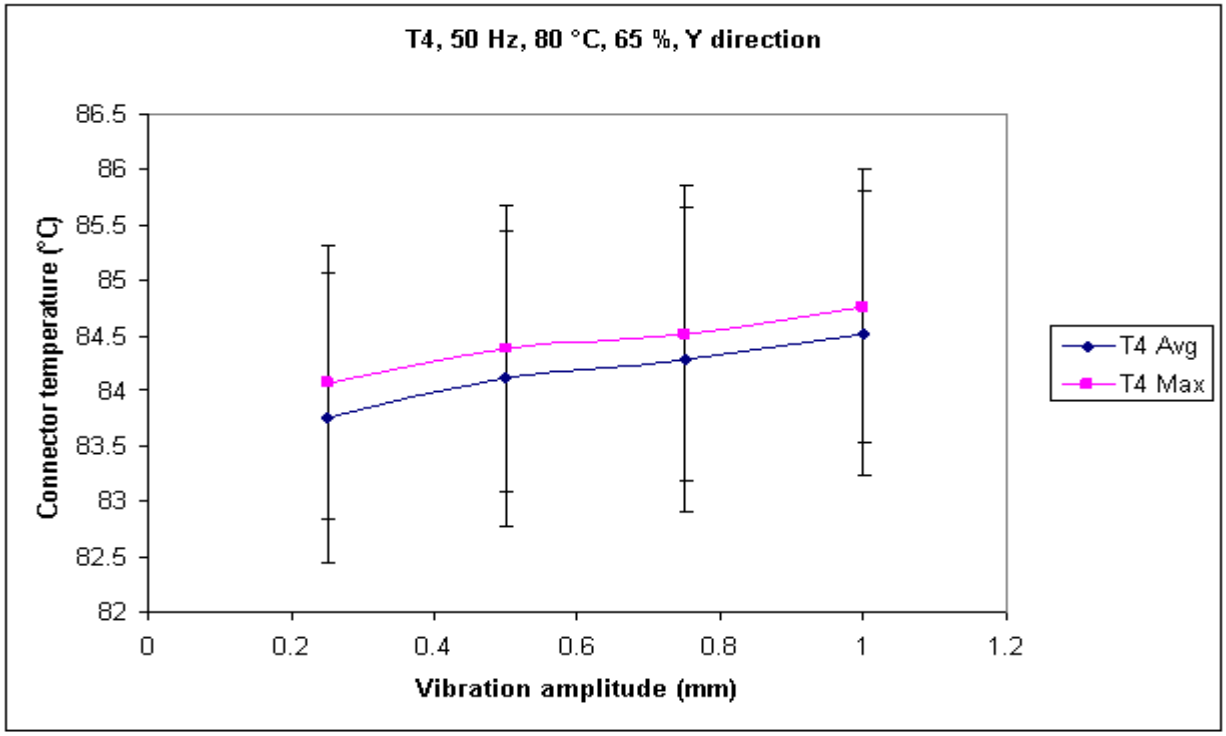

Figure 6-21: Connector temperature versus vibration amplitude for test T4

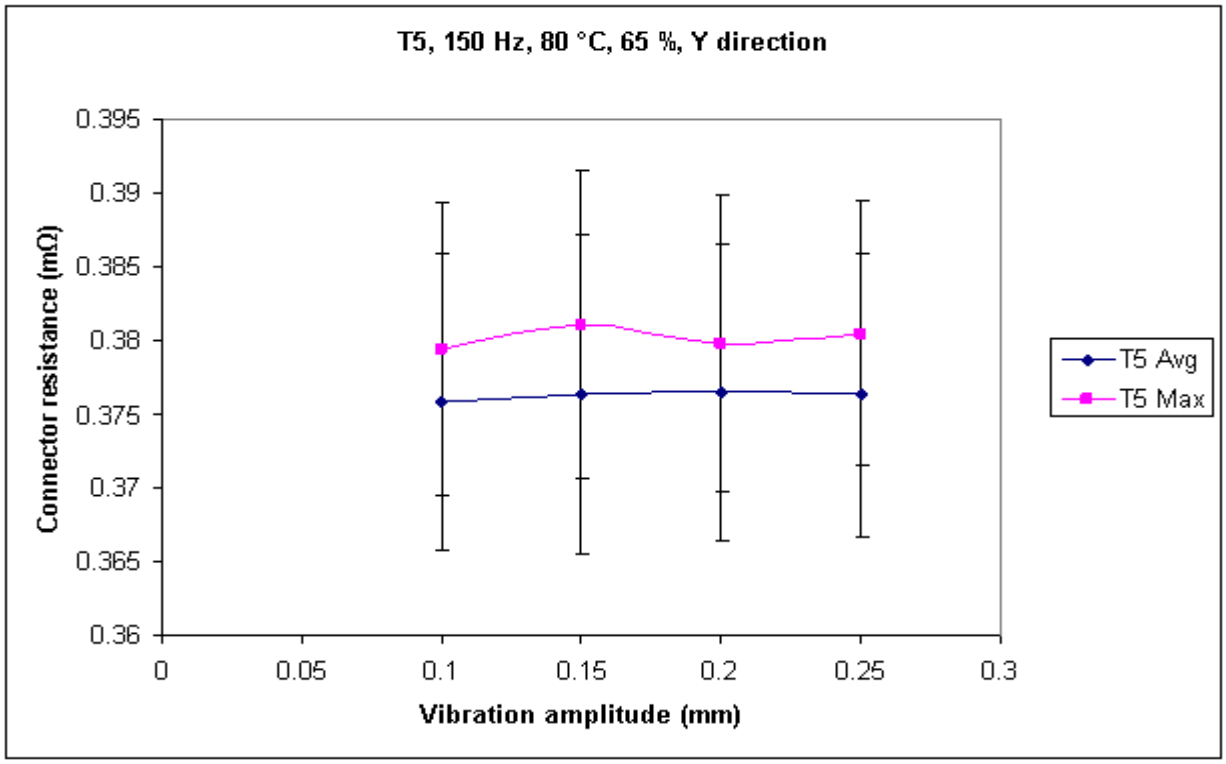

Figure 6-22: Connector resistance versus vibration amplitude for test T5

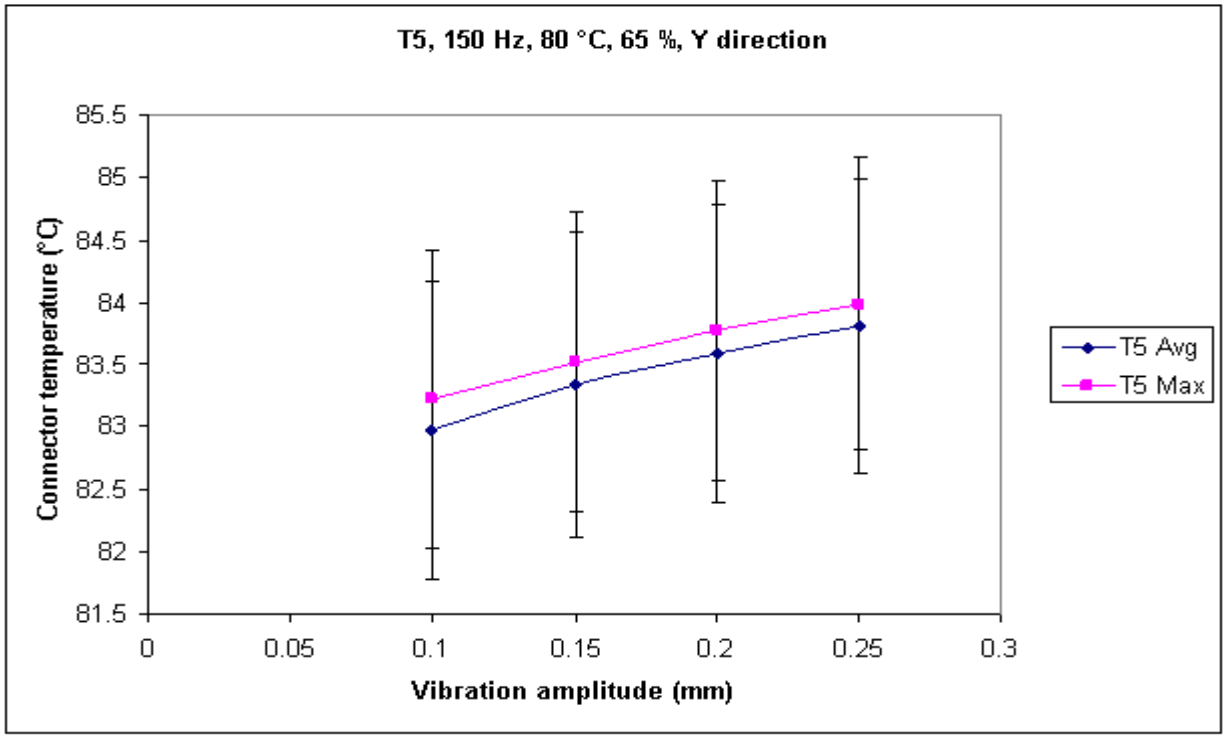

Figure 6-23: Connector temperature versus vibration amplitude for test T5

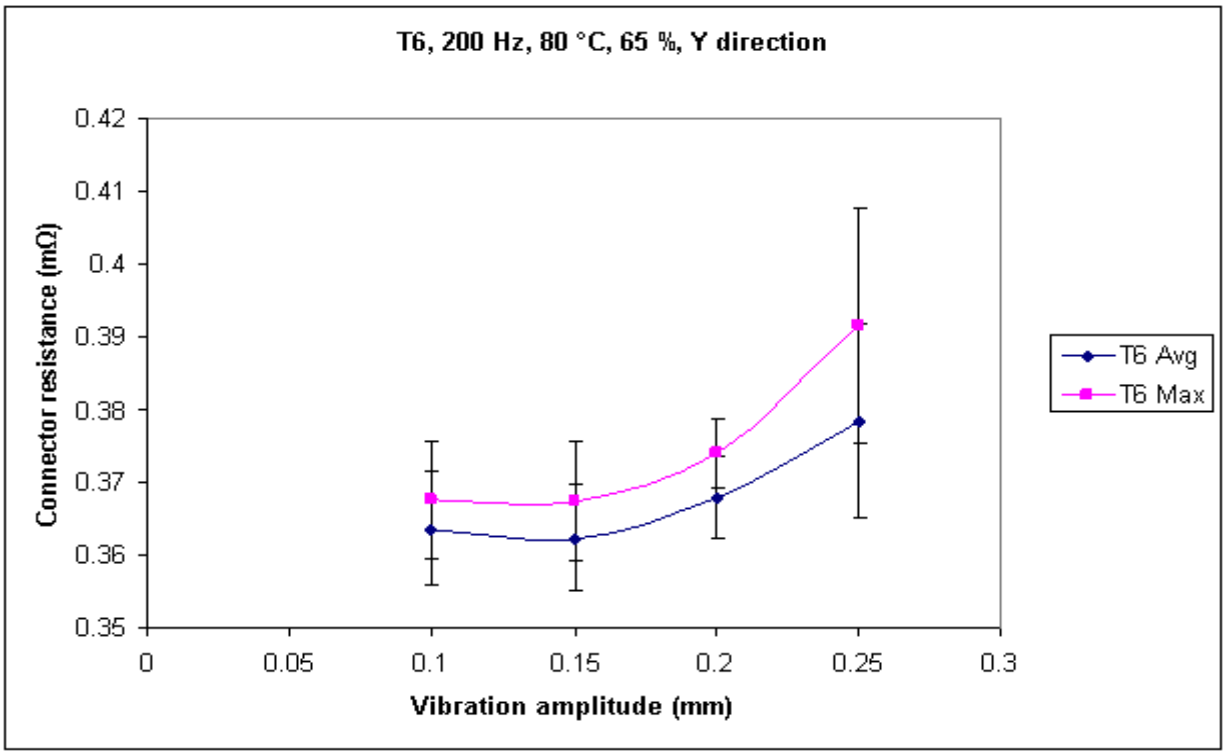

Figure 6-24: Connector resistance versus vibration amplitude for test T6

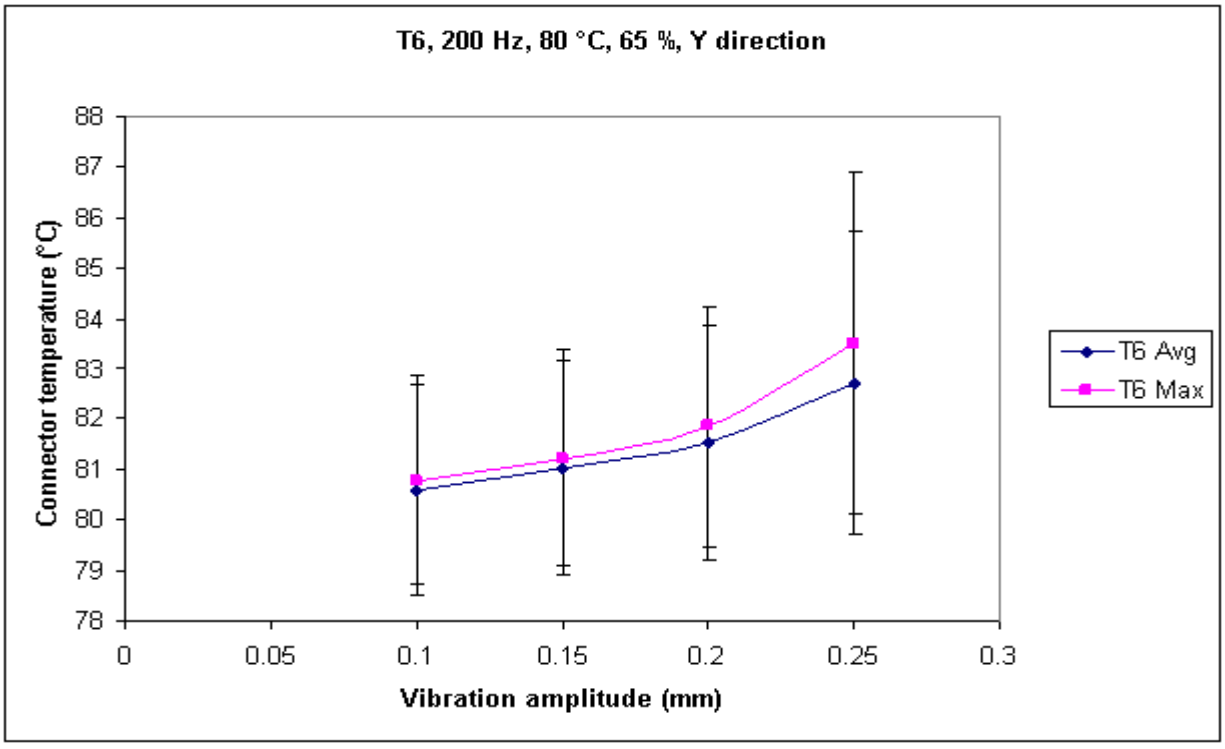

Figure 6-25: Connector temperature versus vibration amplitude for test T6

Again, the values of average and maximum R and T obtained under the same Y vibration direction and for different vibration frequencies and amplitudes are combined and analyzed collectively. In tests T4 and T5, no significant variations in the values of average (Figures 6-20, 6-22 and 6-26) and maximum (Figures 6-20, 6-22 and 6-27) R can be seen. This indicates that the 40A connectors subjected to vibration frequencies of 50 Hz (test T4) and 150 Hz (test T5) will function better.

It can be clearly seen that there is a significant increase in the average (test T6; Figures 6-24 and 6-26) and maximum (test T6; Figures 6-24 and 6-27) R at the highest vibration amplitude of 0.25 mm and at the highest vibration frequency of 200 Hz with the total test duration being only 40 minutes. A similar magnitude of increase in the average (test T3; Figures 6-14 and 6-26) and maximum (test T3; Figures 6-14 and 6-27) R as that in test T6 can also be observed at 1 mm amplitude at a 100 Hz vibration frequency with an entire test duration of 80 minutes. This clearly suggests that when the 40A connector is subjected to amplitudes greater than 0.25 mm and to the same frequency of 200 Hz, catastrophic failure, possibly characterized by fretting corrosion, of the connector in operation can take place within a short time. This is the worst possible combination. Since real vibrations in application will consist of a spectrum of frequencies, those around 200 Hz seem most critical and may indicate that it is near to a resonant frequency. The largest rise in R (either maximum or average) found in both T6 (at 0.25 mm amplitude) and T3 (at 1 mm amplitude) tests may again be attributed to severe fretting corrosion, wear and very high frictional heating. Also, at this particular vibration amplitude (0.25 mm), the value of maximum R (see Figure 6-27) in test T6 (200 Hz) is also the highest when compared to all other values obtained in tests T3 (100 Hz), T4 (50 Hz) and T5 (150 Hz).

When the entire test duration is considered, the total rise in the values of either average (Figures 6-25 and 6-28) or maximum (Figures 6-25 and 6-29) connector temperature (T) noticed is about 2.5 °C for a vibration frequency of 200 Hz (test T6). Likewise, for 50 Hz (test T4; Figures 6-21, 6-28 and 6-29), 100 Hz (test T3; Figures 6-15, 6-28 and 6-29) and 150 Hz (test T5; Figures 6-23, 6-28 and 6-29) tests, the total rise in the values of maximum and average T is about 0.7 °C, 1.7 °C and 0.8 °C, respectively. Therefore, as expected, higher vibration frequency (200 Hz) causes a large amount of frictional heating that leads to a higher rise in temperature in the 40A connector. On the other hand, only a moderate temperature rise occurs during vibration with frequencies below 200 Hz since frictional heating is lesser.

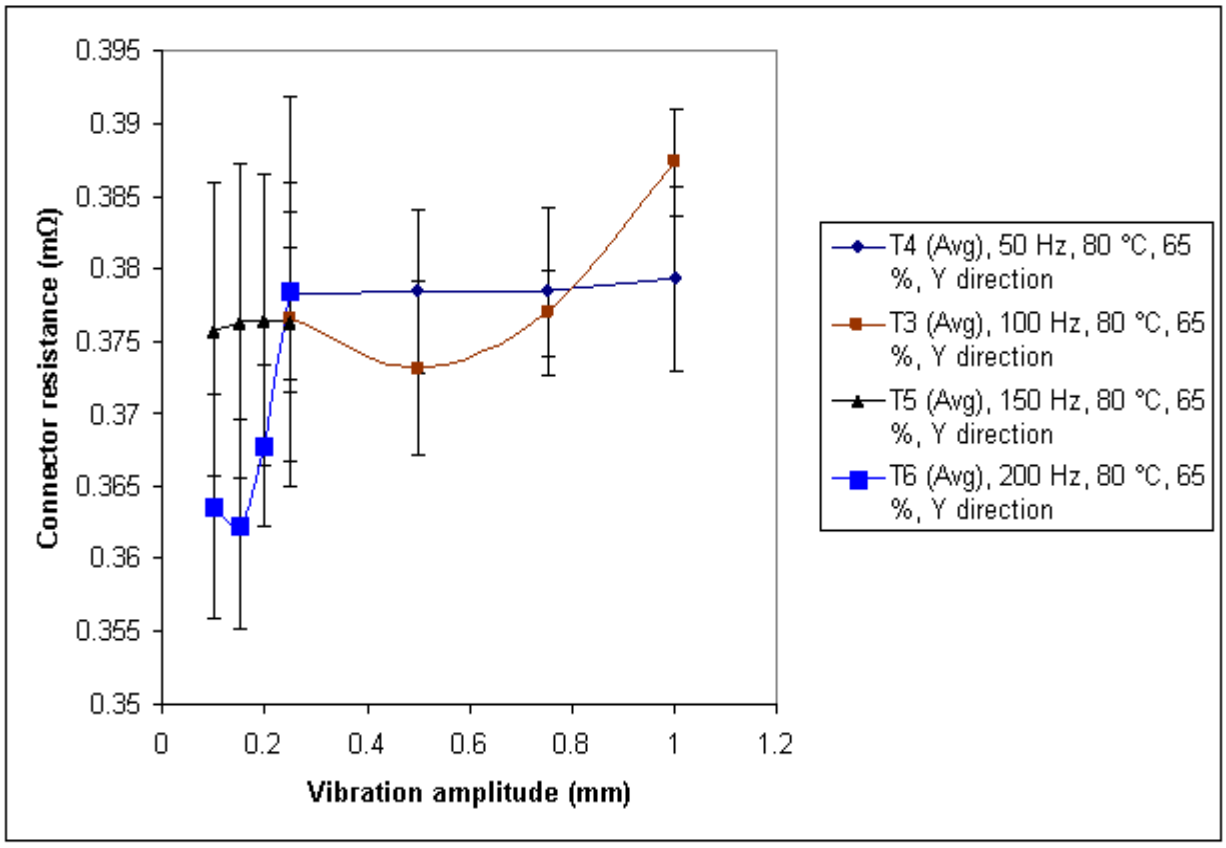

Figure 6-26: Average connector resistance versus vibration amplitude for different vibration frequencies

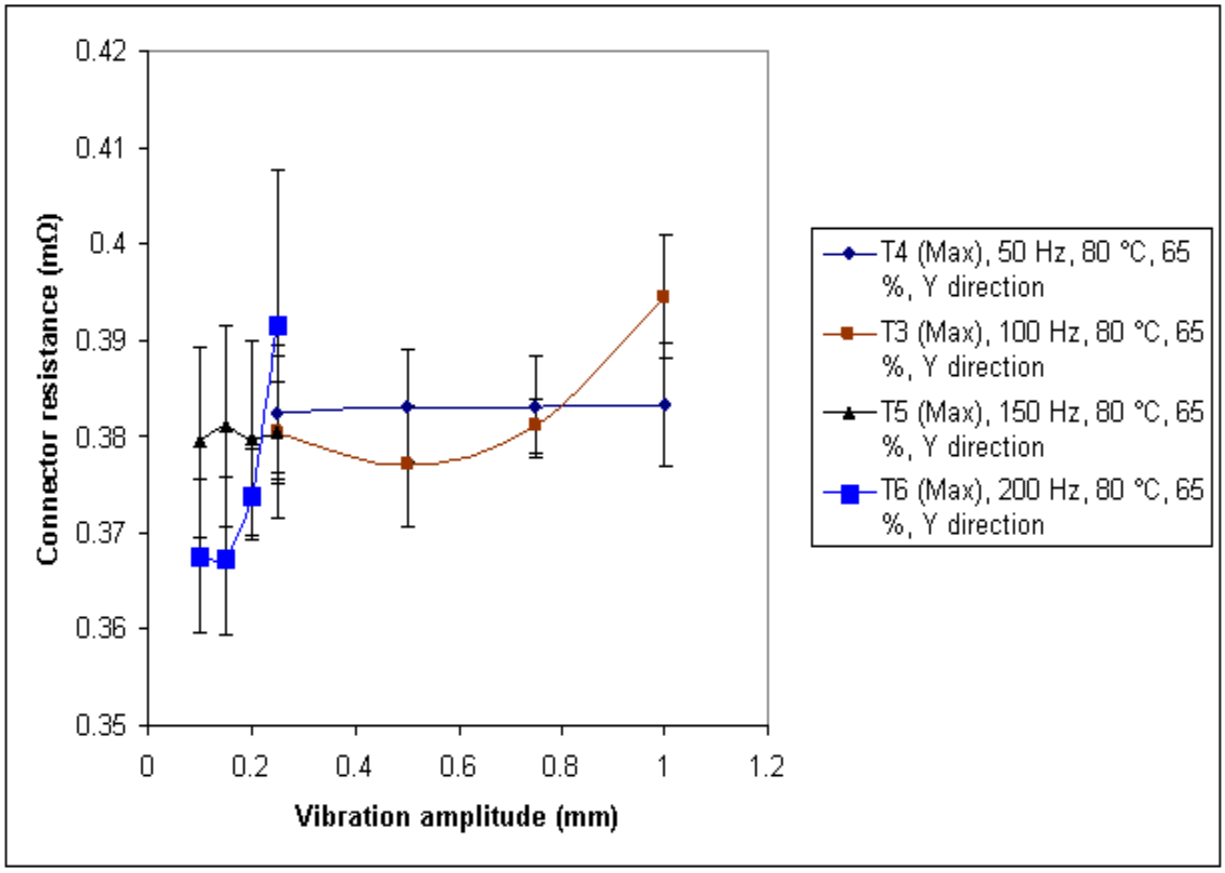

Figure 6-27: Maximum connector resistance versus vibration amplitude for different vibration frequencies

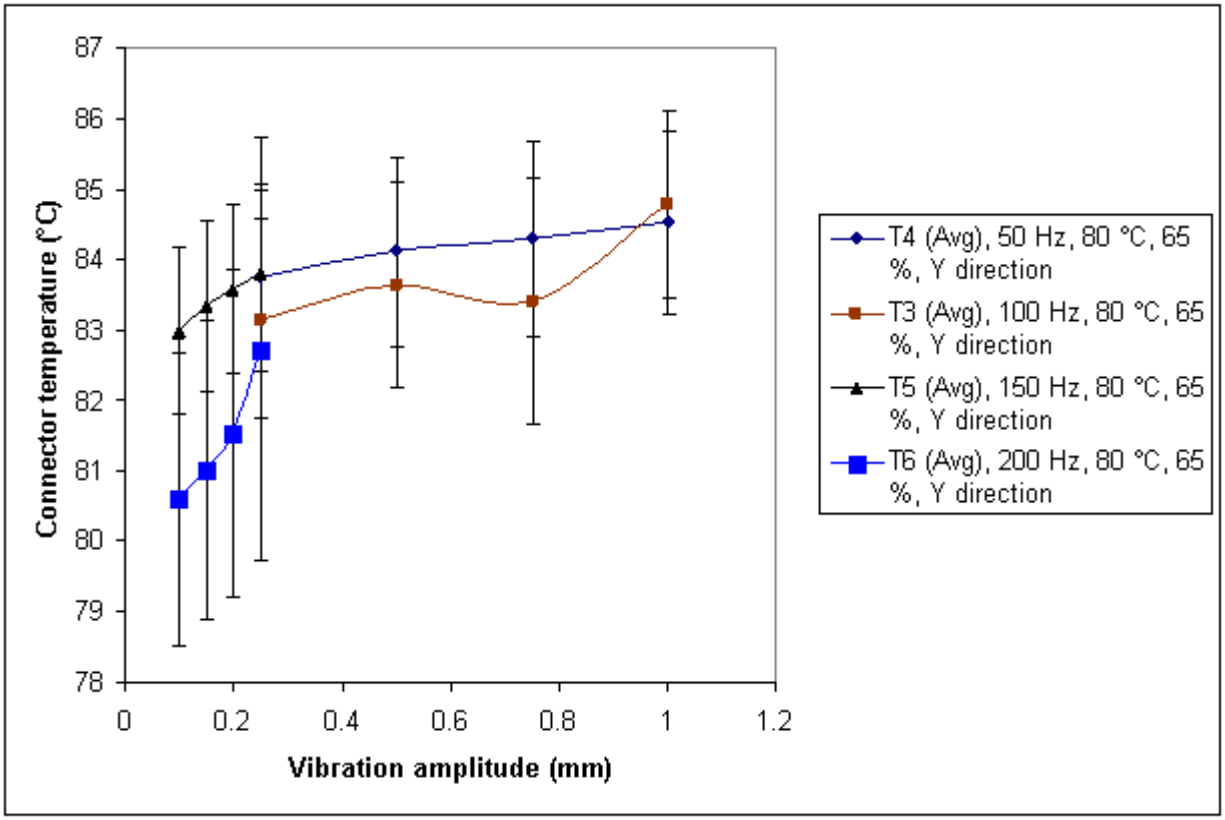

Figure 6-28: Average connector temperature versus vibration amplitude for different vibration frequencies

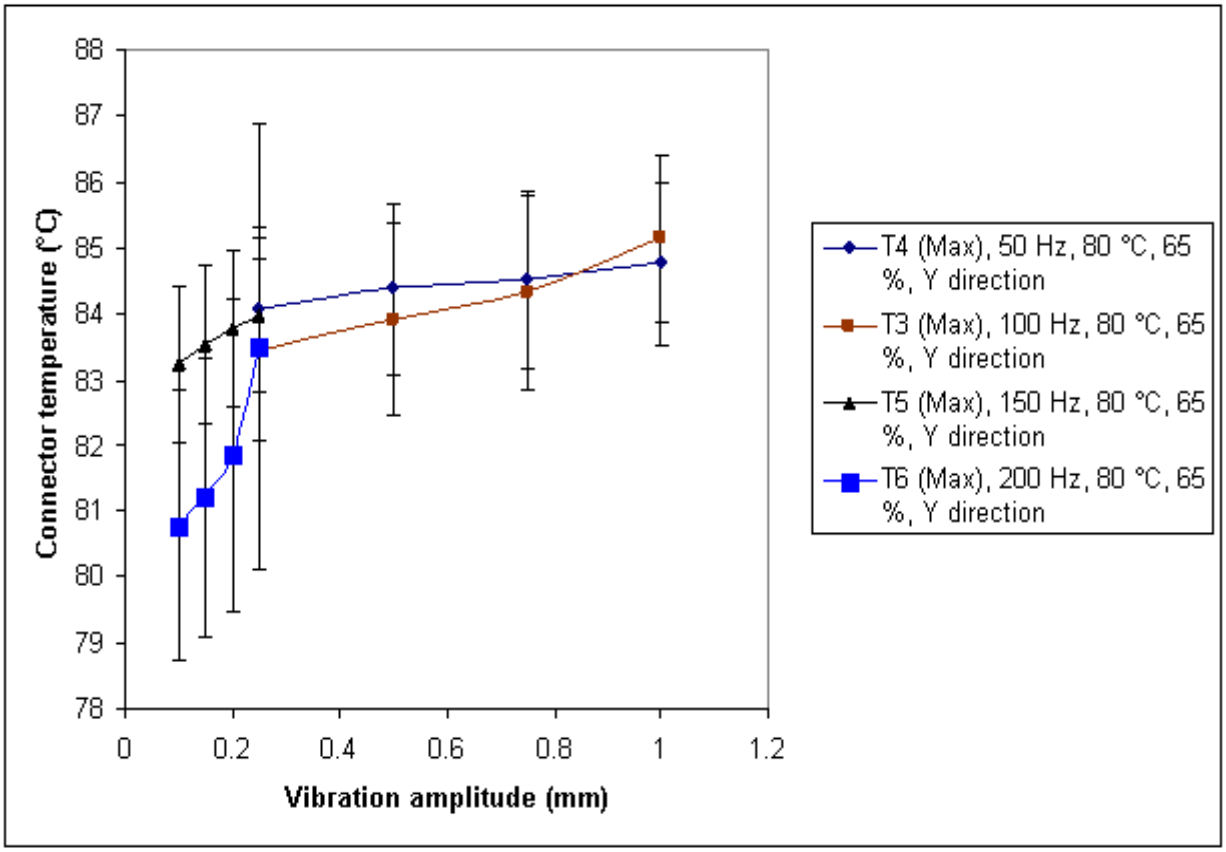

Figure 6-29: Maximum connector temperature versus vibration amplitude for different vibration frequencies

6.2.3 Effect of ambient temperature on R and T

Now, the ambient temperature is varied in the thermal chamber to study its effect on the 40A connector performance under different vibration amplitudes. Figures 6-30 (test T7; 25 °C) and 6-32 (test T8; 120 °C) display the variations in the values of maximum and average R under different vibration amplitudes. Similarly, Figures 6-31 (test T7; 25 °C) and 6-33 (test T8; 120 °C) exhibit the changes in the values of average and maximum T.

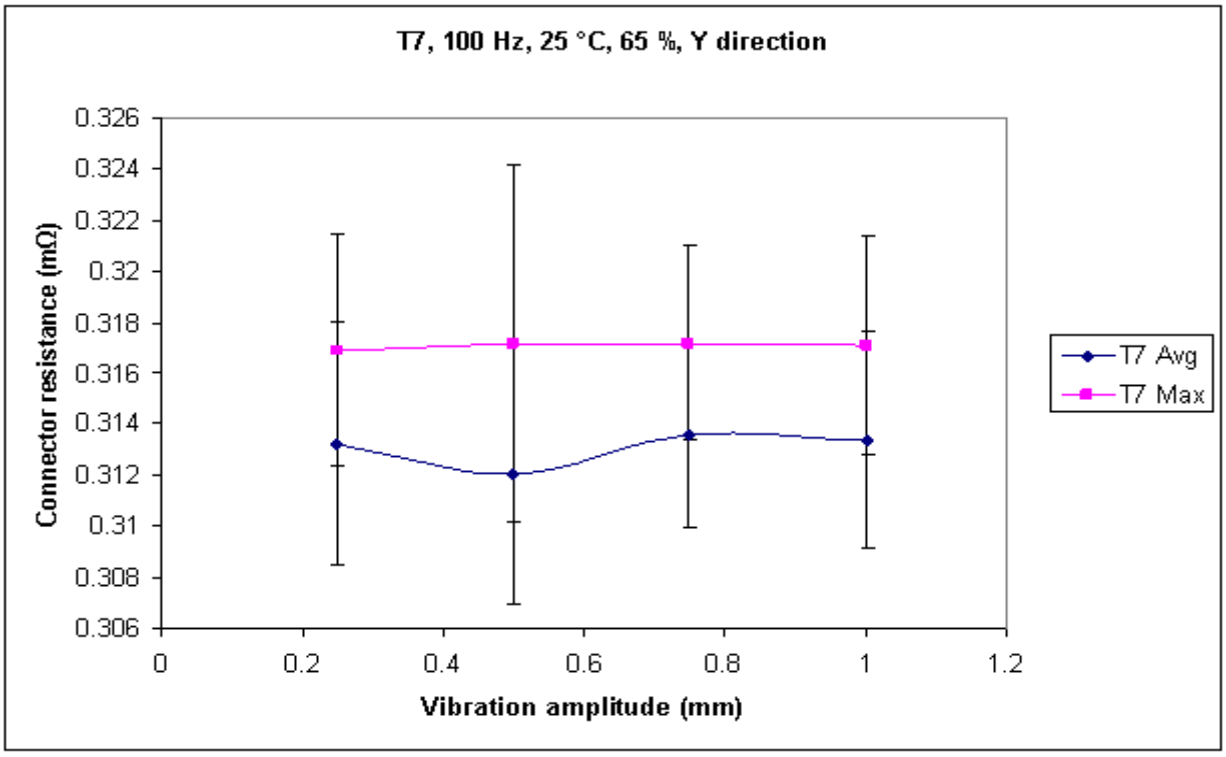

Figure 6-30: Connector resistance versus vibration amplitude for test T7

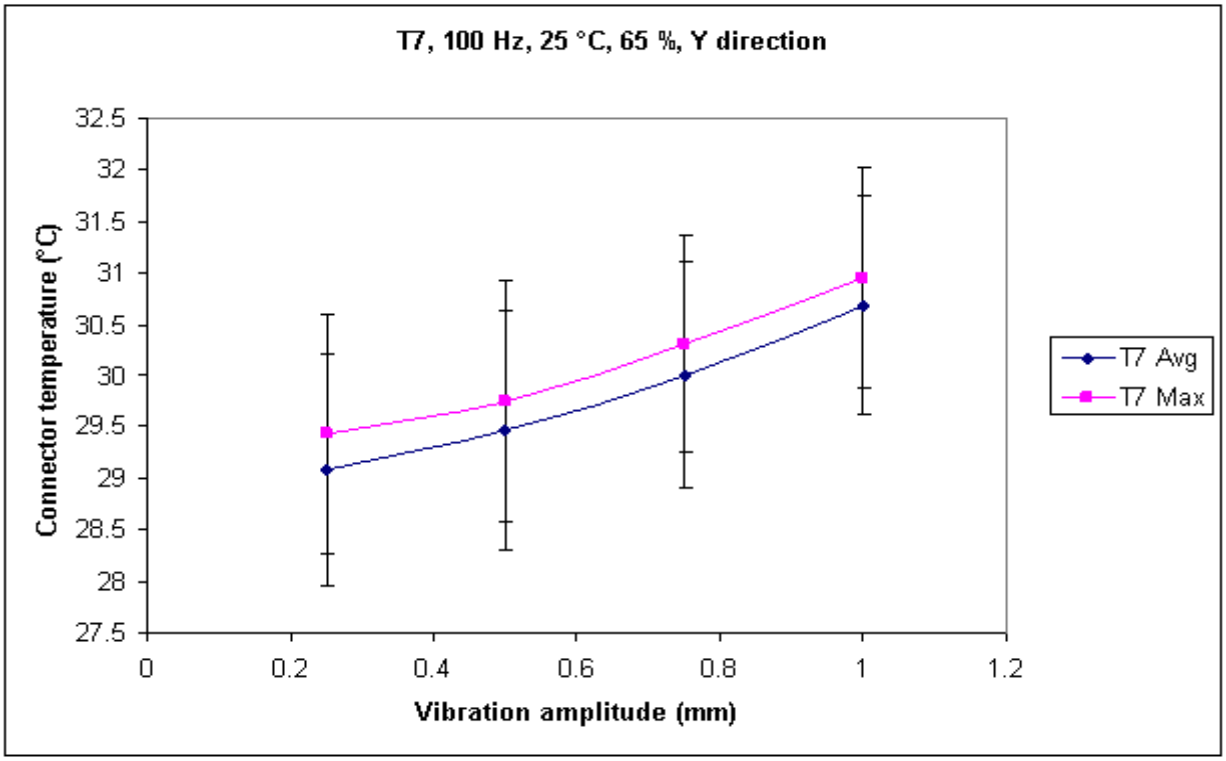

Figure 6-31: Connector temperature versus vibration amplitude for test T7

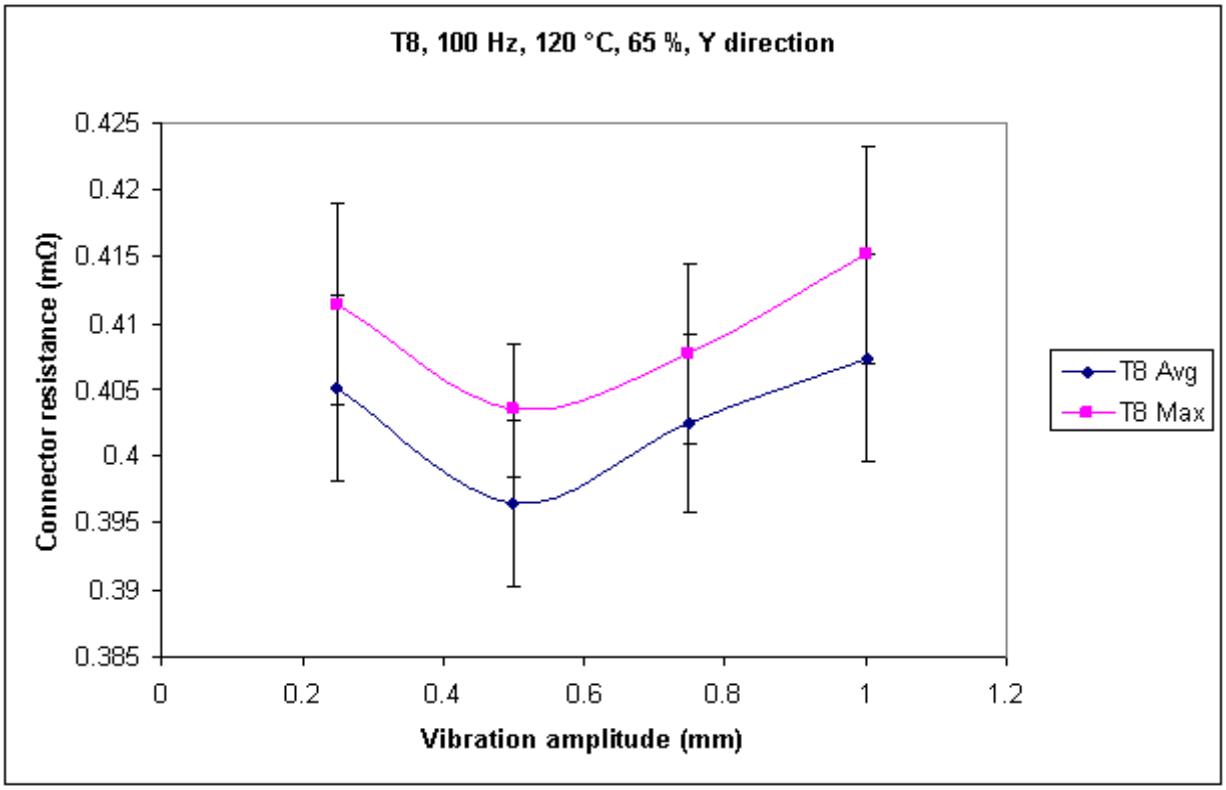

Figure 6-32: Connector resistance versus vibration amplitude for test T8

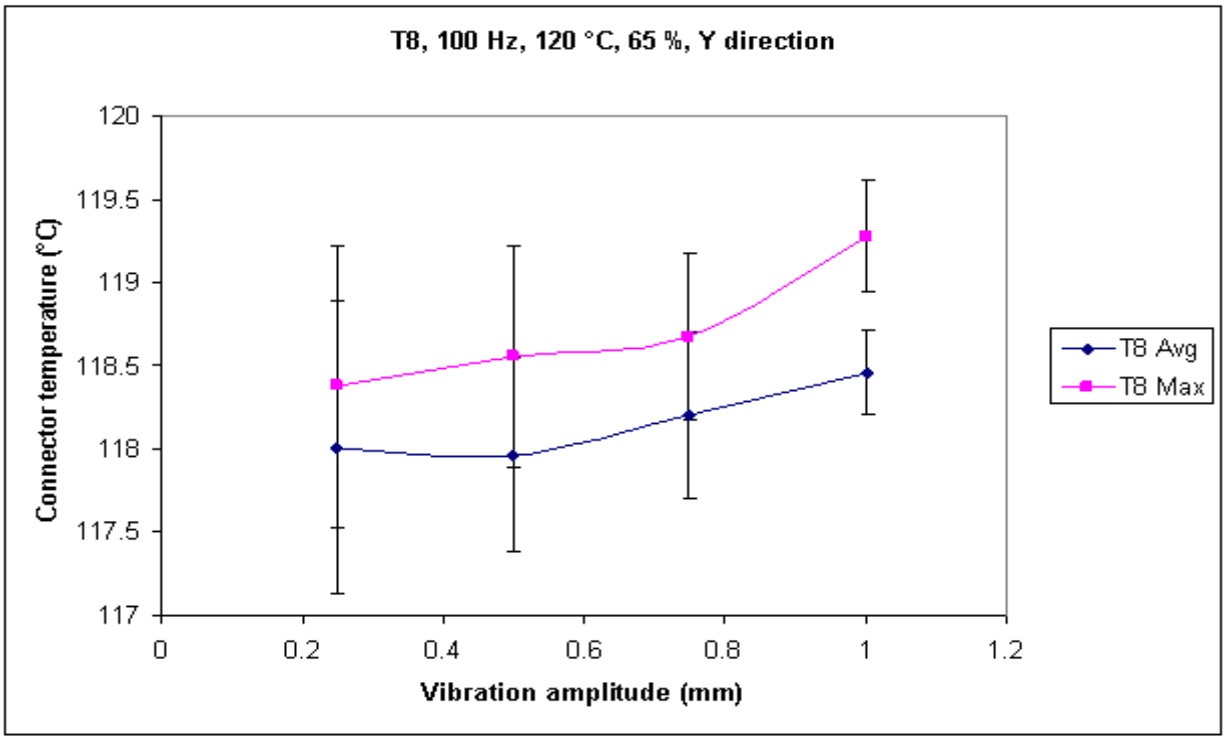

Figure 6-33: Connector temperature versus vibration amplitude for test T8

Now, similar to the previous 2 sub-sections, the values of average (see Figure 6-34) and maximum (see Figure 6-35) connector resistance (R) obtained for different ambient temperatures and vibration amplitudes are examined. At a room temperature of 25 °C (test T7), the values of average (Figures 6-30 and 6-34) and maximum (Figures 6-30 and 6-35) R remain almost constant during the entire test. This indicates that the 40A connectors will operate normally under room temperature. However, at 120 °C (test T8), there is a slight decrease in the values of average (Figures 6-32 and 6-34) and maximum (Figures 6-32 and 6-35) R followed by an increase in these values over the complete test duration. This decrease in R is again due to an increased current flow resulting from a better contact among the connector terminals. Also, the higher the ambient temperature, the more the connector gets heated in turn leading to an increase in R. There is also increased oxidation, reduced friction and melting of asperity contacts. Also, in tests T3 (ambient temperature 80 °C) and T8 (ambient temperature 120 °C), as expected, the measured values of both the maximum and average R for any vibration amplitude, when compared to those values in test T7 (ambient temperature 25 °C), are much higher because the 40A connectors are subjected to very high ambient temperatures.

Figures 6-36 and 6-37 show the values of average and maximum T for various ambient temperature and vibration amplitude conditions. In each of the 3 tests (tests T3; Figure 6-15, T7; Figure 6-31 and T8; Figure 6-33), over an entire test duration minor increments in the values of average and maximum T can be seen again due to the frictional heating and more Joule heating. Since the connectors are subjected to higher ambient temperatures during their vibration test, higher values of average and maximum T are measured accordingly.

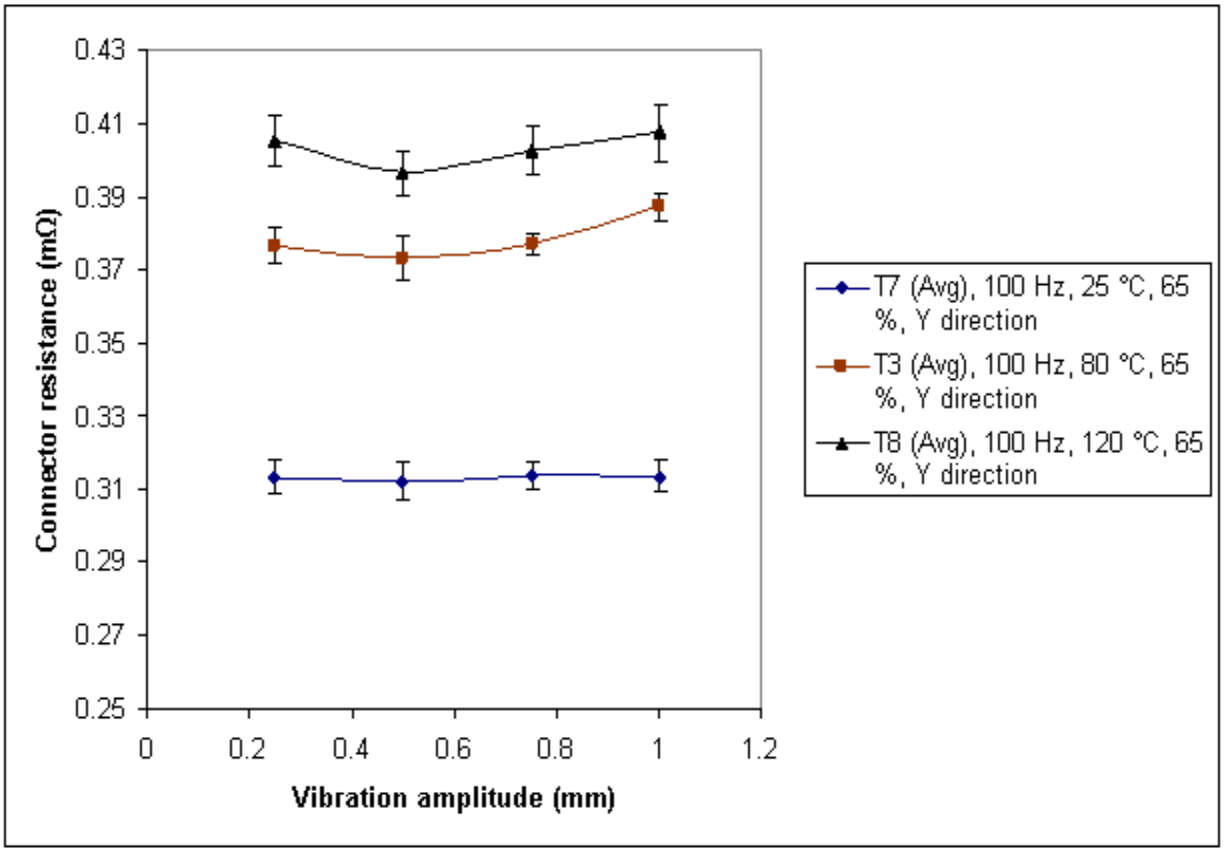

Figure 6-34: Average connector resistance versus vibration amplitude for different ambient temperatures

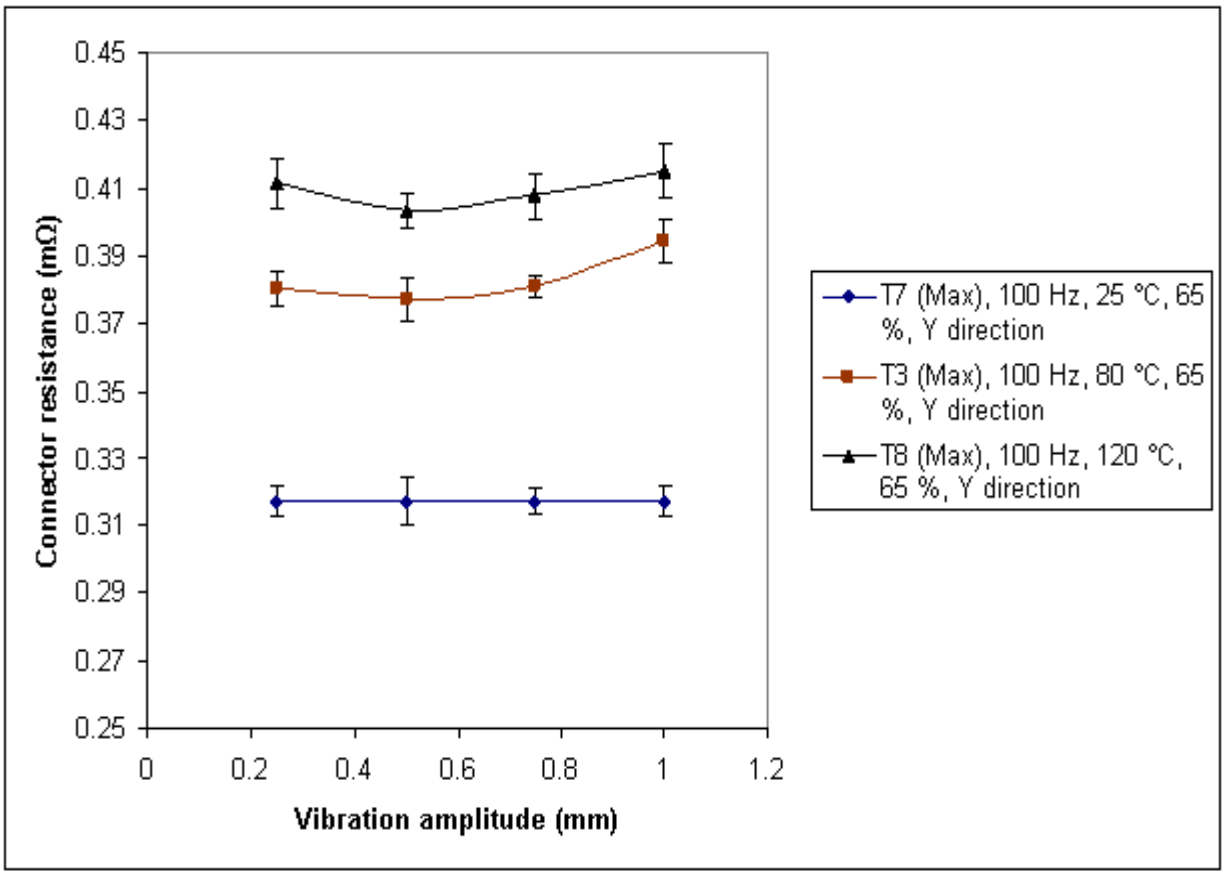

Figure 6-35: Maximum connector resistance versus vibration amplitude for different ambient temperatures

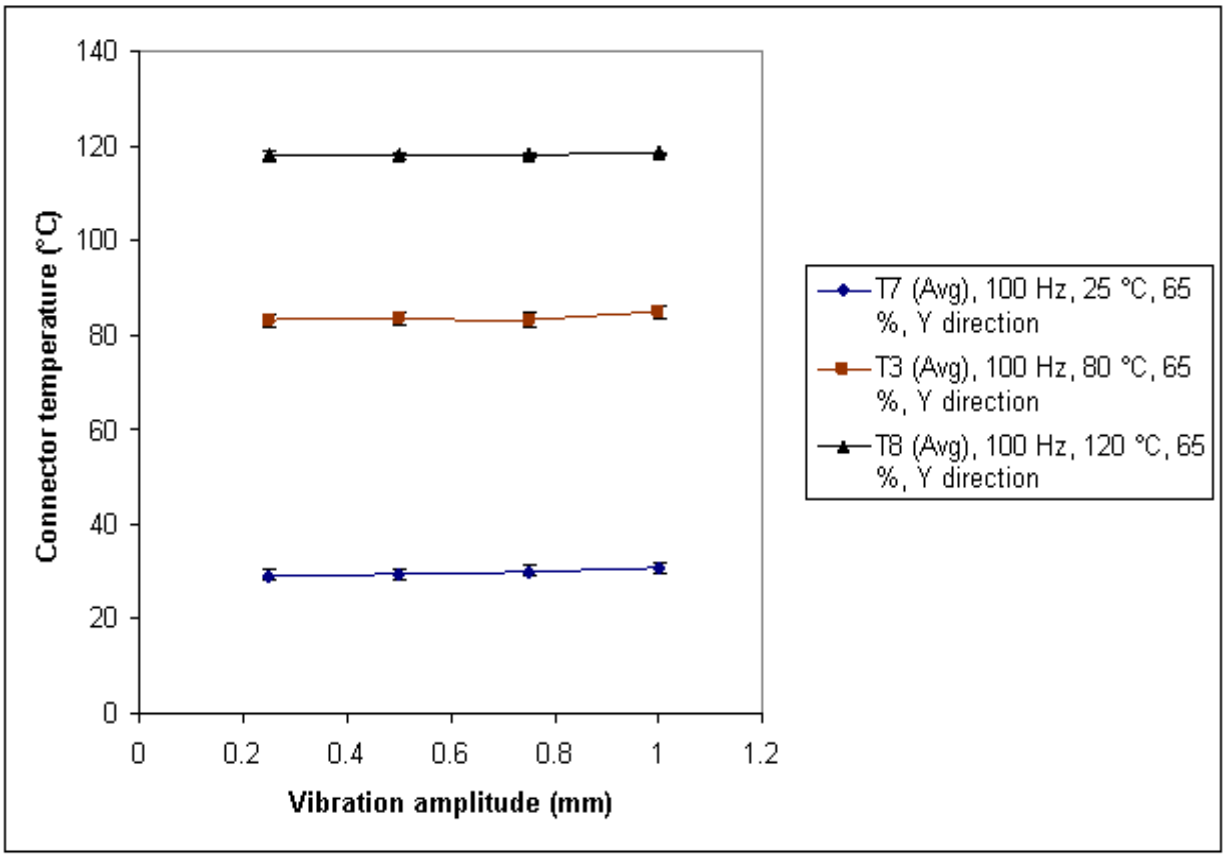

Figure 6-36: Average connector temperature versus vibration amplitude for different ambient temperatures

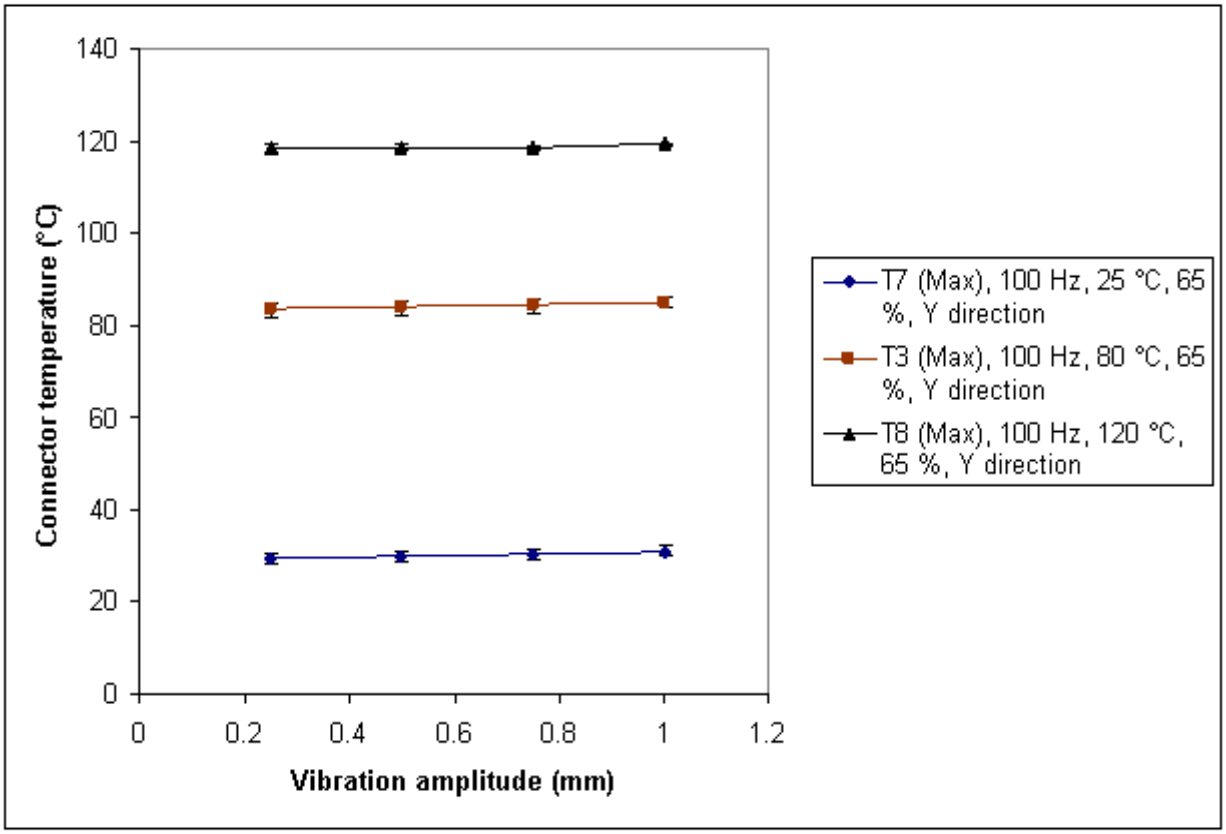

Figure 6-37: Maximum connector temperature versus vibration amplitude for different ambient temperatures

CHAPTER 7

Conclusions

An inclusive multi-physics finite element based model including multiscale rough surface contact of high power connectors (specifically 40A connector) is established that enables faster convergence than previous methods. The model is solved by employing ANSYS™ with only the need for an external code to make initial predictions of ECR and TCR vs. contact pressure. It provides predictions of the stresses, displacements (deformations), Joule heat effects, current density, electric potential and the temperature distributions in the parts of a 40A connector. Also, upon convergence of the solution in the 40A connector model, force balance on the pin terminal is achieved which implies that the entire connector system in ANSYS™ is under equilibrium. This new model serves as a comprehensive and effective tool for developing future automotive connector designs and performing an analysis including the coupled mechanical, thermal, electrical fields and rough surface contact made of different surface finishes and materials.

Conduction of current takes place mostly through a very small region in the connector that is usually near the contacting surfaces. This indicates that the connector designs can be optimized for more efficient use of the available conducting material. In addition, for instance, the preliminary results from the multiscale rough surface contact model predicted temperatures as high as 1000 °C at the contact. This suggests that the local asperity temperature could be very high which may cause micro-welding.

Current density may be used to predict local asperity temperature analytically. Maximum Joule heating occurs in the regions where highest current density is seen in the 40A connector. It was also found that the bulk temperature rise is fairly small, even though experimental measurements indicate otherwise. It is therefore believed that a large portion of the temperature rise in actual connectors is due to the Joule heating in the supply cables. This is proven theoretically and experimentally.

As a verification of the multi-physics model, the connector resistance (R) increases with the rise in applied currents in both the 40A connector model and the experimental tests (without vibration). Also, under stationary conditions, the steady state values of connector temperatures increase in a parabolic way with an increase in applied current in accordance with Joule heating.

Coming to the accelerated vibration tests on 40A connectors, the effects of vibration amplitude, direction of vibration, vibration frequency, ambient temperature and humidity on the behavior of the connector are studied. The changes in the maximum and average connector resistance and connector temperature (T) under various conditions are summarized. Several prominent findings emerge from this experimental study. First, greater increases in the values of average and maximum R are seen in vibration tests conducted along Y direction. Since T increases due to frictional heating and increased Joule heating, R also increases. Higher vibration frequency (200 Hz) and higher vibration amplitude (0.25 mm) give rise to a much higher rise in the connector resistance (either maximum or average) which indicates the most likelihood of failure of the 40A connector catastrophically due to severe fretting corrosion and wear occurring in the connector terminals. Also, the maximum rise in the connector temperature (again, either maximum or average) is noticed under testing conditions of vibration frequency (200 Hz) and Y direction.

REFERENCES

1. Bowden, F. P. and Williamson, J. B. P., *Electrical conduction in solids. I. Influence of the passage of current on the contact between solids.* Proceedings of the Royal Society A, 1958. 246(1244): pp. 1-12.
2. Johnson, K. L., Greenwood, J. A., and Higginson, J. G., *The contact of elastic regular wavy surfaces.* International Journal of Mechanical Sciences, 1985. 27(6): pp. 383-396.
3. Miller, J. M., *Propulsion systems for hybrid vehicles*. IEE Power and Energy Series. Vol. 45. 2004, Bodmin, Cornwall: MPB Books Limited.
4. Allen, S. E., *Compact, low resistance, low force electrical connection for high current applications.* IEEE transactions on power apparatus and systems, 1984. PAS-103(10): pp. 3049-3055.
5. Olsson, K.-E. and Oberg, A., *Influence of mechanical design parameters on electrical contact performance*. in *Proceedings of the 35th IEEE Holm Conference on Electrical Contacts*. 1989. Chicago, IL, USA: Illinois Inst of Technology.
6. Bryant, M. D., *Resistance buildup in electrical connectors due to fretting corrosion of rough surfaces*. in *Proceedings of the 39th IEEE Holm Conference on Electrical Contacts*. 1993. Pittsburgh, PA, USA: IEEE.
7. Minowa, I. and Nakamura, M., *Simulation for current density distribution in contact spot.* Electronics and Communications in Japan, Part II: Electronics (English translation of Denshi Tsushin Gakkai Ronbunshi), 1994. 77(2): pp. 88-95.

8. Ando, Y. and Imori, Y., *Contact resistance properties on plastic deformation connector contacts.* Electronics and Communications in Japan, Part II: Electronics (English translation of Denshi Tsushin Gakkai Ronbunshi), 1997. 80(3): pp. 47-59.

9. Rudolphi, A. K. and Jacobson, S., *The contact resistance of rolling silver coated copper contacts*. in *Proceedings of the 43rd IEEE Holm Conference on Electrical Contacts*. 1997. Philadelphia, PA, USA: IEEE.

10. Tristani, L., Zindine, E. M., Boyer, L., and Klimek, G., *Mechanical modeling of fretting cycles of electrical contacts*. in *Proceedings of the 44th IEEE Holm Conference on Electrical Contacts*. 1998. Arlington, VA, USA: IEEE.

11. Antler, M., *Contact fretting of electronic connectors.* IEICE Transactions on Electronics, 1999. E82-C(1): pp. 3-12.

12. Swingler, J., *Automotive connector: The influence of powering and lubricating a fretting contact interface.* Proceedings of the Institution of Mechanical Engineers, Part D: Journal of Automobile Engineering, 2000. 214(6): pp. 615-623.

13. Swingler, J. and McBride, J. W., *Fretting corrosion and the reliability of multicontact connector terminals.* IEEE Transactions on Components and Packaging Technologies, 2002. 25(4): pp. 670-676.

14. Malucci, R. D., *Fretting corrosion degradation, threshold behavior and contact instability*. in *Proceedings of the 49th IEEE Holm Conference on Electrical Contacts*. 2003. Washington, DC, USA: IEEE.

15. Flowers, G. T., Xie, F., Bozack, M. J., and Malucci, R. D., *Vibration thresholds for fretting corrosion in electrical connectors.* IEEE Transactions on Components and Packaging Technologies, 2004. 27(1): pp. 65-71.

16. Takano, E., *The determination of equivalent constriction resistance and film resistance by using low DC voltages*. in *Proceedings of the 50th IEEE Holm Conference on Electrical Contacts and the 22nd International Conference on Electrical Contacts*. 2004. Seattle, WA, United states: IEEE.

17. He, Z. and Xu, L., *Micro motion at the failed contact interfaces*. in *Proceedings of the 51st IEEE Holm Conference on Electrical Contacts*. 2005. Chicago, IL, USA: IEEE.

18. Flowers, G. T., Xie, F., Bozack, M. J., Horvath, R., Malucci, R. D., and Rickett, B. I., *Modeling early stage fretting of electrical connectors subjected to random vibration.* IEEE Transactions on Components and Packaging Technologies, 2005. 28(4): pp. 721-727.

19. Jemaa, N. B. and Carvou, E., *Electrical contact behaviour of power connector during fretting vibration*. in *Proceedings of the 52nd IEEE Holm Conference on Electrical Contacts*. 2006. Montreal, QC, Canada: IEEE.

20. Tamai, T., *Friction and contact resistance through true contact interface.* IEICE Transactions on Electronics, 2006. E89-C(8): pp. 1122-1128.

21. Park, Y. W., Narayanan, T. S. N. S., and Kang, Y. L., *Fretting wear behavior of tin plated contacts: Influence on contact resistance.* Surface Review and Letters, 2006. 13(5): pp. 635-644.

22. Wang, X. and Xu, L.-J., *Finite element model analysis of thermal failure in connector.* Journal of Zhejiang University: Science A, 2007. 8(3): pp. 397-402.

23. Ossart, F., Noel, S., Alamarguy, D., Correia, S., Gendre, P., *Multilayer contacts in electrical connectors: Experimental results and modelling.* WIT Transactions on Engineering Sciences, 2007. 55: pp. 89-98.

24. Carvou, E. and Jemaa, N. B., *Time and level analysis of contact voltage intermittences induced by fretting in power connector*. in *Proceedings of the 53rd IEEE Holm Conference on Electrical Contacts*. 2007. Pittsburgh, PA, USA: IEEE.

25. Park, Y. W., Narayanan, T. S. N. S., and Lee, K. Y., *Fretting corrosion of tin-plated contacts.* Tribology International, 2008. 41(7): pp. 616-628.

26. El Abdi, R. and Benjemaa, N., *Experimental and analytical studies of the connector insertion phase.* IEEE Transactions on Components and Packaging Technologies, 2008. 31(4): pp. 751-758.

27. El Abdi, R., Beloufa, A., and Benjemaâ, N., *Contact resistance study of high-copper alloys used in power automotive connectors.* Proceedings of the Institution of Mechanical Engineers, Part D: Journal of Automobile Engineering, 2008. 222(8): pp. 1375-1383.

28. McBride, J. W., *The relationship between surface wear and contact resistance during the fretting of In-Vivo electrical contacts.* IEEE Transactions on Components and Packaging Technologies, 2008. 31(3): pp. 592-600.

29. Xie, F., Flowers, G. T., Chen, C., Bozack, M., Suhling, J., Rickett, B. I., Malucci, R. D., and Manlapaz, C., *Analysis and prediction of vibration-induced fretting motion in a blade/receptacle connector pair*. in *Proceedings of the 53rd IEEE Holm Conference on Electrical Contacts*. 2007. Pittsburg, PA, USA: IEEE.

30. Chen, C., Flowers, G. T., Bozack, M., Suhling, J., Rickett, B. I., Malucci, R. D., and Manlapaz, C., *Modeling and analysis of a blade/receptacle pair for the prediction of vibration-induced fretting degradation*. in *Proceedings of the 54th IEEE Holm Conference on Electrical Contacts*. 2008. Orlando, FL, USA: IEEE.

31. Chudnovsky, B. H., Livshitz, A., and Chudnovsky, B. A., *Thermal model of electrical contacts based on experimental data*. in *Proceedings of the 54th IEEE Holm Conference on Electrical Contacts*. 2008. Orlando, FL, USA: IEEE.

32. Park, Y. W., Bapu, G. N. K. R., and Lee, K. Y., *The influence of current load on fretting of electrical contacts.* Tribology International, 2009. 42(5): pp. 682-689.

33. Williams, J., *Engineering Tribology*. 2005, New York: Cambridge University Press.

34. Greenwood, J. A. and Williamson, J. B. P., *Contact of nominally flat surfaces.* Proceedings of the Royal Society A, 1966. 295(1442): pp. 300-319.

35. Chang, W. R., Etsion, I., and Bogy, D. B., *An elastic-plastic model for the contact of rough surfaces.* Journal of Tribology, 1987. 109(2): pp. 257-263.

36. Jackson, R. L., *The effect of scale-dependent hardness on elasto-plastic asperity contact between rough surfaces.* Tribology Transactions, 2006. 49(2): pp. 135-150.

37. Jackson, R. L. and Green, I., *A statistical model of elasto-plastic asperity contact between rough surfaces.* Tribology International, 2006. 39(9): pp. 906-914.

38. Kogut, L. and Etsion, I., *A finite element based elastic-plastic model for the contact of rough surfaces.* Tribology Transactions, 2003. 46(3): pp. 383-390.

39. Majumdar, A. and Bhushan, B., *Fractal model of elastic-plastic contact between rough surfaces.* Journal of Tribology, 1991. 113(1): pp. 1-11.

40. Kogut, L. and Komvopoulos, K., *Electrical contact resistance theory for conductive rough surfaces.* Journal of Applied Physics, 2003. 94(5): pp. 3153-3162.

41. Ciavarella, M., Murolo, G., Demelio, G., and Barber, J. R., *Elastic contact stiffness and contact resistance for the Weierstrass profile.* Journal of the Mechanics and Physics of Solids, 2004. 52(6): pp. 1247-1265.

42. Ganti, S. and Bhushan, B., *Generalized fractal analysis and its applications to engineering surfaces.* Wear, 1995. 180(1-2): pp. 17-34.

43. Kogut, L. and Jackson, R. L., *A comparison of contact modeling utilizing statistical and fractal approaches.* Journal of Tribology, 2006. 128(1): pp. 213-217.

44. Bora, C. K., Flater, E. E., Street, M. D., Redmond, J. M., Starr, M. J., Carpick, R. W., and Plesha, M. E., *Multiscale roughness and modeling of MEMS interfaces.* Tribology Letters, 2005. 19(1): pp. 37-48.

45. Ciavarella, M., Demelio, G., Barber, J. R., and Jang, Y. H., *Linear elastic contact of the Weierstrass profile.* Proceedings of the Royal Society A, 2000. 456(1994): pp. 387-405.

46. Jackson, R. L. and Streator, J. L., *A multi-scale model for contact between rough surfaces.* Wear, 2006. 261(11-12): pp. 1337-1347.

47. Archard, J. F., *Elastic deformation and the laws of friction.* Proceedings of the Royal Society A, 1957. 243(1233): pp. 190-205.

48. Krithivasan, V. and Jackson, R. L., *An analysis of three-dimensional elasto-plastic sinusoidal contact.* Tribology Letters, 2007. 27(1): pp. 31-43.

49. Holm, R., *Electric Contacts*. 1967, New York: Springer.

50. Madhusudana, C. V., *Thermal Contact Conductance*. 1996, New York: Springer-Verlag.

51. Cooper, M. G., Mikic, B. B., and Yovanovich, M. M., *Thermal contact conductance.* International Journal of Heat and Mass Transfer, 1969. 12(3): pp. 279-300.

52. Kohlrausch, F., *Uber das problem eines elektrisch erwarmten leiters.* Ann. Phys. Lpz, 1900. 1: pp. 132-158.

53. Greenwood, J. A. and Williamson, J. B. P., *Electrical conduction in solids. II. Theory of temperature-dependent conductors.* Proceedings of the Royal Society A, 1958. 246(1244): pp. 13-31.

54. Braunovic, M., Konchits, V. V., and Myshkin, N. K., *Electrical Contacts: Fundamentals, Applications and Technology*. 2007, Boca Raton, FL, USA: CRC Press.

55. Angadi, S. V., Wilson, W. E., Jackson, R. L., Flowers, G. T., and Rickett, B. I., *A multi-physics finite element model of an electrical connector considering rough surface contact*. in *Proceedings of the 54th IEEE Holm Conference on Electrical Contacts*. 2008. Orlando, FL, USA: IEEE.

56. Wilson, W. E., Angadi, S. V., and Jackson, R. L., *Surface separation and contact resistance considering sinusoidal elastic-plastic multi-scale rough surface contact.* Wear, 2010. 268(1-2): pp. 190-201.

57. Incropera, F., Dewitt, D., Bergman, T., and Lavine, A., *Fundamentals of Heat and Mass Transfer*. Sixth ed. 2007, Hoboken, New Jersey: John Wiley & Sons, Inc.

APPENDIX A

For each of the applied currents in the 40A connector ANSYS™ model, the following steps are followed to solve the model and to obtain convergence:

1. At first, read the input text file within ANSYS™.
2. Apply displacement δ/2 to both the top-most and the bottom-most surfaces of the sidewalls of the spring terminal of the connector in ANSYS™ so that total thermal expansion (thermal deformation, δ) of the sidewalls can be considered in the model.
3. Now, the pin terminal in the ANSYS™ model is adjusted (moved downwards) so that the spring and pin terminals just overlap. This helps to achieve force balance on the pin terminal of the model.
4. Then, 3 contact pairs are created for 3 contacting regions.
5. Specific solution controls are then assigned in ANSYS™ which will enable the solution to converge through iterative approach. These controls include:
    a) Large displacement static
    b) Number of substeps: 20
    c) Number of equilibrium iterations: 20

Finally, the entire connector model is now solved and convergence of the solution is attained.

APPENDIX B

The filtered graphs of connector resistance (R) and connector temperature (T) vs. time for each of the three iterations for tests T1 to T8 (see Table 6-1) are included in this appendix.

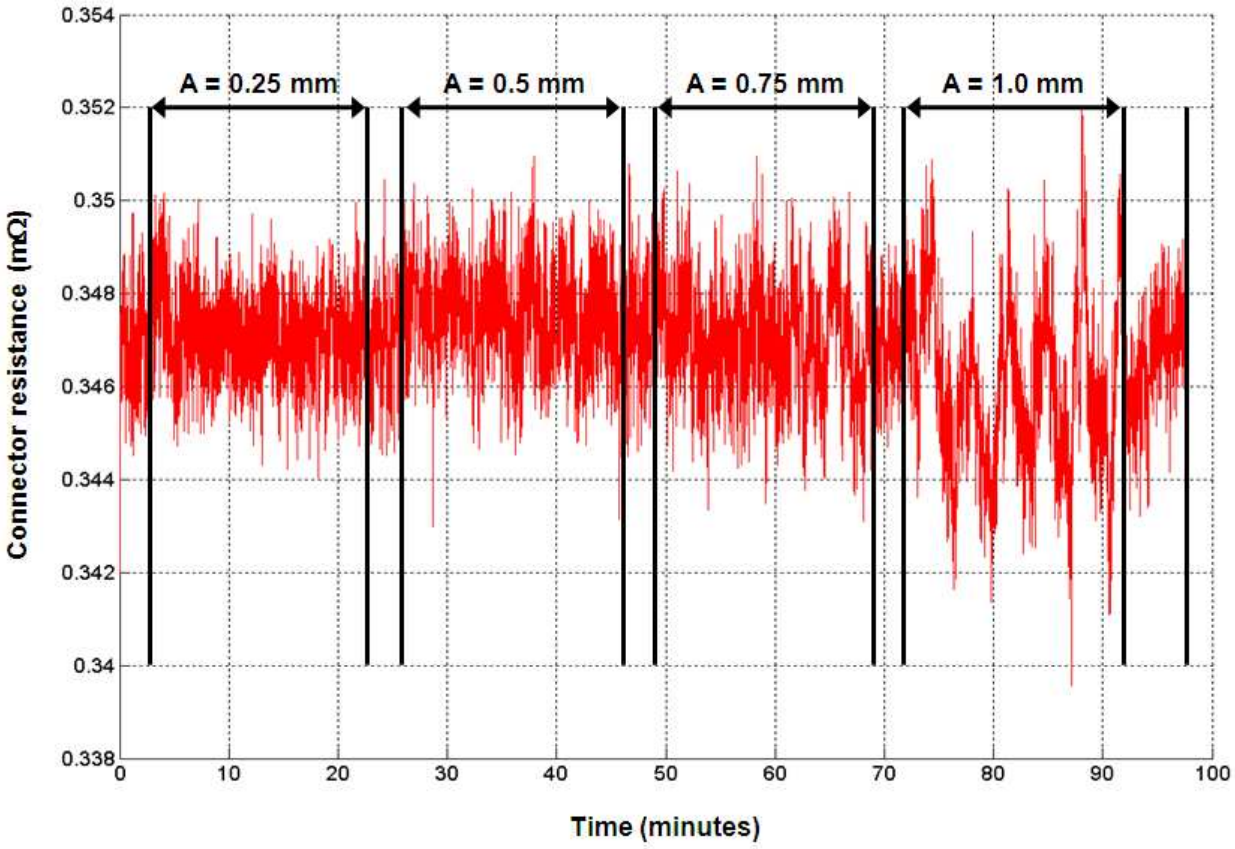

Figure B-1: Plot of connector resistance versus time for test T1 iteration 1

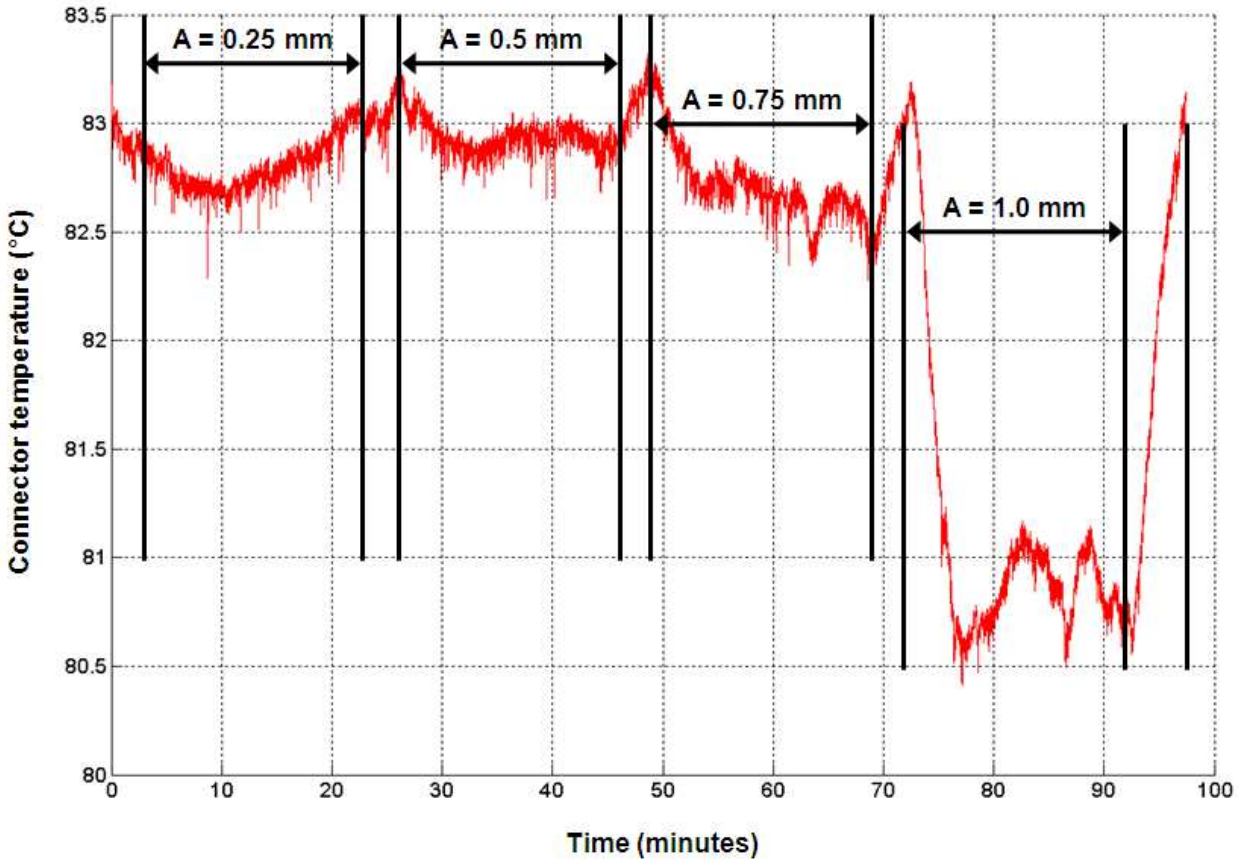

Figure B-2: Plot of connector temperature versus time for test T1 iteration 1

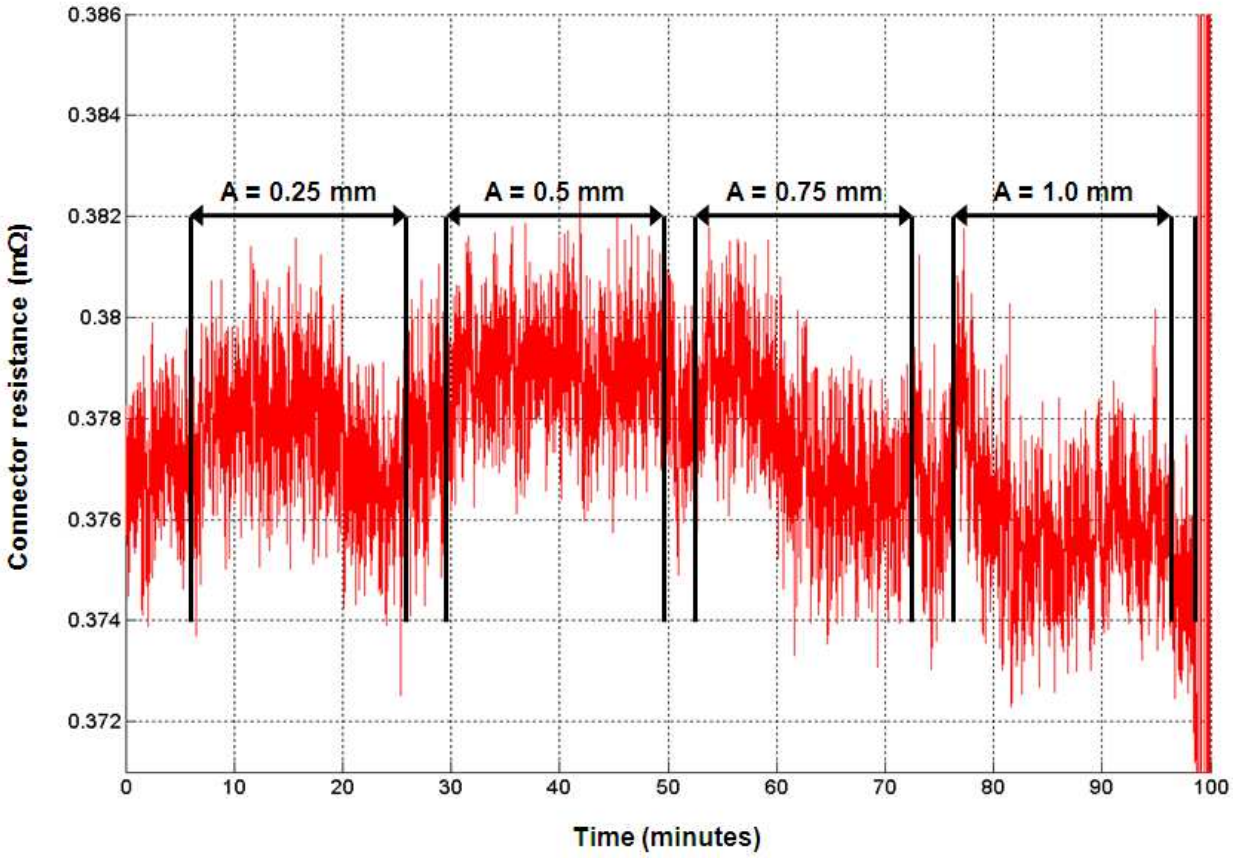

Figure B-3: Plot of connector resistance versus time for test T1 iteration 2

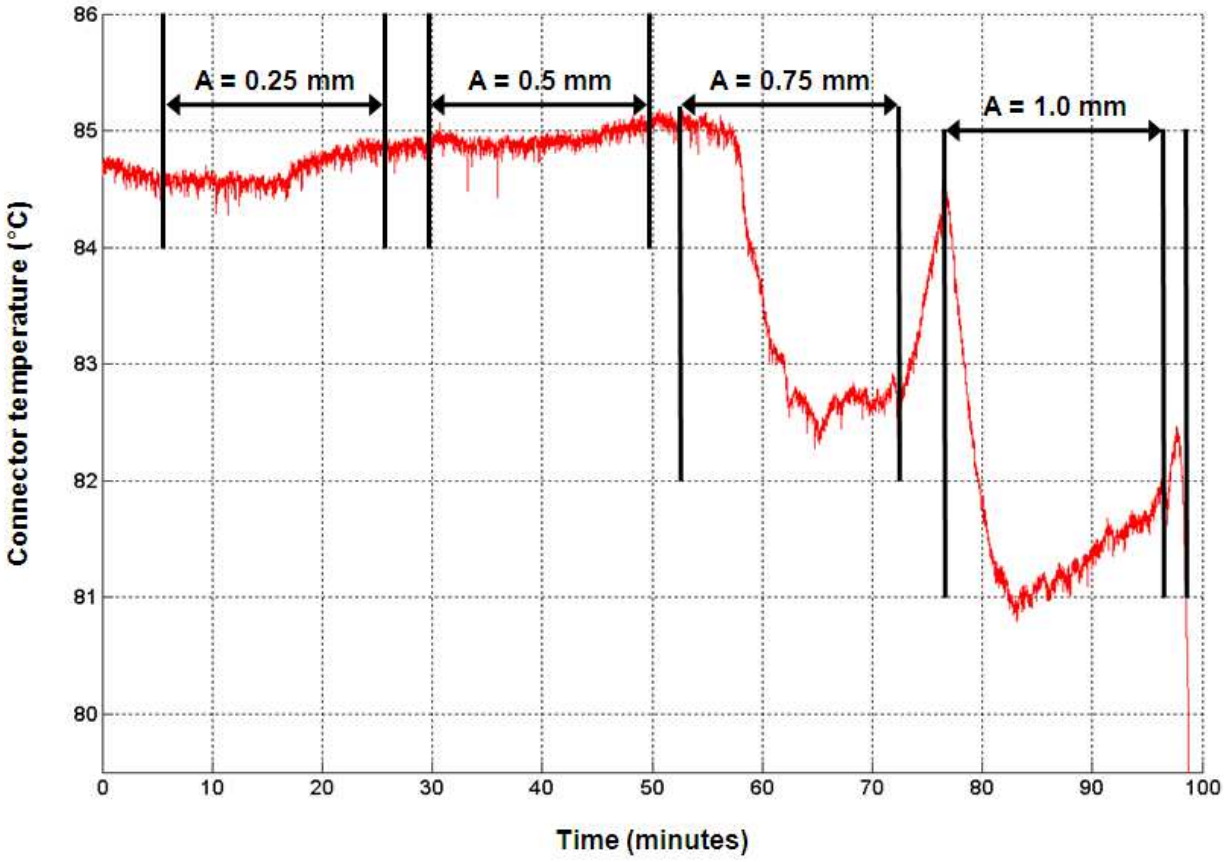

Figure B-4: Plot of connector temperature versus time for test T1 iteration 2

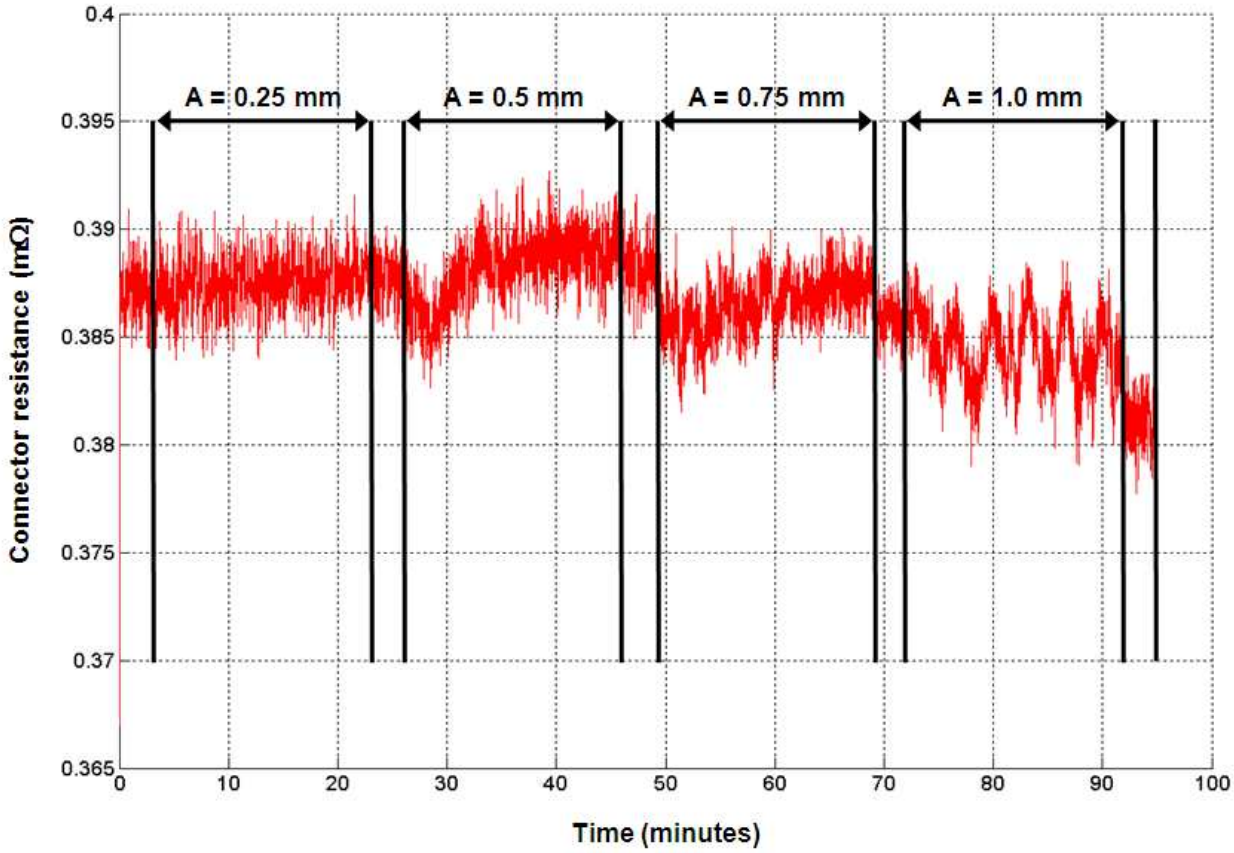

Figure B-5: Plot of connector resistance versus time for test T1 iteration 3

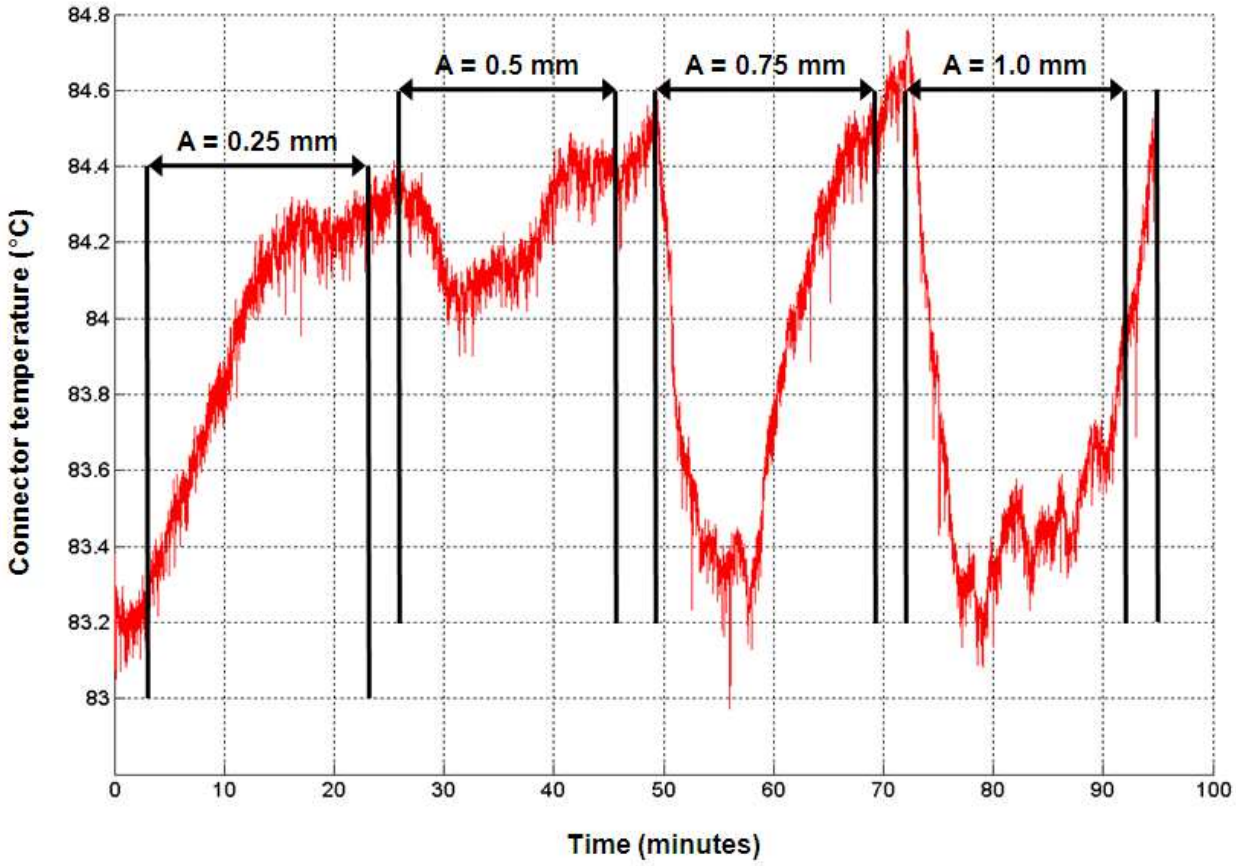

Figure B-6: Plot of connector temperature versus time for test T1 iteration 3

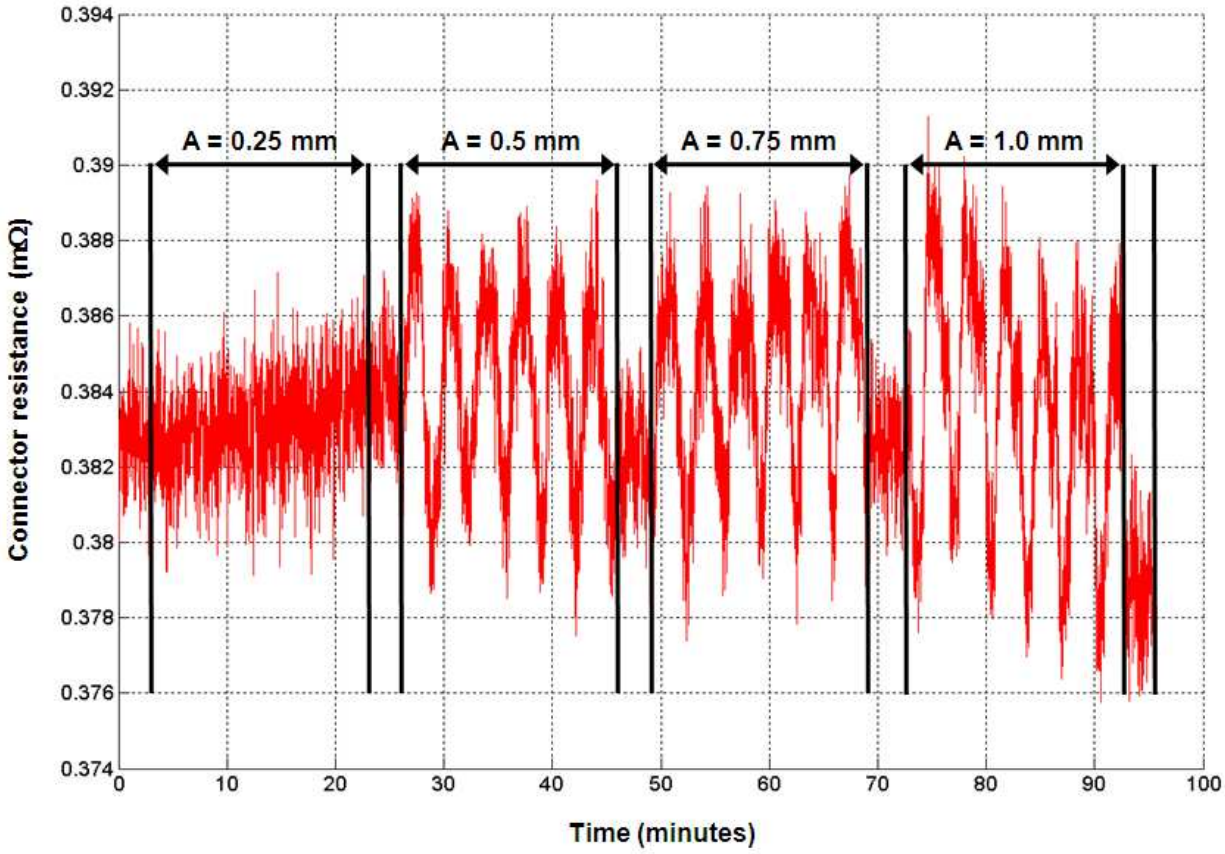

Figure B-7: Plot of connector resistance versus time for test T2 iteration 1

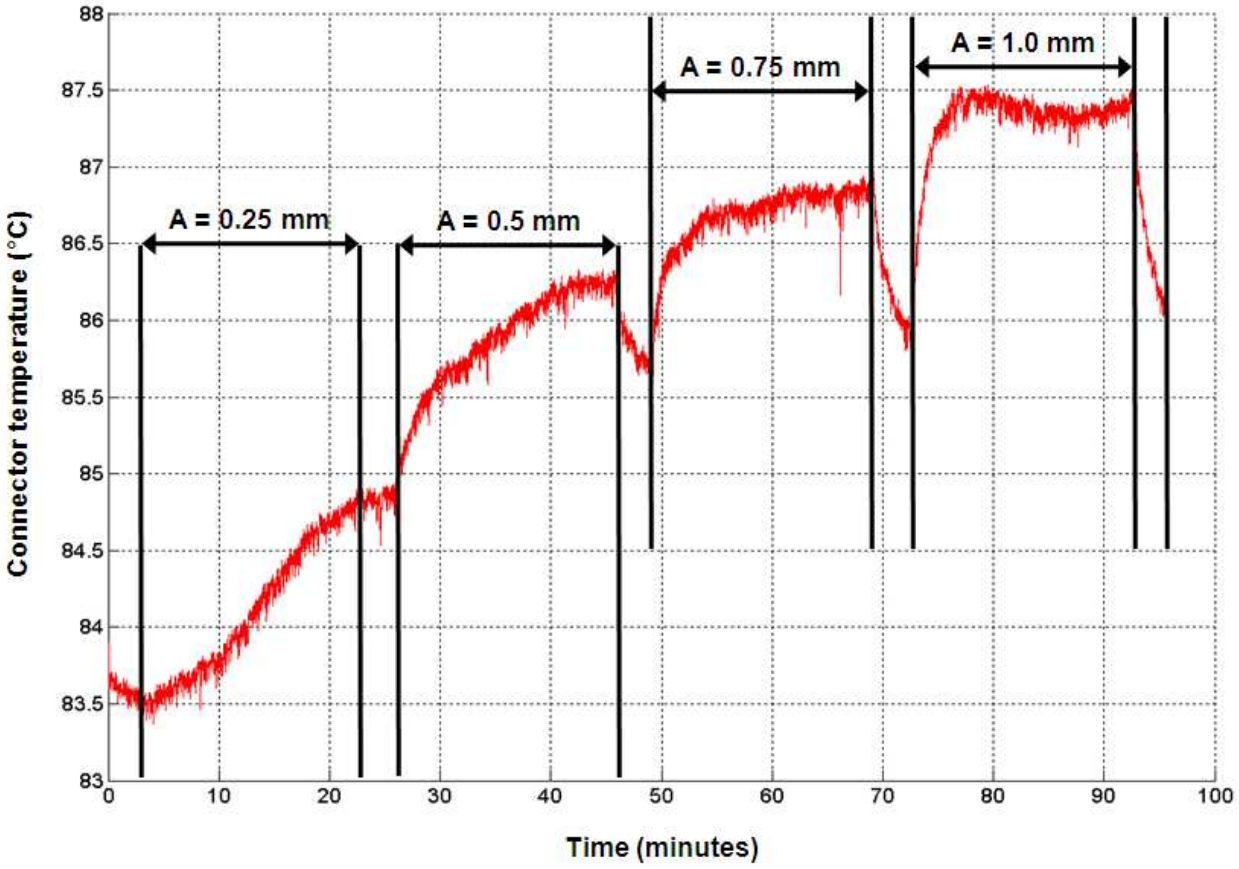

Figure B-8: Plot of connector temperature versus time for test T2 iteration 1

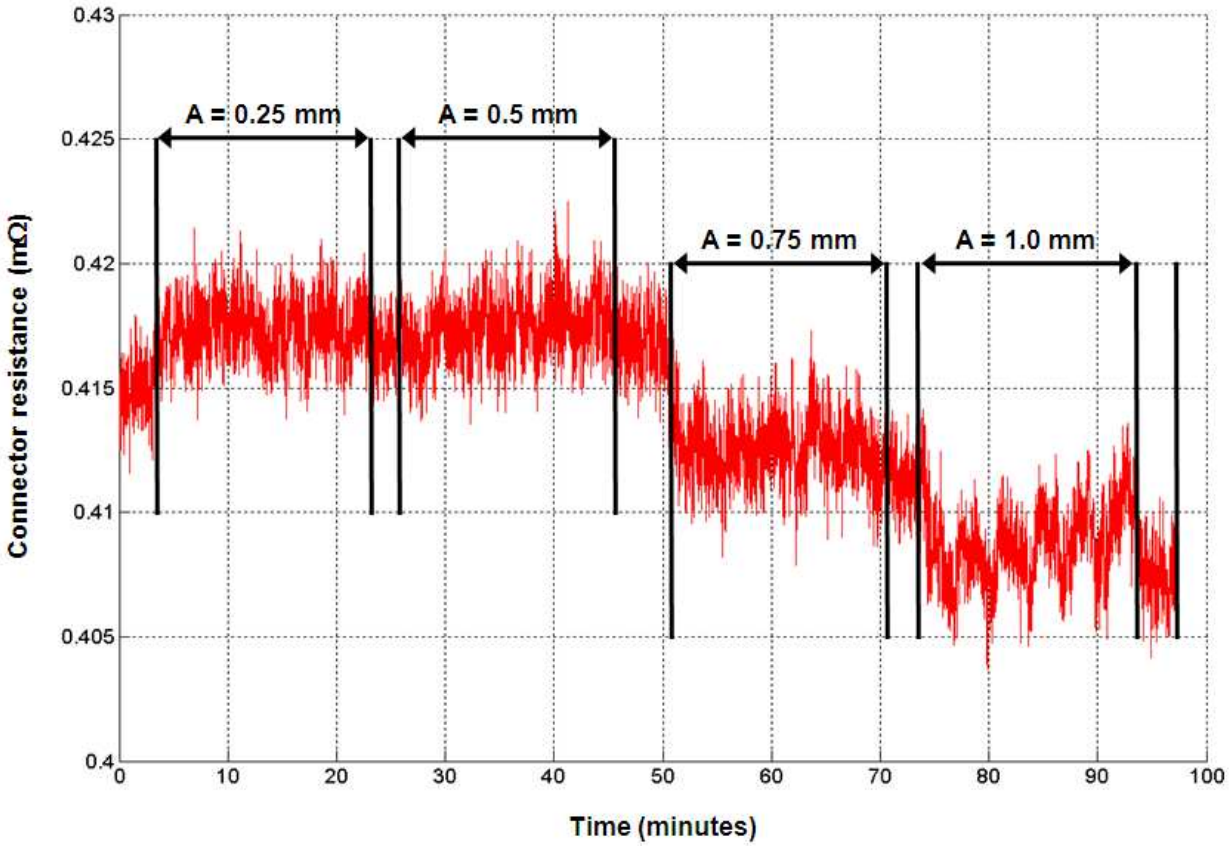

Figure B-9: Plot of connector resistance versus time for test T2 iteration 2

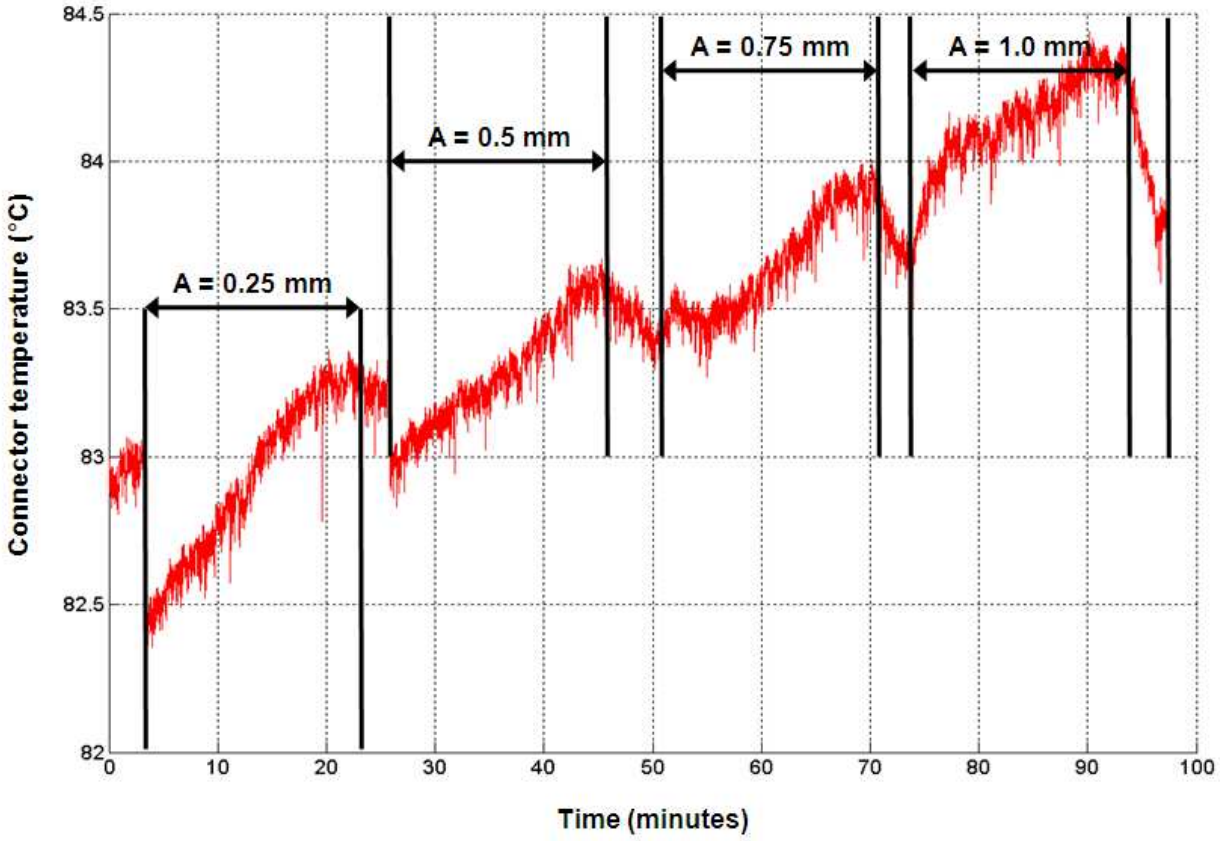

Figure B-10: Plot of connector temperature versus time for test T2 iteration 2

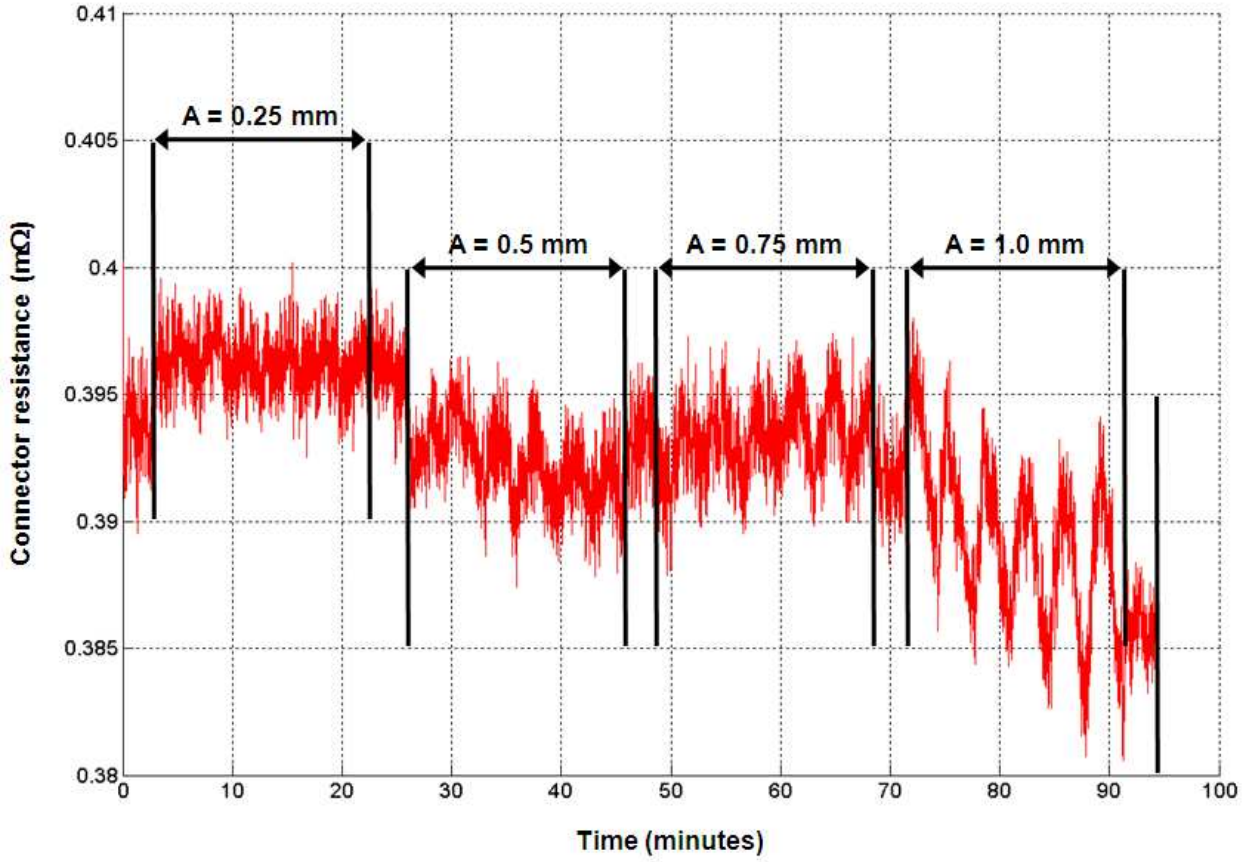

Figure B-11: Plot of connector resistance versus time for test T2 iteration 3

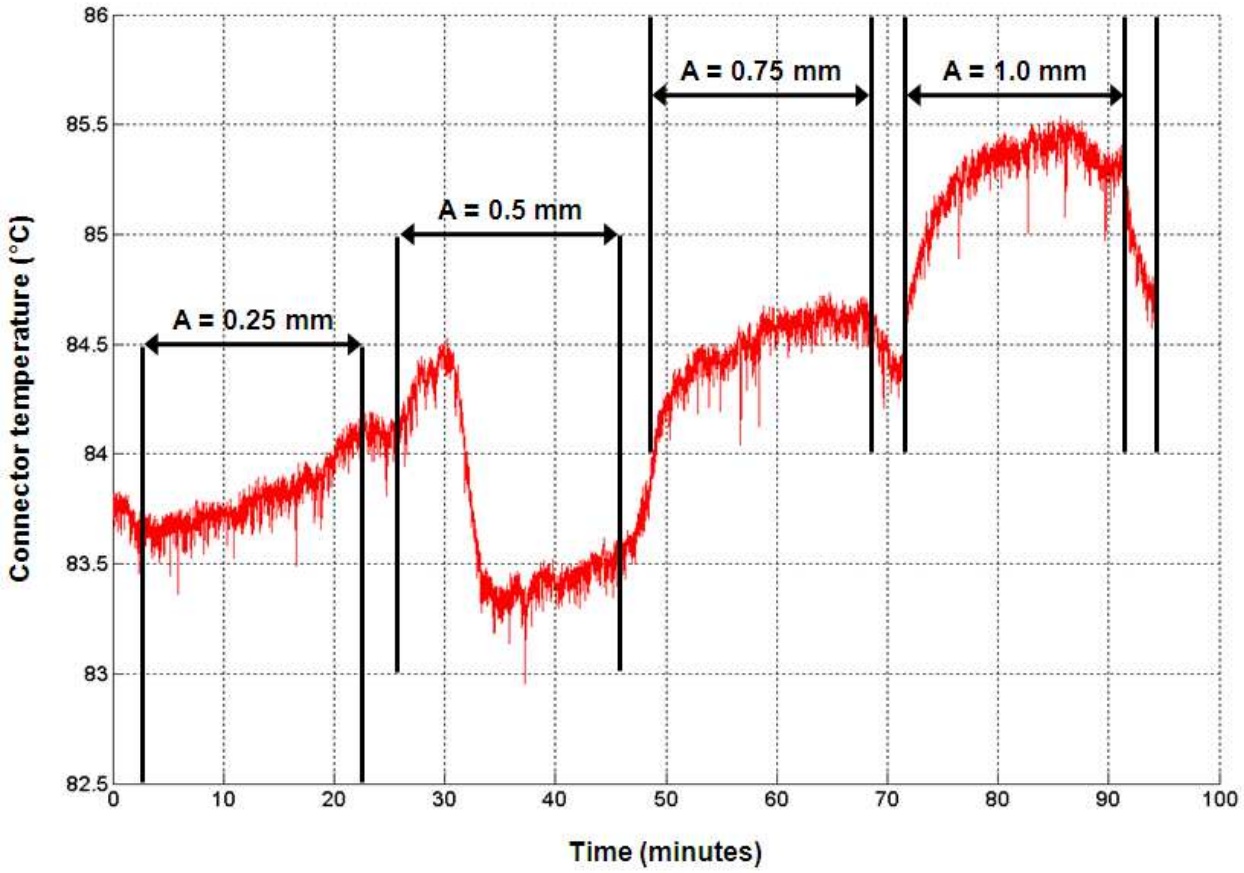

Figure B-12: Plot of connector temperature versus time for test T2 iteration 3

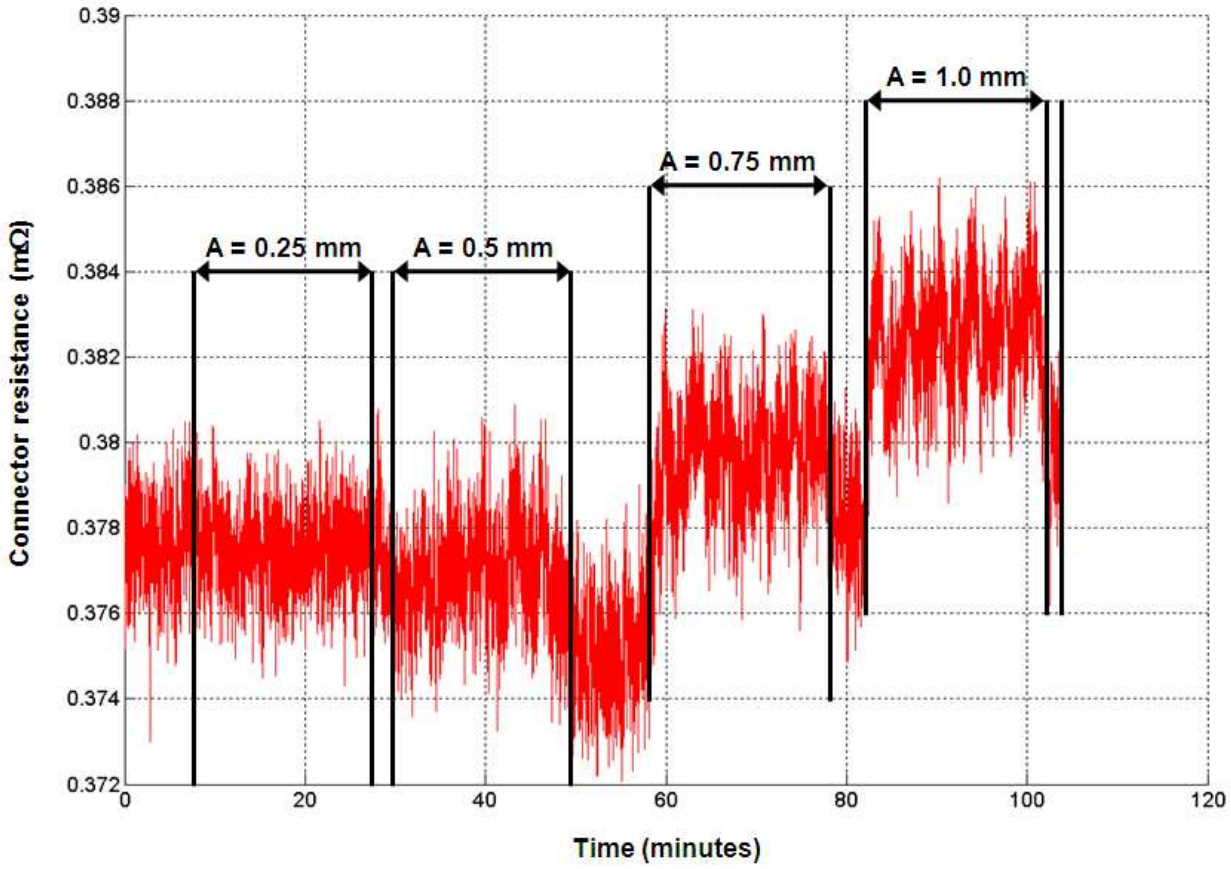

Figure B-13: Plot of connector resistance versus time for test T3 iteration 1

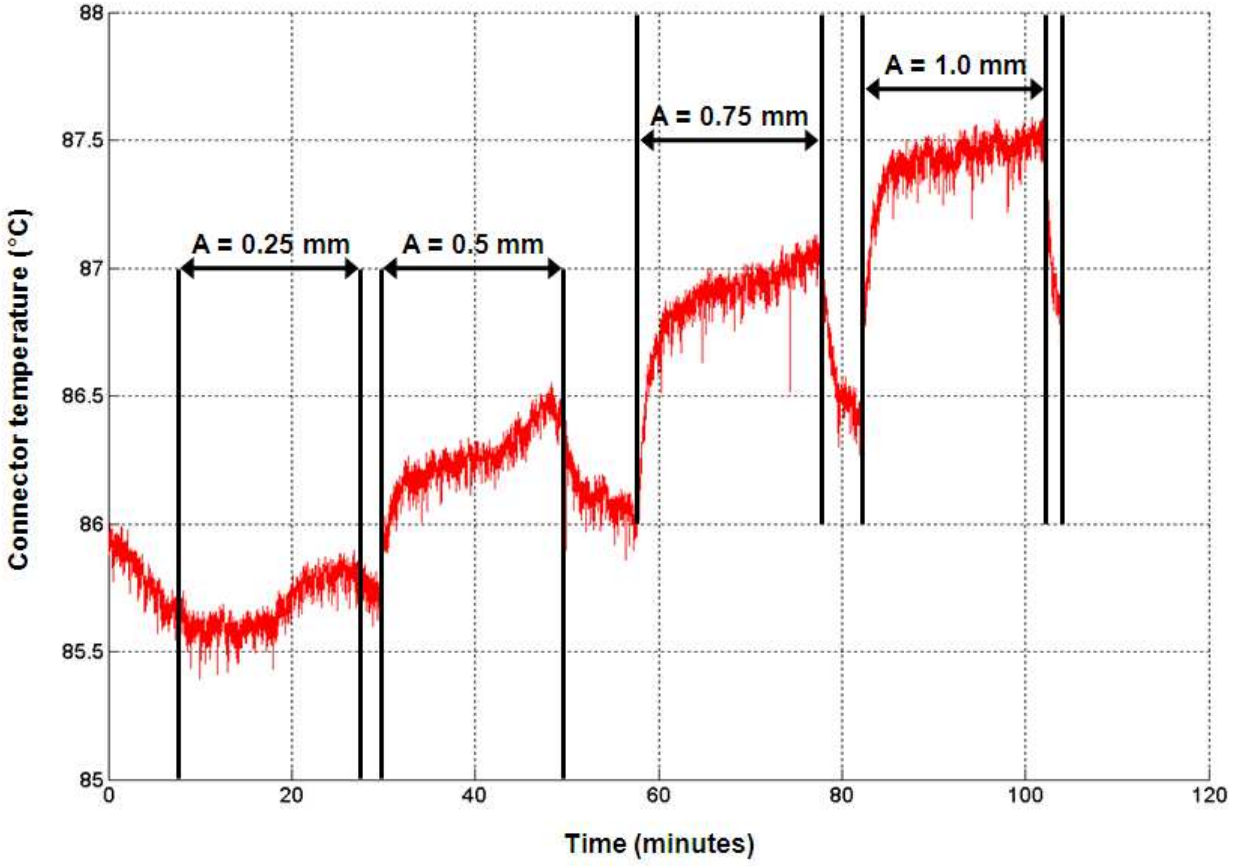

Figure B-14: Plot of connector temperature versus time for test T3 iteration 1

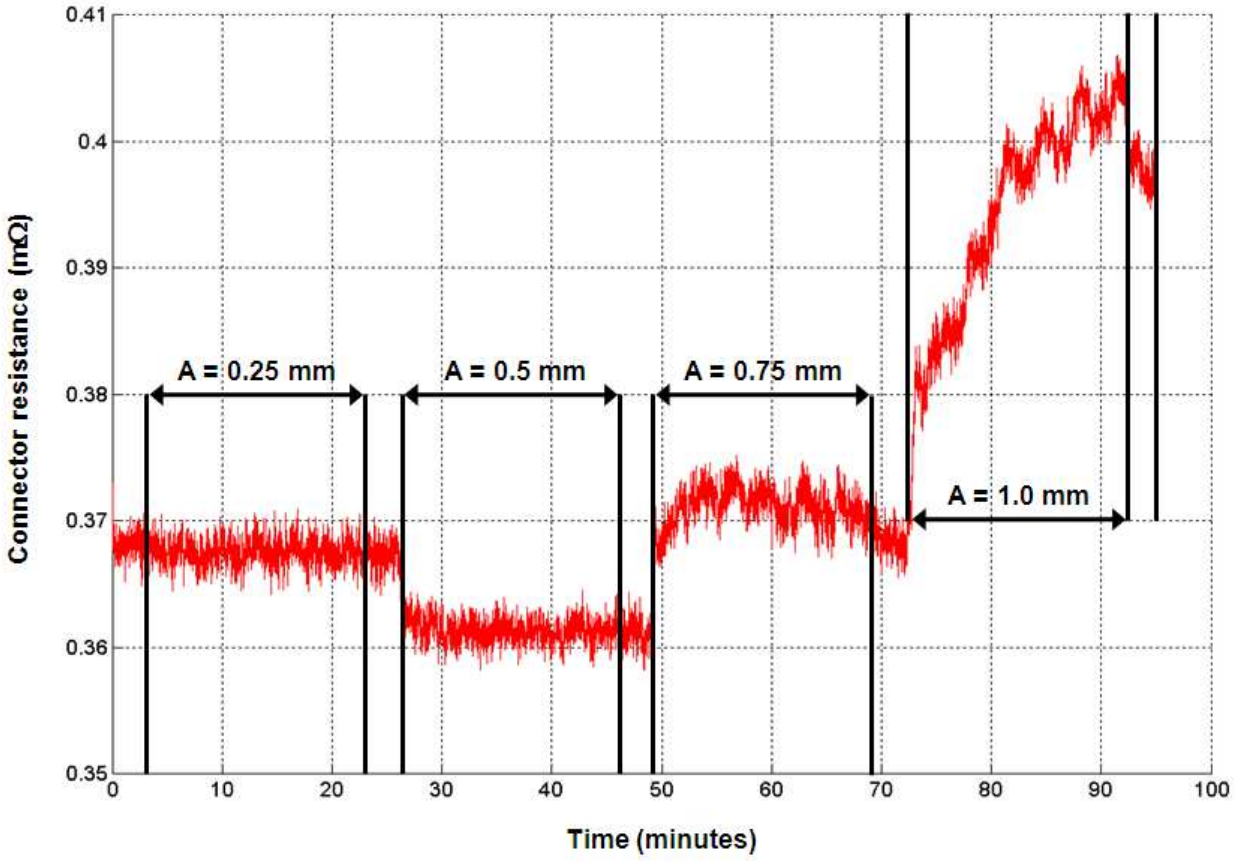

Figure B-15: Plot of connector resistance versus time for test T3 iteration 2

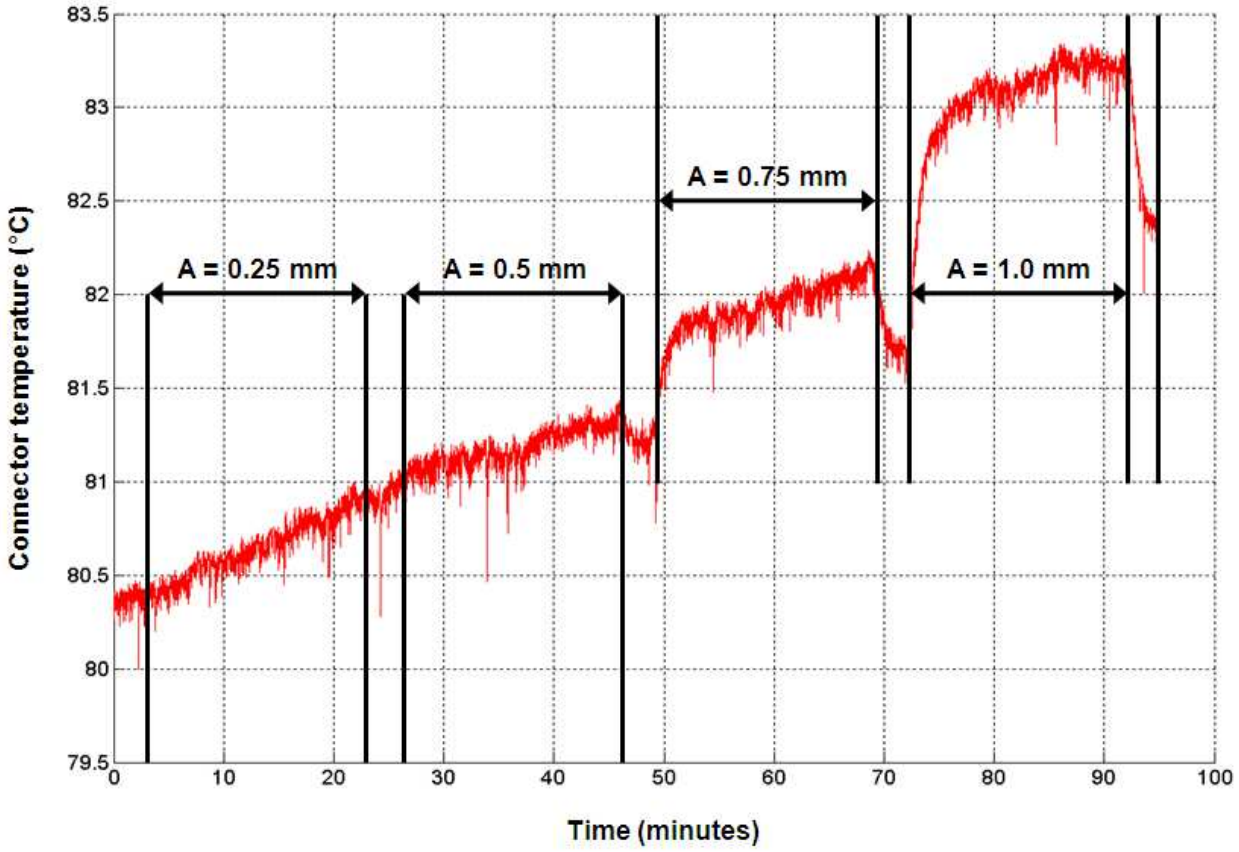

Figure B-16: Plot of connector temperature versus time for test T3 iteration 2

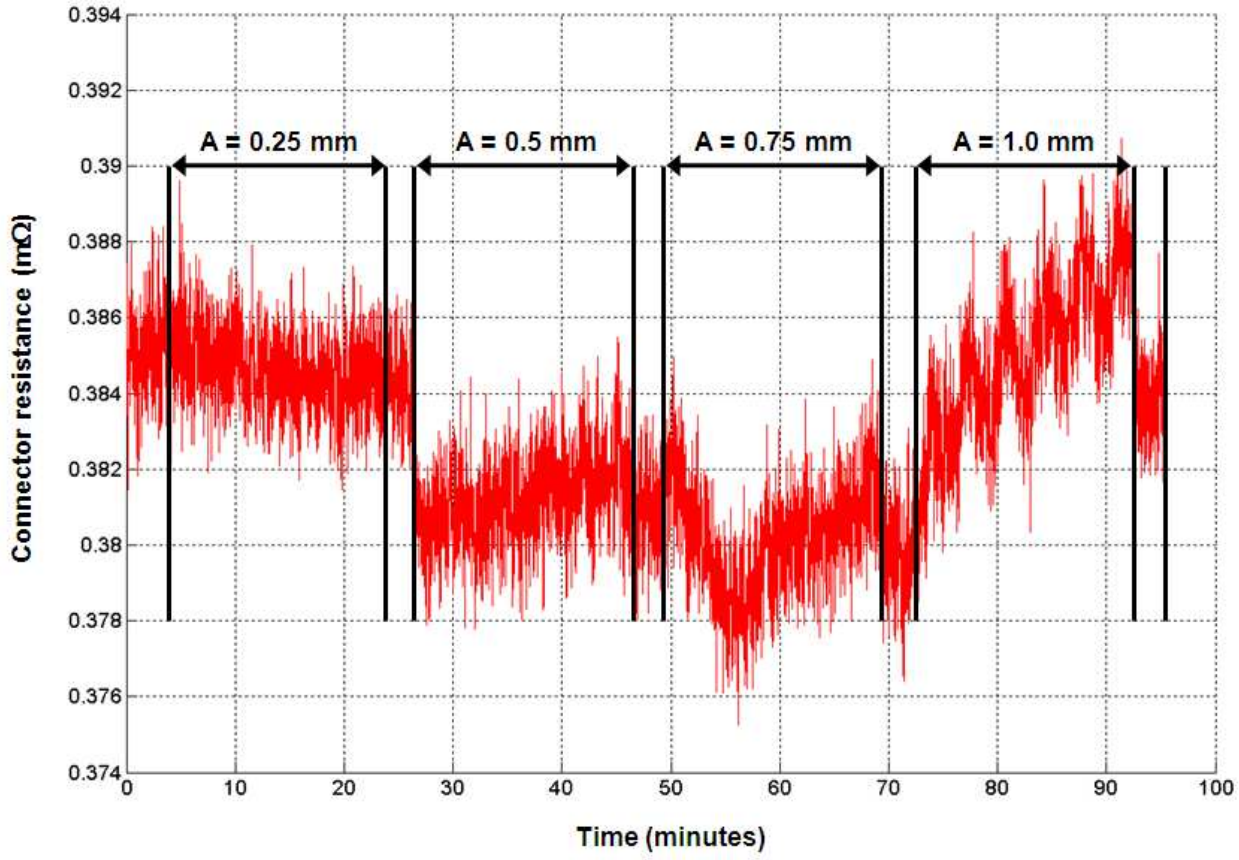

Figure B-17: Plot of connector resistance versus time for test T3 iteration 3

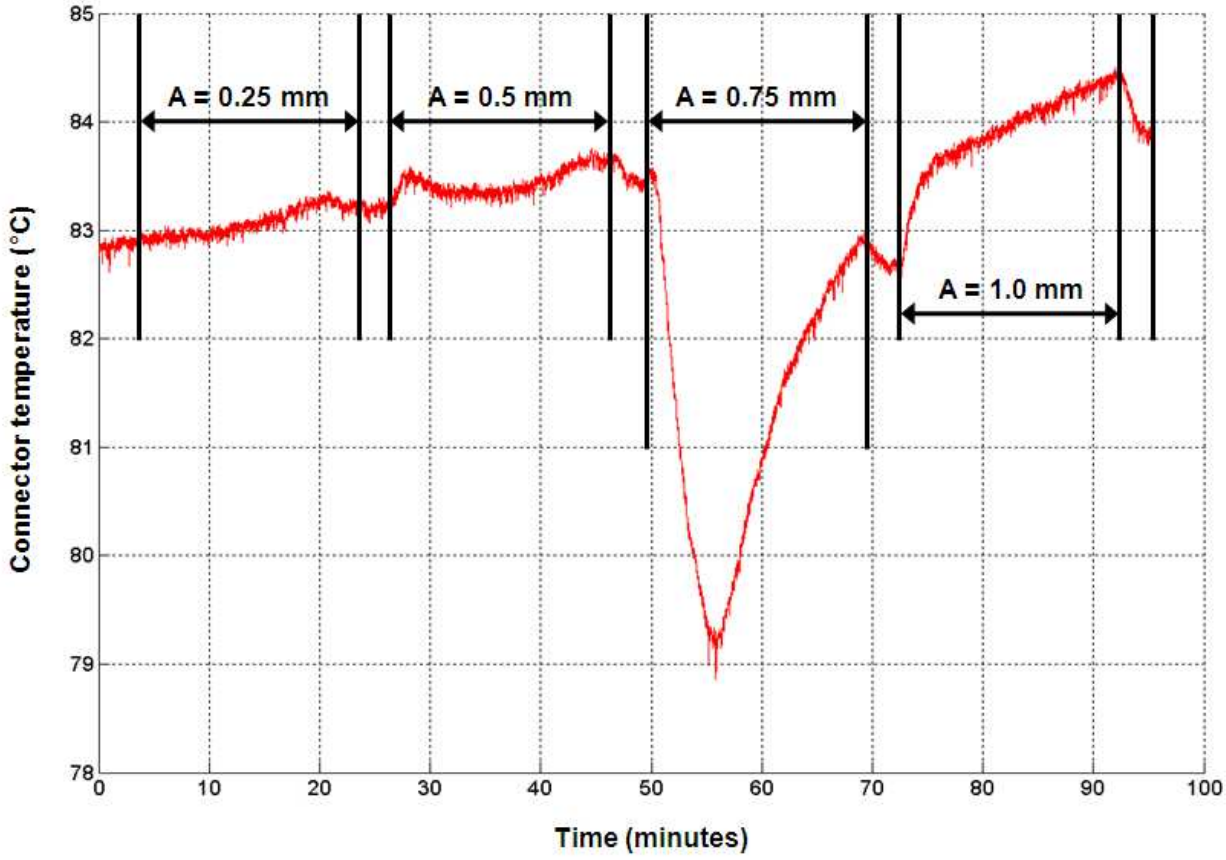

Figure B-18: Plot of connector temperature versus time for test T3 iteration 3

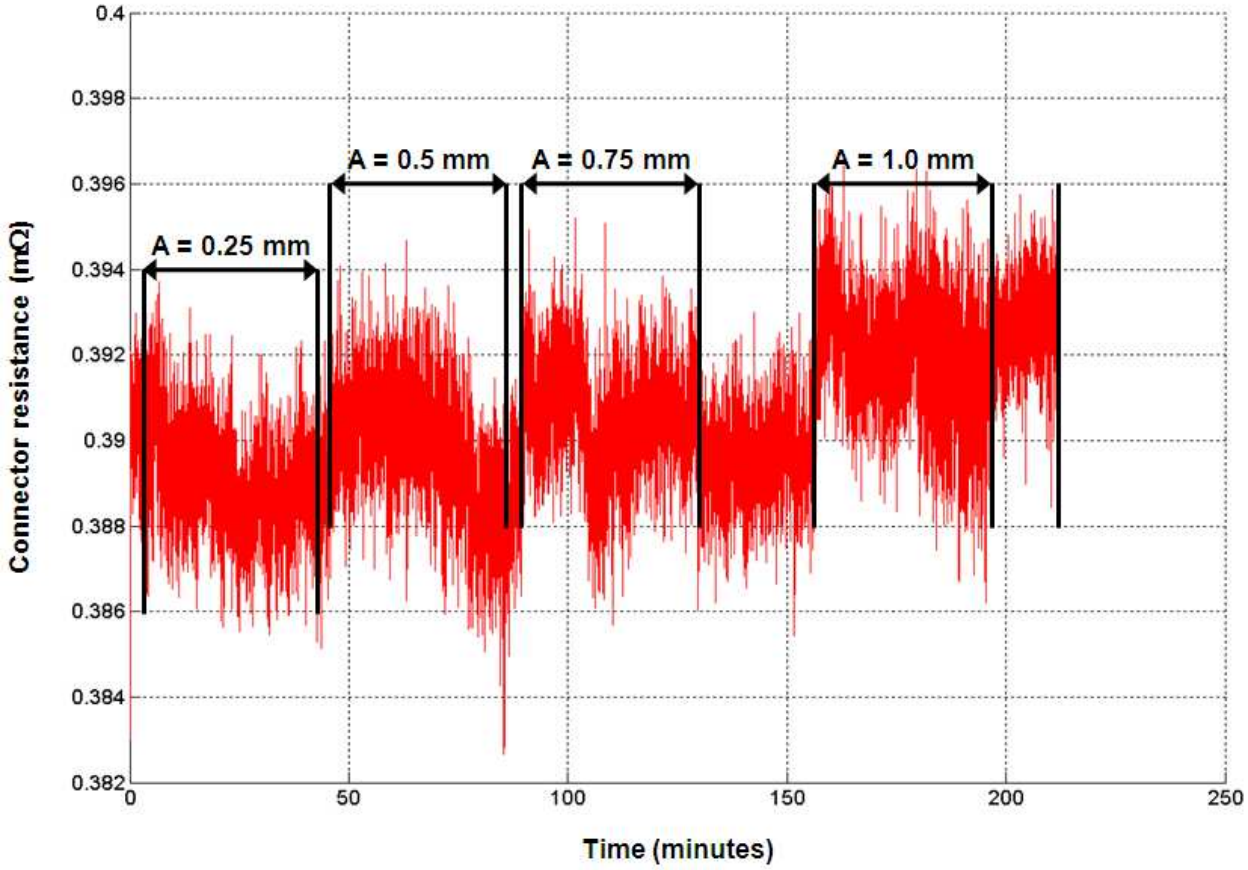

Figure B-19: Plot of connector resistance versus time for test T4 iteration 1

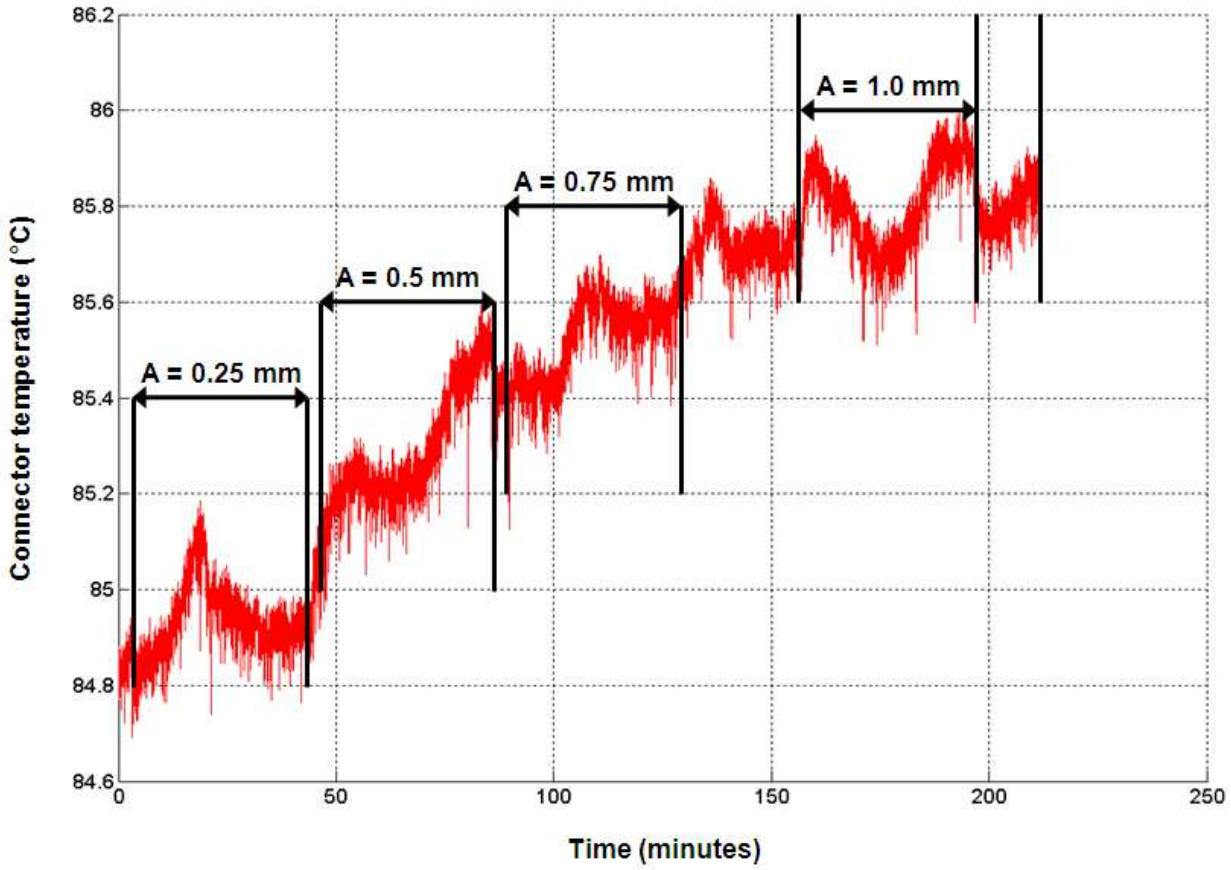

Figure B-20: Plot of connector temperature versus time for test T4 iteration 1

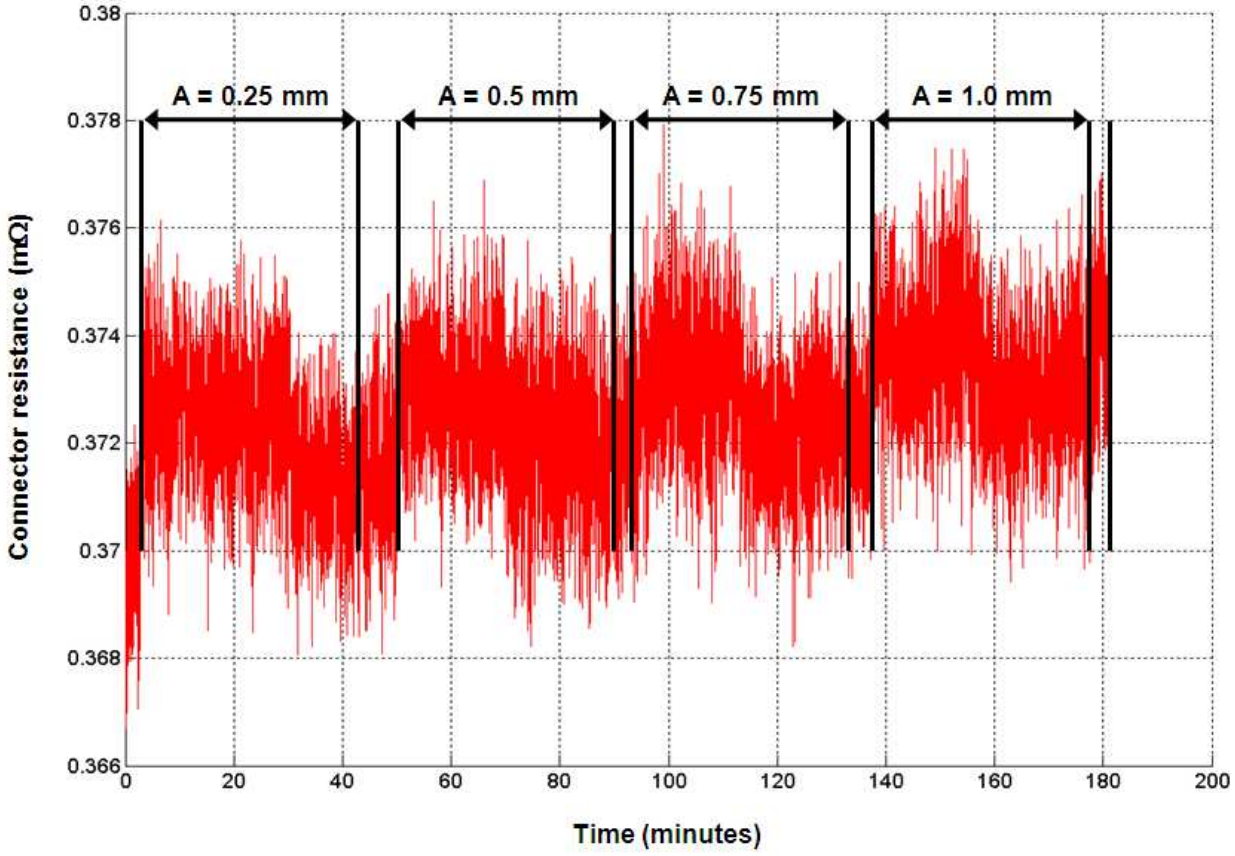

Figure B-21: Plot of connector resistance versus time for test T4 iteration 2

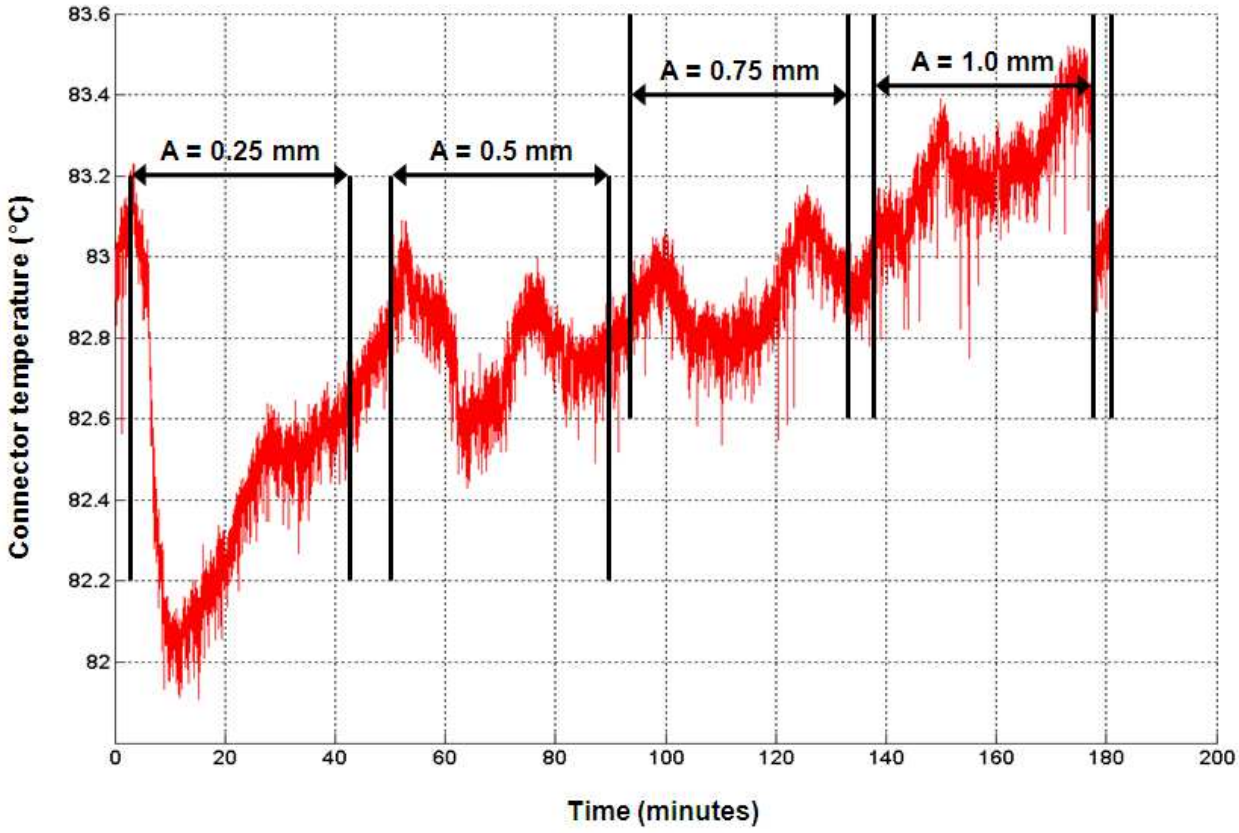

Figure B-22: Plot of connector temperature versus time for test T4 iteration 2

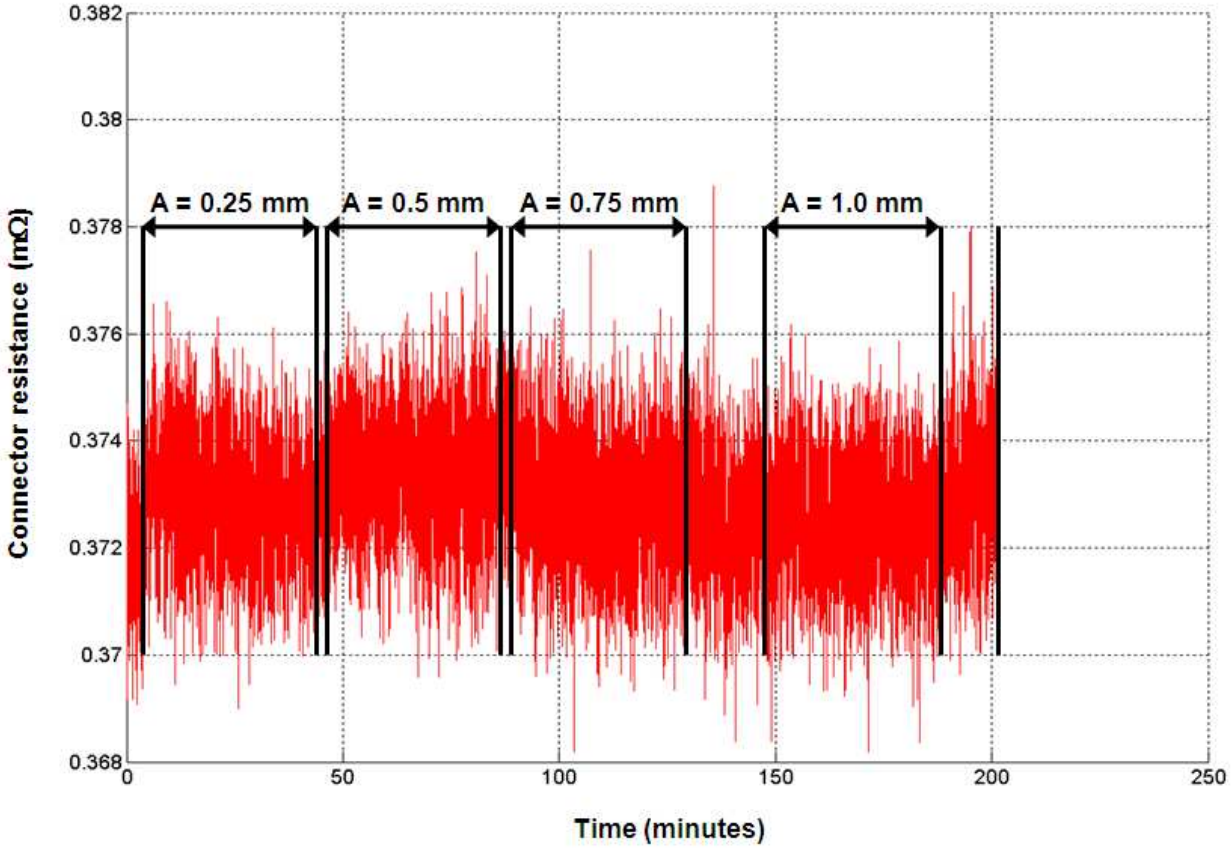

Figure B-23: Plot of connector resistance versus time for test T4 iteration 3

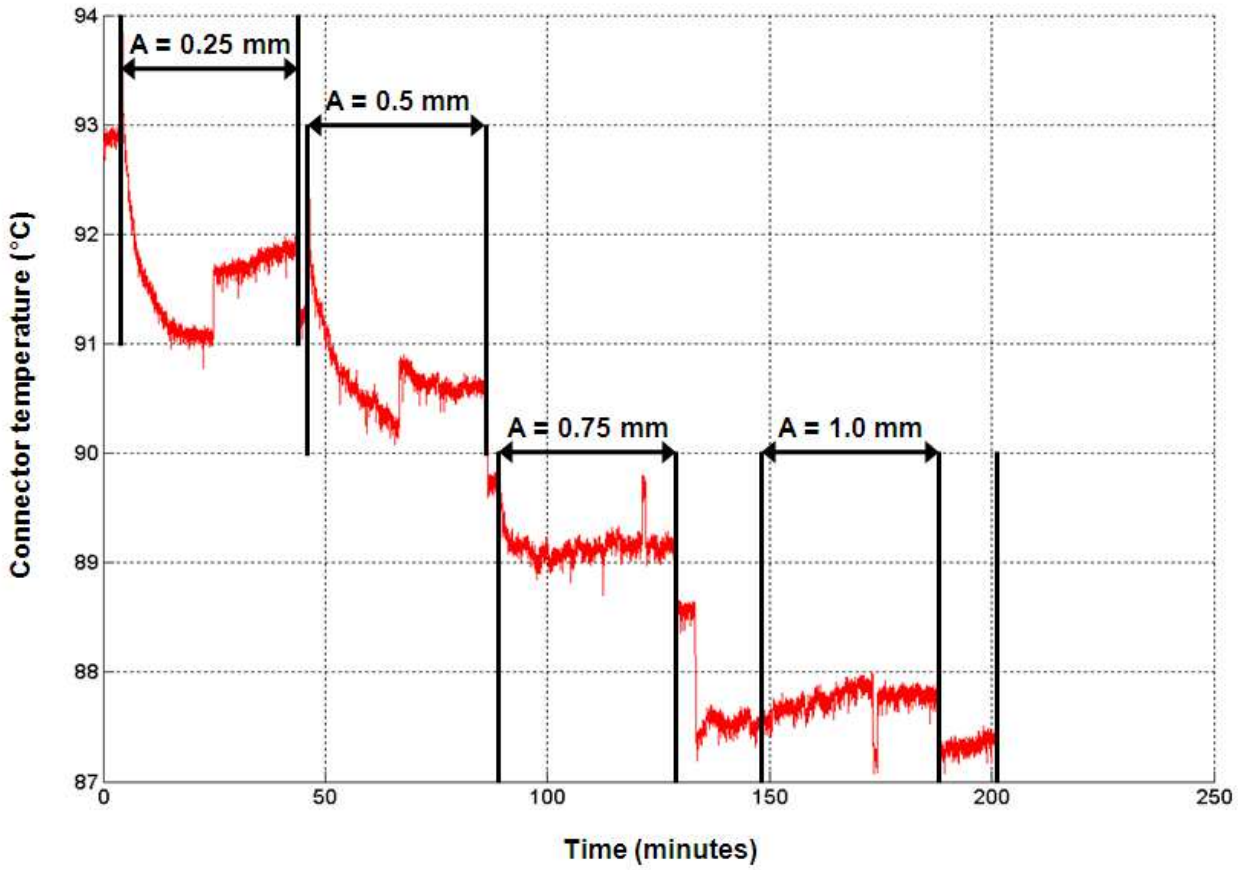

Figure B-24: Plot of connector temperature versus time for test T4 iteration 3

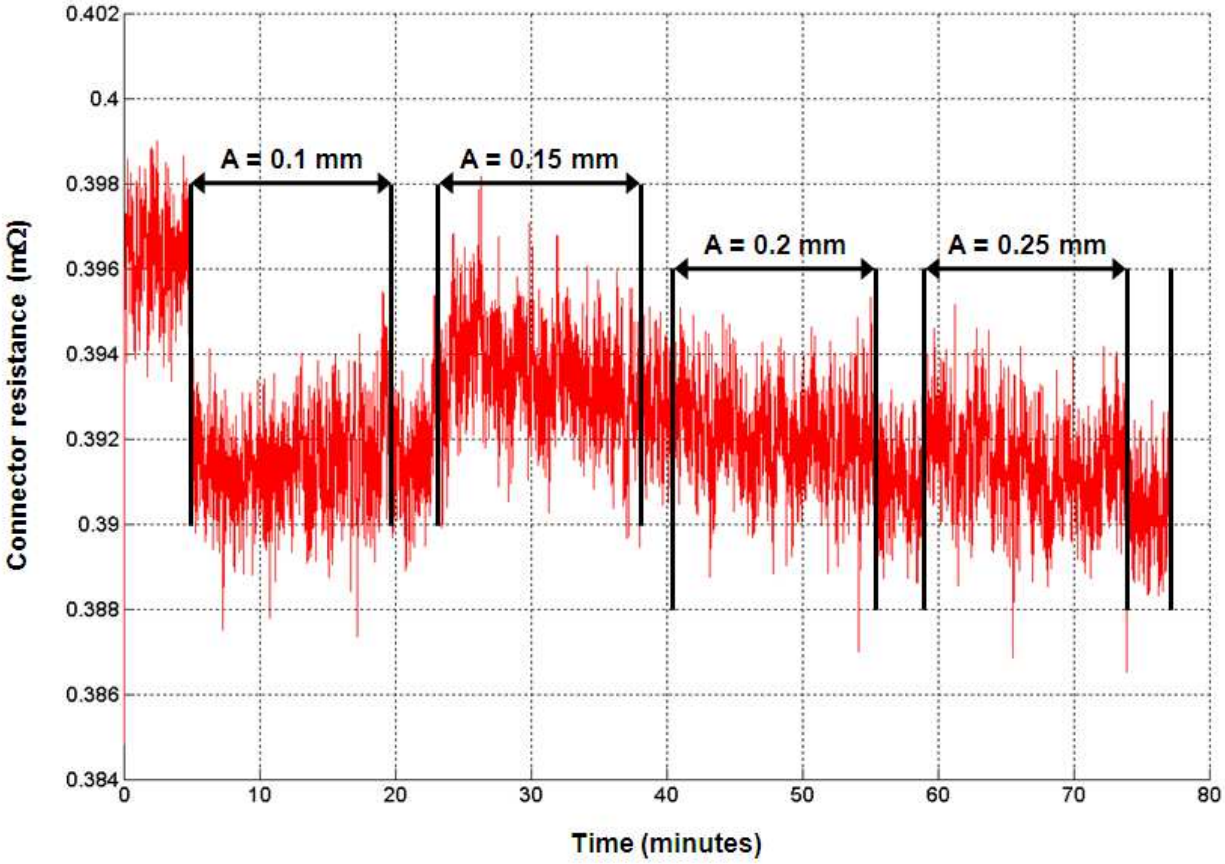

Figure B-25: Plot of connector resistance versus time for test T5 iteration 1

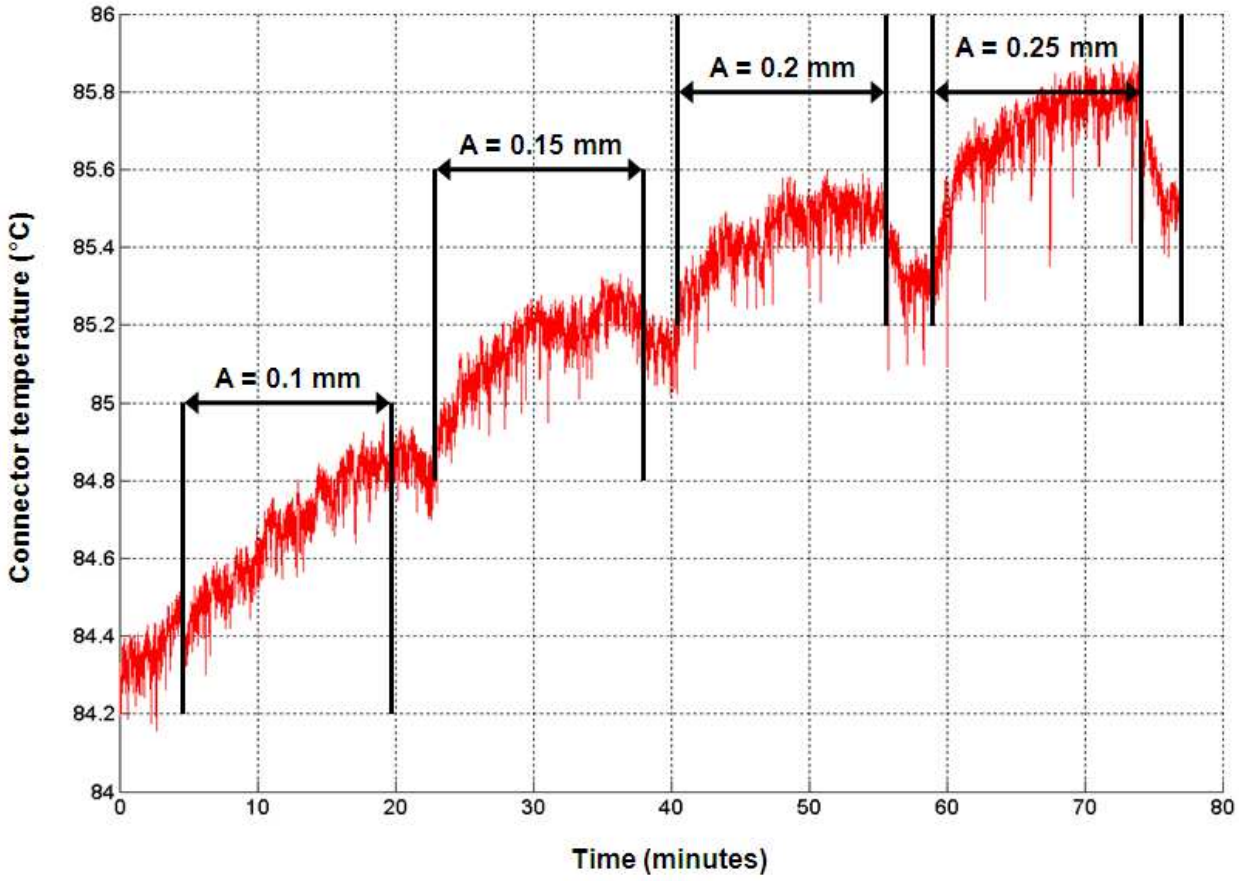

Figure B-26: Plot of connector temperature versus time for test T5 iteration 1

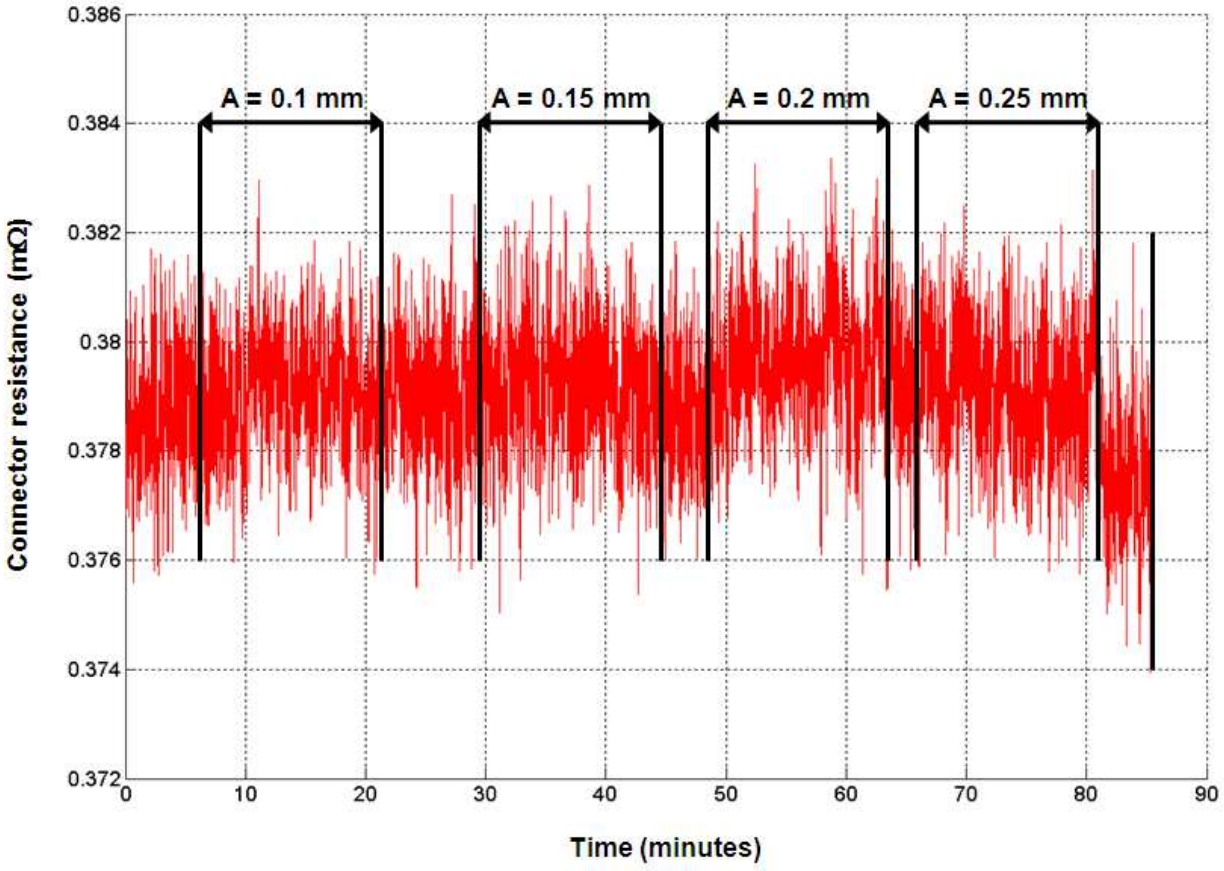

Figure B-27: Plot of connector resistance versus time for test T5 iteration 2

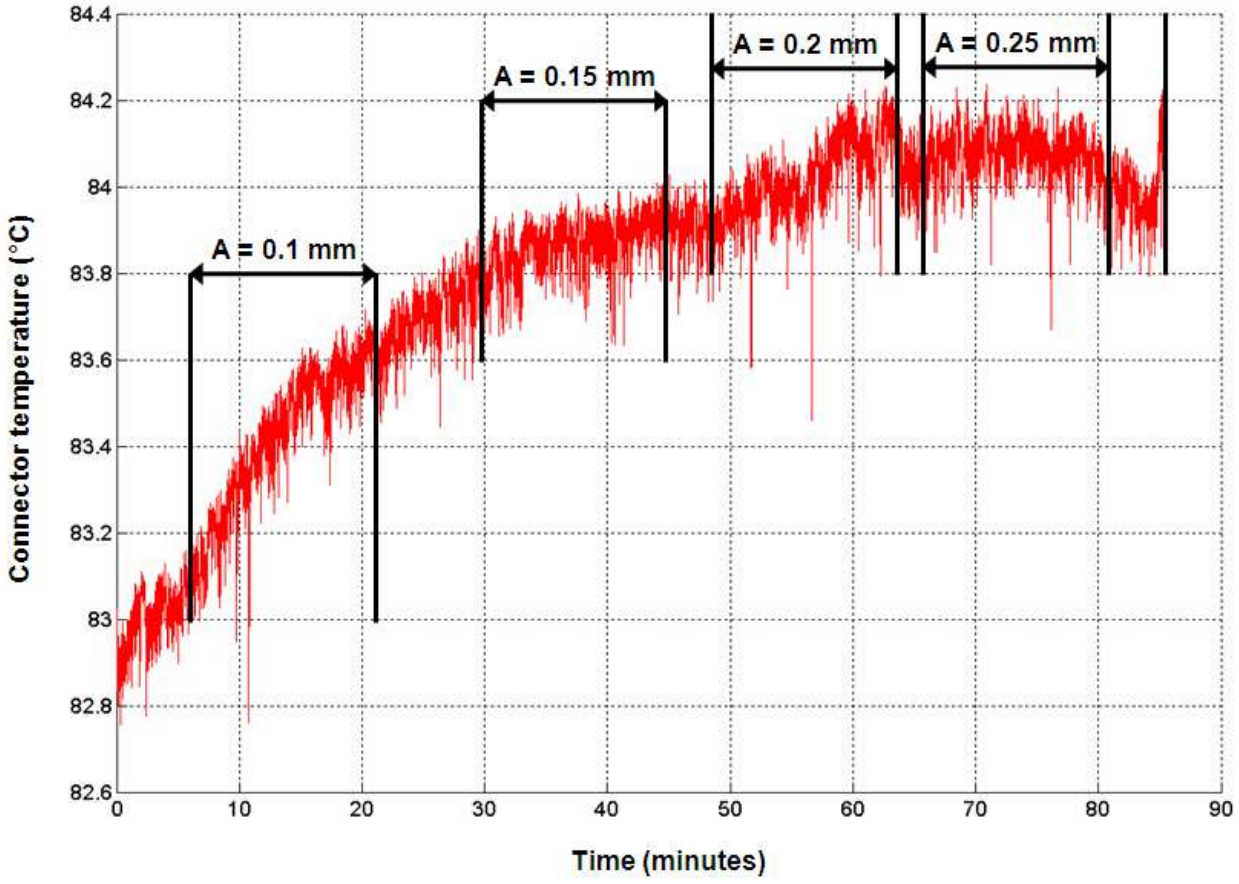

Figure B-28: Plot of connector temperature versus time for test T5 iteration 2

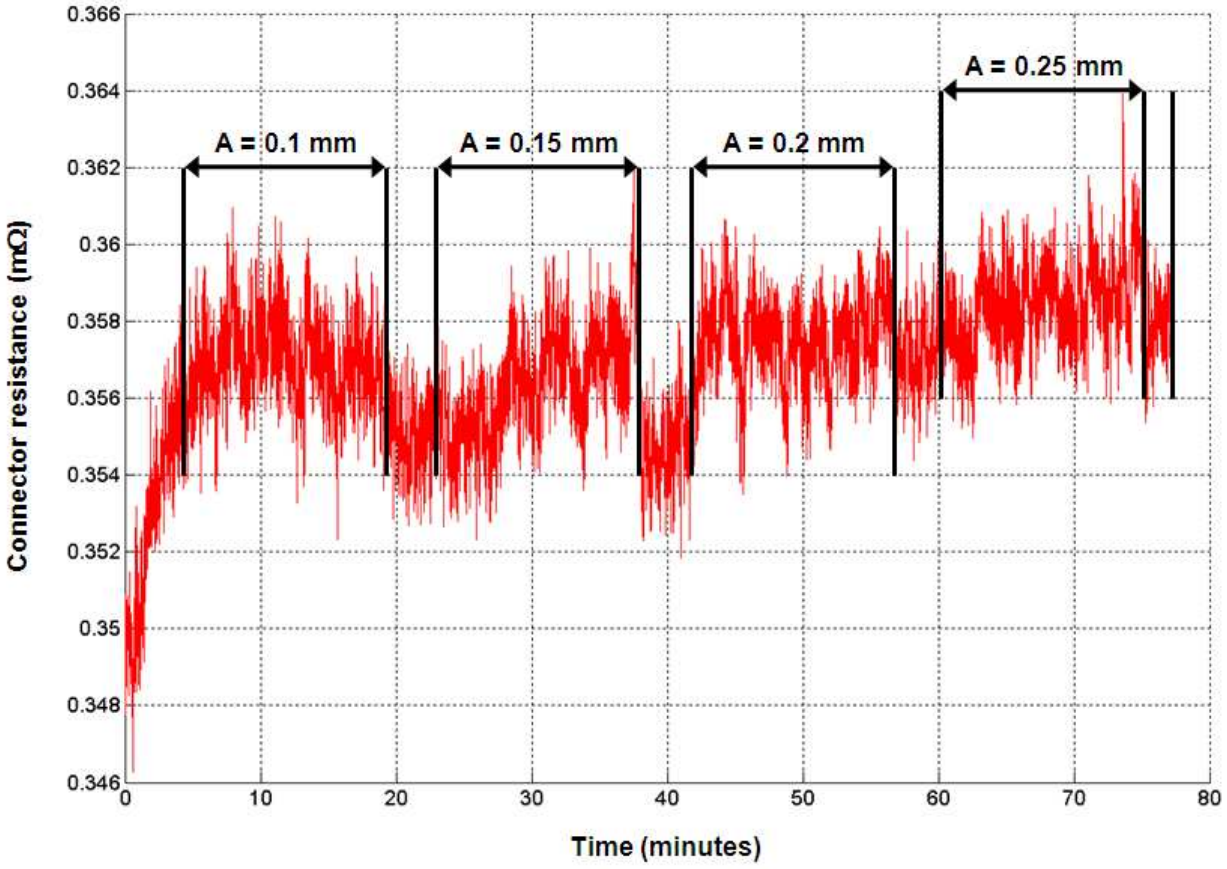

Figure B-29: Plot of connector resistance versus time for test T5 iteration 3

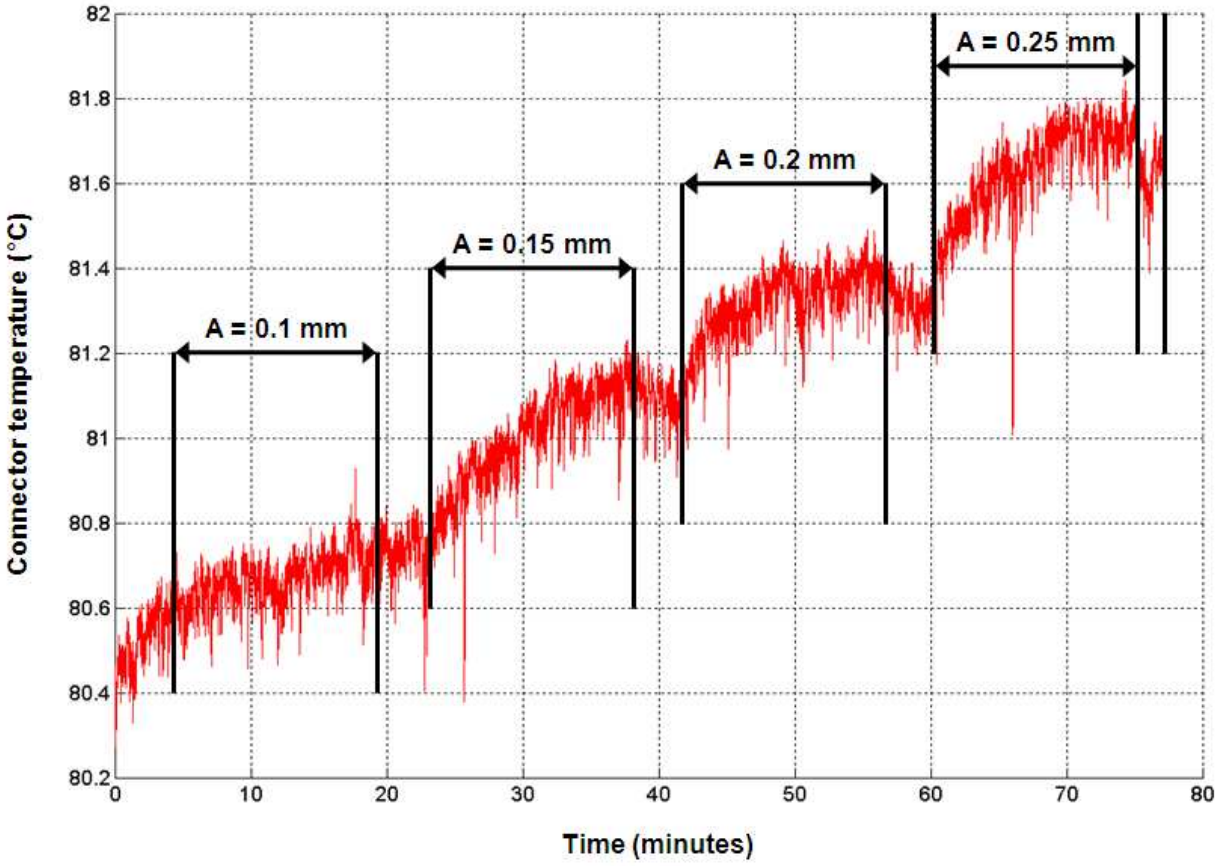

Figure B-30: Plot of connector temperature versus time for test T5 iteration 3

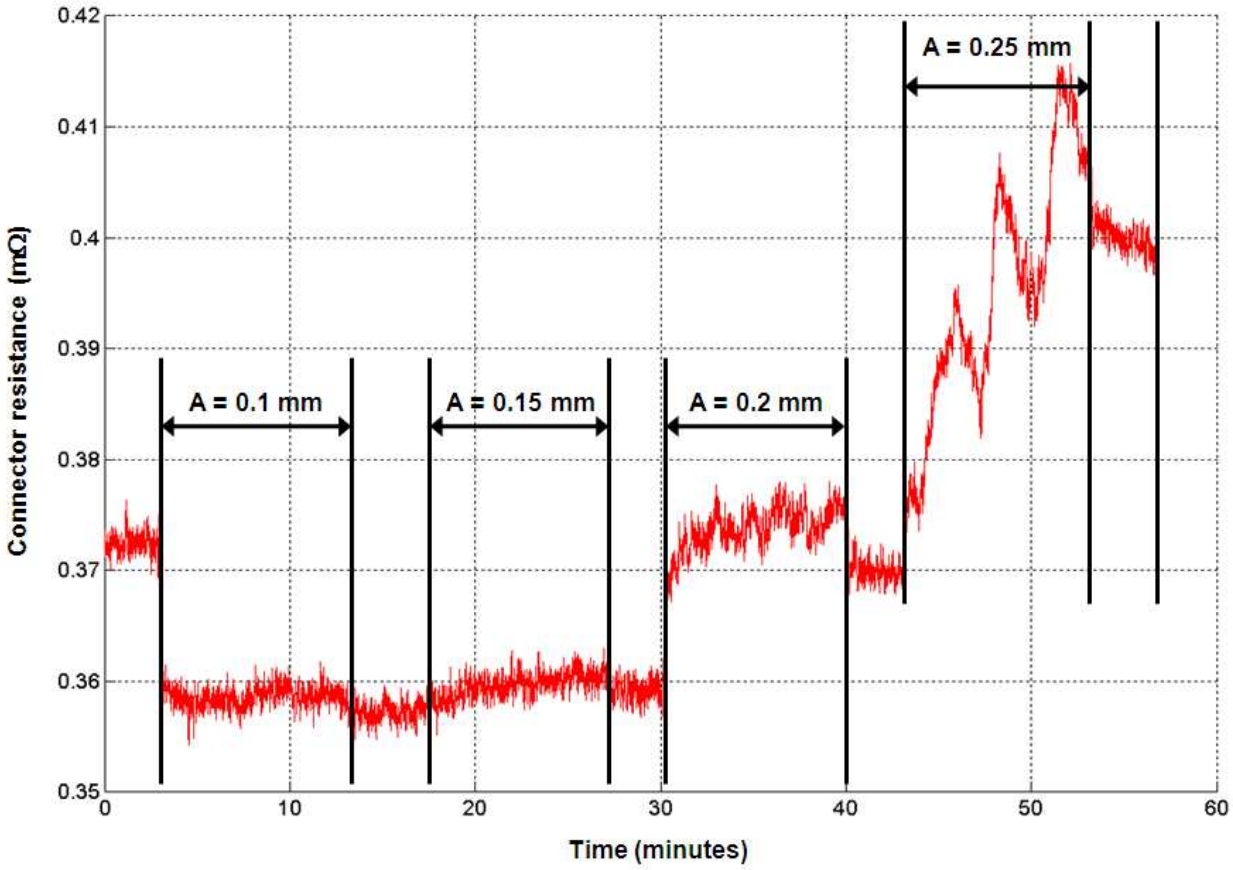

Figure B-31: Plot of connector resistance versus time for test T6 iteration 1

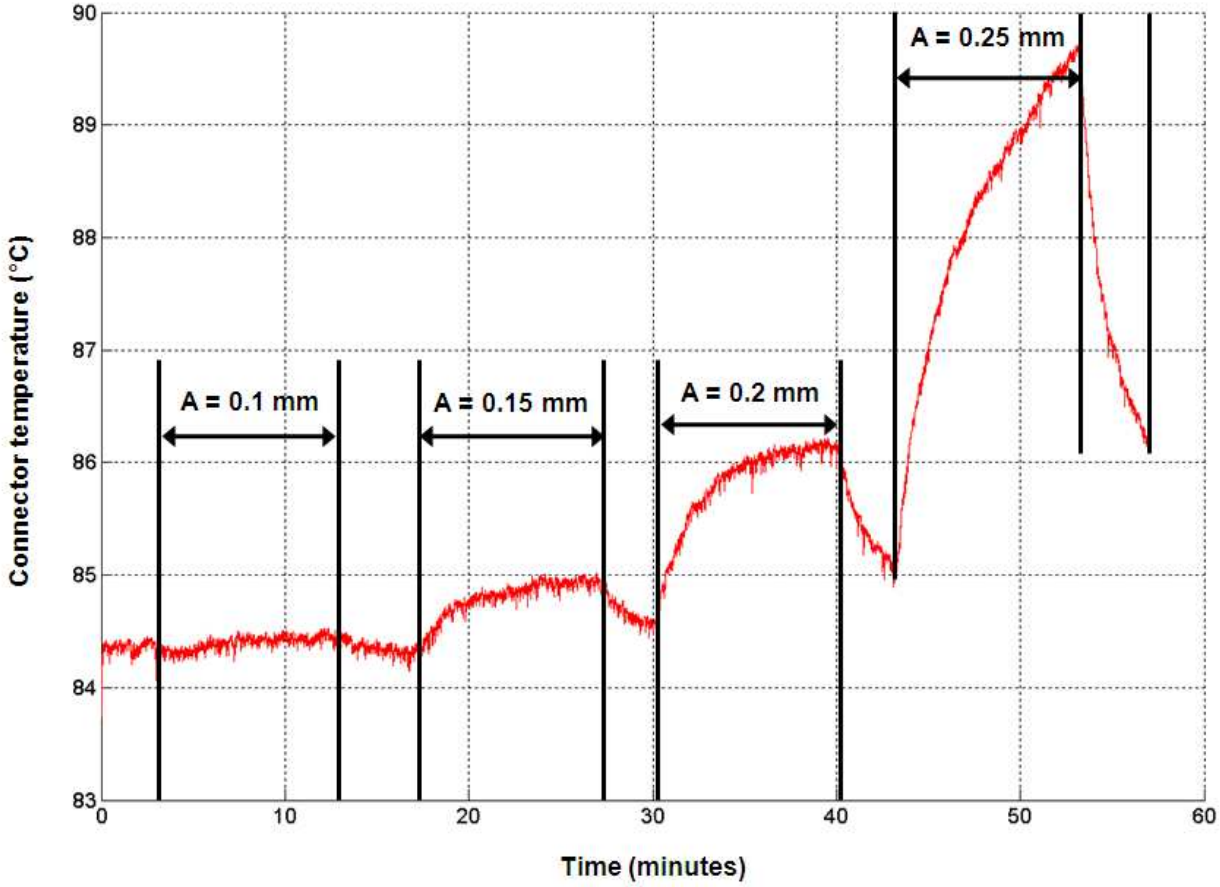

Figure B-32: Plot of connector temperature versus time for test T6 iteration 1

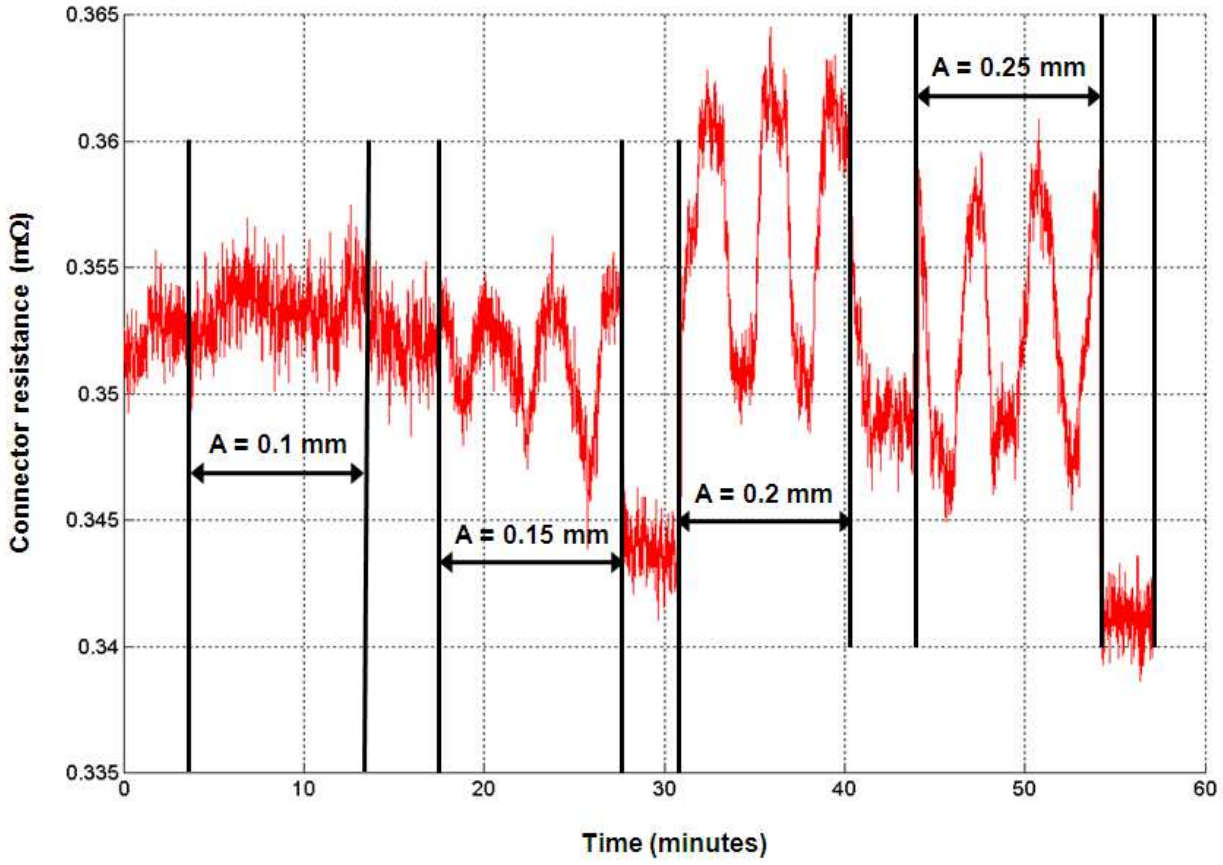

Figure B-33: Plot of connector resistance versus time for test T6 iteration 2

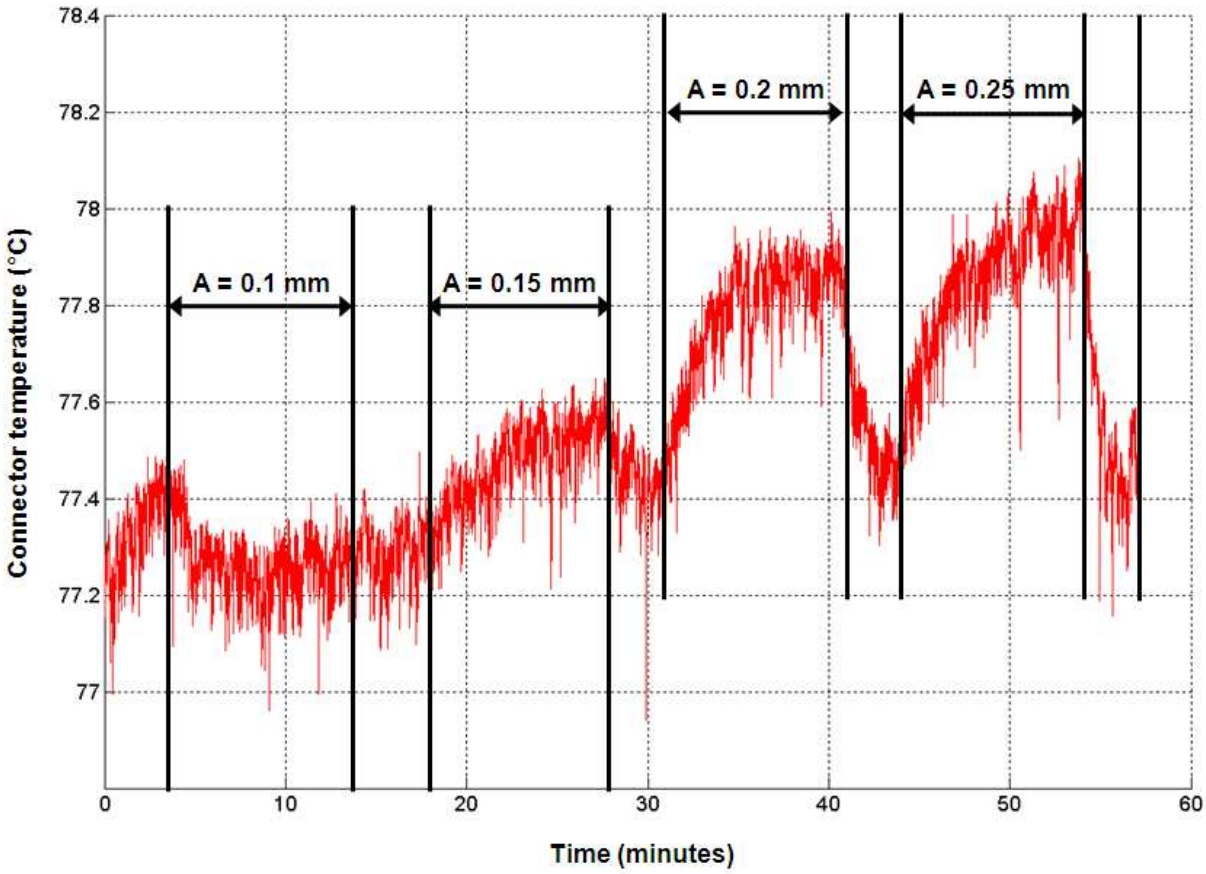

Figure B-34: Plot of connector temperature versus time for test T6 iteration 2

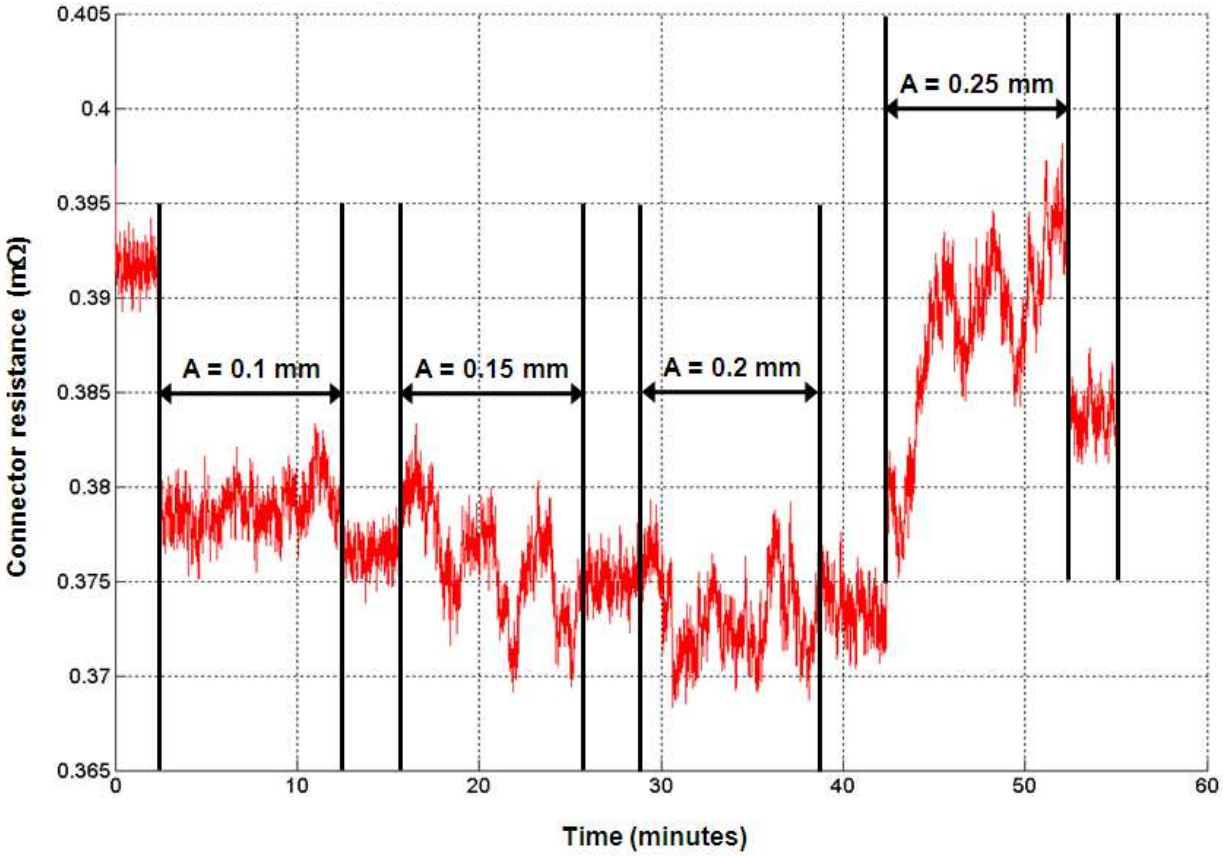

Figure B-35: Plot of connector resistance versus time for test T6 iteration 3

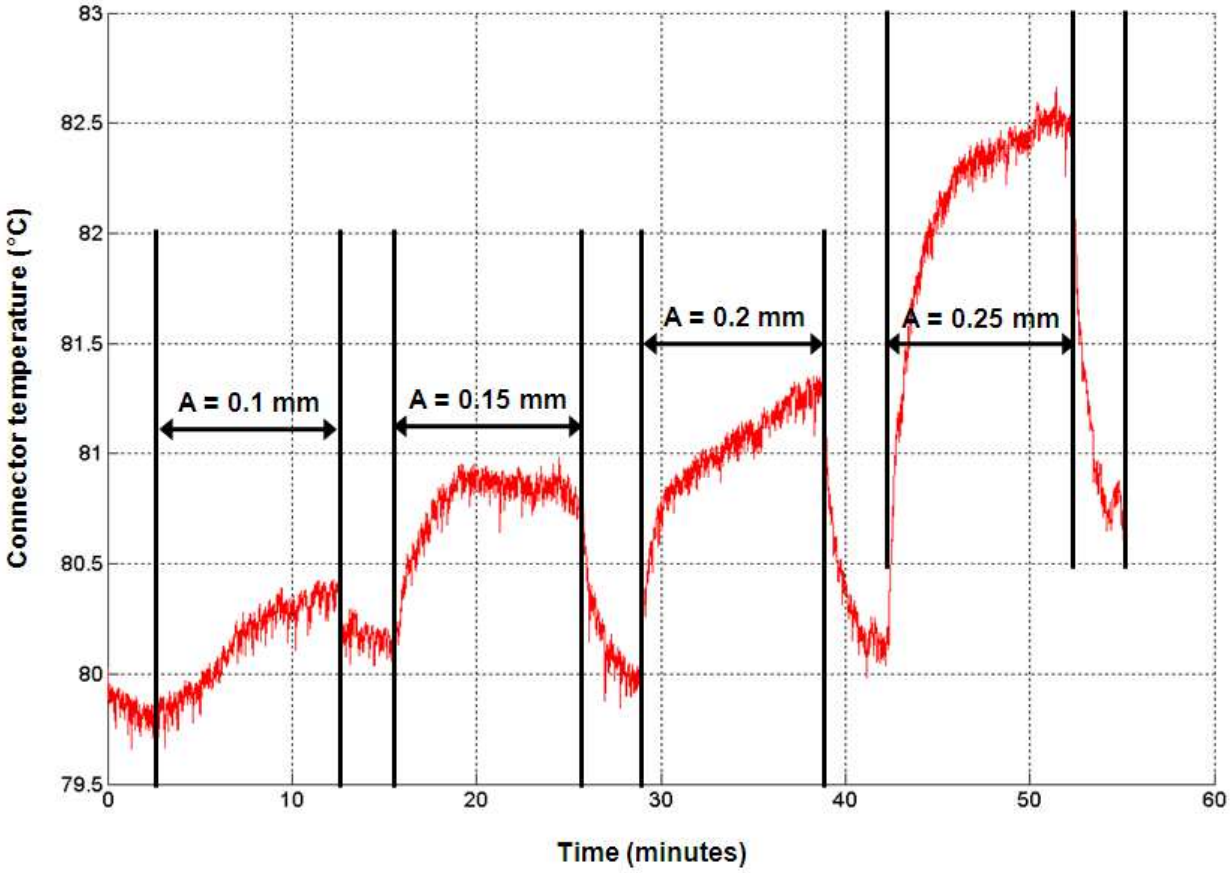

Figure B-36: Plot of connector temperature versus time for test T6 iteration 3

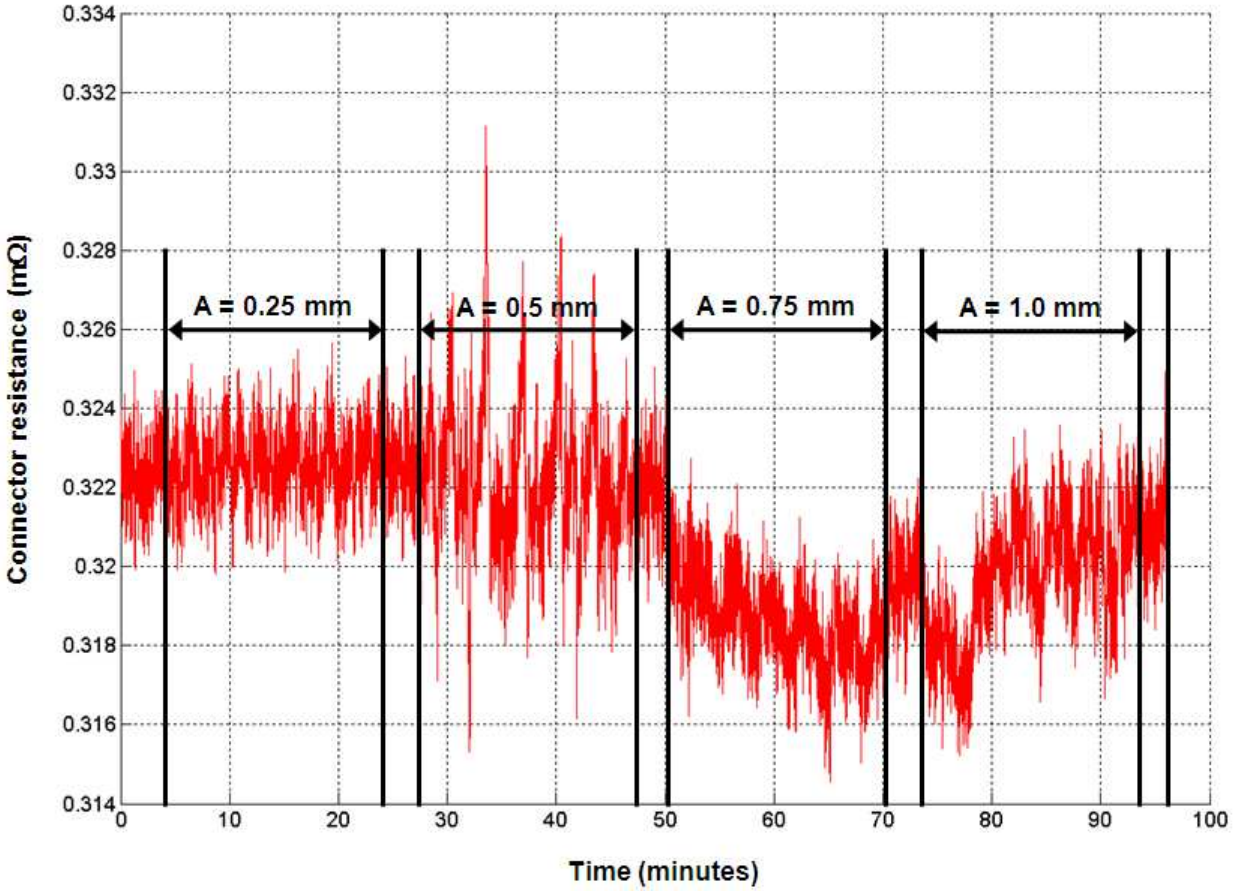

Figure B-37: Plot of connector resistance versus time for test T7 iteration 1

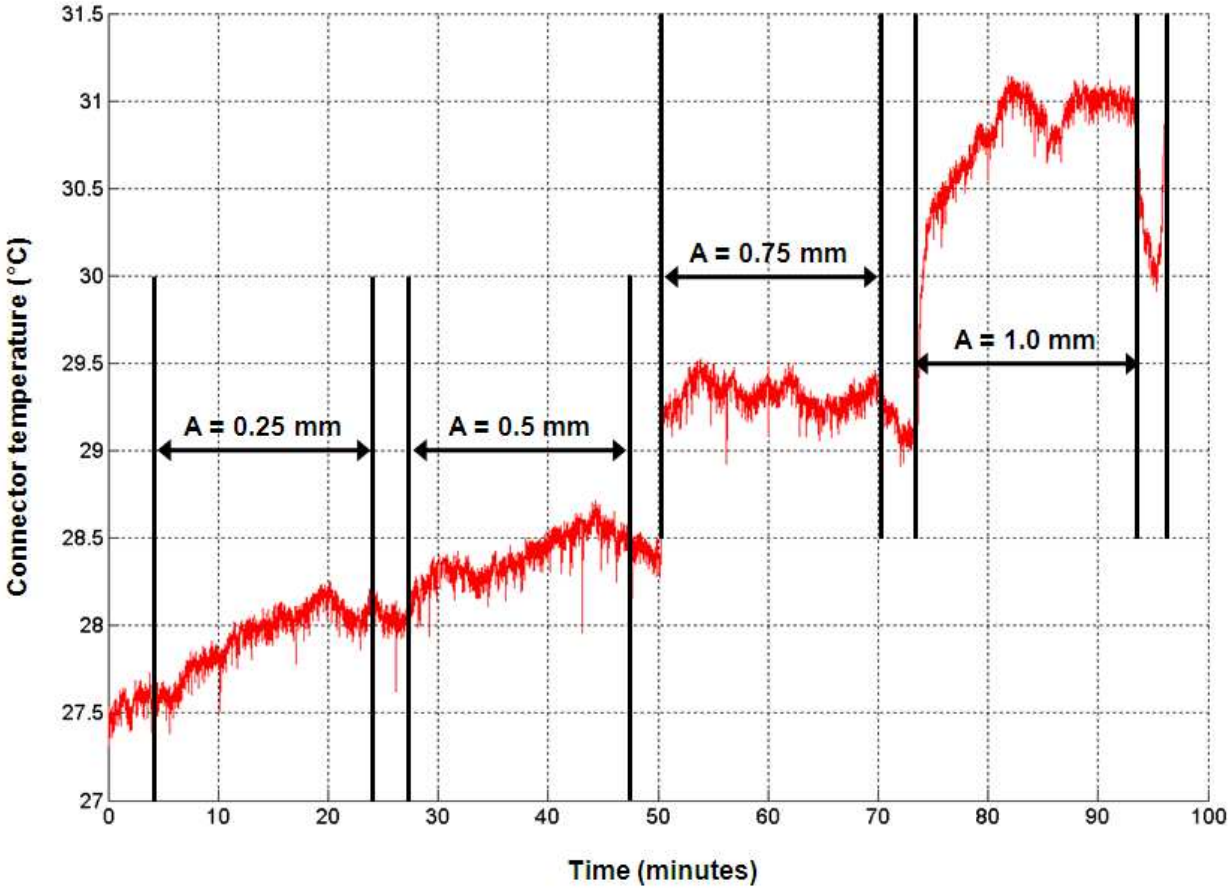

Figure B-38: Plot of connector temperature versus time for test T7 iteration 1

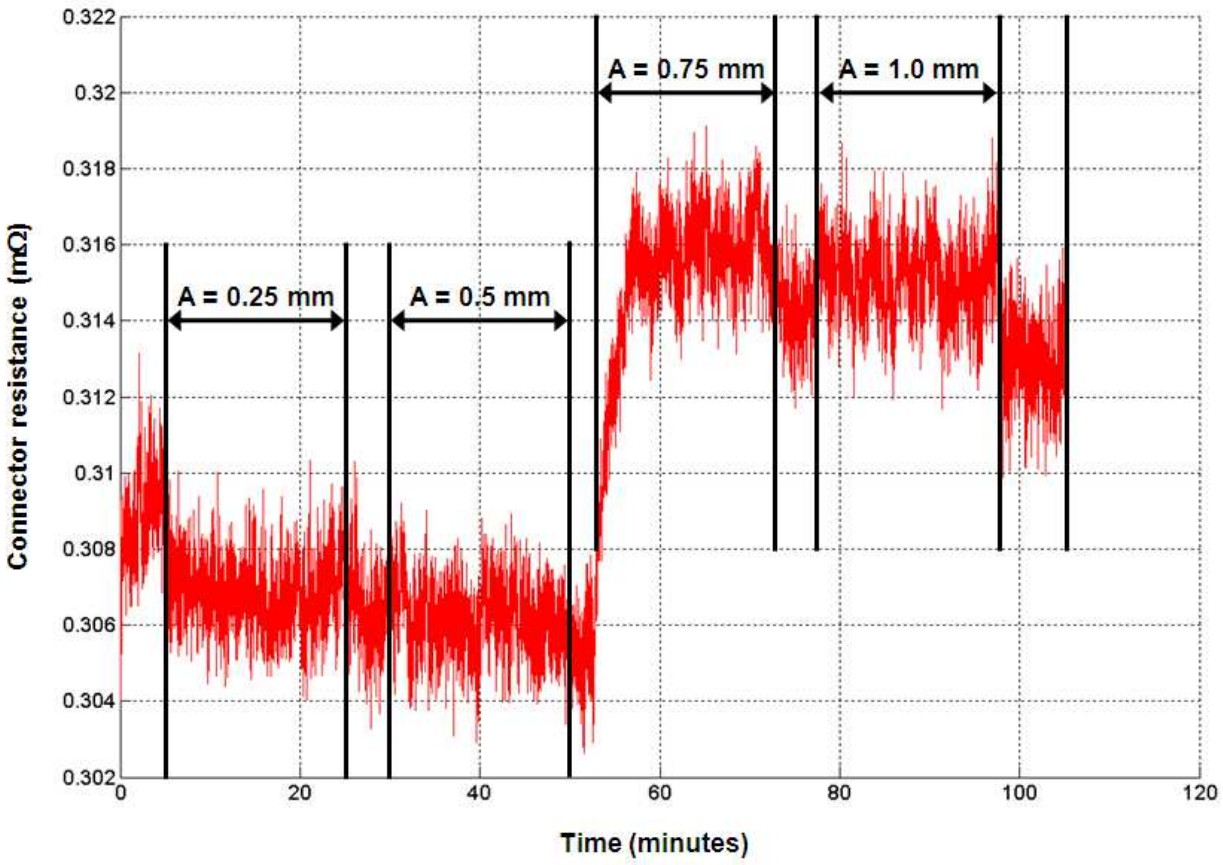

Figure B-39: Plot of connector resistance versus time for test T7 iteration 2

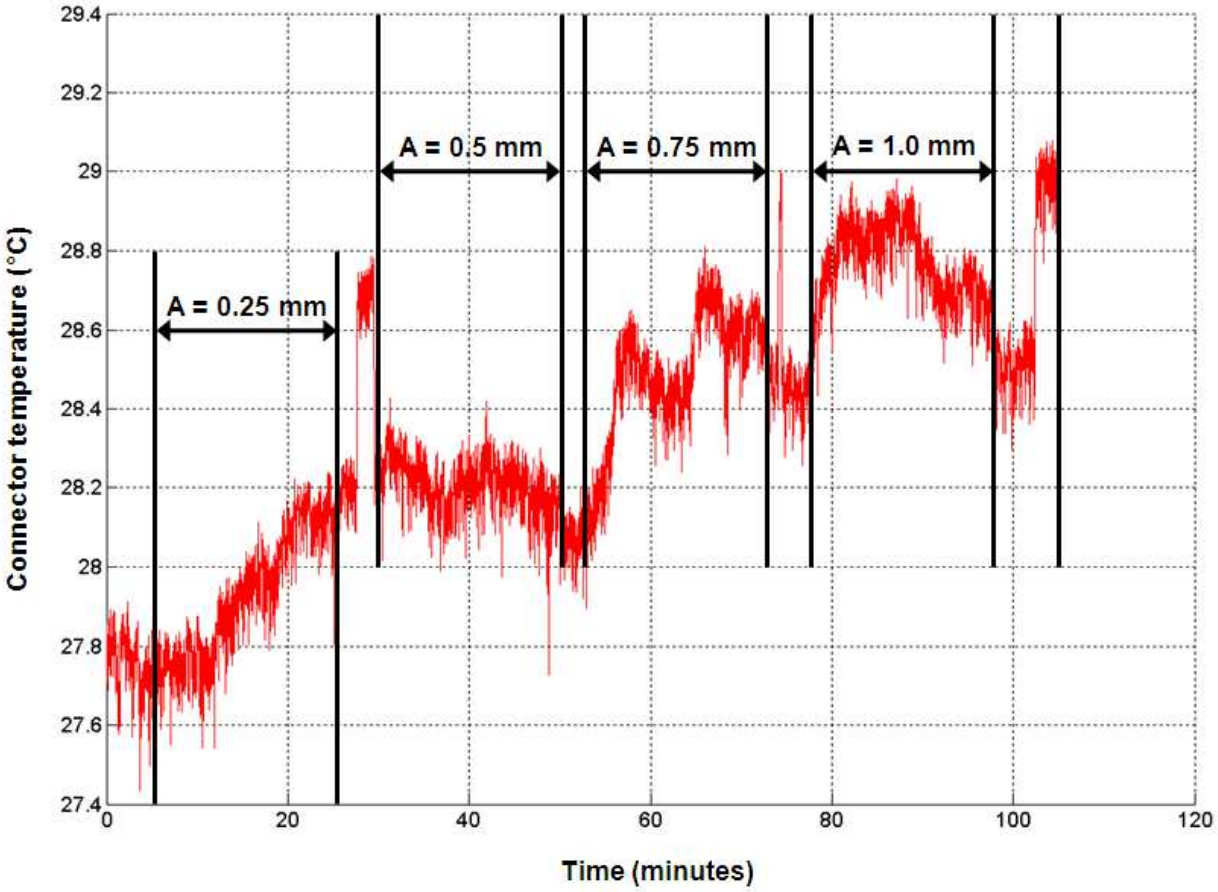

Figure B-40: Plot of connector temperature versus time for test T7 iteration 2

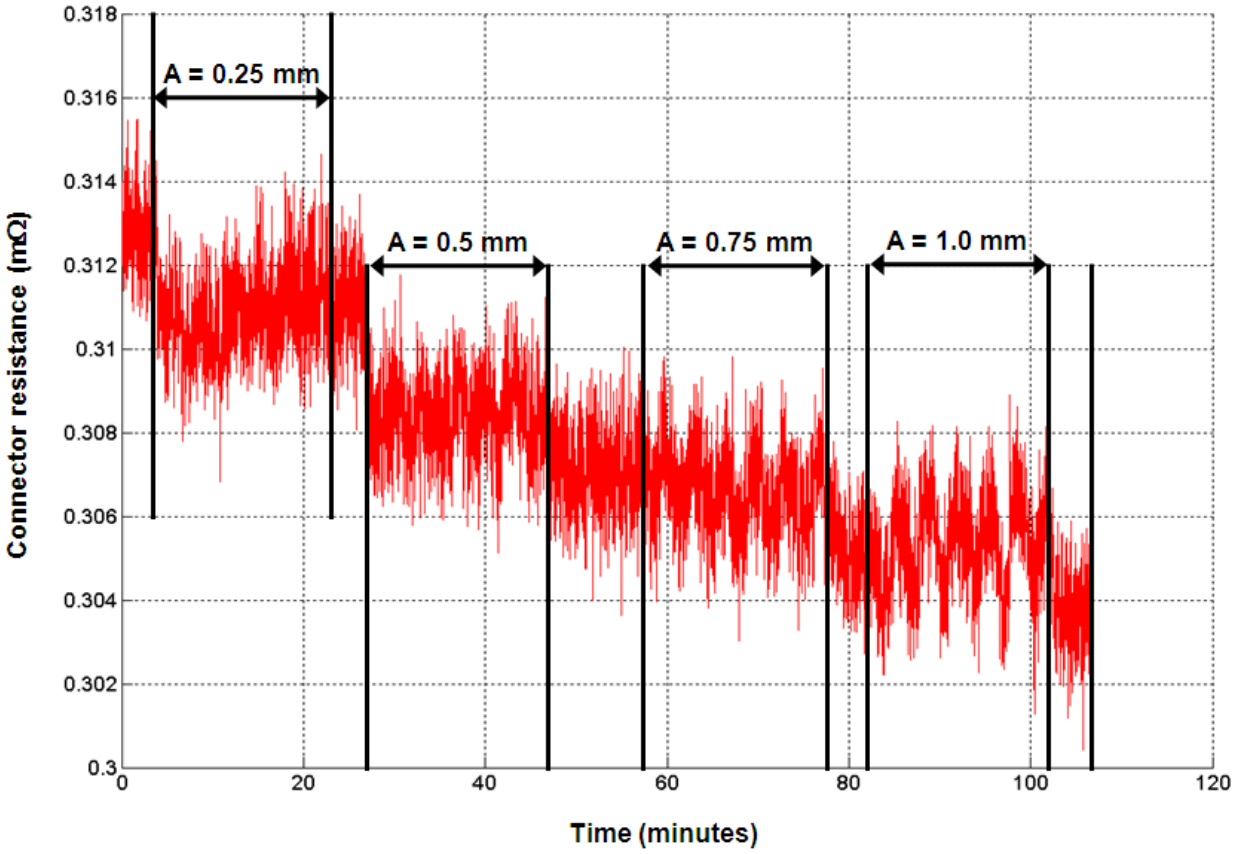

Figure B-41: Plot of connector resistance versus time for test T7 iteration 3

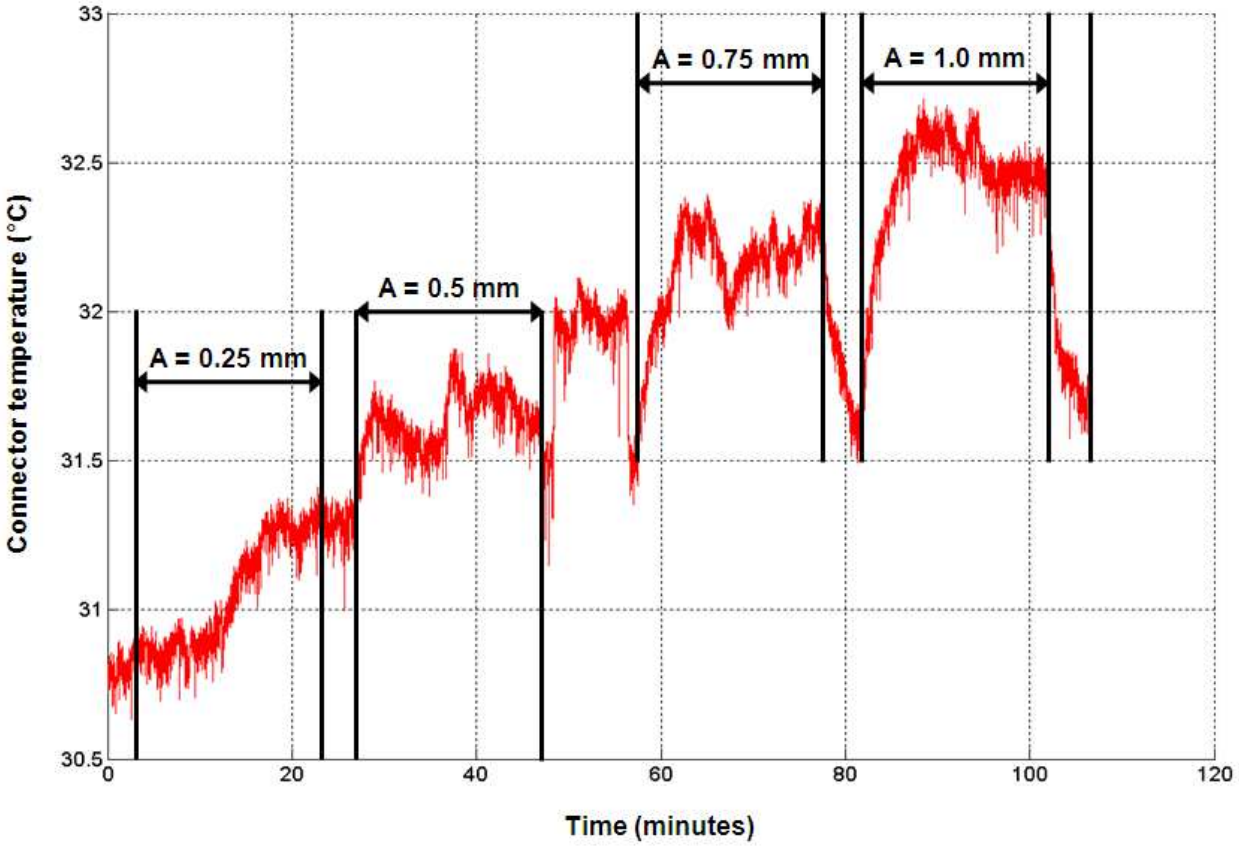

Figure B-42: Plot of connector temperature versus time for test T7 iteration 3

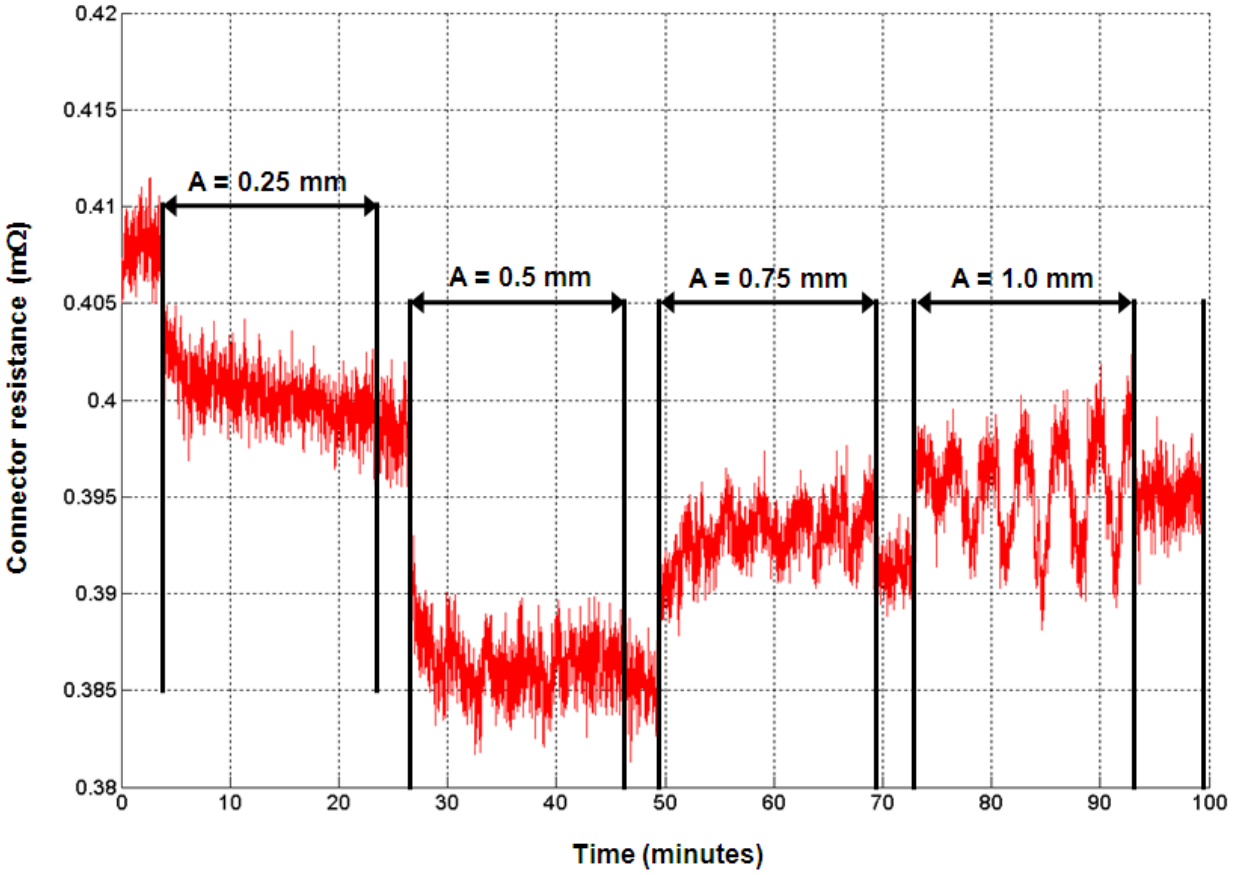

Figure B-43: Plot of connector resistance versus time for test T8 iteration 1

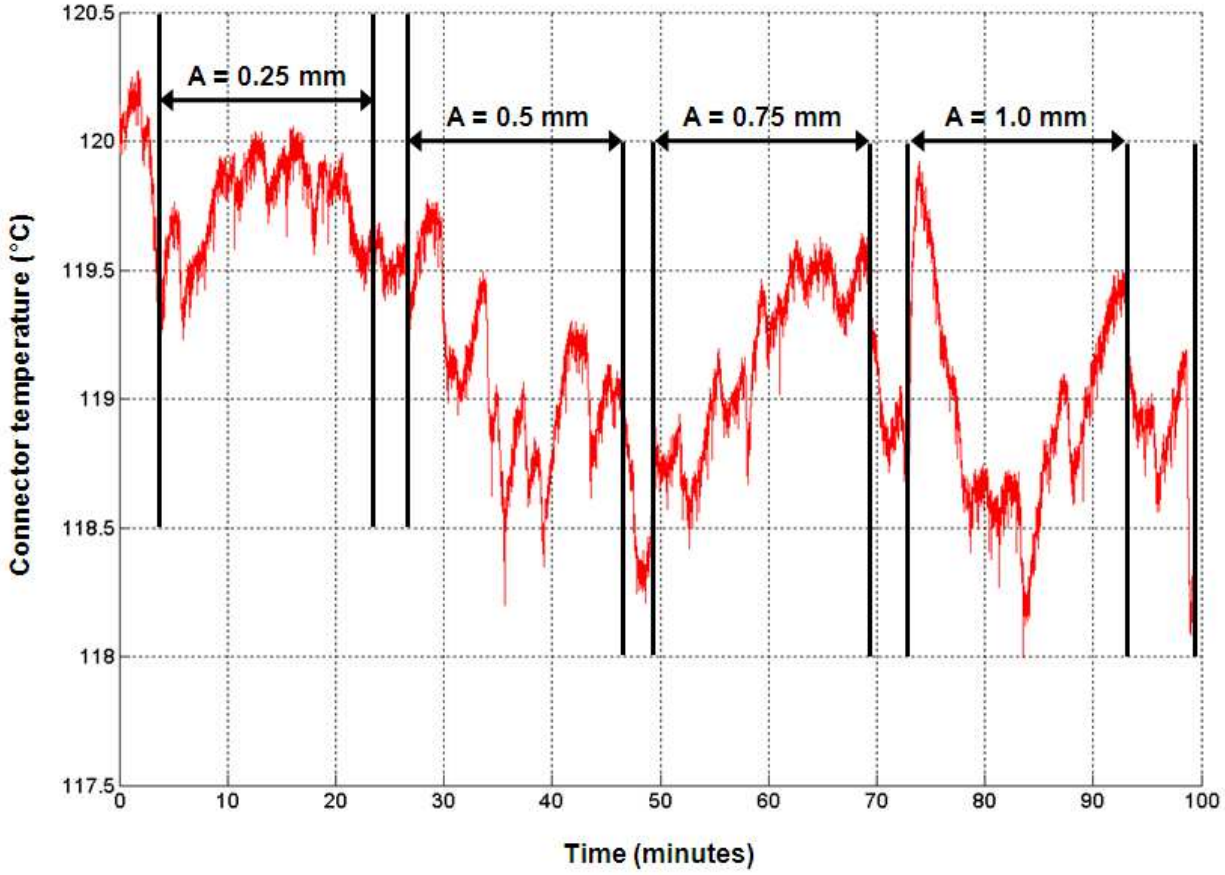

Figure B-44: Plot of connector temperature versus time for test T8 iteration 1

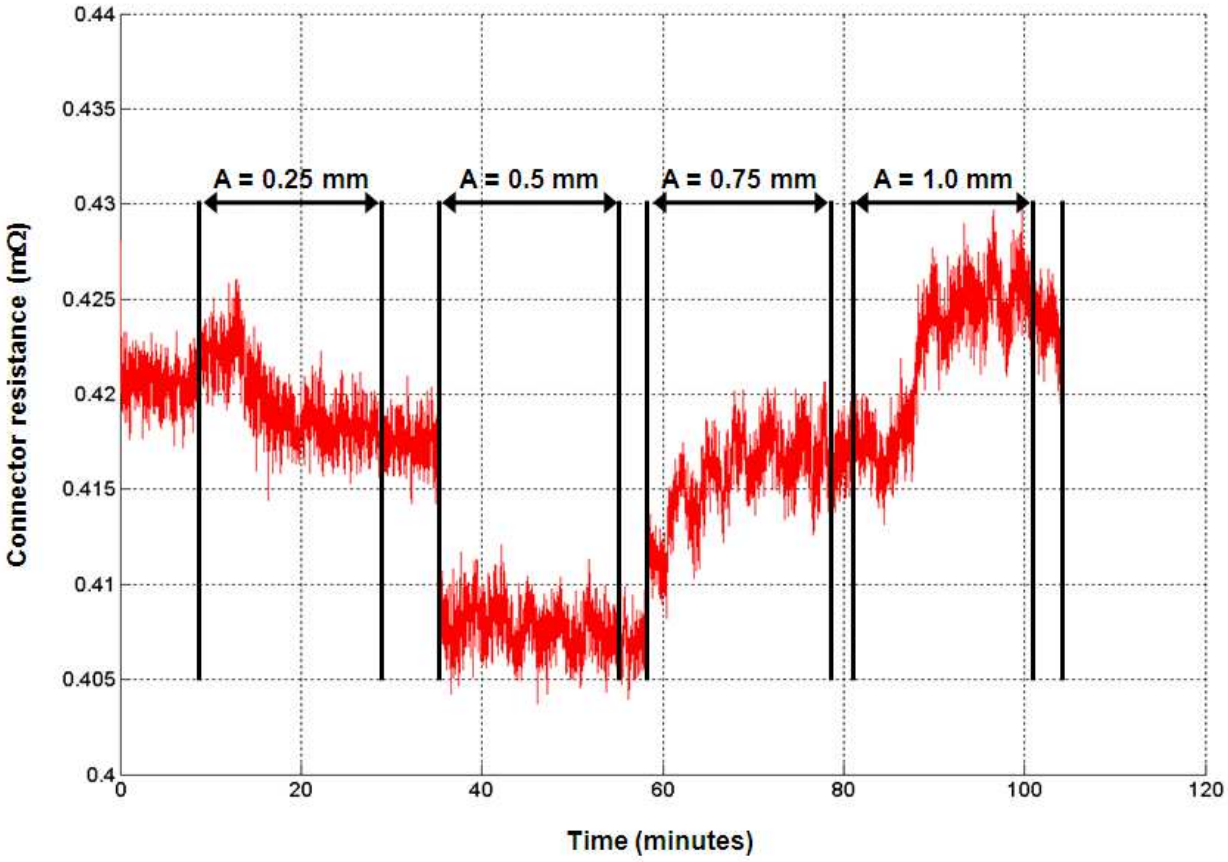

Figure B-45: Plot of connector resistance versus time for test T8 iteration 2

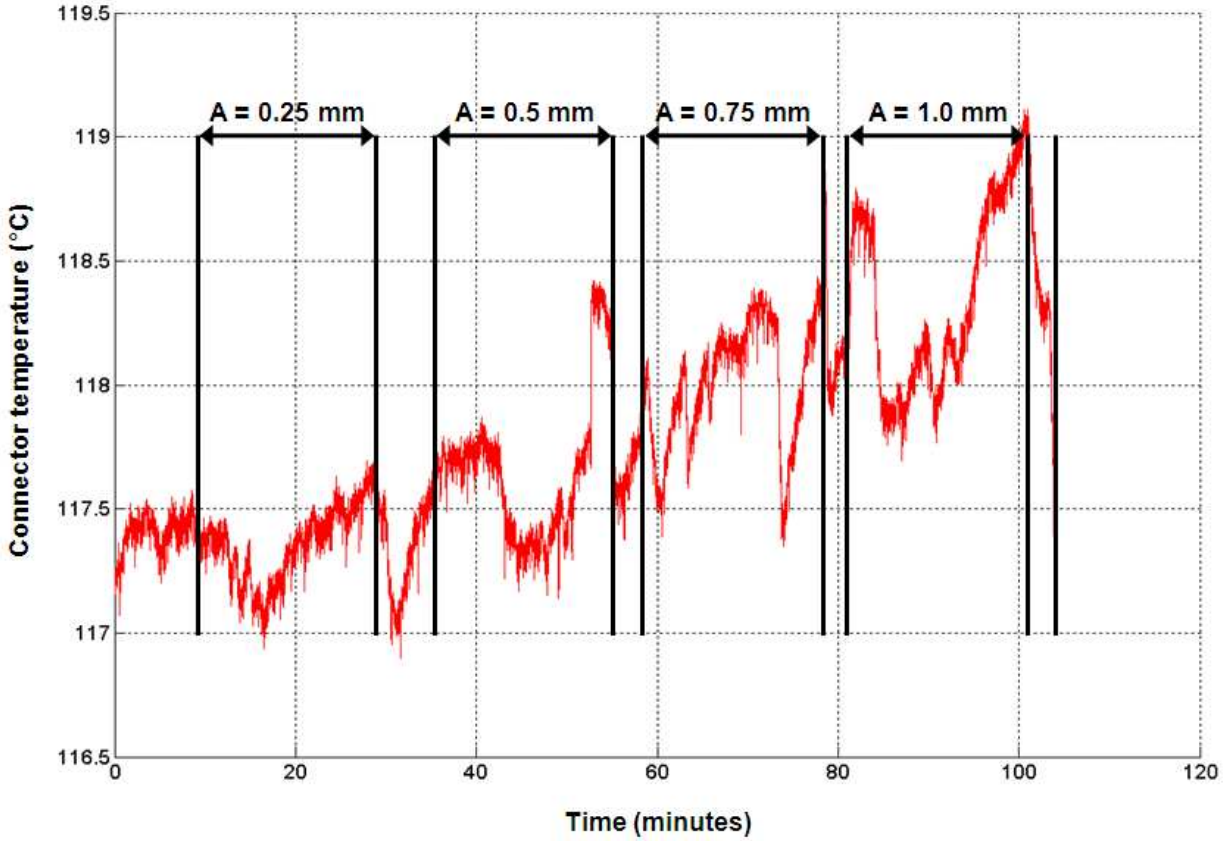

Figure B-46: Plot of connector temperature versus time for test T8 iteration 2

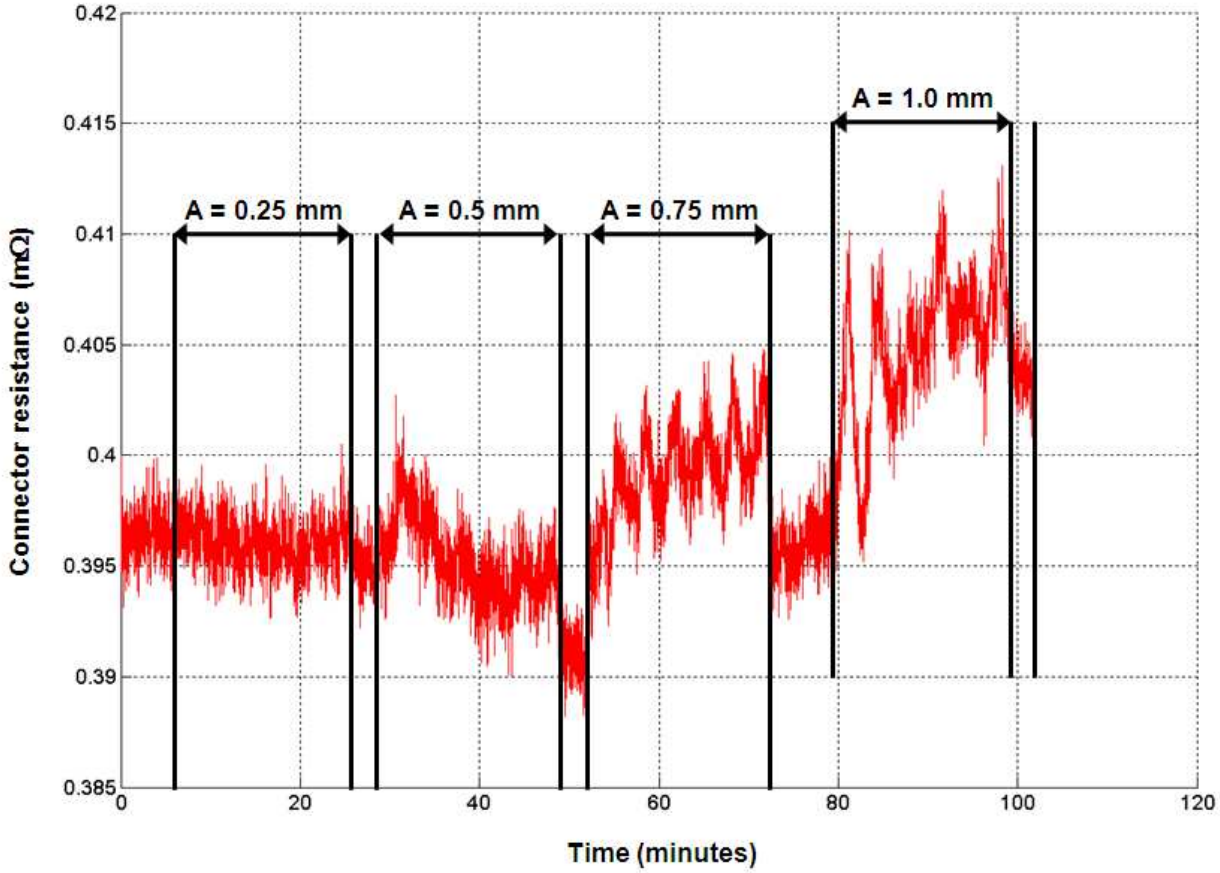

Figure B-47: Plot of connector resistance versus time for test T8 iteration 3

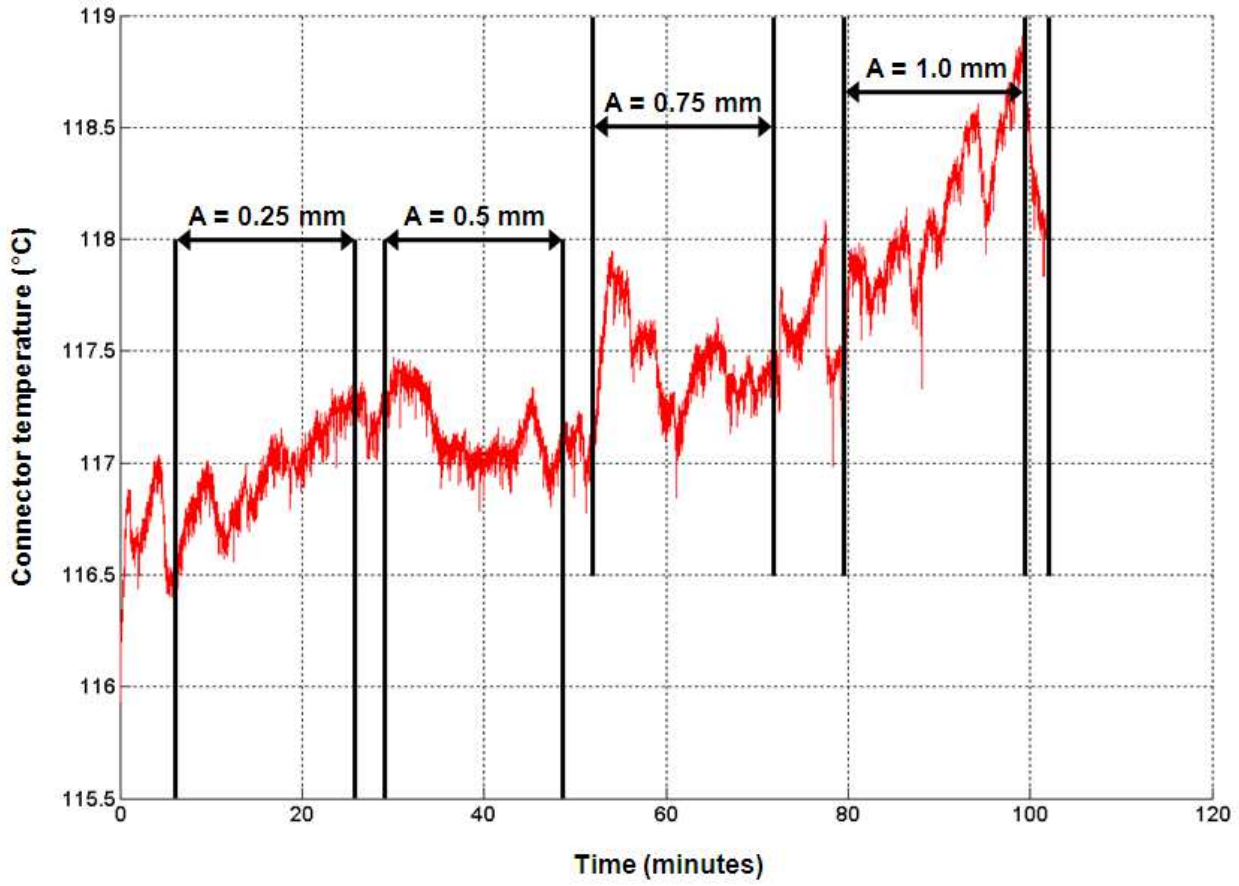

Figure B-48: Plot of connector temperature versus time for test T8 iteration 3